Study of the influence of the Reynolds number on the organization of wall-bounded turbulence

Sophie Herpin

n° d'ordre : 95

THÈSE

(version finale)
Pour l'obtention en Cotutelle du Grade de

Docteur de l'Ecole Centrale de Lille
Doctor of philosophy de l'université de Monash

Spécialité : Génie Mécanique

Présentée par :

Sophie HERPIN

Étude de l'influence du nombre de Reynolds sur l'organisation de la turbulence de paroi

Direction de thèse : Michel Stanislas / Julio Soria

soutenue le 20 avril 2009 devant le jury d'examen:

- JURY -

I. MARUSIC	Professeur, Université de Melbourne, Australie	Rapporteur
B. AUPOIX	Directeur de recherche à l'ONERA, HDR, France	Rapporteur
W. K. GEORGE	Professeur, Université Technologique de Chalmers, Suède	Examinateur
J. JIMÉNEZ	Professeur, Université polytechnique de Madrid, Espagne	Examinateur
M. STANISLAS	Professeur, Ecole Centrale de Lille, France	Directeur de thèse
J. SORIA	Professeur, Université de Monash, Melbourne, Australie	Directeur de thèse

- INVITÉ -

J.-M. FOUCAUT	Maitre de conférence, Ecole Centrale de Lille, France	Co-encadrant

Thèse préparée au sein du LML (France) et du LTRAC (Australie)
Ecole Doctorale SPI 072

Ph.D. THESIS

(final version)
submitted to obtain the joint degree of

Docteur de l'Ecole Centrale de Lille
Doctor of philosophy of Monash University

Department : Mechanical engineering

Presented by :

Sophie HERPIN

Study of the influence of the Reynolds number on the organization of wall-bounded turbulence

supervisors: Michel Stanislas / Julio Soria

Oral defence on the 20th of April 2009

- EXAMINATION BOARD -

I. MARUSIC	Professor, Melbourne University, Australia	Reviewer
B. AUPOIX	Director of research at ONERA, HDR, France	Reviewer
W. K. GEORGE	Professor, Chalmers University of Technology, Sweden	Examiner
J. JIMÉNEZ	Professor, Universidad Politécnica de Madrid, Spain	Examiner
M. STANISLAS	Professor, Ecole Centrale de Lille, France	Supervisor
J. SORIA	Professor, Monash University, Melbourne, Australia	Supervisor

- INVITED -

J.-M. FOUCAUT	Senior Lecturer, Ecole Centrale de Lille, France	Co-supervisor

Acknowledgments

This research work was realized in cotutelle between 'Ecole Centrale de Lille' (at Laboratoire de Mécanique de Lille) and Monash University (at Laboratory for Turbulence Research in Aerospace and Combustion).

- First of all, I would like to thank my two PhD supervisors, Prof. Michel Stanislas and Prof. Julio Soria, for their availability and scientific guidance during the course of this thesis. More specifically, I would like to thank Michel Stanislas for his expertise in the physics of near-wall turbulence, and Julio Soria for his contagious enthusiasm about scientific research.
- I would also like to thank my co-supervisor, Dr. Jean-Marc Foucaut, for his support and multiple discussions on the PIV experiments, but also for his guidance in my teaching activities at 'Ecole Centrale de Lille' during the last year of this PhD degree.
- I would like to thank the members of my examination board, including Prof. Ivan Marusic, Dr. Bertrand Aupoix, Prof. Bill George and Prof. Javier Jiménez for raising interesting points during the PhD defense. The valuable comments of Bertrand Aupoix and Ivan Marusic when reviewing this thesis are much appreciated.
- Sincere thanks to Dr. Sebastien Coudert, research engineer at LML, for his help during the PIV experiments in Lille and for usefull advice regarding the development of the post-processing software.
- I also wish to thank Dr. Chong Yau Wong for his support with the water-tunnel facility and the PIV equipment at LTRAC.
- The support of the technical and administrative staff, both at 'Laboratoire de Mécanique de Lille' and at Monash University is also gratefully acknowledged.
- I also wish to thank all my colleagues at both institutions, and especially at Monash (Daniel Mitchell, Jérémy Basley, Callum Atkinson, Jim Kostas, Romain Mathis ...) for their friendship that made this year in Australia a fantastic experience. I also enjoyed the friendly company of my colleagues in Lille: Julien Jouanguy (and Gaëlle), Laurent Perret, Julianna Abrantes, Callum Atkinson (again !!), Javier Lechuga, Vincent Magnier, Ludovic Cauvin, Rostislav Dolganov...
- And last and not least, I wish to express my sincere gratitude to my partner, my family and my friends for their unconditionnal support during this hard-working period.

Abstract

This work is an experimental study of the influence of the Reynolds number on the characteristics of the streamwise and spanwise vortical structures in near-wall turbulence.
Stereo-PIV measurements in streamwise/wall-normal (XY) and spanwise/wall-normal (ZY) planes of turbulent boundary layer flow are conducted in the LTRAC water-tunnel and LML wind-tunnel at six Reynolds numbers comprised between $Re_\theta = 1300$ and $Re_\theta = 18950$. The measurements feature good spatial resolution and low measurement uncertainty. The database is validated through an analysis of some single-points statistics (mean and RMS velocity, PDF of the fluctuations) and of the power spectra, compared with reference profiles from theory, hot-wire measurements and DNS data.
A coherent structure detection is then undertaken on the SPIV database, as well as on a DNS dataset at $Re_\tau = 950$. The detection is based on a fit of an Oseen vortex to the velocity field surrounding extrema of 2D swirling strength. The wall-normal evolution of some statistical quantities (mean, RMS, PDF) of the vortex characteristics (radius, vorticity, circulation, convection velocity...) is analyzed, using two different scalings: the wall-unit scaling and the Kolmogorov scaling. In wall-unit scaling, a good universality in Reynolds numbers is observed in the near-wall and logarithmic region, but some Reynolds number effects are visible in the outer region of the flow. In contrast, the Kolmogorov scaling was found to be universal both in Reynolds number and wall-normal distance across the three regions investigated. Finally, the results obtained are interpreted in terms of vortices generation mechanisms.

Extended abstract in French (Résumé en Francais)

Ce travail est une étude experimentale de l'influence du nombre de Reynolds sur les structures tourbillonnaires longitudinales et transverses de la turbulence de paroi.
Le mémoire de thèse est organisé en 7 chapitres.

Chapitre 1 : Les structures cohérentes de la turbulence de paroi
L'étude des écoulements turbulents proches paroi revêt une importance de premier plan pour de nombreuses applications indutrielles. La production et la dissipation de la turbulence sont liées à l'organisation de l'écoulement en structures cohérentes (Robinson (1991)); parmi ces structures, les tourbillons longitudinaux et tranverses jouent un rôle essentiel car ils assurent le transport de masse et de quantité de mouvement à travers le gradient moyen de vitesse normal à la paroi. Les caratéristiques physiques de ces structures, leur origine ainsi que l'influence du nombre de Reynolds demeurent des problèmes non resolus de la turbulence. L'objectif de cette étude est d'apporter des éléments nouveaux de compréhension à ces questions fondamentales.

Chapitre 2 : la Vélocimétrie par Images de Particules
La Vélocimétrie par Images de Particules (PIV) est une technique de mesure de champs qui donne accès à la distribution de vitesse instantanée, projetée dans un plan de l'écoulement. L'usage de deux caméras pour enregistrer les images de particules sous deux angles de vues différents permet d'éliminer les erreurs de perspectives, mais aussi d'accéder à la composante de vitesse orthogonale au plan de mesure. Cette technique s'appelle la PIV stéréoscopique (SPIV). Elle est particulièrement adaptée à l'étude des structures tourbillonaires de la turbulence, qui, par essence, est tridimensionnelle. Comme toute technique de mesure, la PIV stéréoscopique présente des incertitudes de mesure et dispose d'une résolution spatiale limitée. Leur niveau est critique pour l'étude des structures tourbillonaires turbulentes (Herpin et al (2008)), et les paramètres de la stéréo-PIV doivent être soigneusement ajustés en conséquence.

Chapitre 3 : Mesures SPIV dans le tunnel à eau du LTRAC
La stéréo-PIV est employée pour mesurer l'écoulement dans un plan longitudinal/normal (XY) à la paroi de la couche limite turbulente dans le tunnel à eau du LTRAC, à deux nombres de Reynolds modérés : $Re_\theta = 1300$ et $Re_\theta = 2200$. L'écoulement extérieur présente un taux de turbulence élevé de l'ordre de $2.6\%U_\infty$ et $5.4\%U_\infty$ respectivement. Les différents paramètres PIV sont résumés dans la table 3.2. Le setup employé est constitué de 4 caméras PCO 4000 disposant d'un large capteur CCD ($4008 * 2672$ px^2),

arrangées en deux systèmes stéréoscopiques alignés dans la direction longitudinale. Les champs de vue de ces deux systèmes présentent une région de recouvrement pour assurer la continuité des données. Ce dispositif permet d'augmenter la taille du champ total mesuré tout en conservant une bonne résolution des petites échelles. L'angle de vue stéréoscopique nominal est fixé à 30°. L'évaluation des images SPIV est réalisé avec le code du LML, et utilise une reconstruction de Soloff (Soloff et al (1997)) avec correction de désalignement entre la mire de calibration et le plan laser. La taille finale des fenêtres d'interrogation est de 15^+. L'incertitude de mesure est évaluée dans la zone de recouvrement des deux systèmes stéréoscopiques : elle est de l'ordre de $0.75\%U_\infty$ sur les composantes de vitesse dans le plan, et de $1.5\%U_\infty$ sur la composante normale au plan. Finalement, les champs de vitesse sont obtenus sur un maillage avec un pas de 4.5^+, et leur taille est de $[S_x; S_y] = [4\delta; 1.4\delta]$ à $Re_\theta = 1300$ et de $[S_x; S_y] = [2.6\delta; 0.75\delta]$ à $Re_\theta = 2200$ (cf table 3.5).

Chapitre 4 : Mesures SPIV dans la soufflerie du LML
Les mesures stéréo-PIV dans la soufflerie du LML sont réalisées dans des plans longitudinaux/normaux (XY) et dans des plans normaux/transversaux (YZ) de la couche limite turbulente, à 4 nombre de Reynolds plus élevés: $Re_\theta = 7630, 10140, 13420, 18950$. Le principe de mesure est similaire à celui employé dans le LTRAC, avec 4 caméras disposées en 2 systèmes stéréo, mais cette fois avec les champs de vue alignés dans la direction normale à la paroi. L'angle de vue stéréoscopique nominal est fixé à 45°. Pour les mesures dans le plan orthogonal à l'écoulement moyen (YZ) les 2 nappes laser sont décalées dans la direction 'x' afin de garder un haut niveau de corrélation et une bonne dynamique de mesure malgré les mouvements hors-plan importants. Les paramètres PIV sont rassemblés dans la table 4.3, et les images sont évaluées avec le même code (celui du LML) sur des fenêtres d'interrogation dont la taille est comprise entre 11^+ et 21^+, selon le nombre de Reynolds. L'incertitude de mesure est évaluée dans la zone de recouvrement des deux systèmes stéréoscopiques : elle est de l'ordre de $0.7\%U_\infty$ sur toutes les composantes de vitesse. Finalement, les champs de vitesse sont obtenus sur un maillage avec un pas compris entre 3^+ et 6^+, et ont une taille entre $[S_{x/z}; S_y] = [0.08\delta; 0.3\delta]$ et $[S_{x/z}; S_y] = [0.15\delta; 0.6\delta]$ environ (cf table 4.7).

Chapitre 5 : Validation de la base de données
La base de données constituée des champs de vitesse dans les plans XY et YZ aux 6 nombres de Reynolds compris entre $Re_\theta = 1300$ et $Re_\theta = 18950$ est validée aux travers de l'analyse du profil moyen de vitesse, des composantes du tenseur de Reynolds, des densités de probabilité (PDF) des fluctuations normalisées, et des spectres de puissance. Ces grandeurs sont comparées à des profils de référence issus de la théorie, de mesures fils chauds, ou de données de Simulation Numérique Directe (DNS). Les profils moyens et les composantes du tenseur de Reynolds obtenus par la PIV montrent un très bon accord avec les profils de référence, à l'exception d'un effet du fort taux de turbulence dans le tunnel à eau du LTRAC. L'analyse des PDFs des fluctuations mettent en évidence un effet de peak-locking sur l'ensemble de la base de données, mais sur la composante dans le plan non-reconstruite uniquement. Le peak-locking est quantifié, et il est montré que son impact sur les moments de la vitesse est négligeable. Les spectres de puissance présentent un très bon accord avec la référence à nombre d'ondes faibles et moyens; en revanche, l'effet du bruit de mesure est notable dans la gamme des hauts nombres d'onde. Une méthodologie developpée dans Herpin et al (2008), et s'appuyant sur un modèle du spectre de PIV proposé par Foucaut et al (2004), permet de retrouver le nombre d'onde à un rapport signal sur bruit (SNR) de 1, et d'en déduire le rayon des tourbillons résolus

avec SNR=1.

Chapitre 6 : Détection des structures cohérentes

La méthodologie employée pour détecter et caractériser les structures tourbillonnaires dans les champs de vitesse se décompose en trois étapes principales : le calcul d'une fonction locale de detection de tourbillon, la localisation des extréma de cette fonction, et l'ajustement d'un modèle de tourbillon sur le champs de vitesse PIV dans le voisinnage de ces extréma. La fonction de détection utilisée est basée sur l'intensité tourbillonnaire, définie comme la partie imaginaire des valeurs propres complexes du tenseur de gradient de vitesse. Cette fonction est normalisée par son profil d'écart-type, et seuls les extréma excédant une valeur seuil de cette fonction normalisée sont retenus. Le modèle choisi pour l'ajustement est un tourbillon d'Oseen. Cette étape permet d'une part de valider que les extréma correspondent effectivement à une structure tourbillonnaire, et le cas échéant d'obtenir les caractéristiques des tourbillons (rayon, circulation, position du centre, vitesse de convection...) au travers des paramètres du modèle ajusté.

Cette technique est appliquée à la base de données expérimentale, ainsi qu'à une base de données issue de la DNS d'un canal plan à $Re_\tau = 950$ (DelAlamo et al (2006)). Les tourbillons détectés dans les plans XY correspondent aux tourbillons transverses, et les tourbillons détectés dans les plans YZ correspondent aux tourbillons longitudinaux. L'effet de la résolution spatiale de la PIV sur l'estimation du rayon des tourbillons détectés est caractérisé : il est montré qu'une détoriation de la résolution résulte en une sur-estimation du rayon.

Une analyse statistique est ensuite menée sur la densité, le rayon, la vorticité, et la vitesse de convection des tourbillons détectés. L'évolution avec la distance à la paroi des valeurs moyennes de ces grandeurs est notamment étudiée. Les PDF de rayon et de vorticité, ainsi que les écarts-type des vitesses de convection sont également analysés. L'influence du nombre de Reynolds est étudiée au travers de deux représentations adimensionnées : l'une en unités de paroi, l'autre en unités de Kolmogorov.

Chapitre 7 : Discussion

Les résultats statistiques de la détection des tourbillons sont interprétés pour obtenir une description précise de la population de tourbillons, étudier l'influence du nombre de Reynolds sur leur rayon et vorticité, et discuter des mécanismes responsables de leur formation.

Dans l'ensemble, il apparait que les tourbillons sont convectés en moyenne avec la vitesse de l'écoulement, l'écart-type de cette vitesse de convection étant légèrement inférieure à celle de l'écoulement, indiquant que les tourbillons sont en moyenne plus stables que leur environnement. A tout les nombres de Reynolds, la région très proche de la paroi est la plus densément peuplée, majoritairement avec des tourbillons longitudinaux qui sont en moyenne plus petits et plus intenses que les tourbillons transversaux. Ces derniers sont majoritairement de la forme prograde (qui tournent dans le sens du gradient de vitesse moyen). Les zones logarithmique et externe, quand à elles, sont constituées à part égales de tourbillons longitudinaux et transversaux, de rayon et vorticité semblables, et dont la densité diminue lorque la distance à la paroi augmente.

Deux adimensionnements sont testés pour le rayon et la vorticité : celui en unités de paroi, et celui de Kolmogorov. En unités de paroi, une bonne universalité en Reynolds est observée dans la zone tampon et la zone log : la vorticité est maximale à la paroi, et décroit de facon exponentielle avec la distance à la paroi. Le rayon moyen, pour sa part, augmente lentement avec la distance à la paroi dans ces deux zones, à l'exception

des tourbillons longitudinaux dont le rayon augmente fortement avec 'y' dans la zone très proche paroi. L'adimensionnement en unité de paroi présente des déficiences dans la zone externe où des effets de Reynolds sont notables. En revanche, l'adimensionnement en unités de Kolmogorov permet d'atteindre l'universalité à la fois en Reynolds et en 'y' à travers les trois régions de l'écoulement étudiées, avec dans la zone log un rayon de 8η et une vorticité de $1.5\tau^{-1}$ en valeurs moyennes, et un rayon de 7η et une vorticité de $0.9\tau^{-1}$ en valeurs les plus probables.
Enfin, les profils de densités moyennes de tourbillons semblent indiquer que les tourbillons longitudinaux et transverses prograde sont crées dans la zone proche paroi. Les tourbillons transverses retrogrades quand à eux semblent être crées à partir d'un retournement des prograde survenant dans la zone externe de l'écoulement (où le gradient de vitesse moyenne est le plus faible).

Contents

List of Figures

List of Tables

Introduction

Flat plate turbulent boundary layer is a canonical flow configuration of prime importance for many engineering applications. Despite its apparent random character, this type of flow is organized into coherent structures which are believed to play a key role in the maintenance of turbulence. In particular, the streamwise and spanwise oriented vortices, through their ability to transport mass and momentum across the mean velocity gradient, are a fundamental feature of near-wall turbulence. The scaling laws and generation mechanism of these structures have been the focus of many studies, but still remain unclear.

The present study aims at providing some new insight into these outstanding issues through an original approach combining:

- two unique and complementary flow facilities: the different flow regimes of the LTRAC water-tunnel in Melbourne (Australia) and LML wind-tunnel in Lille (France) allow to cover a range of Reynolds number spanning more than one order of magnitude ($Re_\theta \in [1300; 18950]$).
- a modern, full-field and quantitative measurement technique: stereoscopic particle image velocimetry (SPIV) can give access to instantaneous two-dimensional and three components velocity field, with high spatial resolution and low uncertainty.
- advanced post-processing tool: a detection based on the discriminant of the 2D velocity gradient tensor, used in conjunction with a pattern recognition method allow a reliable detection and full characterization of vortical structures in turbulent boundary layers.

The work undertaken consist of four main tasks:

- the acquisition of SPIV data in streamwise/wall-normal and spanwise/wall-normal planes of the LML and LTRAC boundary layers at 6 Reynolds numbers distributed in the range $Re_\theta \in [1300; 18950]$.
- the validation of the SPIV data through the computation and analysis of average flow properties such as the mean velocity, the Reynolds stresses, the PDF of the fluctuations and the power spectra.
- the development of a vortex detection program based on the extrema of the 2D swirling strength and a non-linear fit to an Oseen vortex

- the analysis of the vortex characteristics in the entire SPIV database as well as in an existing DNS dataset at a Reynolds number similar to that of the LTRAC boundary layer.

This document is organized in the following chapters:

- **chapter 1** provides a literature review on the coherent structures in near-wall turbulence, including definition and classification, models of organization, and results of recent PIV, hot-wire and DNS studies. A concluding paragraph specifies the aims of this thesis with respect to the unresolved issues.
- **chapter 2** gives an extensive presentation of the stereoscopic PIV technique, from the basic principles to the most recent developments. Emphasis is put on the assessment of measurement uncertainty and spatial dynamic range, which are essential for coherent structure investigation in near-wall turbulence.
- **chapters 3 and 4** are devoted to the experiments in the LTRAC water-tunnel and LML wind-tunnel respectively. After a brief presentation of the facilities, the experimental procedure is described extensively. The uncertainty of the experiments is thoroughfully assessed, and a summary of the database is given.
- **chapter 5** consist of a validation of the SPIV database through an analysis of some single points statistics (mean velocity, Reynolds stresses, PDF of the fluctuations) and of the power spectra. These quantities are validated against profiles derived from theory, hot-wire measurements, or DNS data.
- **chapter 6** focusses on coherent structure detection. The detection program is extensively described, and the effects of PIV averaging on the estimation of the vortex characteristics are assessed. Then, the vortices detected in the SPIV database as well as in a DNS dataset are analyzed in detail, and in particular the wall-normal evolution of their mean radius, vorticity, density and convection velocity.
- **chapter 7** discusses the results of this thesis in the context on the current knowledge on coherent structures in the scientific community.

Chapter 1

Coherent structures in wall-bounded turbulence

1.1 A (brief) description of the underlying concepts

The study of flows developping along a solid boundary is of primary importance for many engineering problems, such as drag reduction of airplane wings in the aeronautics field. In the boundary layer concept, introduced by Prandtl (1904), the field of wall-bounded flows can be divided into two regions:

- a thin region near the wall called the boundary layer, where strong velocity gradients occur, inducing large viscous shearing forces that must be taken into account and
- the region outside the boundary layer, where the frictions forces can be neglected, and where, therefore, inviscid fluid theory offers a good approximation

The major contribution of the boundary layer concept was to overcome D'Alembert paradox and to reunify theoretical hydrodynamics (derived in the framework of the perfect fluid hypothesis) with empirical laws from hydraulics. It is presented and discussed extensively in Schlichting and Gersten (2001).

Fundamental research on boundary layers is focused on the study of canonical configurations such as pipe flow, channel flow or flow over a flat plate. The development of a boundary layer on a flat plate and its transition to turbulence have been described in White (1974) and are sketched in figure 1.1. Near the leading edge of the plate, the regime of the boundary layer is *laminar*: the flow is two-dimensional and steady. As the boundary layer develops, the flow becomes critical and undergoes transition from the laminar to the turbulent regime: Tollmien-Schlichting instabilities appear and propagate, giving birth to turbulent spots, irregularly distributed in space and time. As the distance x from the leading edge increases, these turbulent spots grow in size and become more frequent, until they ultimately merge and occupy the full field. The transition is then complete, and the flow is fully turbulent. It can be observed that, in the turbulent regime, the boundary layer thickness increases more rapidly with x, and that the wall friction coefficient is in

general higher than it would be in the laminar regime. Sometimes, a tripping device can be placed close to the leading edge of the plate to promote a repeatable transition to turbulence. Erm and Joubert (1991) investigated the effects of different tripping devices on the development of turbulent boundary layers.

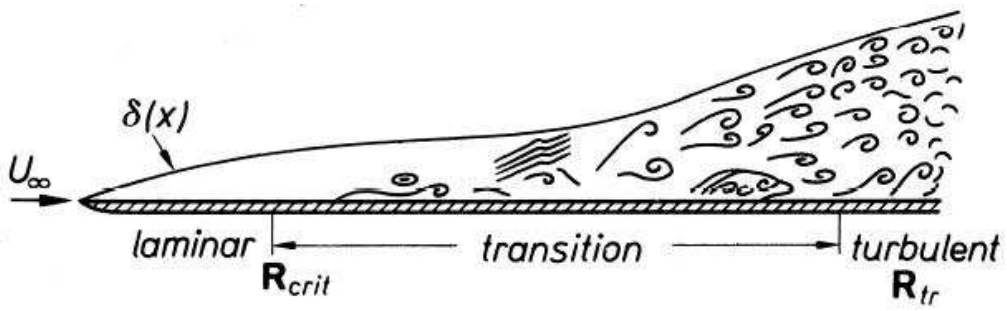

Figure 1.1: Flat plate boundary layer, transition from laminar to turbulent flow taken from White (1974)

Turbulence always occurs at large Reynolds numbers. The Reynolds number Re is an important similarity parameter of turbulent flows: it is defined as a characteristic length multiplied by a characteristic velocity and divided by the kinematic viscosity, and represents the relative magnitude of the inertial and viscous forces. The Reynolds number Re_x built from the distance x and the free stream velocity U_∞ is said to be 'critical' at the abscissa where the transition begins, and 'transitional' where the transition is complete. It is difficult to give a precise definition of turbulence. Turbulent flows are governed by the Navier-Stokes equations, and possess a certain number of specificities (Tennekes and Lumley (1972)). Turbulence is:

- non-linear: turbulence arise from the coupling between the viscous terms and the non-linear inertial terms in the Navier-Stokes equation.

- chaotic: a small perturbation introduced at any point of the field can affect the entire flow, and turbulent flow are therefore impossible to predict.

- three-dimensional and rotational: turbulence is characterized by high levels of fluctuating vorticity, which are maintained mainly through three-dimensional vortex stretching.

- diffusive: turbulence causes rapid mixing and increased rate of momentum, heat and mass transfer along but also across the mean flow streamlines.

- dissipative: the kinetic energy is dissipated into internal energy via the action of the viscous shear stresses; this process is enhanced for turbulent flows because of higher deformation rate.

- multiscale: a wide range of length scale exists in turbulent flow, bounded from above by the dimensions of the flowfield, and from below by the action of molecular viscosity (Kolmogorov scales).

1.2 Mean properties of turbulent boundary layer

The first important physical features of wall bounded turbulence were actually retrieved using a statistical approach. It is based on an idea of Reynolds (1895) who suggested to decompose the instantaneous flow variables into their mean and fluctuating part. This decomposition leads to averaged forms of the Navier-Stokes equations, which can be further simplified using some boundary layer approximations. The resulting equations for mass, momentum, and turbulent kinetic energy are called the turbulent boundary layer equations, and can be found in many classical textbooks (Schlichting and Gersten (2001), Cousteix (1989)). The mean properties of the turbulent boundary layer can be analyzed through the study of the different terms appearing in these equations: the mean streamwise velocity, the Reynolds stresses, the production and dissipation of turbulent kinetic energy...

In the early days of turbulent boundary layer research, the mean streamwise velocity profile was studied theoretically, using a mixture of physical understanding and dimensional analysis to derive similarity laws. Prandtl (1932) suggested that the boundary layer can be divided into two regions:

- an inner region, where the mean streamwise velocity profile depends only on the characteristics of the fluid (the density ρ and the dynamic viscosity μ) and on the wall shear stress τ_w:

$$\frac{U}{U_\tau} = f_1\left(\frac{\rho y U_\tau}{\mu}\right) \quad \text{with} \quad U_\tau = \sqrt{\frac{\tau_w}{\rho}} \tag{1.1}$$

  This law is called the law of the wall, and is valid for $y < 0.2\delta$. This region can be decomposed again into a region where the turbulent shear stress $-\rho < u'v' >$ is negligible with respect to the viscous shear stress $\mu dU/dy$ (the 'viscous' or 'linear' sublayer for $0 \leq y^+ \leq 5$, where $y^+ = \frac{yu_\tau}{\nu}$), a region where the two stresses are of comparable magnitude (the 'buffer layer', for $5 \leq y^+ \leq 40$), and a region where the viscous shear stress is negligible with respect to the turbulent shear stress ($40 \leq y^+$ and $y \leq 0.2\delta$).

- an outer region where the mean streamwise velocity profile depends no more on the viscosity but only on the wall shear stress τ_w, the density ρ, the free stream velocity U_∞ and the boundary layer thickness δ:

$$\frac{U - U_\infty}{U_\tau} = f_2\left(\frac{y}{\delta}\right) \quad \text{with} \quad U_\tau = \sqrt{\frac{\tau_w}{\rho}} \tag{1.2}$$

  This formulation is called the velocity defect law, and is valid for $40 \leq y^+$ (approximately). The 'wake law' proposed by Coles (1956) is the most accepted description of this region.

Using dimensional analysis, some fundamental laws were theoretically derived at the overlap of these 'inner' and 'outer' regions. The 'overlap region' present a logarithmic mean streamwise velocity profile (Millikan (1939)) and a constant shear stress. It is often called the 'logarithmic region', and is reputed to be valid not only for boundary layers, but also

for pipe and channel flows. To summarize, a typical mean streamwise velocity profile, showing the different regions of the turbulent boundary layer, is represented in figure 1.2. Recently, George (2006) and George (2007) questioned the validity of the outer region velocity defect law as written in equation 1.2 for boundary layer flow, an proposed an alternative form where the velocity deficit scale on U_∞ rather than on U_τ. It is argued that this alternative form is a similarity solution of the Reynolds-averaged equations, yielding to a power law equation of the overlap region. However, George (2006) and George (2007) admit that the logarithmic law provide a good empirical description of the overlap region, indistinguishable from the power-law solution.

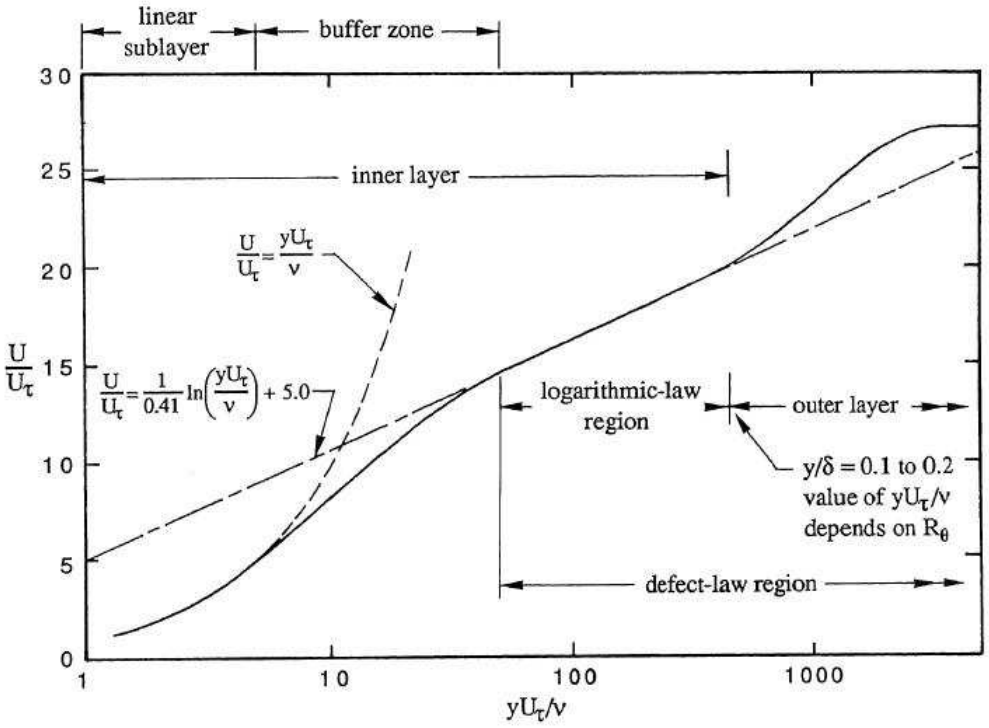

Figure 1.2: A typical mean streamwise velocity profile, in wall units, showing the different regions of the turbulent boundary layer, adapted from Erm (1988)

In the spectral domain, Perry et al (1986) derived similarity laws for the longitudinal power spectra. They identified three regions of the spectra: a low wavenumber range with an outer scaling, the intermediate range with an inner scaling, and the high wavenumber range with a Kolmogorov scaling. Assuming the existence of overlap between these three regions, '-1' and '-5/3' power laws were derived.

With the advent of the hot-wire anemometry, quantitative results could be obtained experimentally, with the possibility to verify these theoretical laws. The universality of other representations could also be tested, by looking at how experimental data collapse when plotted with different sets of scaling coordinates.
Klebanoff (1955) was the first to employ hot-wire anemometry to measure the mean streamwise velocity but also the Reynolds stresses, the probability density functions of the streamwise fluctuations, and power spectra of a turbulent boundary layer at $Re_\theta = 7500$. The turbulent kinetic energy budget was estimated, showing that production and

dissipation concentrate in a thin layer close to the wall: the buffer layer. Coles (1962) undertook a comparative survey of the mean streamwise velocity profiles of incompressible turbulent boundary layers. He identified a normal state for the layer and expressed this state in terms of a relationship between the strength of the wake $\Delta U/U_\tau$ (maximum deviation of a profile from the logarithmic law) and the Reynolds number Re_θ based on the momentum thickness. It was shown that high levels of free-stream turbulence intensity can decrease the strength of the wake.

Later on, Fernholz and Finley (1996) compiled existing data in a wide range of Reynolds number ($Re_\theta \in [400; 211000]$). They confirmed that the mean streamwise velocity profile is universal when scaled using U_τ and ν (wall unit scaling) in the inner layer and using the boundary layer thickness δ and the free-stream velocity U_∞ (outer scaling) in the outer layer. No universal scaling could be found for the Reynolds stresses, although a limited collapse was observed in the outer region using mixed scaling, where the stresses are scaled using U_τ and the wall normal distance using an integral thickness. In the inner region, only $< u'u' >$ and $< u'v' >$ were found to scale satisfactorily using a wall-units scaling. Finally, good collapse of the spectra could be observed using the similarity laws from Perry et al (1986).

The laser Doppler velocimetry experiments performed by Degraaff and Eaton (2000) in a range of Reynolds numbers Re_θ varying from 1430 to 31000 also confirmed that the logarithmic law provide a universal law for the mean velocity in the inner region. The scaling of the Reynolds stresses was also investigated: $< v'v' >$ and $< u'v' >$ were found to show a good collapse in inner scaling, contrary to $< u'u' >$ for which a mixed scaling involving both the friction velocity U_τ and the free-stream velocity U_∞ was proposed.

1.3 Discovery and classification of coherent structures

The presence of coherent structures in turbulent flow is apparent statistically in the non-zero Reynolds shear stress $-\rho u'v'$ and two points space-time correlations. Coherent motions are defined by Robinson (1991) as *'three-dimensional region[s] of the flow over which at least one fundamental flow variable exhibits significant correlation with itself or with another flow variable over a range of space and/or time that is significantly larger than the smallest local scales of the flow'*. They are believed to play a key role in the maintenance (production and dissipation) of turbulence in boundary layers. Coherent structures were first discovered, characterized, and classified using flow visualization techniques and hot-wire anemometry. An extensive review of this first era of coherent structures investigation can be found in Cantwell (1981) and in Robinson (1991). The various forms of the experimentally observed coherent structures can be classified into the following groups:

- **hairpin vortices**: from the analysis of the vorticity transport equations, Theodorsen (1952) postulated that boundary layers were populated by horseshoe structures, originating from the stretching of perturbed spanwise vorticity. This structure is often described as being made of two counter-rotating streamwise oriented 'legs' connected to a spanwise oriented 'head' via a neck. The smoke visualization experiments using inclined cross-stream light sheets in turbulent boundary layers

($Re_\theta \in [500; 17500]$) performed by Head and Bandyopadhyay (1981) demonstrated that the hairpin was a major constituent of the outer region of the layer. The morphology of this structure could be assessed: it possesses a characteristic angle of 45° to the wall close (possibly resulting from the conflicting effects of shear and self-induction), and its aspect ratio evolves from that of a horseshoe to that of a hairpin as the Reynolds number of the flow increases. Using an asymmetry-preserving conditional averaging technique, Guezennec (1989) showed that the hairpin structure present some degree of asymmetry, and that its more probable form was in fact that of a single-legged cane. This was confirmed by Robinson (1991) on his analysis of Spalart (1988) DNS.

- **ejections and sweeps**: the ejections of low-speed fluid away from the wall and the sweeps of high speed fluid toward the wall were first visualized using a high speed camera by Corino and Brodkey (1969). Ejection and sweeps explain why the joint PDF on u' and v' is higher in the second quadrant 'Q2' ($u' < 0$ and $v' > 0$) and fourth quadrant 'Q4' ($u' > 0$ and $v' < 0$) respectively, and hence account for the non-zero Reynolds shear stress $-\rho < u'v' >$. Using hot-wire anemometry and conditional averaging, Wallace et al (1972) showed that the sweeps contribute more than the ejections to the production of turbulent kinetic energy in the region $y^+ < 15$, and less in the region $y^+ > 15$.

- **streamwise vortices**: Blackwelder and Eckelmann (1979), using hot-film anemometry, showed that strong streamwise vortices with an upward tilt evolving as counter-rotating pairs populate the near wall region. Their streamwise extent is subject to controversy: the findings of Blackwelder and Eckelmann (1979) indicate an extent of 1000^+, while a much smaller length of 100^+ was observed by Praturi and Brodkey (1978) using a stereoscopic flow visualization technique. The results of Kim and Moin (1986), using a direct numerical simulation (DNS) at $Re_\tau = 180$ (to complement results of a large eddy simulation (LES)) corroborates the findings of Praturi and Brodkey (1978).

- **spanwise vortices**: prograde (that with rotation in the same sense as the mean shear, $\omega_0 < 0$) and retrograde ($\omega_0 > 0$) spanwise vortices were identified in the log and wake region of turbulent boundary layers by Nychas et al (1973) by photographying the motion of solid particle in water with a high speed camera moving with the flow. They were interpreted as the result of the rolling up of a shear layer created by the interaction of low-speed fluid ejection with high-speed fluid sweeps.

- **low-speed and high speed streaks**: narrow regions of low speed flow, elongated in the streamwise direction, are commonly observed in the near-wall region ($0 < y^+ < 40$). They are known as the 'low-speed streaks' and are separated in the spanwise direction by 'high-speed streaks'. They were first studied in details using hydrogen bubble visualization by Kline et al (1967) , and their characteristics were summarized in Blackwelder (1997): the low-speed streaks appear below $y^+ < 10$, their mean dimensions are about 1000^+ in length, from 20^+ to 40^+ in span, and from 5^+ to 10^+ in height, with a mean spanwise spacing of about 100^+.

- **large-scale three dimensional bulges**: large scale bulge in the outer region (scaling with δ in both x and z) were observed by Falco (1977) using flow visualization and hot-wire anemometry, and evidenced through two-point correlation of a hot

wire signal by Brown and Thomas (1977). They are characterized by a slow rotational motion in the direction of the mean strain and by deep crevasses of high-speed potential fluid around the edges.

1.4 Models of organization

Far from being independent, these different groups of coherent structures are intimately related. One major objective of near wall turbulence research actually consists in unifying these structures into a model of organization that would ultimately explain the cycle of turbulence as well as the scaling laws applying to the mean flow properties. There is currently no consensus among the scientific community on a unique model of organization and self-sustaining mechanism of near-wall turbulence. In the following, a brief overview of the existing models is first given. Then, a family of models based on the hairpin structure is described into more details.

1.4.1 Overview of the existing models

In 1997, Panton edited a book of contributions from different research groups, providing an extensive overview of the existing models for the self-sustaining mechanisms of wall turbulence (Panton (1997)). From flow visualization evidence, three categories of structures are accepted by all research groups as being the main constituent of near-wall turbulent flows (or at least of one of their regions): the streamwise vortices (Blackwelder and Eckelmann (1979)), the hairpin structures (Head and Bandyopadhyay (1981)), and the low-speed streaks (Kline et al (1967), Blackwelder (1997)). The different models differ as to which one of these structures plays the central role in the self-sustaining mechanisms of near-wall turbulence (the other structures being 'passive' secondary features). The other point of disagreement is related to the mechanisms responsible for the generation of this central structure. Schoppa and Hussain (1997) identified two types of generation mechanisms: parent-offspring scenario, where new vortices are created by direct action of existing vortices; and instability-based mechanism, where new vortices are created from a local instability. Regarding these two issues, most of the existing models can be classified in two families.

In the first family of models, streamwise vortices occupy the central role in near-wall turbulence, and are selfsustained via low-speed streaks instabilities. The models of Blackwelder (1997), Waleffe and Kim (1997), Schoppa and Hussain (1997) and Schoppa and Hussain (2002) pertain to this family. After their initial discovery in flow visualizations studies, the streamwise vortices were abundantly observed in the near-wall region of DNS data by Jeong et al (1997) and Robinson (1991), confirming their proeminent role. The generation of streamwise vortices is assumed to be linked to turbulence production occurring during an instability sequence of the low-speed streaks, referred to as the 'bursting' process (Kline et al (1967)): in this concept, the low-speed streaks lifted away from the wall undergo spanwise and wall-normal oscillations before breaking up in a turbulent burst outward from the wall. A similar behavior of the streaks induced by Gortler vor-

tices was investigated by Swearingen and Blackwelder (1987) and Blackwelder (1997), while the different instability modes of the streaks were analyzed theoretically by Waleffe and Kim (1997) and Schoppa and Hussain (1997). Furthermore, these authors proposed feed-back mechanisms describing the creation of streamwise vortices. Interestingly, the feed-back mechanism of Schoppa and Hussain (1997) and Schoppa and Hussain (2002) not only gives birth to streamwise vortices, but also to internal shear layer that can roll-up to create spanwise vortices which connect to the downstream end of streamwise vortices to form canes. Hence this model is consistent with the observation of cane vortices in wall-bounded turbulence.

The second family of models is based on the hairpin structure and a parent-offspring auto-generation mechanism. The models of Smith and Walker (1997), Zhou et al (1997), Zhou et al (1999) and Adrian et al (2000b) pertain to this family. After their first identification in flow visualization studies, hairpin structures were evidenced in LES data by Moin and Kim (1985). The auto-generation mechanisms of hairpin structures have been observed in experimental studies using an external disturbance in a laminar boundary layer (Acarlar and Smith (1987a) and Acarlar and Smith (1987b)) and using a hairpin-like structure convected with a unidirectional mean flow as an initial condition in a DNS study (Zhou et al (1999)). However, the generation mechanisms of the parent hairpin remain unclear. In this family of models, uniform zones of low-momentum flow are interpreted as being the result of low-speed fluid ejections in between the hairpin legs. This type of model tends to dominate on-going research on coherent structures, and is therefore described into more details in the next paragraph.

1.4.2 A deeper insight into the hairpin-based models

Two models using the hairpin structure as a building block of near-wall turbulence organization may be distinguished: the model based on a random distribution of hairpins, and the model assuming a coherent arrangement of individual hairpin in a packet.

Model based on random distribution of hairpins

A first model of near turbulence was proposed using the concept of randomly distributed hairpins in the flow. It is based on the fact that a single hairpin can explain many observed flow events, as depicted in figure(1.3) taken from Adrian et al (2000b). In this model, the legs of a hairpin correspond to the quasi-streamwise vortices observed in the buffer layer, and its head to the prograde transverse vortex observed in the outer region; the low-momentum fluid lifted away in between the legs of the hairpin agglomerate to form a low-speed streak-like region; the strong pumping of fluid between the hairpin legs create ejection events, associated with second quadrant (Q2) fluctuations; a sweep event associated to fourth quadrant (Q4) fluctuations opposes the (Q2) event, forming a stagnation point and an inclined shear layer upstream.

Using this concept of randomly distributed hairpins as well as the attached eddy hypothesis from Townsend (1976), Perry and Chong (1982) constructed theoretically the

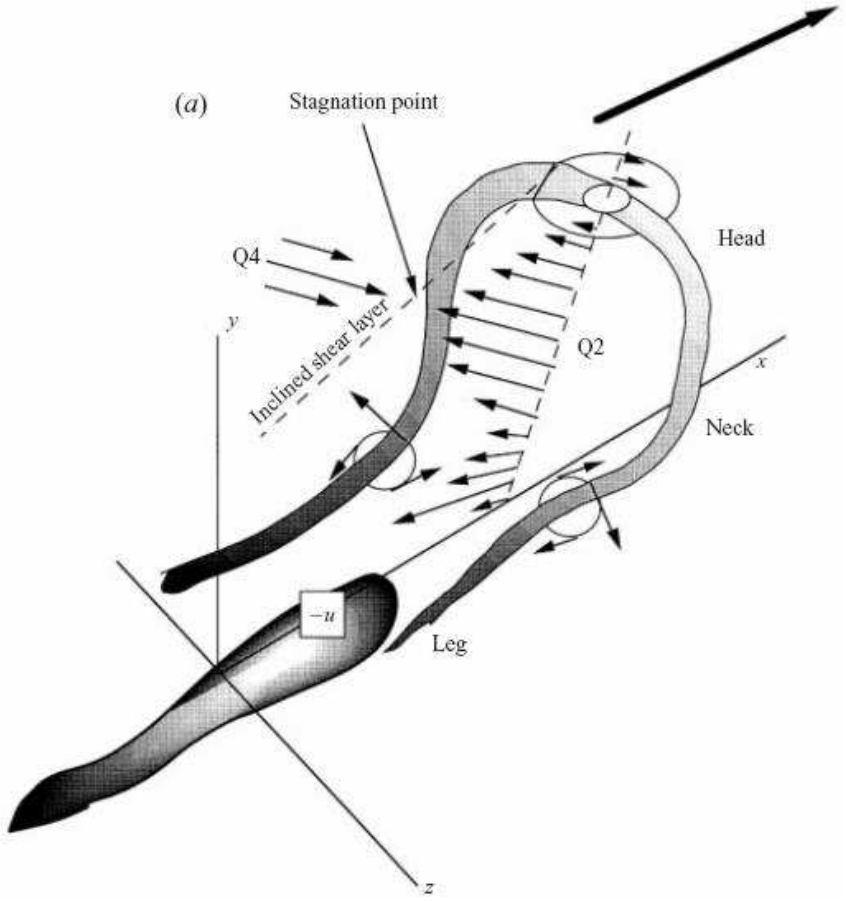

Figure 1.3: Schematic of a hairpin structure attached to the wall and the induced motion, from Adrian et al (2000b)

first physical model able to reproduce many statistical aspects of the overlap region such as the logarithmic evolution of the mean streamwise velocity, the constant shear stress and the -1 power law of the u power spectra. A subsequent article by Perry et al (1986) dedicated to the scaling of the spectra provides in its introduction a very clear summary of this model. The model relies on the existence of geometrically similar hierarchies of lambda shape vortices in a range of scales varying from the wall unit lengthscale up to the boundary layer thickness (a hierarchy is defined as a random array of λ shape vortices, all at different stages of stretching but with the same circulation).

Distribution of the hairpins: from randomness to coherence

The random distribution of hairpins may provide an interesting explanation for some of the near-wall turbulent flow features, however, a major discrepancy exists between the predicted size of the low momentum region between the legs of a single hairpin (typically on the order of 100^+, calculated from the extent of the streamwise vortices as obtained by Praturi and Brodkey (1978) and Kim and Moin (1986)), and the extent of the low-speed streaks experimentally observed by many researchers (on the order of 1000^+, see Blackwelder and Eckelmann (1979)). To overcome that contradiction, Smith (1984) suggested

that the long low-speed streak could be created by the coherent arrangement of two or three hairpins in the streamwise direction. This suggestion was based on flow-visualization experiments performed in a low Reynolds number water flow using H_2 bubble patterns, showing the in-line formation of successive hairpins. Two experimental investigations were subsequently undertaken by Acarlar and Smith to study this hypothesis. It involved the artificial generation of hairpins in a laminar boundary layer using hemisphere protuberance at the wall (Acarlar and Smith (1987a)) or continuous injection of low-speed flow at the wall (Acarlar and Smith (1987b)). The induced flow features were investigated using flow visualization and hot-film anemometry. In both experimental configurations, it was observed that a primary hairpin generates on the upstream side of its plane of symmetry secondary vortices. This autogeneration process can be interpreted as a possible source of streamwise coherence between distinct hairpins. Furthermore, Acarlar and Smith (1987b) noticed that a hairpin street can induce extremely long and persistent low-speed concentrations between its counter-rotating legs, demonstrating its potential role in the formation of the low-speed streaks.

Model based on coherent packets of hairpin

The advent of quantitative and full field techniques such as Particle image velocimetry (PIV) or Direct numerical simulations (DNS) provided new insight into the organization of wall-bounded turbulence. It allowed to correct and refine the previously developed concepts, and to finally re-unify them in the so-called 'hairpin packet model'. A packet is defined by Adrian (2007) as a group of hairpins having small dispersion in their velocity of propagation, and therefore keeping its coherence over a significant time.

The mechanisms that yields to the formation of these packets at low Reynolds number were investigated numerically in great details by Zhou et al (1999). In this study, an initial structure is built from the linear stochastic estimation of the flow field, conditioned by a symmetric Q2 event in a DNS of turbulent channel flow at $Re_\tau = 180$ from Kim et al (1987); this structure is then placed into a unidirectional mean flow from the DNS (with no fluctuations), and the dynamics of the flow starting from this initial condition is then simulated with the Navier Stokes equations. The vortical structures of the flow are then visualized and tracked using isosurfaces of swirling strength (imaginary part of the velocity gradient eigenvalues). The principle of generating an artificial hairpin in a quiet environment present striking similarities with the experimental study from Acarlar and Smith (1987a) and Acarlar and Smith (1987b). However, a significant difference arises from the fact that the initial structure used by Zhou and co-workers provides the advantage of having lengthscales, shape and vorticity consistent with the eddies occurring in this turbulent channel flow, since it was constructed using the correlation tensor of the DNS database itself. The initial structure has a lambda shape and quickly evolves into a omega-head hairpin with an average tilt angle of 45°. Unexpectedly, it also possessed a pair of quasi-streamwise vortical tongues sticking out from the head of the hairpin on its downstream side. The ability of this primary hairpin to generate or not secondary structures was found to depend on its initial strength with respect to the background flow. A primary hairpin with enough initial strength generates similar secondary hairpins on its plane of symmetry, both on its upstream and downstream side. The mechanism responsible for the generation of the upstream hairpin resembles the formation of the

primary hairpin out of the initial lambda structure. A kink forms in the long legs owing to the mutual induction process, and the shear layer between the legs of the primary hairpin rolls up into a compact spanwise vortex, which viscously connects with the section of the legs upstream of the kink to form the secondary hairpin. The secondary hairpin can in turn generate a tertiary, upstream of it. The hairpin forming at the downstream side of the primary hairpin grows out of the pair of vortical tongues, and it is not concluded whether it is or not an artifact of the stochastically estimated initial condition. Finally the hairpin packet formed from the primary, secondary, and tertiary hairpins has a tent-like envelop, with an upstream angle to the wall of 15° and a downstream angle to the wall from $-7°$ to $-15°$. The constitutive hairpins have a streamwise spacing similar to their individual extent (about 400^+), and their cooperative action results in a low speed streak that is significantly longer. Although the heads of these hairpins are at different height, the dispersion in their convection velocity remains small, maintaining the coherence of the packet. Finally, the effect of asymmetry on the evolution of the initial structure was assessed. For a sufficiently strong degree of asymmetry of the initial structure, the secondary and tertiary hairpin resemble one-sided canes. Additionally, the autogeneration mechanism seems enhanced, with hairpins forming more rapidly with a smaller streamwise separation, in better agreement with the experiments.

The hairpins and their organization within packets was studied experimentally by Adrian et al (2000b) at moderate to high Reynolds numbers. Instantaneous velocity fields in a XY plane of a boundary layer at three Reynolds numbers in the range $930 < Re_\theta < 6845$ were measured using PIV. Hairpins were detected in the instantaneous flow field through their planar signature consisting of a spanwise vortex core (visualized either using the X-Y flow pattern in a convected frame or using swirling strength) located just above a region of strong Q2 fluctuations that occur on a locus inclined at $30° - 60°$ to the wall. It was found that hairpin structures populate the boundary layer abundantly. Groups made of up to ten hairpins aligned in the streamwise direction and spaced several hundreds of viscous lengthscale apart are commonly observed from the outer edge of the buffer layer to the outer wake region at each Reynolds number. The dispersion in the propagation velocity within a group is small (approximately 7%). The most probable length of a packet is found to be of 1.3δ for the highest Reynolds number, and the angle of the envelop connecting the head of the hairpins is found to be fairly constant, around a mean value of 12°. Within the envelop, the spatial coherence between the velocity fields induced by each hairpin result in the formation of a region of strongly retarded streamwise momentum. These low-momentum zones extend far above the low speed streaks commonly observed in the buffer layer, and should not be confused with them. It is suggested that the buffer layer streaks are actually part of the low-momentum-zone phenomenon. The fact that one area of uniform momentum is often observed to nest within another area of distinct uniform momentum is interpreted as an indication that young packets lying close to the wall exist *within* larger and older packets.

Finally, Adrian et al (2000b) combined their own experimental results at moderate Reynolds number regarding hairpins and hairpin packets with the numerical results at low Reynolds number from Zhou et al (1999) regarding the autogeneration and growth mechanism of a hairpin packet. It resulted in an idealized conceptual model of the structure of wall-bounded turbulent flows in the context of hairpin packet. This model is represented graphically in figure 1.4.

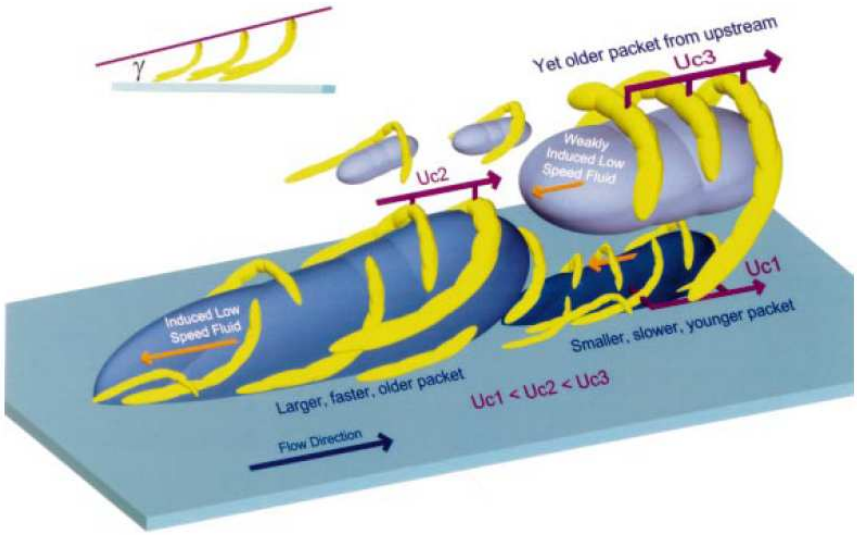

Figure 1.4: The hairpin packet model, from Adrian et al (2000b)

1.5 Recent results and on-going research

A first picture of the structure and organization of near-wall turbulence was given by the hairpin packet model from Adrian's group. With the continuous progress of numerical simulations, measurement techniques, and post-processing tools, recent studies have provided and continue to provide a more extensive characterization of the structure of near-wall turbulence.

1.5.1 PIV studies

The original flow-visualization study by Head and Bandyopadhyay (1981) inspired two experimental studies with the same inclined cross-stream light sheet configuration but using stereo-PIV to obtain quantitative results on coherent structures. Hutchins et al (2005) investigated a range of Reynolds numbers of $Re_\theta \in [1430; 7440]$, while Carlier and Stanislas (2005) investigated the range $Re_\theta \in [8000; 19000]$. Therefore these two studies can be viewed as complementary.
Using in-plane instantaneous swirl, Hutchins et al (2005) showed that the majority of the vortices were detected in the 135° plane, consistently with the reported inclination of the hairpin vortices. Linear stochastic estimation and conditional averaging revealed that these eddies had a predisposition to appear with a pair of counter rotating legs, and were bordering low-momentum fluid regions. An investigation of the two-points velocity correlation contour revealed the existence of a distinct two-regime behavior, either attached or detached from the wall, with the demarcation in the wall-normal direction scaling with outer variables.
Carlier and Stanislas (2005) also evidenced that more vortices were present in the 135° plane than in the 45° plane. Additional measurement were also taken in a XY plane and a YZ plane. The wall-normal evolution of the mean characteristics of the detected vortices

(radius, vorticity) were found to be universal in wall-units, with a constant circulation: the radius was found to increase slowly and the vorticity to decrease slowly with increasing wall-normal distance.

After Adrian et al (2000b) pioneering PIV investigation in a streamwise/wall-normal plane, Tomkins and Adrian (2003) undertook a complementary study of the same turbulent boundary layer ($930 < Re_\theta < 6845$), but in streamwise/spanwise (XZ) planes throughout the outer region. The dominant motions of the flow are shown to be large scale regions of low-momentum elongated in the streamwise direction. Using a XZ hairpin signature, it was shown that these momentum deficit regions are bordered with vortices, offering strong support for the hairpin packet model. Two types of growth mechanism for the spanwise structure are evidenced: a self similar growth revealed by the linear variation of the mean spanwise lengthscale (computed statistically), and a growth via the merging of vortex packets on an eddy-to-eddy basis (observed in the instantaneous velocity fields).
Stereo-PIV measurements in the same orientation plane (XZ) were undertaken by Ganapathisubramani et al (2003) in a turbulent boundary layer at $Re_\theta = 2500$ at $y^+ = 92$ and 150. The same large-scale organization was found in the logarithmic layer, but seems to break down at larger wall-normal distances. In this configuration, the stereoscopic technique allowed to retrieve the wall-normal velocity component, and it was shown that a large portion of the Reynolds shear stress is generated by groups of hairpins.
Ganapathisubramani et al (2006) extended this work by applying a more sophisticated dual-plane technique at the same Reynolds number ($Re_\theta = 2500$) in XZ planes at $y^+ = 110$ and $y/\delta = 0.53$. Thanks to the dual-plane technique, all three components of the velocity gradient tensor could be computed, and vortices with all inclination angles could be detected. The results reveal that a broad distribution of inclination angles exists in the logarithmic and wake regions. A vast majority of the vortices are leaning forward at a characteristic angle close to 45°, but a non-negligible amount of the vortices is also leaning backwards. The authors suggest that these backward-leaning cores are part of smaller, weaker structures that have been distorted and convected by larger, predominantly forward-leaning eddies associated with the local shear.
Hambleton et al (2006) performed simultaneous SPIV measurement in a XZ plane at $y^+ = 98$ and in a XY plane of the same turbulent boundary layer ($Re_\theta = 2500$). Using linear stochastic estimation, they investigated the velocity fields in the two planes conditioned by a prograde and a retrograde swirling event in the XY plane at the top of the log region ($y/\delta = 0.19$). It was shown that the prograde swirling event at $y/\delta = 0.19$ has a large footprint in the flow in the XZ plane at $y^+ = 98$, inducing an elongated low-momentum region flanked in z by regions of high momentum and swirling activity at the shear layer between the low and high speed regions. On the contrary, a retrograde swirling event at $y/\delta = 0.19$ (for which less candidate were found) does not seem to influence the flow in the XZ plane at $y^+ = 98$, but induces a prograde vortex in the XY plane downstream and above of the condition point. The authors suggest that it is consistent with an omega-shaped hairpin or with a vortex ring structure.
The population trends of prograde and retrograde spanwise vortices as a function of wall-normal position, Reynolds number (in a range $Re_\tau \in [570; 3450]$) and flow (either boundary layer flow or channel flow) was documented in detail by Wu and Christensen (2006) using PIV in a XY plane. Vortices were identified using two-dimensional swirling strength, and a simple threshold was used to retrieve the area occupied by these vortices. Prograde and retrograde vortices are found to populate densely the logarithmic region of both flows. The vortices were found to be advected with the local mean velocity, with

a significant distribution around this mean related to local turbulence levels. The prograde spanwise vortices have characteristics consistent with that of hairpin heads, while retrograde vortices are often observed to nest near clusters of prograde vortices that form hairpin vortex packets. It was found that the region of the channel flow at $\pm 0.55\delta$ about the centerline can be considered as a region of interaction where structures from both walls commonly exist. Reynolds number dependence of the outer-scaled and inner-scaled population densities are also quantified.

The streamwise oriented vortical structures in the logarithmic region of turbulent boundary layers at $Re_\theta = 7800$ and $Re_\theta = 15000$ were investigated by Stanislas et al (2008) using stereo-PIV measurements in a plane orthogonal to the mean flow (YZ). Vortices are detected using the two-dimensional swirling strength, and subsequently characterized using a fit to an Oseen vortex. The PDF of their radius and intensity are found to be universal both in Reynolds number and in wall-normal distance when scaled with the local Kolmogorov scales η and v. The most probable diameter of the vortices is found to be about 10η, and the most probable vorticity about $1.6\tau^{-1}$. The equation for the mean square vorticity fluctuations was revisited, and a new balance was proposed in the near-wall region. The large organization of the vortices was retrieved through an analysis of the two-points correlation on the swirling strength. Two regions of different dynamics are distinguished: the near-wall region below $y^+ = 150$ with strongly interacting vortices, and the region above $y^+ = 150$ where the vortices appear more isolated.
The buffer layer was quantitatively investigated by Lin et al (2008b) through the analysis of a database consisting of ten XZ planes from $y^+ = 14.5$ up to $y^+ = 48$ of a turbulent boundary layer at $Re_\theta = 7800$, measured with Stereo-PIV. Low-speed and high-speed streaks were detected using a detection function based on the streamwise velocity fluctuations; this function was subsequently thresholded, binarized, and then treated with image processing tools based on mathematical morphology. In the lower part of the buffer layer $14.5 < y^+ < 30$, it was found that the frequency of appearance of the high speed streaks decreases rapidly with increasing wall-normal distance, while the frequency of the low-speed streaks stays constant. In the upper part of the buffer layer ($30 < y^+ < 48$), the frequency of both types of streaks decreases linearly with increasing wall-normal distance, at a comparable rate. It is confirmed that the spanwise spacing of the streaks is about 120^+, and that the high-speed streaks are slightly larger than the low-speed ones. The mean width of the low-speed streaks is 31^+ in the lower part of the buffer layer, and then increases to 39^+ in the upper part, while the width of the high speed streaks stays nearly constant, comprised between 42^+ and 47^+.
The instantaneous 3D flow structure in the inner part (viscous sublayer, buffer layer and inner part of the logarithmic layer) of a turbulent boundary at $Re_\tau = 1400$ was measured by Sheng et al (2008) using a digital holographic microscope and a particle tracking algorithm. The measurements have a high spatial resolution and low uncertainty. The 2D wall shear stress distribution and 3D flow structures in the buffer layer could be retrieved, showing that the buffer layer structures leave strong footprints on the spatial distribution of wall shear stresses. In particular, counter-rotating streamwise vortex pairs are correlated with streak-like regions of low and high stress on the wall. The frequency of occurrence of coherent structures in the buffer layer was estimated: out of 100 realizations, 31 contain pairs of counter-rotating streamwise vortices, 30 multiple quasi streamwise vortices, and 2 a baby hairpin (the remaining 37 realizations did not contain any structures).

1.5.2 Hot-wire studies

The extent of PIV velocity field is usually too limited to assess the maximum dimensions of the large scale motions in the streamwise direction. In contrast, hot-wire measurements can be acquired over a very long time, and then converted to the spatial domain using a Taylor hypothesis. Therefore, although this measurement technique is only single-point, it can provide useful information regarding the streamwise extent of the large scale motions.
Using a hot-wire anemometer, Kim and Adrian (1999) were among the first to evidence very large scale motions (VLSM) in the form of long regions of streamwise velocity fluctuation in the outer region of a pipe flow. Using spectral analysis, they documented streamwise wavelength increasing through the logarithmic layer, and reaching a maximum between 12 and 14 pipe radii R, and then decreasing to $2R$ on the pipe centerline. These VLSM are about 4 times longer than a typical hairpin packet. A scenario was proposed to integrate this new feature into the hairpin packet model, where the VLSM are the result of the coherent alignment of packets of hairpin vortices.
Later on, Guala et al (2006) undertook a similar study in the outer region of a pipe flow in a range of Reynolds number $4000 < Re_\tau < 8000$. Pre-multiplied spectra of streamwise velocity fluctuations revealed very-large-scale energy-containing motions with mean wavelengths of up to 16 radii in the logarithmic region of pipe flow, and large-scale motions with mean wavelengths between 2 and 3 pipe radii throughout the layer. It was established that the VLSM contain half of the turbulent kinetic energy, of the Reynolds shear stress and of the net Reynolds shear force. In contrast, the main turbulent motions (defined as being the small scale and large scale motions) are found to contribute little to the Reynolds shear stress, but are responsible for half of the net Reynolds shear force.
Hutchins and Marusic (2007) used a spanwise rake of ten anemometers to measure the instantaneous streamwise velocity in a turbulent boundary layer in a range of Reynolds number of $1120 < Re_\tau < 19960$. They showed that very long meandering features populate the log region of turbulent boundary layers, extending to over 20δ in length, and possibly corresponding to the VLSM first evidenced by Kim and Adrian (1999).
Recently, a boundary layer at $Re_\theta = 9800$ and at $Re_\theta = 19100$ was measured by Tutkun et al (2009) using 143 hot-wire probes distributed in a plane perpendicular to the mean flow. The two-points correlation statistics were analyzed in a streamwise/spanwise plane and in a streamwise/wall-normal plane. At both Reynolds numbers and in both planes, the maximum streamwise extent of the correlation occurring in the logarithmic layer is about 7δ. The analysis in the XY plane revealed the existence of some degree of correlation between the near wall region and the intermittent region.

Finally, the large scale structure of the logarithmic layer was investigated in a range of Reynolds number spanning three decades by Marusic and Hutchins (2008). Two point correlation analysis was performed on data acquired in three facilities: simultaneous combined-plane stereo PIV data at $Re_\tau \approx 1000$ (see Hambleton et al (2006)), spanwise hot-wire rake measurements at $Re_\tau \approx 14000$ (see Hutchins and Marusic (2007)), and using a spanwise array of ten sonic anemometers in the atmospheric surface layer in Utah at $Re_\tau \approx 10^6$. Over the whole range of Reynolds number, the two point correlation statistics confirmed the existence of very large scale motions scaling with the boundary layer thickness δ.

1.5.3 DNS studies

Direct numerical simulation (DNS) are of special interest because they provide time-resolved and three-dimensional data with a large spatial dynamic range. The development of the computational ressources have recently allowed DNS of channel flow to reach Reynolds number which can be considered as relevant and free from low Reynolds number effects.

Direct numerical simulations of turbulent channel flows were performed by Tanahashi et al (2004), Das et al (2006) and Kang et al (2007) in a range of Reynolds number varying from $Re_\tau = 100$ to $Re_\tau = 1270$. A specific three-dimensional vortex detection algorithm based on the second invariant Q of the velocity gradient tensor was developed by Tanahashi et al (2004). For $100 < Re_\tau < 800$, they showed that the probability density functions of the vortices diameter and maximum azimuthal velocity were universal in Re and have a weak dependence in y when non-dimensionalized with the local Kolmogorov scales η and v. In the near wall region ($y^+ < 40$), the most expected diameter is about 10η, and the most expected maximum azimuthal velocity is $2.0v$. Away from the wall, the most expected diameter and maximum azimuthal velocity are 8η and $1.2v$ respectively. Kang et al (2007) extended this scaling of the fine scale eddies up to $Re_\tau = 1270$. In addition, clusters of fine-scale eddies and their dynamics were also investigated. The clusters are observed within low-momentum regions of the outer region, and their size increases with increasing wall-normal distance. Using conditional averaging, they showed that the low momentum regions play an important role in the production of the Reynolds shear stress and in the dissipation of turbulent kinetic energy. Finally, Das et al (2006) showed that the velocity field of a vortex projected on a plane normal to the vorticity vector is well approximated by a Burgers vortex. A theoretical description of coherent eddies was then realized based on the Burgers vortex approximation.

The largest range of Reynolds number in DNS of turbulent channel flow have been achieved thanks to a joint effort of Stanford, Madrid and Urbana Champaign universities. The vortex large-scale organization in the logarithmic region of turbulent channel flow was studied by DelAlamo et al (2006) in a range of Reynolds number varying from $Re_\tau = 180$ up to $Re_\tau = 1900$. A vortex detection criterion based on the discriminant of the velocity gradient tensor was used, and neighboring points satisfying the criterion were connected to define individual vortices. The individual spanwise vortices were characterized using a fit to an elliptical Gaussian vortex: the mean radius and maximum azimuthal velocity were found to depend little of Re_τ and y when scaled with the Kolmogorov lengthscale η and the RMS turbulence intensity. These spanwise vortices are about 20% thinner and twice as strong as the vortices detected in all directions in Tanahashi group. A study of the large-scale clusters of vortices was then undertaken. Both tall cluster attached to the wall and small clusters detached from the wall were identified. The scaling of the attached clusters is self-similar such that their dimensions Δ_x, Δ_y and Δ_z are given by $\Delta_x = 3\Delta_y$ and $\Delta_z = 1.5\Delta_y$. The detached clusters are found to scale with the Kolmogorov scales. The attached clusters are parts of larger regions of low-momentum flow whose average geometry is consistent with a cone tangent to the wall along the streamwise axis. It is assumed that the low-momentum region and the clusters are part of a self-sustaining and self-similar process, where the low-momentum region are wakes left behind clusters, while the clusters themselves are triggered by the wakes left by yet larger clusters in front of them.

1.6 Unresolved issues and aims

1.6.1 Unresolved issues

Although the hairpin-packet model is attractive in many aspects, a number of details on this model remains unclear and sometimes even controversial in the light of recent results. More specifically, the following issues on the structure of near-wall turbulence remain outstanding:

- **the picture of near-wall turbulence in the inner region remains incomplete**.
  Adrian et al (2000b) description is mostly limited to the outer region, and does not account for the predominant structures on the inner layer, that is the streamwise vortices (Robinson (1991), Jeong et al (1997) and Sheng et al (2008)) and the low-speed streaks (Kline et al (1967), Blackwelder (1997))). Regarding the streamwise vortices, Zhou et al (1999) argued that a primary hairpin was found to generate quasi-streamwise vortices along its legs, but no information was given on the evolution of these streamwise vortices, and more specifically on their ability or not to generate in turn new hairpin vortices. Regarding the low-speed streaks, they are often identified to the low-momentum regions observed inside hairpin packet (Adrian et al (2000b)) or vortex clusters (DelAlamo et al (2006)), but it should be emphasized that these two structures do not seem to coincide in wall-normal position and size (an extensive characterization of the low-speed streaks can be found in Lin et al (2008b)). In fact, subsequent studies by Tomkins and Adrian (2003) in XZ planes in the upper buffer layer and log regions have evidenced low-momentum fluid alongside vortical structure, but the streamwise extent of the PIV velocity fields was too limited to conclude on the consistency with the elongated low-speed streaks.

- **the origin of the very large scale motion is not accounted for**.
  Inactive Very large-scale motions have been evidenced with hot-wire anemometry (Kim and Adrian (1999), Guala et al (2006), Hutchins and Marusic (2007) and Marusic and Hutchins (2008)) in the outer region of wall-bounded turbulent flows in a wide range of Reynolds numbers. Although some efforts have been made by Kim and Adrian (1999) to integrate them in the hairpin packet model, these suggestions remain purely hypothetical and lack some experimental or numerical evidence.

- **the role of retrograde spanwise vortices is poorly understood**.
  Although a non negligible portion of the spanwise vortices were found to rotate in the opposite sense to the mean shear (Carlier and Stanislas (2005), Wu and Christensen (2006)), these structures have been ignored in Adrian's model. They deserve further assessment of their characteristics and role in the organization of near-wall turbulence.

- **the self-sustaining mechanism can be further discussed**
  The parent-offspring generation mechanisms proposed by Smith (1984) and Zhou et al (1999) are based on investigations that provide valuable information. However, in these studies, the initial parent hairpin was introduced artificially. Moreover, these studies were carried out in a quiet environment (laminar boundary layer, or

an initial velocity field without fluctuations). Finally, the study of the initial hairpin used by Zhou et al (1999) was constructed from DNS data at very low Reynolds number ($Re_\tau = 180$). For these reasons, the question arises as to whether these initial conditions are representative of near-wall turbulence phenomenon. Also, it is worth noting that the secondary and tertiary hairpins were generated in the outer region of the channel flow, and therefore do not account for the generation mechanisms in the inner region.

- **statistical results are required for a reliable discussion**
  The qualitative analysis of a few instantaneous velocity fields certainly provide useful scenarios for the organization of near-wall turbulence (Adrian et al (2000b)). However, numerical or experimental statistical results on coherent structures are required to assess the representativeness of these models. In addition, the scaling laws of coherent structures can only be investigated on the basis of statistical data.

- **scaling laws of vortical structures must be extended**
  Recently, Carlier and Stanislas (2005) studied the wall-normal evolution of vortices characteristics in the logarithmic region and found that they were universal in Reynolds number (in the range $Re_\theta \in [7500; 19000]$) when scaled in wall-units. A different scaling, based on the Kolmogorov local scales, was investigated by Tanahashi et al (2004) and by Stanislas et al (2008). A good universality both in Reynolds number and in wall-normal distance was observed. However, the PIV results of Stanislas et al (2008) were restricted to two Reynolds number ($Re_\theta = 7800$ and $Re_\theta = 15000$) and to streamwise-oriented vortices, while the DNS investigation of Tanahashi et al (2004), took into account all orientations of the vortices but were restricted to low Reynolds number ($Re_\tau \in [100; 1270)$. Therefore, the validity of this new scaling needs to be extended to a larger range of Reynolds number, and to spanwise oriented structures.

1.6.2 Aims of the thesis

Among these outstanding issues, the present thesis aims at providing statistical results over a large range of Reynolds numbers on:

- the characteristics of streamwise and spanwise oriented vortices in the upper buffer layer and logarithmic regions of turbulent boundary layer, with emphasis on the specificities of prograde and retrograde vortices and
- the scaling laws of these structures.

In addition, these results are interpreted in order to contribute to the understanding of the self-sustaining mechanisms of near-wall turbulence.

For that purpose stereo-PIV measurements with high spatial resolution are undertaken in two facilities: the LTRAC water-tunnel in Melbourne (Australia) and the LML wind-tunnel in Lille (France). The measurements are carried out in streamwise/wall-normal and spanwise/wall-normal sections of turbulent boundary layers in the range $Re_\theta \in [1300; 18950]$. After a careful validation of the database through the analysis

of the mean properties of the flow, advanced post-processing tools are utilized to educt and characterize vortical structures. Finally, statistical results on the detected vortices are discussed in the context of the current knowledge on coherent structures.

Chapter 2

Particle Image Velocimetry

Particle image velocimetry (PIV) is a measurement technique that gives access to a quantitative and instantaneous estimation of the velocity distribution in the flowfield. It takes its roots into flow visualization and 'laser speckle photography' employed in solid mechanics to measure surface deformations. Meynart (Meynart (1983), Meynart (1984)) realized some pioneering work on PIV, and was among the first to apply this technique to the measurement of complex flows. Excellent review papers on this technique can be found in Adrian (1991), Grant (1997), Raffel et al (1998) and more recently in Raffel et al (2007). With the addition of multiple cameras, high speed cameras and high speed lasers, the original 2D-2C PIV technique has given birth to a series of more elaborate techniques. Stereoscopic PIV (Prasad (2000)) gives access the out-of-plane velocity component, time-resolved PIV (Baur and Koengeter (2000)) to the Eulerian evolution of the flow, and dual plane PIV (Kahler and Kompenhans (2000)) to the out-of-plane velocity gradient. Volumetric techniques, such as Holographic PIV (Pu and Meng (2000)), Tomographic PIV (Elsinga et al (2006)) or Tomo-Holo PIV (Soria and Atkinson (2008)) are still in development. In the following, the working principle of 2D-2C PIV is first presented; then, the fundamentals of stereoscopic PIV are given; finally, the spatial dynamic range of this technique is discussed.

2.1 Conventional 2D-2C PIV

2.1.1 Working principle

The working principle of planar PIV is depicted in figure 2.1. The flow is seeded with small tracer particles, assumed to follow faithfully the motion of the fluid elements. A laser beam is shaped into a light sheet and directed into a plane of the flow. It is pulsed twice within a short time delay, and the Mie scattering of the illuminated particles is imaged via a lens, and recorded on a single frame or on two frames of either a photographic film or the sensor of a digital camera. Three different types of evaluation schemes can then be used on these recordings to extract displacement information: the statistical scheme, the tracking technique (Agui and Jiménez (1987), Guezennec et al (1994)) or

the super resolution algorithm (Keane et al (1995)). As discussed in Raffel et al (1998), the tracking technique is restricted to low image density and is then not suitable for obtaining high density data; the super resolution algorithm is an hybrid technique between the statistical and the tracking approach and is more of interest for photographic PIV. Therefore, only the statistical evaluation will be presented and discussed in this chapter. The statistical evaluation consist in performing an autocorrelation or a crosscorrelation (for single frame or double frame images respectively) on small subregions of the recording called 'interrogation window' (IW); the location of the correlation peak represents the average displacement vector over the IW between the two illumination pulses. The underlying assumption of the statistical evaluation is that the motion of the particle images within the interrogation window is approximately uniform. For each interrogation window, the projection of the local velocity vector into the plane of the light sheet (a two-components velocity vector) is then retrieved by taking into account the time delay and the magnification at imaging.

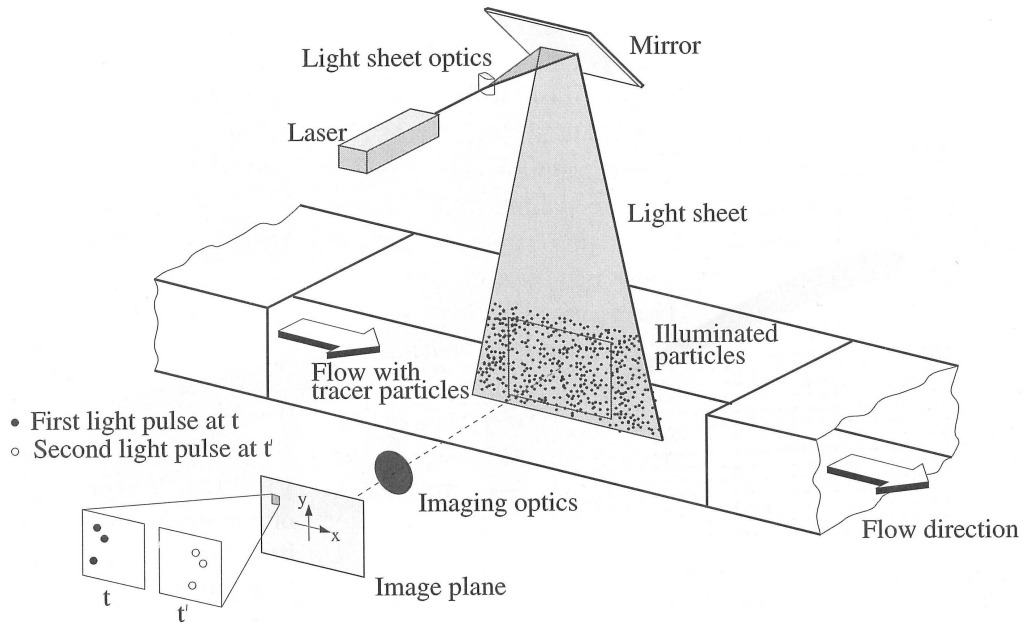

Figure 2.1: Experimental arrangement for Particle Image Velocimetry, taken from Raffel et al (1998)

Nowadays, the PIV images are recorded on a CCD array of a video camera and cross-correlated computationally: this technique is called digital PIV (Willert and Gharib (1991), Westerweel (1993), Westerweel (1997)). Contrary to photographic films, video camera enables a real time viewing of the measurement region, and hence a real-time optimization of the PIV parameters (seeding concentration, illumination, focus). When the particle images are discretized on more than one pixel, a fit of a function to the cross-correlation peak (typically a 3 points Gaussian fit) can be performed in order to retrieve the displacement with sub-pixel accuracy (on the order of $1/10^{th}$ of a pixel).

2.1.2 Advanced evaluation algorithm for digital PIV

The advent of digital PIV, along with improved computing ressources, has promoted the improvement of interrogation algorithms. Three advanced algorithm for the PIV statistical evaluation are briefly presented: the multipass algorithm, the multigrid algorithm, and the image deformation schemes.

The multipass algorithm with integer offset, as proposed by Westerweel et al (1997) allows to significantly decrease the number of unpaired particles that enter or exit the interrogation window during the two exposures, and hence to get a better signal-to-noise ratio. The working principle is the following: a first interrogation is performed using a window offset close to the global mean displacement; the displacement estimate from the first interrogation is used as a new window offset for a second interrogation; the process is repeated until the integer offset vector converge to ± 1 pixel.

The multigrid algorithm is an improved version of the multipass algorithm. It consist in reducing the interrogation window size and refining the evaluation grid during the successive evaluation of the multipass algorithm. It was first used by Soria (1996) for the investigation of the near wake of a circular cylinder and then characterized in Soria et al (1999). The spatial dynamic range of the experiment, which depends directly on the size of the averaging area, is drastically improved.

Finally image deformation schemes (Scarano (2002) and Lecordier and Trinite (2003)) can be of interest in flows where a significant velocity gradient over the interrogation window exists. The PIV recordings are iteratively deformed according to the computed velocity field.

2.1.3 Assessment of measurement error

There exists multiple sources of noise that can affect the accuracy of a PIV measurement:

- unpaired particles due to out-of-plane motions,
- unpaired particles due to in-plane displacements that are too large with respect to the IW,
- non-uniform displacement over the IW due to mean velocity gradients or turbulent fluctuations,
- non-optimal seeding concentration and non-uniform distribution of the bright particles over the IW,
- non-optimal imaging parameters (discretization of the particles...),
- etc...

The resulting interrogation error can be decomposed into the measurement random error $\sigma(\epsilon_{int})$ (the RMS error, corresponding to the absolute value of the measurement uncertainty with a confidence interval of 68%) and the measurement bias error $< \epsilon_{int} >$. This measurement error can be assessed in a variety of ways.

The first way consists in generating synthetic PIV images of known content, using Monte Carlo simulation. The artificial recordings can then be evaluated and compared with the known result. The behavior of the PIV error with the variation of each PIV and flow parameter (particle diameter, concentration, velocity gradient, third component,...) can be assessed. By varying one parameter at a time, Keane and Adrian (1990), Soria (1996), Raffel et al (1998) and Foucaut et al (2003) realized parametric studies of the PIV error and determined optimal design rules for the PIV parameters: particle images should be discretized on 2-3 pixels, the particle concentration should be of 10 per IW, and there should be no gradient and no out-of plane motion. Foucaut et al (2003) and Soria (1996) found a PIV random error on the order of $0.06px$ for optimal PIV parameters and a uniform in-plane displacement of $\pm 0.5px$ (any uniform displacement can be reduced to $\pm 0.5px$ using a multipass algorithm with integer offset). Over the range of parameters explored, Foucaut et al (2003) showed that the RMS error $\sigma(\epsilon_{int})$ was one order of magnitude larger than the bias error $< \epsilon_{int} >$.
For a given PIV experiment, it is possible to use an existing parametric study to retrieve the PIV error: with an appropriate scaling, each PIV parameter can be related to a parameter of the synthetic study, and hence associated to an RMS error. The greatest of these RMS error is then be taken as the global PIV uncertainty. The only constraint is that the evaluation algorithm used in the synthetic study must have the same features than the evaluation algorithm used for PIV experiment. This methodology has been used recently in Herpin et al (2008) to assess the uncertainty of their PIV experiment.
However, synthetic studies present some disadvantages: in most studies, the influence of fluctuations or non constant gradients that can occur in wall-bounded turbulent flows is not assessed; also, the transfer functions of the imaging optics and of the CCD array are not taken into account. Two exceptions are worth mentioning: Lecordier and Westerweel (2003) have developed a CCD model in the EUROPIV SIG; also synthetic images based on DNS data of turbulent channel flow have been used in the second international PIV challenge (Stanislas (2005)). However, as mentioned in conclusion of this challenge, synthetic images are not yet fully representative of real experimental conditions.

The second option to assess the PIV error is to use real images of a printed random particle pattern displaced with a translation stage. This test presents the advantage of being feasible *in situ*, using the configuration of interest for the camera and the imaging optics. It has been used by Willert and Gharib (1991) to study the influence of seeding density and translation displacement. Of course, this method is incomplete as the real particle are not used.

The third option to assess the PIV error is to use real images of real particles for which the displacement is known. For instance, PIV recordings of naturally buoyant particle in a quiescent flow have been used in Foucaut et al (2004). Here again, this technique presents the interest of using the camera and imaging configuration of interest. However, all the flow-related sources of error (unpaired particle, gradients, fluctuations...) are not taken into account. Also real images of self similar turbulent jet, for which the turbulence statistics are known, have been tested in the second international PIV challenge (Stanislas (2005)).

Because they do not take into account all the possible sources of PIV noise, these first three methods are expected to provide a lower bound of PIV uncertainty. A novel way of accessing to the actual PIV uncertainty have been shown in Kostas et al (2005) and in

Herpin et al (2008): it consists in realizing a series of two instantaneous but independent measurements of the same phenomenon. More specifically, Herpin et al (2008) used two stereoscopic PIV systems just overlapping in the streamwise direction to measure a XY plane of a turbulent boundary layer. The measurement random error was retrieved as the RMS of the difference between the two 2D-3C velocity fields in the overlap region. This technique presents the advantage of including all the sources of noise (optical, recording, flow and evaluation related) present in the experiment.

2.2 Stereoscopic technique

One important shortcoming of the 'Classical' PIV is that it is only capable of recording the in-plane projection of the velocity vector into the plane of the light sheet. In contrast, the stereoscopic technique is capable of retrieving the out-of plane motion of the flow, and it also eliminates perspective error which can contaminate the measurement of the in-plane components.

2.2.1 Experimental configuration

The basic principle of SPIV is to use two cameras to record simultaneous but distinct off-axis views of the same region of interest. The different stereoscopic configurations have been reviewed in great details in Prasad (2000). The two cameras can either be arranged in a translation configuration (where the axes of both cameras are placed parallel to each other, and orthogonal to the light sheet), or in an angular configuration (where the axes of the cameras are rotated such that they intersect with the object plane along the same axis). The translation configuration presents two severe limitations: the small common area viewed by the two camera, and the upper bound on the off-axis angle ($\theta \approx 15°$) which limits the accuracy of the out-of-plane component. Therefore, the angular configuration is generally preferred. Two implementations of the angular configuration exist: either the cameras are set up on the same side of the laser sheet, as shown in figure 2.2, or the camera are placed on either side of the laser sheet, as proposed by Willert (1997). The second option present two benefits: first of all, with a suitable orientation of the direction of propagation of a laser, it is possible to operate both camera in forward scattering; besides, the image field of both camera enjoy identical stretching, which allows a more accurate reconstruction of the 3C displacement. In the angular configuration, it is necessary to enforce the Scheimpflug condition (Prasad and Jensen (1995)) in order to achieve a sharp focus over the entire field of view: the image plane of each camera must be tilted with respect to the lens plane, so that they intersect on a same line with the object plane.

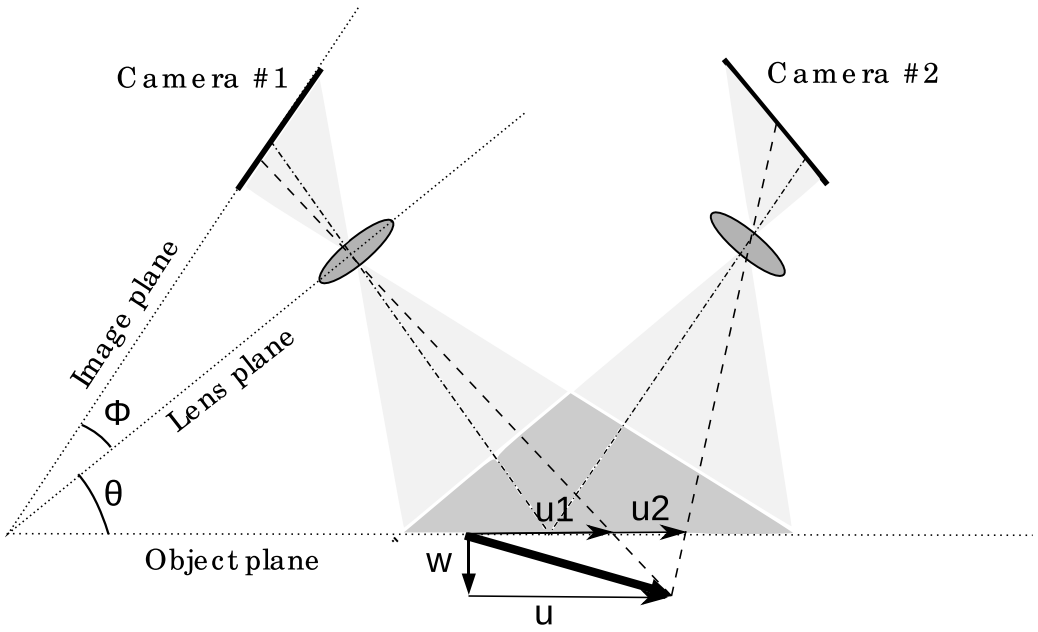

Figure 2.2: Basic angular configuration for Stereoscopic PIV, with enforcement of the Scheimpflug condition. 'u1' is the in-plane projection of the velocity measured by camera 1; 'u2' is the in-plane projection of the velocity measured by camera 2; the true velocity vector (of in-plane component 'u' and out-of plane component 'w') is reconstructed through a triangulation of 'u1' and 'u2'

2.2.2 Mapping between the object space and the image space

In the angular configuration, the magnification is no longer uniform over the field of view. For each camera, a mapping function between the object space (coordinate system X_o,Y_o,Z_o) and the image plane (coordinate denoted X_i,Y_i) is required. This mapping function can either consist in a pinhole model, polynoms, or rational polynoms. Two types of transformation may be considered: a $2D \leftrightarrow 2D$ transform where a plane in the object space is related to a plane in the image space, and $3D \leftrightarrow 2D$ transform where a volume in the object space is related to a plane in the image space. The forward projection ('$\rightarrow$') is defined as the projection from the object space to the image space, the backward projection ('$\leftarrow$') being the inverse transformation.

Pinhole model In the pinhole model, the camera lens is approximated by a pin-hole; all rays originating from the object and reaching the sensor are assumed to pass through this point. The pinhole model is a $3D \rightarrow 2D$ transform. It basically consists in a translation/rotation to pass from the object volume coordinate to the image plane coordinate, a central projection about the center of each camera lens, and finally a metric to pixel transformation. The central projection involved in the pinhole model is illustrated in figure 2.2. A point in the image plane of each camera can be back-projected into the object volume as the intersection of the two rays passing for each camera through the image point on the sensor and through the center of the lens. This back-projection is referred to as 'triangulation'. Following Calluaud and David (2004), the pinhole model

can be formalized for each camera as:

$$\begin{bmatrix} X_i \\ Y_i \\ 1 \end{bmatrix} = M \begin{bmatrix} X_o \\ Y_o \\ Z_o \\ 1 \end{bmatrix} \quad \text{with} \quad M = \begin{bmatrix} k_u f & 0 & u_0 & 0 \\ 0 & k_v f & v_0 & 0 \\ 0 & 0 & 1 & 0 \end{bmatrix} . \begin{bmatrix} r_{11} & r_{12} & r_{13} & t_x \\ r_{21} & r_{22} & r_{23} & t_y \\ r_{31} & r_{32} & r_{33} & t_z \\ 0 & 0 & 0 & 1 \end{bmatrix} \tag{2.1}$$

where the focal distance f, the vertical and horizontal scale factor k_u and k_v, the intersection between the optical axis and the image plane (u_0, v_0) are the intrinsect parameters of the system, and the rotations coefficient r_{ij} and translation coefficients t_j are the extrinsic parameters. As such, the pinhole model does not account for distorsions that may occur due to imperfect lens or imaging non-linearities. Radial distorsions can be taken into account by adding additional parameters to the model (Wieneke (2005)).

Polynoms models Polynomial functions are another possibility. It is not based on geometry optics, but high order terms can account for lens distorsion and image non-linearities. Westerweel and van Oord (2000) employed second order polynomials in X and Y to realize a $2D \leftarrow 2D$ transform:

$$\begin{aligned} X_o &= a_1 X_i^2 + a_2 Y_i^2 + a_3 X_i Y_i + a_4 X_i + a_5 Y_i + a_6 \\ Y_o &= b_1 X_i^2 + b_2 Y_i^2 + b_3 X_i Y_i + b_4 X_i + b_5 Y_i + b_6 \end{aligned} \tag{2.2}$$

Soloff et al (1997) suggested the use of $3D \rightarrow 2D$ polynom with cubic dependence in X_o and Y_o and quadratic dependence in Z_o:

$$\begin{aligned} &a_0 + a_1 X_o + a_2 Y_o + a_3 Z_o + a_4 X_o^2 + a_5 X_o Y_o + a_6 Y_o^2 \\ &+ a_7 X_o Z_o + a_8 Y_o Z_o + a_9 Z_o^2 + a_{10} x_o^3 + a_{11} x_o^2 Y_o + a_{12} x_o Y_o^2 + a_{13} Y_o^3 \\ &+ a_{14} x_o^2 Z_o + a_{15} x_o Y_o Z_o + a_{16} Y_o^2 Z_o + a_{17} X_o Z_o^3 + a_{18} Y_o Z_o^2 \end{aligned} \tag{2.3}$$

Rational polynoms models Willert (1997) noted that the projection equation based on the pinhole model can be expressed as a ratio of first-order polynoms. He proposed to extend it to a higher order to take into account imperfect imaging optics :

$$\begin{aligned} X_o &= \frac{a_{11} X_i^2 + a_{12} Y_i^2 + a_{13} X_i Y_i + a_{14} X_i + a_{15} Y_i + a_{16}}{b_{11} X_i^2 + a_{12} Y_i^2 + a_{13} X_i Y_i + a_{14} X_i + a_{15} Y_i + a_{16}} \\ Y_o &= \frac{a_{21} X_i^2 + a_{22} Y_i^2 + a_{23} X_i Y_i + a_{24} X_i + a_{25} Y_i + a_{26}}{b_{21} X_i^2 + b_{22} Y_i^2 + b_{23} X_i Y_i + b_{24} X_i + a_{45} Y_i + b_{26}} \end{aligned} \tag{2.4}$$

Willert (1997) used a simplified form of these equations where $b_{1j} = b_{2j}$. This method can easily be extended to the $3D \leftarrow 2D$ case by adding a third equation:

$$Z_o = \frac{a_{31} X_i^2 + a_{32} Y_i^2 + a_{33} X_i Y_i + a_{34} X_i + a_{35} Y_i + a_{36}}{b_{31} X_i^2 + b_{32} Y_i^2 + b_{33} X_i Y_i + b_{34} X_i + a_{35} Y_i + b_{36}} \tag{2.5}$$

Calibration of the models parameters All these three models depend on a certain number of parameters: the intrinsect and extrinsic parameters for the pinhole, and the coefficients for the polynomials functions. These parameters need to be calibrated in order to calculate the mapping functions. The parameters of the pinhole model can be simply

deduced from the measurement of the imaging geometry of the setup (focal distance, viewing angles, Scheimpflug angle...). However, in most situations, these parameters cannot be retrieved with enough accuracy, and therefore this method is not recommended. The alternative method (applicable for all models) consists in placing a calibration target aligned with the laser sheet and coincident with the field of view. The calibration target is made of a precise grid of reference marks (cross, circles, or lines intersection), regularly spaced. The image of the calibration target is recorded on each camera sensor. For the $2D \leftrightarrow 2D$ mappings, only a planar target is needed, but for the $3D \rightarrow 2D$ transforms, depth information must be provided. It is obtained either by translating the target in the out-of-plane (Z) direction (Soloff et al (1997)), or by using a multilevel target with reference markers at different heights. These two types of calibration will be referred to as '2D calibration' and '3D calibration' respectively. In both case, the position of each mark on the images of the calibration target is easily detected with simple image processing techniques, providing a set of correspondent points between the object space and the image space. The parameters of the model can then be retrieved through a fit to these correspondent points. For the polynomials models, care should be taken to have markers covering the whole field of view as these functions perform poorly outside of the fitting domain. As far as the 3D calibration is concerned, the different views in the out-of-plane direction must at least embed the laser sheet thickness. These 'calibration-based' techniques present the advantage that no-apriori information on the setup is required. Used in conjunction with the pinhole model, this technique actually allows the retrieval of the setup geometry.

2.2.3 Evaluation of the SPIV images

A stereoscopic evaluation consists in three elementary operations:

- a backprojection from the image space to the object space for each camera,
- a two dimensional cross-correlation between the particles for each camera, using the same algorithm as for standard PIV and
- a three component reconstruction using the two 2D-2C velocity fields of each camera

A variety of stereoscopic evaluation techniques can be found in the literature, depending on the sequence into which these operations are executed, on the mapping model (pinhole or polynomial function) used for the backprojection and 3C reconstruction, and finally on the method employed to calibrate coefficients of these model (measurement based, or target based calibration). The techniques can be classified in three main groups: the '2D vector warping' techniques, the '3D vector warping' techniques and the 'particle mapping' techniques.

2D vector warping With the 2D vector warping technique, the cross-correlation is performed in the image space of each camera. The 2D-2C vectors are then backprojected into the reference plane in the object space ('dewarping') using a $2D \leftarrow 2D$ transformation. Finally a 3C reconstruction is realized using a triangulation method on the two 2D-2C vectors. While a calibration target is usually used to calibrate the mapping function the parameters required for the triangulation are usually measured on the setup. If

the cross-correlation is realized on a Cartesian grid on each camera image space, then the 2D-2C vectors from each camera will be mapped on a different and non-Cartesian grid in the object space. An interpolation on a common Cartesian grid in the object space is then necessary before the 2D-2C vectors are recombined into a 3C vector. As proposed by Coudert and Schon (2001), this interpolation step can be avoided if the cross-correlation in the image space of each camera is performed on a 'warped' grid defined as the forward projection of a common Cartesian grid in the object space.

3D vector warping This technique is similar the '2D vector warping', except that the vectors are backprojected into a volume rather than a plane of the object space using a $3D \leftarrow 2D$ transformation. In this manner, the dewarping and 3C reconstruction are realized in a single step. In this technique, all the parameters are retrieved using a 3D calibration. Two possible implementations of this model exist. The first possibility is to use a pinhole model to retrieve the origin and the end of the 3C displacement vector in the object space. In this case, the parameters of the pinhole model are retrieved using a target-based 3D calibration. This method was recently used in Calluaud and David (2004), in Wieneke (2005) and in Scarano et al (2005). The second possibility is known as the 'Soloff method' (Soloff et al (1997)): it consist in a Taylor series expansion to the first order of a $3D \rightarrow 2D$ forward projection function of polynomial type $F_i^{(c)}(X_o, Y_o, Z_o)$, to relate the 3D object displacement to the 2D image displacements:

$$\overrightarrow{\Delta X_i^{(c)}} = F^{(c)}(\overrightarrow{X_o} + \overrightarrow{\Delta X_o}) - F^{(c)}(\overrightarrow{X_o}) \quad \Leftrightarrow \quad \overrightarrow{\Delta X_o} = \nabla F^{(c)} \overrightarrow{\Delta X_i}$$

where superscript (c) stands for the camera index, subscript i stands for the image space coordinates, and subscript o stands for the object space coordinate. The relation between the 3D object displacement and the 2D image displacements can be expressed in a matricial form:

$$\begin{bmatrix} \Delta X_i^{(1)} \\ \Delta Y_i^{(1)} \\ \Delta X_i^{(2)} \\ \Delta Y_i^{(2)} \end{bmatrix} = \begin{bmatrix} F_{Xi,Xo}^{(1)} & F_{Xi,Yo}^{(1)} & F_{Xi,Zo}^{(1)} \\ F_{Yi,Xo}^{(1)} & F_{Yi,Yo}^{(1)} & F_{Yi,Zo}^{(1)} \\ F_{Xi,Xo}^{(2)} & F_{Xi,Yo}^{(2)} & F_{Xi,Zo}^{(2)} \\ F_{Yi,Xo}^{(2)} & F_{Yi,Yo}^{(2)} & F_{Yi,Zo}^{(2)} \end{bmatrix} \cdot \begin{bmatrix} \Delta X_o \\ \Delta Y_o \\ \Delta Z_o \end{bmatrix} \tag{2.6}$$

The matrix ∇F can then be inverted to retrieve the 3D object plane displacement $\overrightarrow{\Delta X_o}$ directly from the 2D images planes displacement $\overrightarrow{\Delta X_i^{(c)}}$.

Particle image mapping The other option, implemented by Willert (1997), consists in mapping for each camera the image fields containing the particles to the reference plane of the object space using a $2D \leftarrow 2D$ transformation. The backward projection of squared pixels (in the image space) being distorted pixels (in the object space), each image mapped into the object space needs to be resampled. The cross-correlation is then performed for each camera PIV image on a common Cartesian grid in the object space. Finally, the two 2D-2C vectors in the object space are triangulated to obtain the 2D-3C displacement vector. While a calibration target is usually used to calibrate the mapping function, the parameters required for the triangulation are usually measured on the setup.

2.2.4 Misalignment correction

All the stereoscopic evaluation techniques assume that the reference object plane into which the particle images or the displacement vectors origins are backprojected coincides exactly with the measurement area. For that purpose the reference position of the calibration target (or its reference level for 3D multilevel targets) needs to be placed in perfect alignment with the plane of maximum light intensity of the laser sheet. As pointed out by Prasad (2000), this condition is almost impossible to meet.
Misalignment results in a mismatch between the information used from each camera to reconstruct the 2D-3C velocity field. This type of error is called the 'registration error' (Prasad (2000)), or 'misalignment error' (Willert (1997)). Willert (1997) proposed a way to quantify the existing misalignment : two PIV images, taken *at the same instant* from different viewing angles (typically from the 2 camera of the stereo system) are backprojected in the reference plane of the calibration target and then cross-correlated. The resulting map is called the disparity map between the two stereo camera. Each point of this disparity map can then be related to the local misalignment via triangulation, giving access to an estimate of the actual position of laser sheet. From the knowledge of the disparity map, several techniques can be employed to correct the misalignment error.
In the framework of the 2D and 3D warping techniques, Coudert and Schon (2001) proposed to shift each node of the common Cartesian grid in the object plane by half the local disparity, in opposite directions for each camera of the stereo pair. The two shifted object grids are then projected on the image plane of each camera, to form the 2 mesh onto which the 2D-2C PIV interrogation will be performed. This shift between the 2 image-grid compensates for the recombination error occurring during the stereoscopic reconstruction.
In the framework of the 3D warping technique using a pinhole model, Wieneke (2005) correct the misalignment by modifying the projection function themselves. For that purpose, a plane is fitted through the laser sheet points. This plane is chosen as a new origin for the mapping functions; the translation/rotation functions involved in the mapping from the object volume coordinate to the image plane coordinate are modified accordingly. This misalignment correction scheme is called 'self-calibration' by Wieneke (2005), although this may not be the most appropriate terminology.

Comparison of the techniques A comparison between the image mapping, 2D warping and Soloff technique was realized by Lin et al (2008a), based on the estimation of accuracy, the spatial spectra and velocity PDFs. It was found that the Soloff method was giving the best results (in term of accuracy, and estimation of the spatial spectra and velocity PDFs) although the differences from the other two methods (mapping and warping) were fairly limited. The main advantage of the Soloff method is that it requires no-apriori knowledge of the setup geometry for the reconstruction step. Lin et al (2008a) also found that the misalignment correction improved significantly the quality of the results. Scarano et al (2005) compared the image mapping technique with misalignment correction to the pinhole model. They found that these two techniques were almost equivalent for a correctly aligned system. Finally, as far as the CPU time is concerned, the image mapping techniques are more demanding than the warping techniques, because the number of pixels to backproject in the mapping technique is much larger than the number of vectors to backproject in the warping techniques.

2.2.5 Error analysis

All stereoscopic techniques make use of a two dimensional PIV evaluation, performed for each camera of the stereo arrangement. This evaluation is realized using the same algorithm as for standard PIV; the random error of this evaluation $\sigma(\epsilon_{int})$ was assessed in a number of studies, as summarized in section 2.1.3. Assuming that this error is identical for both camera, it is possible, in the framework of the pinhole model, to relate analytically the evaluation error $\sigma(\epsilon_{int})$ in the image space to the error on the in-plane $\sigma(\epsilon_{in-plane})$ and out of plane $\sigma(\epsilon_{out-of-plane})$ displacements in the object space (Prasad (2000)):

$$\begin{aligned} \sigma(\epsilon_{in-plane}) &= \frac{1}{\sqrt{2}}\frac{1}{M}\sigma(\epsilon_{int}) \\ \sigma(\epsilon_{out-of-plane}) &= \sqrt{2}\frac{d_o}{MS}\sigma(\epsilon_{int}) \end{aligned} \tag{2.7}$$

where M is the camera nominal magnification, S is the distance between the center of the lenses, d_o is the object distance, and θ is the off-axis angle. Hence the relative error in the out-of-plane component is:

$$\frac{\sigma(\epsilon_{out-of-plane})}{\sigma(\epsilon_{in-plane})} = 2\frac{d_o}{S} = \frac{1}{\tan\theta} \tag{2.8}$$

As can be seen in equation 2.7, the stereoscopic in-plane error is smaller (by $1/\sqrt{2}$) than the corresponding error for a single camera, because two camera contribute equally to the final result. Also, as given by equation 2.8, the relative error between the out-of-plane and in-plane error is equal to the inverse of the off-axis angle tangent. Therefore, a viewing angle of 45° is recommended to get as much accuracy on the out-of-plane component as on the in-plane component. Although this error analysis is exact for the translation configuration only, Zang and Prasad (1997) showed that it is indeed a good approximation for an angular Scheimpflug configuration.

2.3 Spatial dynamic range of PIV

The spatial dynamic range (SDR) represents the ability of a PIV experiment to resolve spatial variations in a flow. It is a quantity of special interest in the context of turbulent flow and coherent structures investigations (Herpin et al (2008)).

2.3.1 Definition of the spatial dynamic range

The aptitude of a PIV system to resolve spatial variations in the flow is difficult to assess: a PIV system is a complex measurement chain, and it is not always easy to discriminate which *independent* parameters of the experiment are the *most* limiting ones in terms of SDR. By definition, the SDR is bounded at the upper end by the largest resolvable spatial variation SV_{max}, and at the lower end by the smallest resolvable one SV_{min}. The former is straightforward to characterize: SV_{max} is equal to the extent of the field of view S, and hence is limited only by the resolution of the recording medium,

typically the number of pixels of a video-camera CCD arrays. SV_{min} (or its spectral counterpart the cut-off wavenumber $kc = \frac{2\Pi}{SV_{min}}$) is less straightforward to quantify. The PIV measurement technique (used in conjunction with the statistical evaluation) can be considered as a spatial averaging filter over a volume Vol_{PIV} delimited by the interrogation window IW and extending across the laser sheet thickness l_z (Willert and Gharib (1991)). As the laser sheet presents a non-uniform light intensity distribution across its thickness (this distribution is usually approximated as being Gaussian), only the particles located within an illuminated region of *effective* thickness $lz_{eff} < lz$ will contribute to the PIV correlation (Westerweel (1996)). The PIV averaging volume reads $Vol_{PIV} = L_{IW}^2 * lz_{eff}$ for a square IW of size L_{IW}, and, following a Nyquist criterion, the smallest spatial variation theoretically resolvable $SV_{min,th}$ is given by:

$$SV_{min,th} = 2 * max(L_{IW}, lz_{eff}) \tag{2.9}$$

Note that in most PIV applications, lz and hence lz_{eff} are smaller than L_{IW} and one immediately gets $SV_{min,th} = 2 * L_{IW}$. The theoretical spatial dynamic range (SDR_{th}) of PIV is finally given by:

$$SDR_{th} = \frac{S}{2 * L_{IW,obj}} \text{ in the object space, and } SDR_{th} = \frac{CCDsize}{2 * L_{IW,im}} \text{ in the image space} \tag{2.10}$$

In the spectral domain, the response of PIV was characterized by Foucaut et al (2004) by taking measurements in quiet water. They established that the PIV transfer function is a squared cardinal sine function, due to the windowing effect. The cut-off wavenumber kc_{th} for an attenuation of $-3dB$ is $kc_{th} = \frac{2.8}{L_{IW}}$, leading to $SV_{min,th} = 2.2 * L_{IW}$ (in good agreement with the value predicted with the Nyquist criterion). Wavenumbers exceeding kc_{th} are increasingly filtered out up to the highest wavenumber $k_{max} = \frac{2\Pi}{2\Delta_{IW}}$ (Δ_{IW} representing the distance between adjacent interrogation windows). Δ_{IW} was found to have no influence on the amount of information retrieved, provided the overlap was at least 50% of the IW size (larger overlaps result in an oversampling of the PIV signal).
It has been shown by a number of studies that the SDR *effectively* achieved in PIV measurements of near-wall turbulence differs from the theoretically predicted one. Westerweel et al (1993) compared photographic PIV measurements of a turbulent pipe flow to a DNS simulation at similar conditions, and later on Westerweel (1996) undertook the same type of comparison using digital PIV recordings. On the other hand, Guichard et al (1998) used synthetic particle images from a DNS of isotropic turbulence to study the performance of different PIV interrogation algorithms. Using the DNS spectra as the reference, they all found that, at high wavenumbers, the velocity spectra retrieved from PIV are obscured by noise before kc_{th} is reached. The actual cut-off wavenumber kc_{exp} depends on the signal-to-Noise ratio (SNR) of the measurement: closer to the wall, flow-related sources of measurement error (velocity gradients, out-of-plane motions...) result in a lower value of kc_{exp}. More specifically, Guichard et al (1998) investigated the influence of the interrogation window size by comparing the rms and the spectra obtained from the PIV data and the DNS data. It was confirmed that using smaller interrogation windows (typically 16px*16px) lowers the actual cut-off wavenumber of the spectrum: the benefit of having a smaller averaging area is cancelled out by an increased level of noise. At the other extreme, if one goes to too large IWs (typically 128px*128px), the velocity fluctuations of the small structures are averaged out in the interrogation process. The correct choice of interrogation window size thus appears to be a trade-off between the size of the averaging area and the signal-to-noise-ratio. The nature of the spectral noise and its influence on

the cut-off wavenumber kc_{exp} of PIV was further investigated by Foucaut et al (2004). The actual cut-off wavenumber kc_{exp} was formally defined as the wavenumber at which a SNR of 1 is reached. At the optimal interrogation window size, Foucaut et al (2004) suggested that one should get $kc_{th} = kc_{exp}$.

In summary, the different regions of a typical PIV spectrum measured in turbulent flow

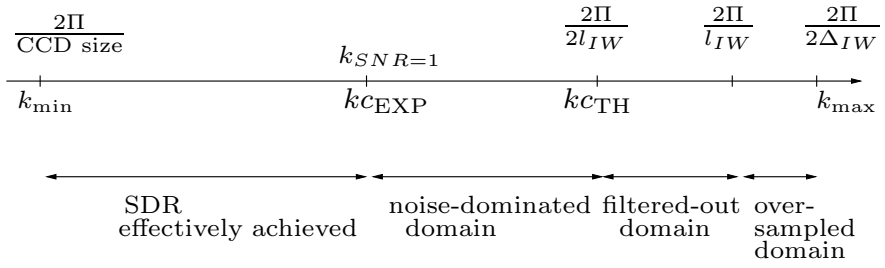

Figure 2.3: Different wavenumber regions of a typical PIV spectrum of turbulent flow

is shown in Figure 2.3. The two mains limitations applying on the *effective* SDR of PIV find their origin in the number of pixels of the camera CCD array, and in the level of noise in the measurements.

In the context of coherent structures investigations, the spatial dynamic range of a PIV experiment should be compared with the range of structures W_{str} to be measured in the flow. As recalled in the previous chapter, in the framework of the hairpin packet paradigm (Adrian et al (2000b)), the small scale structures formed by the hairpins and their cores, and the large scale structure are formed by the streamwise organization of these hairpins into the so-called hairpin packets. The fine eddies of near-wall turbulence were recently revisited using PIV by Stanislas et al (2008) and using DNS by Tanahashi et al (2004). They both find that their diameter are universal (both in wall-normal position and in Reynolds number) when scaled with the local Kolmogorov length scale (η). The detected vortex cores have a most expected diameter of 10η, which corresponds, in wall units, to vortices as small as $d^+ = 20$ close to the wall. As far as the hairpin packets are concerned, these motions have a commonly accepted maximum streamwise extent of 3δ (Guala et al (2006), Adrian (2007)). As a consequence, W_{str} reads:

$$W_{str} = \frac{3\delta^+}{20^+} \tag{2.11}$$

In order to be consitent, the field of view size that appear in the equation for SDR_{th} should be taken along the streamwise direction. In order to get a full resolution of the structures in the flow, one should have $SDR = W_{str}$.

2.3.2 Theoretical SDR of recent PIV studies

The expression for SDR_{th} and W_{str} given in equation 2.10 and 2.11 respectively can be utilized to estimate the theoretical resolution of coherent structures achieved in recent digital PIV studies (Carlier and Stanislas (2005), Ganapathisubramani et al (2006), Hambleton et al (2006), Hutchins et al (2005)), in the context of coherent structures investigations. In Table 2.1, their interrogation window size, as well as the extent of their

field of view, SDR_{th} and W_{str} are reported. On the whole, Table 2.1 shows that the theoretically achieved SDR in digital PIV experiments is never large enough to capture the whole range of structures: the ratio $\frac{SDR_{th}}{W_{str}}$ varies from 0.04 for Hutchins et al (2005) at $\delta^+ = 2800$ up to 0.15 for Ganapathisubramani et al (2006) at $\delta^+ = 1160$. By choosing an appropriate optical magnification, this limited SDR is then used to resolve very specific parts of the range of coherent structures present in the flow. In Ganapathisubramani et al (2006), moderate values of both the field of view extent $(S_1, S_2) = (\delta, \delta)$ and the IW size ($L^+_{IW} = 20$) allow the study of coherent structures of intermediate size. On a different note, Hambleton et al (2006) favor the larger structures ($[S_1, S_2] = [2\delta, 2\delta]$, $L^+_{IW} = 30^+$) and Carlier and Stanislas (2005) the smaller ones ($[S_1, S_2] = [\delta, \delta]$, $L^+_{IW} = 10$). The influence of the Reynolds number on the SDR of PIV experiments is clearly visible in Hutchins et al (2005): when the Reynolds number increases, the same PIV setup obviously leads to the same SDR_{th}, while W_{str} increases. The small structures are increasingly filtered out with $L^+_{IW} : 15^+ \rightarrow 24^+ \rightarrow 69^+$ for $\delta^+ : 690 \rightarrow 1010 \rightarrow 2800$.

Reference	Technique (Plane 1-2)	Re_θ	δ^+ Re_τ	Field of View S_1, S_2	$L^+_{IW,1}, L^+_{IW,2}$	SDR_{th} $\frac{S_i^+}{2*IW^+}$	W_{str} $\frac{3\delta^+}{20^+}$
Carlier and Stanislas (2005)	SPIV(y-z)	7500	2500	500^+, 750^+	11,11	23	188
Hutchins et al (2005)	SPIV(z-d),(z-u)	1430	690	$0.8\delta, 0.8\delta$	15,15	18	104
		2680	1010		24,24	17	152
		7440	2800		69,69	16	420
Hambleton et al (2006)	SPIV(x-y)	2600	1100	$1.2\delta, 1.2\delta$	32,32	21	165
	SPIV(x-z)	2600	1100	$2\delta, 2\delta$	35,35	21	165
Ganapathisubramani et al (2006)	DualPIV(x-z)	2800	1160	$1.1\delta, 1.1\delta$	24,24	27	174
DelAlamo et al (2006)	DNS		185	$12\pi\frac{h}{2}$,$4\pi\frac{h}{2}$	14,7	250	28
			547	$8\pi\frac{h}{2}$,$4\pi\frac{h}{2}$	13,7	530	82
			934	$8\pi\frac{h}{2}$,$3\pi\frac{h}{2}$	11,6	1068	140
			964	$\pi\frac{h}{2}$, $\frac{\pi}{2}\frac{h}{2}$	12,6	126	144
			1901	$\pi\frac{h}{2}$, $\frac{\pi}{2}\frac{h}{2}$	12,6	248	285
Adrian et al (2000b)	Ph-PIV	930	355	$1.5\delta, 1.2\delta$	9,9	30	53
		2370	836	$1.4\delta, 1.3\delta$	20,20	29	125
		6845	2000	$1.4\delta, 1.4\delta$	36,25	39	300

Table 2.1: Literature survey of the Spatial Dynamic Range SDR_{th} of recent PIV studies, compared with the range of scales to be resolved W_{str}

It is of interest to compare these recent digital PIV studies to the photographic PIV (Ph-PIV) study by Adrian et al (2000b) which is widely considered as a milestone in the field of coherent structures investigations. As can be seen in Table 2.1, the SDR_{th} of their experiments compares well with the SDR_{th} of recent digital PIV experiments. At the two Reynolds numbers for which the boundary layer under investigation can be considered as fully turbulent ($Re_\theta = 2370$ and 6845), the ratio SDR_{th}/W_{str} are 0.23 and 0.13 respectively. This is once again on the same order as the most highly resolved digital PIV studies presented in table 2.1. Another interesting comparison to be made is with a recent DNS study (DelAlamo et al (2006)), where, in order to comply with the implementation constraints of the technique, all the structures of the flow must be resolved. In Table 2.1, it can be seen that, for the lower range of Reynolds numbers ($Re_\tau \in [185; 934]$), the ratio $\frac{SDR_{th}}{W_{str}}$ is indeed very large (on the order of 10). In contrast, for the higher range of Reynolds numbers ($Re_\tau \in [964; 1900]$), this ratio is on the order of 1, and the influence of the size of the computational domain on the simulation of the flow may be questioned. As a result of the incapacity of PIV to resolve *simultaneously* the whole spectrum of coherent scales in the flow, a number of controversies persists about the role of coherent structures in the cycle of turbulence. Improving the SDR of PIV is paramount to a better assessment of this role, and to a larger extent to a better comprehension of the physics of near wall turbulence.

2.3.3 Methodology to retrieve the cut-off wavenumber at SNR=1

In this section, the methodology used to retrieve the *effective* cut-off wavenumber kc_{exp} of a PIV experiment is detailed. This cut-off wavenumber is defined as the wavenumber at which the signal-to-noise ratio of the experiment is equal to one.
Following Foucaut et al (2004), the PIV power spectrum $E_{PIV}(k)$ can be expressed as:

$$E_{PIV}(k) = (E_{flow}(k) + E_{noise}(k)) \left(sin_c(k * \frac{L_{IW}}{2}) \right)^2 \tag{2.12}$$

where:

- $E_{flow}(k)$ is the exact spectrum of the flow.
- $E_{noise}(k)$ is the PIV noise (including both recording and processing (at given IW size) sources of noise)
- the squared cardinal sine function $\left(sin_c(k * \frac{L_{IW}}{2})\right)^2$ is the PIV transfer function and represents the filtering over a square interrogation window.

At SNR=1, by definition $E_{flow}(kc_{exp}) = E_{noise}(kc_{exp})$, and one gets:

$$E_{PIV}(kc_{exp}) = (2 * E_{flow}(kc_{exp})) \left(sin_c(kc_{exp} * \frac{L_{IW}}{2}) \right)^2$$

The spectrum of the flow is *a priori* unknown, however, one can make use of a reference spectrum obtained from hot-wire measurement or DNS data in the same kind of turbulent flow. An inner scaling (from Perry et al (1986)) can be applied to the spectra to compensate for Reynolds number differences between the PIV and the reference :

$$\tilde{k} = k * y \quad \tilde{E}(\tilde{k}) = E(\tilde{k})/(u_\tau^2) = E(k)/(u_\tau^2 * y)$$

where u_τ is the friction velocity and y is the wall normal position at which the spectrum is computed. The non-dimensional PIV and reference spectra read:

$$\tilde{k} = k_{PIV} * y_{PIV} \quad \tilde{E}_{PIV}(\tilde{k}) = E_{PIV}(\tilde{k})/(u_{\tau,PIV}^2) = E_{PIV}(k_{PIV})/(u_{\tau,PIV}^2 * y_{PIV})$$

$$\tilde{k} = k_{ref} * y_{ref} \quad \tilde{E}_{ref}(\tilde{k}) = E_{ref}(\tilde{k})/(u_{\tau,ref}^2) = E_{ref}(k_{ref})/(u_{\tau,ref}^2 * y_{ref})$$

Now, assuming that the non-dimensional spectrum of the flow is equal to the non-dimensional reference spectrum, the non-dimensional PIV spectrum at $\tilde{k}c_{exp}$ can be expressed as:

$$\tilde{E}_{PIV}(\tilde{k}c_{exp}) = 2 * \tilde{E}_{ref}(\tilde{k}c_{exp}) \left(sin_c(\tilde{k}c_{exp} * \frac{L_{IW}}{2} \frac{1}{y_{PIV}}) \right)^2 \tag{2.13}$$

The multiplication factor $\left(sin_c(\tilde{k}c_{exp} * \frac{L_{IW}}{2} \frac{1}{y_{PIV}}) \right)^2$ represents the low-pass filtering effect of PIV due to the averaging over the interrogation window. Equations 2.13 indicates that $\tilde{k}c_{exp}$ can be retrieved as the wavenumber at which $\tilde{E}_{PIV}(\tilde{k})$ intersects with $2 * \tilde{E}_{ref}(\tilde{k}) \left(sin_c(\tilde{k}c_{exp} * \frac{L_{IW}}{2} \frac{1}{y_{PIV}}) \right)^2$.
Finally, the cut-off wavenumber $\tilde{k}c_{exp}$ can be related to the radius r^+ of a vortex that will be resolved with a signal to noise ratio of 1 by the PIV experiment at the wall distance y^+:

$$r^+_{SNR=1} = \frac{1}{2} \frac{2\Pi * y^+_{PIV}}{\tilde{k}c_{exp}} \tag{2.14}$$

This process is illustrated using SPIV data acquired in a XY plane of a turbulent boundary layer at $\delta^+ = 820$, and using as a reference the spectrum from a DNS of channel flow at $\delta^+ = 950$ (DelAlamo et al (2004)). The Reynolds number of these two datasets are quite close. More details on the SPIV data are given in the next chapter of this thesis. In both datasets, the longitudinal spectra of the streamwise velocity are computed at $y^+ = 100$. As can be seen in 2.4, they are in excellent agreement in an inner scaling. The methodology employed to retrieve $\tilde{k}c_{exp}$ is shown in figure 2.5. The non-dimensional cut-off wavenumber of the PIV spectrum at SNR=1 is found to be $\tilde{k}c_{exp} = 12.8 \pm 0.5$: a vortex of radius $r^+ = 20$ will be resolved with a signal-to-noise ratio of 1 by the PIV measurements. It has been shown in Herpin et al (2008) that this methodology can also be applied when there exists a substantial difference between the Reynolds number of the PIV dataset and of the reference dataset, thanks to the inner scaling of Perry et al (1986).

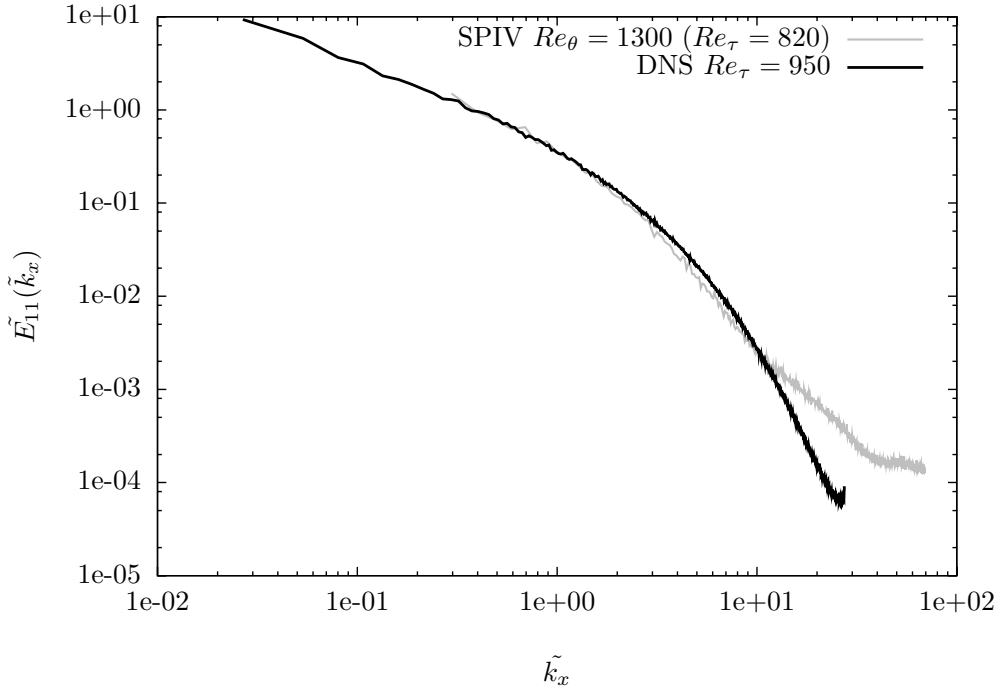

Figure 2.4: Spectra of the SPIV dataset and DNS dataset at $y^+ = 100$ in inner scaling

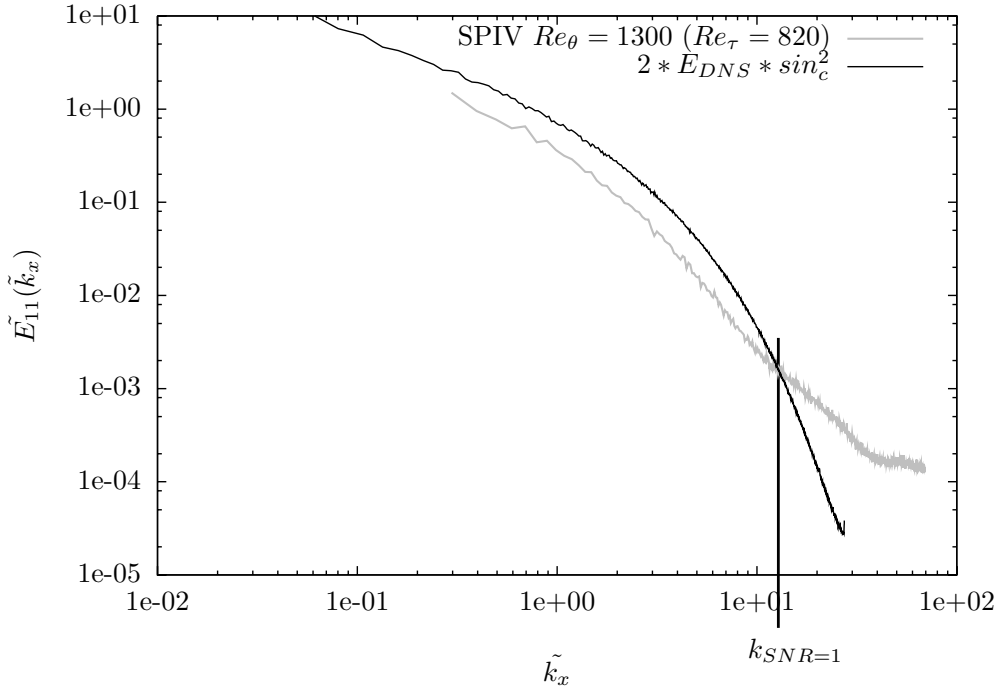

Figure 2.5: Methodology employed to retrieve $kc_{SNR=1}$

Chapter 3

Experiments in the LTRAC water-tunnel

The stereoscopic PIV technique, described in chapter 2, is employed to measure the flow in a streamwise/wall-normal section of turbulent boundary layers at $Re_\theta = 1300$ and $Re_\theta = 2200$ developing in the LTRAC water-tunnel. After a brief presentation of this facility, the PIV setup is extensively described, and the evaluation parameters for the particle images are given. Then, the measurement uncertainty is thoroughfully assessed, and a summary of the database is finally given.

In the following, the 'x' coordinate is along the streamwise direction, the 'y' coordinate is along the wall-normal direction, and the 'z' coordinate is along the spanwise direction. The origin of the reference frame is on the lower-wall of the tunnel.

3.1 Flow under investigation

The turbulent boundary layer measurements are carried out in the LTRAC horizontal water-tunnel. An extensive characterization of the facility can be found in Kostas (2002). The water-tunnel is sketched in figure 3.1. The flow is produced by a three-phase 55KW Western Electric motor coupled to a Goulds pump system(**8**), and conditioned in the settling chamber(**1**) by a perforated settling plate, a honeycomb, screens and a 10:1 smooth contraction(**2**). The horizontal test section(**3**) of the tunnel is made up of 5 elementary working sections, each 1.1m long with a 500mm*500mm cross section. The working sections are fabricated from 25mm thick transparent acrylic (Perspex) sheets allowing full optical access to the flow. The flow rate in the working sections can be set in increments of 1mm/s up to a maximum free-stream velocity of $0.775 m/s$. The flat-plate turbulent boundary layer under interest develops on the floor of the test section. A tripping device was designed to promote transition to turbulence. It is made up of a 3mm diameter stainless steel wire followed by a 40mm streamwise-length of water-resistant sandpaper, both of which span the tunnel width and are attached to a thin stainless steel magnetic plate. During the measurements, the tripping device is positioned on the floor of the tunnel at the inlet of the test section. A collection of rare earth magnets on the outer walls of the

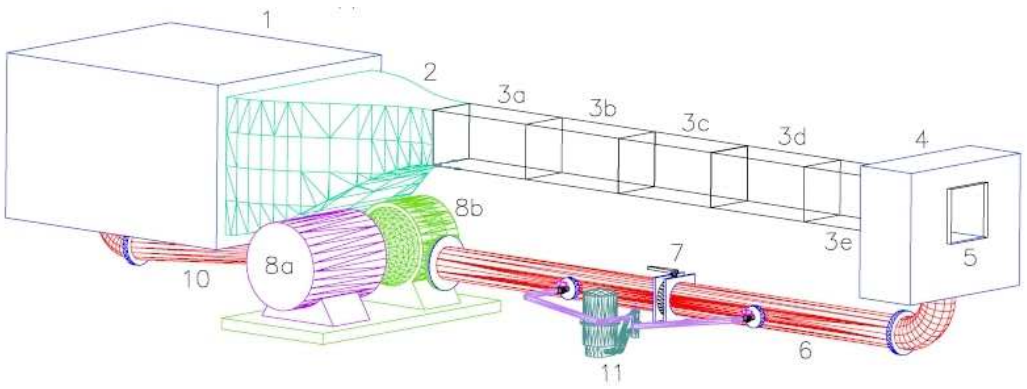

Figure 3.1: The LTRAC water-tunnel. The measurements were taken in section 3d. **1** settling chamber, **2** 10:1 contraction, **3** working sections, **4** plenum chamber, **5** rear observation window, **6** return pipework-suction side, **7** filtration isolating valve, **8** AC motor-centrifugal pump system, **9** orifice plate, **10** return pipework-pressure side, **11** water filtration circuit

tunnel is used to hold the tripping device firmly against the tunnel floor.

The characteristics of the two boundary layers under interest are reported in table 3.1. Both of them were measured 3.7m downstream of the tripping device (section 3d) with a frequency of the motor-pump set at $f = 28Hz$ ($U_\infty \approx 0.425m/s$), but with different levels of free-stream turbulence intensity: $Tu = 5.4\%U_\infty$ and $Tu = 2.6\%U_\infty$. These different levels of Tu are linked to different states of cleanliness of the screens and honeycombs in the settling chamber: over time, seeding particles accumulate on their surface, resulting in an increased turbulence intensity. The lower turbulence intensity ($Tu = 2.6\%U_\infty$) was obtained after a cleaning of the screens and honeycombs was undertaken. The sensitivity of the laminar/turbulent transition behind the tripping device to Tu is responsible for the differences in boundary layer thickness ($\delta = 0.064m$ and $\delta = 0.035m$) and in Reynolds numbers ($Re_\theta = 2200$ and $Re_\theta = 1300$). In both cases, the Reynolds numbers are high enough to guarantee that the boundary layer is free from low-Reynolds number effects, while remaining in the range typically achieved by recent DNS simulations (DelAlamo et al (2006)).

Re_θ	U_∞ (m/s)	Tu ($\%U_\infty$)	θ (m)	δ^+	u_τ (m/s)	δ (m)	1^+ (ν/U_τ) (um)
2200	0.422	5.4%	$4.66e-3$	1390	0.0186	0.064	46
1300	0.429	2.6%	$2.57e-3$	820	0.0198	0.035	43

Table 3.1: Properties of the boundary layer under investigation in the LTRAC water-tunnel

3.2 Setup

The two boundary layers were measured using the same stereo-PIV setup. The experimental procedure has been extensively described in Herpin et al (2008). The setup consists of two separate stereo systems placed next to each other in the streamwise direction: two adjacent XY planes of the flow are measured simultaneously. The field-of-views of the two stereo-systems overlap to ensure continuity of the data. The arrangement is shown in Figure 3.2. The use of multiple stereo-systems was already employed by Kostas et al (2005) to investigate a turbulent boundary layer flow subject to adverse pressure gradient. In our case, the main interest is to increase the spatial dynamic range in the streamwise direction in order to capture the large scale structures elongated in that direction while maintaining good resolution of the small scales. The different parameters of the PIV

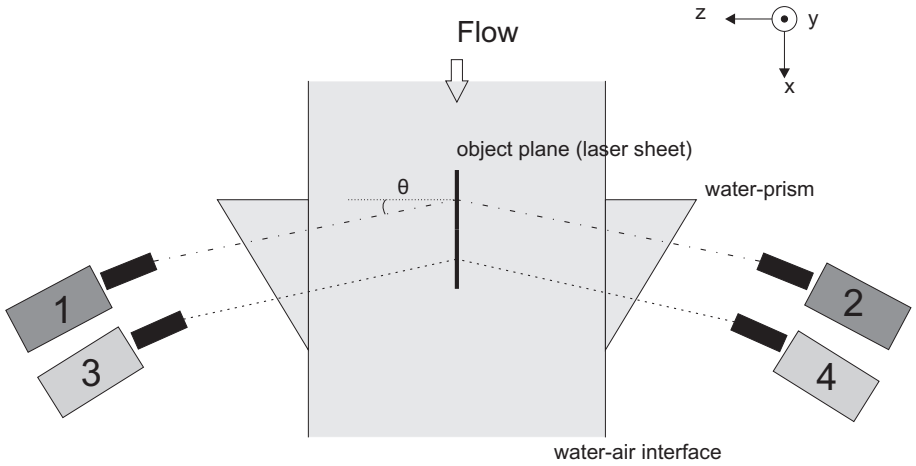

Figure 3.2: Top-view of the Stereo-PIV setup. Note that the coordinate system is indicative only and does not represent the axes-origin.

setup are compiled in Table 3.2, and an extensive description follows. The 4 cameras used are PCO 4000, which feature a large CCD array ($4008px * 2672px$) with a pixel size of $9\mu m * 9\mu m$. They are oriented such that the larger side of the CCD ($4008px$) is imaging the streamwise extent of the field of view. Within each stereo system, the two cameras are arranged in an angular configuration (Prasad (2000)). Although an off-axis angle of $\theta = 45°$ is recommended to get as much accuracy on the out-of-plane component as on the in-plane components, the stereo angle was set to a nominal angle of $\theta = 30°$ in the present experiment. This is intended to limit the optical distortions likely to occur on the optical path of the cameras because of the non-orthogonal viewing through the air-water interface. To further reduce this type of optical distortions, water-filled prisms of the same nominal angle were placed on either side on the water-tunnel flush with the walls, in the same fashion as in Parker et al (2005).
A calibration target with reference marks was placed inside the region of interest to adjust the field of view of each camera. The dimensions of the target were large enough to calibrate simultaneously the field of view of the two stereo-systems. The cameras were fitted with 200mm focal length lenses and an average magnification of $M = 0.45$ was used, resulting in each camera having a field of view with a nominal size of $[S_x; S_y] = [86.5mm, 46.5mm]$. This magnification was chosen to center the available spatial dynamic range of the experiment on the range of structures to be resolved in the flow. It corre-

sponds to a spatial resolution of $20.5\mu m/px$. Note that these values of magnification and spatial resolution represent an average between the four cameras and between the two directions of the field of view. Because of the stereoscopic viewing angle, there is a ratio of $\frac{1}{\cos(\theta)} = 1.15$ between the magnification along the streamwise direction and along the wall-normal direction. Specially designed camera adapters allow for fine tuning of camera positioning: the common viewing area between the two cameras of one stereo system was maximized, and the overlap between the two stereo systems was carefully adjusted. As a result, the total field of view of the full stereoscopic arrangement has a size of $[S_x; S_y] = [165mm, 46.5mm]$. A high degree of sharpness was achieved on each CCD's through the use of a limited aperture of the lens ($f_\# = 16$) and through an accurate enforcement of the Scheimpflug condition on the camera adapters (Soloff et al (1997), Prasad and Jensen (1995)).
A two-cavity $200mJ$ Nd:YAG laser system was used at a wavelength of $\lambda = 532nm$ to illuminate the field of view. The laser beam was shaped below the test section into a 0.8mm-thick (lz) laser sheet by a combination of spherical and cylindrical external optics, before being redirected with a front-coated high-energy mirror into a XY plane aligned with the calibration target. The verticality of the laser sheet inside the tunnel was realized by adjusting the angle of the redirection mirror until good coincidence between the incoming laser sheet and its weak reflection on the floor of the test-section was observed. With the laser sheet originating from below the test-section, the 2 stereo systems had their 2 cameras symmetrically placed on either side of the laser sheet. This stereoscopic arrangement was first proposed by Willert (1997). It is attractive because the field of views of both stereo cameras are then identically stretched, allowing for a more accurate reconstruction of the out-of-plane component. The depth of field of the cameras is on the order of 6.8mm, which is much larger than the laser sheet thickness.
The stereoscopic measurement volume was calibrated using the Soloff method (Soloff et al (1997)). The calibration target, initially aligned with the laser sheet, was translated in the out-of-plane direction from z=-2.5mm up to z=2.5mm with steps of $500\mu m$ using a micrometer with $5\mu m$ precision. At each position, the image of the calibration target on the camera CCDs was then recorded.
The flow was seeded with hollow glass spheres with a mean diameter of $d_p = 11\mu m$ and a density of $\rho_p = 1100kg/m^3$. At the selected aperture of the lenses, the diffraction limited particle image diameter is on the order of $d_p = 3.4px$. This value is close to the optimum particle image diameter of $2px$ proposed by Raffel et al (1998) to reduce peak-locking bias error. The number of particle images N_p per IW of $32px * 32px$ was evaluated by a visual inspection of the PIV images and is on the order of 10.
The two cavities of the laser were pulsed with a separation time $\Delta t = 550\mu s$ at a frequency $f_{acq} = 1Hz$. For these conditions, the maximum displacement of the particles between the two exposures of the cameras is of the order of $U_\infty * \Delta t = 12px$. Between two successive velocity field acquisitions, the flow in the free stream has moved a distance equal to $\frac{1}{f_{acq}} \frac{U_\infty}{S_x} = 2.57$ times the extent of the total field of view, corresponding to 6.5δ. This is about 2 times the streamwise extent of the hairpin packet. The number of SPIV records acquired is $N_s = 1815$ for the boundary layer at $Re_\theta = 2200$ and $N_s = 605$ for the boundary layer at $Re_\theta = 1300$.

stereo angle (θ)	$30°$
laser sheet thickness (l_z)	$\approx 0.8mm$
magnification (M)	0.45
resolution (px_{obj})	$20.5\mu m/px$
lens aperture ($f_{\#}$)	16
d_{diff}	$3.4px$
depth of field (δ_z)	$6.8mm$
field of view	$[S_x; S_y] = [165mm; 46.5mm]$
overlap region	$S_{x,overlap} = 7.75mm$
separation time (Δt)	$550\mu s$

Table 3.2: PIV recording parameters in the LTRAC water-tunnel

3.3 Evaluation of the SPIV images

3.3.1 Description of the evaluation software

The different stereoscopic evaluation methods have been reviewed in section 2.2.3 of the present thesis. The in-house code 'pivlml' developped by the LML makes use of a '3D warping' technique with a Soloff back-projection/reconstruction (Soloff et al (1997)). The PIV evaluation is first performed in the image space of each camera, using an FFT based cross-correlation algorithm that is multipass and multigrid (Westerweel et al (1997), Soria (1996), Soria et al (1999)). This cross-correlation is performed on a mesh defined as the forward projection of a common cartesian grid in the object space (Coudert and Schon (2001)). The position of the correlation peak is detected using two one-dimensional Gaussian peak-fitting. The backprojection of the two 2D-2C velocity fields in the object space and the three component reconstruction are realized in a single step using the Soloff method (Soloff et al (1997)). The model used to map the object volume to the image plane is a polynom with cubic dependence in the two in-planes direction and quadratic dependence in the out-of-plane direction (cf eq. 2.3). The coefficients of the polynoms are calibrated using images of a planar calibration target translated in the out-of-plane direction. Finally a misalignement correction is performed, as implemented in Coudert and Schon (2001).

3.3.2 Parameters of the evaluation

The two sets of SPIV images (at $Re_\theta = 2200$ and $Re_\theta = 1300$) were evaluated using the same parameters. These parameters are compiled in Table 3.3. The SPIV images were cross-correlated in three steps in the image plane of each camera, starting with an interrogation window of 64px*64px, and then doing two successive analysis with an interrogation window size of 32px*32px (an overlap of 70% was used between adjacent IWs). The Soloff coefficients were computed from images of the calibration target at three out-of-plane positions (z=-1mm, z=0, z=+1mm), with correction for the laser-sheet/calibration target misalignment. This misalignment is on the order $175\mu m$ at most,

which is smaller than the laser sheet thickness $lz = 800\mu m$, and represents 1/3 of the IW. The Soloff back-projection/reconstruction method is then used to retrieve the 2D-3C velocity field of each stereo system in the object space. The grid in the object space is Cartesian with a mesh step of $200\mu m$ and with the first mesh point at $550\mu m$ away from the wall. The number of points of 2D-3C velocity fields of each stereo-system is reported in Table 3.3. Note that for the measurements at $Re_\theta = 1300$, the quality of the velocity field at the downstream end of the field of view was not satisfactory due to a lack of light intensity, and hence the last 125 points in the streamwise direction were suppressed from the final velocity field.

calibration planes	$-1mm, 0mm, +1mm$
misalignment	$\leq 175\mu m$
number of analysis	3
initial IW (px)	$(64 * 64)$
final IW	$(32 * 32)$
Mesh step	$(200\mu m * 200\mu m)$
Number of points	
upstream syst.	$[N_x, N_y] = [426; 234]$
downstream syst.	$[N_x, N_y] = [439; 234]^*$
total syst.	$[N_x, N_y] = [826; 234]^*$
overlap region (pt)	39
bias of merge (pivlml)	
u	$0.03\%U_\infty$
v	$0.04\%U_\infty$
w	$-0.2\%U_\infty$
rms of merge (pivlml)	
u	$0.9\%U_\infty$
v	$0.6\%U_\infty$
w	$1.65\%U_\infty$

Table 3.3: Parameters of the evaluation of the SPIV images acquired in the LTRAC water-tunnel. * For the measurements at $Re_\theta = 1300$ the number of points of the downstream stereo-system is $[314; 234]$ and the total number of points is $[701; 234]$

The overlap region between the 2D-3C velocity fields obtained from the two stereo systems is 39 mesh points long in x. In this common area, the merging between the two systems is simply realized by taking the average of the two 2D-3C velocity fields. This merging procedure is illustrated in Figure 3.3. A portion of the overlap region of an instantaneous velocity field from the dataset $Re_\theta = 2200$ is represented before the merging in Figure 3.3a (from the two separate 2D-3C velocity fields) and after the merging in Figure 3.3b. Only one in every two vectors is shown. In order to better assess the quality of the merging procedure, only the fluctuating part of the flowfield is shown - a constant convection velocity has been subtracted from the instantaneous velocity field. The selected example is a challenging one, as a vortex is centered at $y^+ = 80$ and extends down to the wall ($y^+ = 15$), crossing the overlap region. Some slight differences between the two 2D-3C velocity fields are visible before the merging. The merged velocity field, visible in figure 3.3b is of good quality, and presents an excellent resolution of a vortex present in the flow field. The merged velocity fields have a final size of $[N_x; N_y] = [826; 234]$ for the measurements at $Re_\theta = 2200$ and $[N_x; N_y] = [701; 234]$ for the measurements at

$Re_\theta = 1300$.

The quality of the merging procedure can be assessed by analyzing some statistical

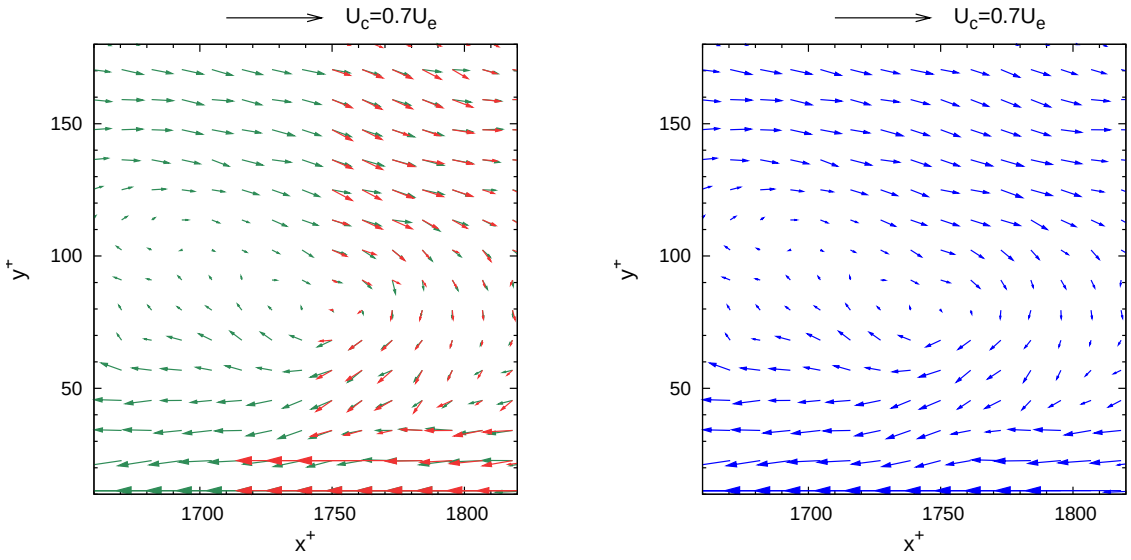

(a) BEFORE the merging

(b) AFTER the merging

Figure 3.3: Fluctuating in-plane velocity field in a portion of the overlap region in the LTRAC dataset at $Re_\theta = 2200$, in wall units. 1 vector shown out of 2

results on the difference between the two 2D-3C velocity fields in the overlap region for each velocity component:

- the bias between the 2D-3C velocity fields for each velocity component :

$$< u_{i,sys1} - u_{i,sys2} >= U_{i,sys1} - U_{i,sys2} \tag{3.1}$$

- the rms of the random part of the difference between the 2D-3C velocity fields for each velocity component :

$$((u_{i,sys1} - u_{i,sys2}) - (U_{i,sys1} - U_{i,sys2}))_{RMS} \tag{3.2}$$

These statistics were found to be comparable for the datasets at $Re_\theta = 2200$ and $Re_\theta = 1300$, as expected since the same PIV setup was used. The values valid for both datasets are presented in table 3.3. The bias between the two stereoscopic systems is always negligible with respect to the RMS between the velocity fields. Among the three velocity components, the RMS is the highest for w with an amplitude of $1.65\%U_\infty$, and the lowest for v with an amplitude of $0.6\%U_\infty$. This ordering is coherent with the measurement configuration, as the out-of-plane velocity component is more sensitive to the SPIV reconstruction than the in-plane non-stretched velocity component.

The cross-correlation of PIV images *taken at the same instant*, used to compute the misalignment, can be further utilized to retrieve the effective laser sheet thickness (defined

as the portion of the laser sheet thickness contributing to the PIV correlation). Following Herpin et al (2008), the *width* of the correlation peak K_{corr} is related to lz_{eff} via:

$$lz_{eff} = \frac{K_{corr}}{2 * tan(\theta)} \tag{3.3}$$

The effective laser sheet thickness is found to be $33px$ on average (or $650\mu m$ in physical units) which is similar to the size of the final interrogation window. Hence we can safely conclude that the interrogation volume approximates a cube, and that $SV_{min,th} = 2 * max(L_{IW}, lz) \approx 2 * L_{IW}$.

3.4 Estimation of the measurement uncertainty

There exist multiple ways of assessing the PIV random error, as reviewed in section 2.1.3. In the following, two techniques are employed to retrieve the error of the LTRAC SPIV experiments: a method using an existing study of numerically simulated PIV recordings, and a method based on the real images acquired in the overlap region of the two stereo-systems.

3.4.1 Using synthetic images

In this section, the parameteric study by Foucaut et al (2003) is used as described in section 2.1.3 to evaluate the uncertainty of the SPIV experiments conducted in the LTRAC water-tunnel. This study made use of the Europiv Synthetic Image Generator described in Lecordier and Trinite (2003) to generate PIV recording of known content, which were then evaluated with an FFT based cross-correlation algorithm, similar to that employed in the LML evaluation software. The evolution of the PIV error with a range of different PIV recording parameters (diameter, concentration, out-of-plane motions, velocity gradient) was established. Using this parametric study, the random error associated to each parameter of the LTRAC experiment can then be retrieved (this is the error on the in-plane projection of the displacement), the greatest of these RMS error being the global uncertainty of the experiment. Foucaut et al (2003) and Soria (1996) showed that for optimal recording parameters (Raffel et al (1998) : $d_{p,opt} = 2 - 3px$, $N_{p,opt} = 10$, and ideally no velocity gradient and no out-of-plane motion), the PIV interrogation uncertainty is $0.06px$. According to table 3.2, the only recording parameters that can be considered as non-optimum in the SPIV experiment are the presence of velocity gradient (the wall-normal gradient of streamwise velocity $\frac{dU}{dy}$), and of out-of-plane motions. The global PIV uncertainty can then be taken as:

$$\sigma(\epsilon_{int}) = max\left(\sigma_{dU/dy}, \sigma_{out-of-plane}, \sigma_{dp}, 0.06px\right) \tag{3.4}$$

Following classical turbulent boundary layer results, the out-of-plane motion $(dw)_{\Delta t}$ is considered to have a zero mean value, a maximum standard deviation of $w_{\mathrm{RMS}} = u_\tau$ and a Gaussian distribution of total width $K = 3w_{\mathrm{RMS}} = 3u_\tau$. The corresponding out-of-plane displacement thus reads:

$$(dw)_{IW,\Delta t} = 3 * u_\tau * \Delta t$$

Scaled with the laser sheet thickness lz, it reads $(dw)_{\Delta t} = 0.04lz$. According to the parametric study by Foucaut et al (2003), this level of out-of-plane motions does not generate any additional uncertainty, and is therefore negligible.
The maximum difference in particle displacement over the IW during Δt induced by the mean velocity gradient is noted $(dU)_{IW,\Delta t}$. It varies with the wall distance, and was evaluated close to the first measured wall-normal position ($y^+ = 16$), at the interface of the buffer region and of the logarithmic region ($y^+ = 40$), and at the heart of the logarithmic region ($y^+ = 100$), using the following set of formulae :

$$(dU)_{IW,\Delta t} = \Delta t * \frac{u_\tau}{px_{\text{obj}}} \int_{y^+ - \frac{l^+_{IW}}{2}}^{y^+ + \frac{l^+_{IW}}{2}} \frac{dU^+}{dy^+} dy^+$$

$$\frac{dU^+}{dy^+} = \frac{2}{1 + \sqrt{1 + 4(Ky^+(1 - exp(-y^+/A^+))^2}} \quad \text{(Van Driest)} \quad \text{for} \quad y^+ = 16, y^+ = 40$$

$$\frac{dU^+}{dy^+} = \frac{1}{Ky^+} \quad \text{(Log law)} \quad \text{for} \quad y^+ = 100$$

This displacement difference is scaled with the particle image diameter, following Keane and Adrian (1990). The results are compiled in table 3.4. At $y^+ = 16$, the mean velocity gradient generates a random error on the order of $\sigma(\epsilon_{int}) = 0.3px$, according to the results of Foucaut et al (2003). At the end of the buffer region ($y^+ = 40$), the velocity gradient has significantly decreased, and the impact on the measurement uncertainty is negligible. As shown in Westerweel (1997), the velocity gradient is also one of the main sources of measurement bias. It is thus of interest to check its influence in the present measurements. According to the results of Soria (2006) rescaled in terms of particle image diameter, the velocity bias becomes negligible for a velocity gradient of $(dU)_{IW,\Delta t} < 0.8d_p$, which is reached within the buffer region.

Finally, one can say that the random error on the image displacement $\sigma(\epsilon_{int})$ in the boundary layer above $y^+ = 40$ is on the order of $0.06px$. Below $y^+ = 40$, the velocity gradient across the interrogation window becomes the dominant source of error, and the related uncertainty at $y^+ = 16$ is on the order of $\sigma(\epsilon_{int}) = 0.3px$.

Using the stereoscopic error analysis proposed by Willert (1997) and Prasad (2000), this noise on the PIV evaluation $\sigma(\epsilon_{int})$ can now be related to the random error on the three velocity components reconstructed in the object plane, using equation 2.7 in section 2.2.5. As the uncertainty $\sigma(\epsilon_{int})$ is presently expressed in terms of displacement in pixels, it needs to be multiplied by the physical size of the pixel on CCD camera array and divided by the time separation Δt to get the uncertainty on the velocity in physical units in the object space (assuming that there is no uncertainty on Δt). Finally the random error on the three velocity components can be simplified using the physical size of the camera pixels in the object space px_{obj}:

$$\sigma(\epsilon_u) = \sigma(\epsilon_v) = \frac{px_{\text{obj}}}{\Delta t} \frac{1}{\sqrt{2}} \sigma(\epsilon_{int}) \qquad \sigma(\epsilon_w) = \frac{1}{tan(\theta)} \sigma(\epsilon_u) \tag{3.5}$$

The measurement uncertainties above $y^+ = 40$ for a confidence interval of 68% are therefore equal to:

$$\pm\sigma(\epsilon_u) = \pm\sigma(\epsilon_v) = 0.0015m.s^{-1} = 0.35\%U_\infty$$

$$\pm\sigma(\epsilon_w) = 0.0027m.s^{-1} = 0.64\%U_\infty$$

$y^+ = 16$	
$(dU)_{IW,\Delta t}$	$4.2px$
$(dU)_{IW,\Delta t}$	$1.2d_{diff}$
$\sigma_{dU/dy}$	$0.3px$
$y^+ = 40$	
$(dU)_{IW,\Delta t}$	$1.0px$
$(dU)_{IW,\Delta t}$	$0.3d_{diff}$
$\sigma_{dU/dy}$	$0.08px$
$y^+ = 100$	
$(dU)_{IW,\Delta t}$	$0.15px$
$(dU)_{IW,\Delta t}$	$0.044d_{diff}$
$\sigma_{dU/dy}$	$0.06px$

Table 3.4: Error induced by the velocity gradient in the LTRAC database

The maximum uncertainties, obtained at $y^+ = 16$, are $\pm\sigma(\epsilon_{u,max}) = \pm\sigma(\epsilon_{v,max}) = 1.8\%$ and $\pm\sigma(\epsilon_{w,max}) = 3.1\%$ when normalized with the free-stream velocity, or $\pm\sigma(\epsilon_{u,max}) = \pm\sigma(\epsilon_{v,max}) = 3.7\%$ and $\pm\sigma(\epsilon_{w,max}) = 6.5\%$ when normalized with the local mean velocity.

This analysis does not take into account the errors linked to the 3D Soloff calibration, which are difficult to estimate and are expected to be negligible with respect to $\sigma(\epsilon_{int})$ (van Doorne et al (2003)). It should now be emphasized that, as any error analysis based on synthetic particle images, it does not take into account all the sources of measurement noise of the experiment: for instance the influence of the turbulent fluctuations, of the CCD transfer function, and of the optics transfer functions are not taken into account. As a consequence, the uncertainties $\sigma(\epsilon_u)$, $\sigma(\epsilon_v)$, $\sigma(\epsilon_w)$ computed in this section should be understood as a *lower bound of the uncertainty.*

3.4.2 Using real images

Another way to compute the measurement uncertainty is to consider the simultaneous measurement of the flow in the overlap region by the two stereo systems as two independent realizations. The rms of the difference between the two 2D-3C velocity fields in the overlap region can the be interpreted as the measurement random error $\sigma(\epsilon_{u_i})$ (Kostas et al (2005)). The SPIV uncertainties with a confidence interval of 68% for the two datasets thus read:

$$\sigma(\epsilon_u) = (u_{sys1} - u_{sys2})_{rms} = 0.9\%U_\infty$$

$$\sigma(\epsilon_v) = (v_{sys1} - v_{sys2})_{rms} = 0.6\%U_\infty$$

$$\sigma(\epsilon_w) = (w_{sys1} - w_{sys2})_{rms} = 1.65\% U_\infty$$

Note that this estimation of the measurement uncertainty is global over the overlap region; in particular it is averaged over the wall-normal direction, and no distinction is made between the region below $y^+ = 40$ (where the noise increase when going down to the wall, cf section 3.4.1) and the region above $y^+ = 40$ (where the noise is independent of y^+, cf section 3.4.1). However, given the ratio between the number of mesh points in these two regions ($\frac{N_{y^+<40}}{N_{y^+>40}} = \frac{7}{227}$), the contribution of the region $y^+ < 40$ is negligible with respect to the contribution of the region $y^+ > 40$. Among the two in-plane velocity components, u shows a slightly higher uncertainty than v, probably linked to the image stretching occurring along the x direction, as explained in Willert (1997). The ratio of the out-of-plane uncertainty over the in-plane uncertainty is in good agreement with the prediction by Willert (1997) and Prasad (2000) given our stereoscopic angle:

$$\frac{\sigma(\epsilon_w)}{\sigma(\epsilon_u)} = 1.9 \approx \frac{1}{tan(30^\circ)}$$

These uncertainties computed from the real PIV images are about two times higher than the a-priori uncertainties computed in section 3.4.1 from synthetic PIV images for $y^+ > 40$. This difference are attributed to the fact that, unlike the study based on synthetic particle images, the uncertainties computed on the real PIV images take into account all the sources of noise of the experiment (and in particular the turbulent fluctuations occurring inside the IW). They can be regarded as the *actual uncertainty* of the SPIV experiment.

3.5 Summary of the database

The characteristics of the entire database acquired in the LTRAC water-tunnel are finally summarized in table 3.5. Using these informations, the spatial dynamic range of the LTRAC experiment and the range of scales to be resolved in the flow were computed and compiled in table 3.6 (cf section 2.3 and equations 2.10 and 2.11). It can be compared to the spatial dynamic range achieved in previous PIV studies (cf table 2.1 in section 2.3). The value of SDR_{th} and of $\frac{SDR_{th}}{W_{str}}$ achieved at $Re_\theta = 2200$ is four times higher than the largest one previously achieved with digital PIV so far (Ganapathisubramani et al (2006)). As for the experiment at $Re_\theta = 1300$, it is remarkable that the spatial dynamic range is equal to the range of structures present in the flow. In conclusion, the LTRAC datasets are suitable for the study of both the small scales and the large scales of the flow.

Plane (1-2)	Re_θ	δ^+ Re_τ	Field of View S_1, S_2	L_{IW}	Mesh step Δ_i	1st mesh point $\frac{L^+_{IW,ini}}{2} \leq y^+$	n° records
XY	2200	1390	2.6δ, 0.75δ	14.2^+	4.3^+	$12 \leq y^+$	1815
XY	1300	820	4δ, 1.4δ	15.2^+	4.7^+	$13 \leq y^+$	605

Table 3.5: Characteristics of the LTRAC database

Plane	Re_θ	SDR_{th}	W_{str}
XY	2200	115	205
XY	1300	120	123

Table 3.6: Spatial dynamic range (SDR_{th}) and range of scales to resolved (W_{str}) of the LTRAC database

Chapter 4

Experiments in the LML wind-tunnel

The stereoscopic PIV technique is now employed to measure the flow in a streamwise/wall-normal and in a spanwise/wall-normal section of turbulent boundary layers developing in the LML wind-tunnel. The Reynolds number of the boundary layers is comprised between $Re_\theta = 7630$ and $Re_\theta = 18950$. After a brief presentation of this facility, the PIV setup is extensively described, and the evaluation parameters for the particle images are given. Then, the measurement uncertainty is thoroughfully assessed, and a summary of the database is finally given.

4.1 Flow under investigation

The LML wind-tunnel has been extensively described and characterized in Carlier and Stanislas (2005) as well as in Carlier (2001). A sketch of the facility is shown in figure 4.1. The working section of the wind tunnel is $1m$ high, $2m$ wide and $21.6m$ long. The flow is produced by a fan and motor that allow the variation of the mean velocity of the external flow continuously from $3m/s$ up to $10m/s$ with a stability better than 0.5%. The turbulence level in the free-stream is about 0.3% of the external velocity U_∞, and the temperature is kept within $\pm 0.2K$ by using an air-water heat exchanger in the plenum chamber. The last five meters of the working sections are made up of glass to give full optical access to the flow.

The turbulent boundary layer under study develops on the lower wall of the working section after being tripped at the entrance by a grid fixed on the floor. Due to the long length of the working section ($21.6m$ at most), this facility is suitable for high spatial resolution measurements at high Reynolds numbers: the Reynolds number based on the momentum thickness Re_θ can reach values up to 20600, with a boundary layer thickness of about 0.3m.

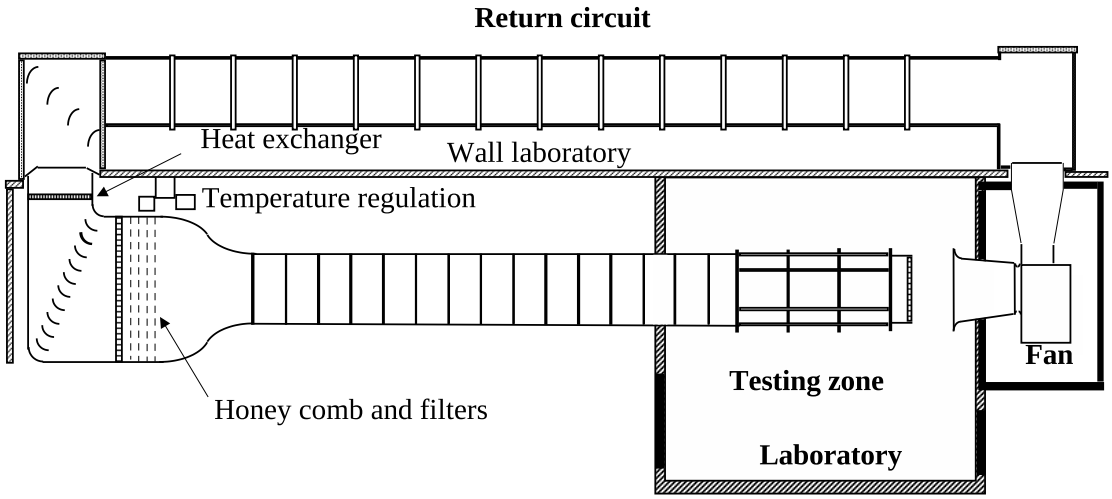

Figure 4.1: The LML wind-tunnel

The boundary layer has been previously characterized with hot-wire anemometry at two measurement stations: $x = 18m$ and $x = 19.6m$ downstream of the tripping device. The measurements at $x = 18m$ were realized using single-wire probes only, and those at $x = 19.6m$ using both single-wire and X-wires probes. The characteristics of the boundary layer at these two measurement stations are reported in tables 4.1 and 4.2.

In this study, particle image velocimetry measurements are carried out $18m$ downstream of the tripping device, at four different flow regimes ($U_\infty = 3m/s$, $5m/s$, $7m/s$, and $10m/s$) and in two measurement planes (a streamwise/wall-normal plane and a wall-normal/spanwise plane). In this chapter, an extensive description of the PIV setup is first given. The evaluation of the SPIV images is then described, and the measurement uncertainty is finally assessed.

Re_θ	U_∞ (m/s)	θ (m)	δ^+	u_τ (m/s)	δ (m)	1^+ (ν/U_τ) (um)	P,x (Pa/m)
7630	3	0.0362	2590	0.112	0.332	128	-0.090
10140	5	0.0291	3620	0.185	0.279	77	-0.200
13420	7	0.0276	5020	0.255	0.281	56	-0.350
18950	10	0.0280	6860	0.350	0.288	42	-0.540

Table 4.1: Properties of the boundary layer in the LML wind-tunnel at x=18m obtained from single wire HWA

Re_θ	U_∞ (m/s)	θ (m)	δ^+	u_τ (m/s)	δ (m)	1^+ (ν/U_τ) (um)	P,x (Pa/m)
8170	3	0.041	2570	0.110	0.350	136	-0.090
11450	5	0.034	3890	0.183	0.319	82	-0.200
14500	7	0.031	4970	0.252	0.298	60	-0.350
20920	10	0.031	7070	0.347	0.304	43	-0.540

Table 4.2: Properties of the boundary layer in the LML wind-tunnel at x=19.6m obtained from single wire HWA

4.2 Setup

The turbulent boundary layers described in table 4.1 are investigated using stereoscopic particle image velocimetry. The flow in a streamwise/wall-normal (XY) plane and a plane orthogonal to the mean flow (YZ) is successively characterized. In total, four PIV setups are used to measure eight different sets of data:

- setup A (with a 200mm focal length): $Re_\theta = 10140$, $Re_\theta = 13420$ and $Re_\theta = 18950$ in the XY plane,
- setup B (with a 105mm focal length): $Re_\theta = 7630$ and $Re_\theta = 10140$ in the XY plane,
- setup C (with a 105mm focal length): $Re_\theta = 7630$ and $Re_\theta = 10140$ in the YZ plane and
- setup D (with a 200mm focal length): $Re_\theta = 10140$, $Re_\theta = 13420$ and $Re_\theta = 18950$ in the YZ plane.

In order to maintain an equivalent resolution of the small scales, some adjustments on the camera magnification were realized throughout the range of Reynolds numbers investigated ($7630 \leq Re_\theta \leq 18950$): while the overall distance between the cameras and the measurement plane was kept constant for the four PIV setups (to minimize the realignments), the focal length of the camera lenses was changed over the range of Reynolds number measured. Note that the Reynolds number at which the change of focal length occurs ($Re_\theta = 10141$) was measured using both focal lengths. The PIV parameters employed for each setup are compiled in table 4.3, and an extensive description follows. The transition from the XY viewing configuration (setup A and B) to the YZ viewing configuration (setup C and D) was achieved by rotating the SPIV bench by 90 degrees around the y axis.

PIV setup	setup A	setup B	setup C	setup D
config.(plane-R_θ)	XY-10140, XY-13420, XY-18950	XY-7630, XY-10140	YZ-7630, YZ-10140	YZ-10140, YZ-13420, YZ-18950
stereo angle (θ)	45°	45°	45°	45°
laser sheet thickness ($l_{z/x}$)	$\approx 1mm$	$\approx 1mm$	$\approx 1mm$	$\approx 1mm$
magnification (M)	0.24	0.1	0.1	0.24
resolution (px_{obj})	$27\mu m/px$	$67\mu m/px$	$67\mu m/px$	$27\mu m/px$
lens aperture ($f_\#$)	8	5.6	8	8
d_{diff}	$1.8px$	$1.2px$	$1.8px$	$1.8px$
depth of field ($\delta_{z/x}$)	$\delta_z = 4.1mm$	$\delta_z = 9.9mm$	$\delta_x = 21.1mm$	$\delta_x = 4.1mm$
field of view (mm)	$[S_x; S_y] = [21; 77.75]$	$[S_x; S_y] = [50; 194.5]$	$[S_z; S_y] = [50; 192]$	$[S_z; S_y] = [20; 74]$
overlap region	$S_{y,overlap} = 1.5mm$	$S_{y,overlap} = 4mm$	$S_{y,overlap} = 3.5mm$	$S_{y,overlap} = 1.mm$

Table 4.3: PIV recording parameters in the LML wind-tunnel

The setup actually consists of two distinct stereo systems placed below the test section, next to each other in the wall normal direction: two adjacent planes are recorded simultaneously, and the fields of view are overlapped to ensure continuity of the data. The main interest of this configuration is to increase the extent of the field of view in the wall-normal direction, while keeping a good resolution of the small scales. Different views of this arrangement are shown in figures 4.2, 4.3, 4.4 and 4.5.

Figure 4.2: Side view of the stereo-PIV setup in the XY configuration (LML)

Figure 4.3: Side view of the stereo-PIV setup in the YZ configuration (LML)

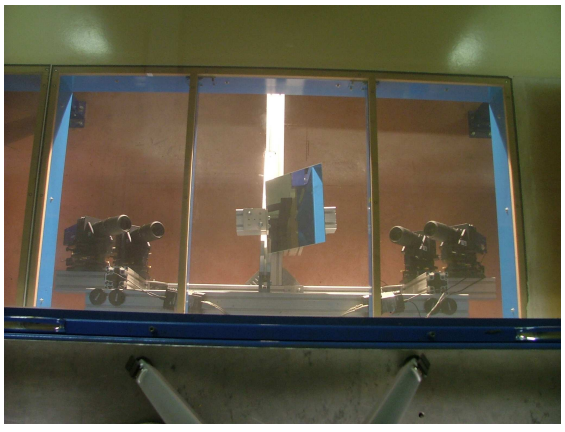

Figure 4.4: Stereo-PIV setup in the YZ configuration: view from the top of the wind-tunnel test section (LML)

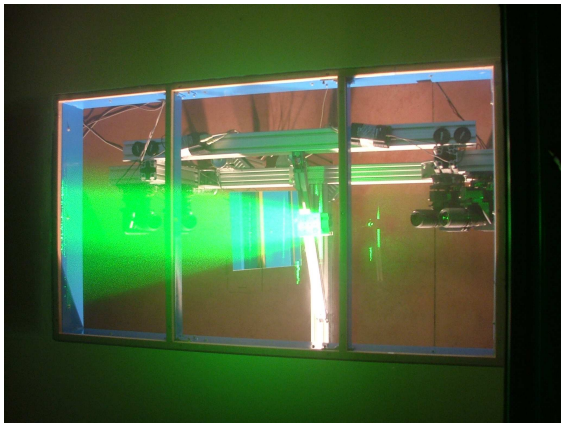

Figure 4.5: Stereo-PIV setup in the YZ configuration: view from the top of the wind-tunnel test section, with the incoming laser sheet (LML)

For the 'lower' stereo system, cameras with a CCD array of $1376px * 1040px$ and a $12bit$ dynamic range are used. For the 'upper' system, cameras with a CCD array of $1280px * 1024px$ and a $10bit$ dynamic range were available. They are oriented in such a way that the wall normal direction of the measurement plane is imaged on the larger side of the cameras ($1376px$ and $1280px$). Within each stereo system, an angular configuration is used with a nominal off-axis angle around 45°, in order to get a comparable accuracy on the in-plane velocity components and on the out-of-plane velocity component (Prasad (2000)). Note that due to the angular configuration, the wall-normal direction is stretched and the ratio between the average magnification along the y and the x/z direction is $\frac{M_y}{M_{x/z}} = \frac{1}{\cos(\theta)} = 0.7$. The magnifications and resolutions given in table 4.3 are averaged over the four cameras and over the two directions of the measurement plane.

The cameras are mounted on specially designed camera adapters for a fine tuning of the camera positioning: the common viewing area between the two cameras of one stereo system was maximized, and the overlap between the two stereo systems was carefully adjusted. For each PIV setup, a calibration target with reference marks was placed inside the region of interest to adjust the field of view of each camera. For the measurements at $Re_\theta = 10140$, $Re_\theta = 13420$ and $Re_\theta = 18950$ (setup A and D), the cameras are fitted with 200mm focal length lenses at aperture of $f_\# = 8$, and an average magnification of 0.24 is achieved. The total extent of the field of views (for the two stereo system) are $[S_x; S_y] = [21mm; 77.5mm]$ (setup A) and $[S_z; S_y] = [20mm; 74mm]$ (setup D) with an overlap region of $S_{y,overlap} = 1.5mm$ (setup A) and $S_{y,overlap} = 1mm$ (setup D). For the measurements at $Re_\theta = 7630$ and $Re_\theta = 10140$ (setup B and C), the cameras are fitted with 105mm focal length lenses at an aperture of $f_\# = 5.6$ (setup B) and $f_\# = 8$ (setup C), and an average magnification of 0.1 is achieved. The total extent of the fields of view (for the two stereo system) are $[S_x; S_y] = [50mm; 194.5mm]$ (setup B) and $[S_z; S_y] = [50mm; 192mm]$ (setup C) with overlap regions of $S_{y,overlap} = 4mm$ (setup B) and of $S_{y,overlap} = 3.5mm$ (setup C) between the two stereo systems.

A two-cavity $200mJ$ Nd:YAG laser system was used at a wavelength of $\lambda = 532nm$ to illuminate the field of view. The laser beam was shaped above the test section into a 1mm thick ($l_{z/x}$) laser sheet by a combination of spherical and cylindrical external optics, before being redirected with a front-coated high-energy mirror into a plane aligned with the calibration target. The switch from the XY laser sheet (setup A and B) to the YZ laser sheet (setup C and D) was simply realized by rotating by 90 degrees the cylindrical lens expanding the laser beam into the laser sheet. With this configuration, the 2 stereo systems are in forward scattering and have their 2 cameras symmetrically placed on either side of the laser sheet. This stereoscopic arrangement was first proposed by Willert (1997). It is attractive because the field of views of both stereo cameras are illuminated by maximum light intensity and are identically stretched, allowing for a more accurate reconstruction of the out-of-plane component. At this laser wavelength, the lens aperture of $f_\# = 8$ result in a diffraction limited particle image diameter of $d_{diff} = 1.8px$ (setup A, C and D) and the lens aperture of $f_\# = 5.6$ in a diameter of $d_{diff} = 1.2px$ (setup B). Raffel et al (1998) recommended a particle image diameter of the order of 2 pixels; the diffraction limited particle image diameter of setup A, C and D is therefore close to the optimum, but some peak-locking effect is expected for setup B. The depth of field of the cameras, depending on the magnification and on the diffraction limited particle image diameter, vary from $\delta_z = 4.1mm$ (setup A and D) up to $\delta_z = 21.1mm$ (setup C). In any case, it is much larger than the laser sheet thickness.

For each one of the four PIV setups, the stereoscopic measurement volume was calibrated using the Soloff method (Soloff et al (1997)). The calibration target, initially

aligned with the laser sheet, was translated in the out-of-plane direction from z=-2.5mm up to z=2.5mm with steps of $500\mu m$ using a micrometer with a $\pm 5\mu m$ accuracy. At each position, the image of the calibration target on the CCD was then recorded.

The flow was seeded with tracer particles delivered by a Poly-Ethylene-Glycol smoke generator. The mean diameter of the particle is about $1\mu m$. The two cavities of the laser were pulsed at a frequency $f_{acq} = 1Hz$ for the acquisition of the SPIV images. The separation time between the two cavities was adjusted at each Reynolds number to get a maximum in-plane displacement of the particles around $10.5px$ (and therefore to get the same accuracy for all measurements). For the YZ configuration, the mean flow is normal to the measurement plane, creating large out-of-plane motions. In order to keep a high level of cross-correlation, the light sheets from the two illumination pulses were therefore shifted in the out-of-plane direction by a distance corresponding to the mean out-of-plane displacement (Raffel et al (1998)). This method reduces the out-of-plane loss of particle pairs while maintaining both a high velocity dynamic range (in contrast to the technique that consist in reducing the separation time) and a high spatial dynamic range (in contrast to the thickening of the laser sheet that induce more spatial averaging).

4.3 Evaluation of the SPIV images

The SPIV images were evaluated using the LML in-house code 'pivlml', described in section 3.3.1. The parameters are compiled in table 4.4, for each PIV setup. For all setups, the SPIV images were cross-correlated in the image plane of each cameras in three successive analysis, on a mesh obtained by projecting a common Cartesian grid into the image plane of each camera. The mesh step of the Cartesian grid was $250\mu m$ for the higher Reynolds number range (setup A and D) and $500\mu m$ for the lower Reynolds number range (setup B and C). This corresponds for all cases to a mesh step of about $8px$ in the image of the cameras. An initial IW size of $64px * 64px$ was used, with no initial window shift. For all setups, the final PIV analysis was realized using interrogation windows of $32px * 32px$, overlapped by approximately 75%. On each stereo system, the Soloff coefficients used to back-project the 2D-2C velocity fields in the object plane and to reconstruct the out-of-plane velocity component were computed using three calibration planes, separated each by $1mm$.

The 2D-3C velocity fields obtained in this manner from the two stereo systems present an overlap region whose extent in the wall-normal direction vary from 5 mesh points (setup D) up to 9 mesh points (setup B). At each realization, the merging between the two systems was realized by taking, in this overlap region, the average of the two instantaneous 2D-3C velocity fields. This process is illustrated in figure 4.6 with an instantaneous YZ velocity field at $Re_\theta = 10140$, measured using setup D. A portion of the overlap region, as measured simultaneously by the lower and upper stereo systems, is shown in subfigure (a). The result of the merging procedure applied to this velocity field is shown in subfigure (b). The selected example is a challenging one, as a vortex is present in the overlap region. Some slight differences are visible in subfigure (a) between the two stereo systems, but, on the whole a good agreement is noted. The merged velocity field, visible in subfigure b is of good quality, and presents an excellent resolution of the vortex.

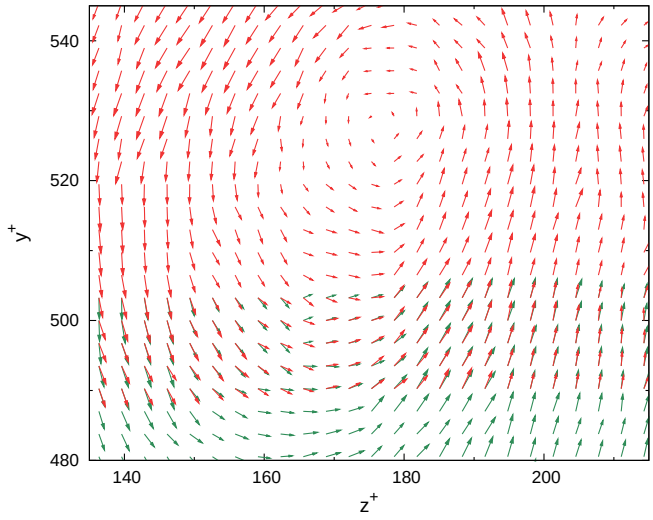

(a) BEFORE the merging

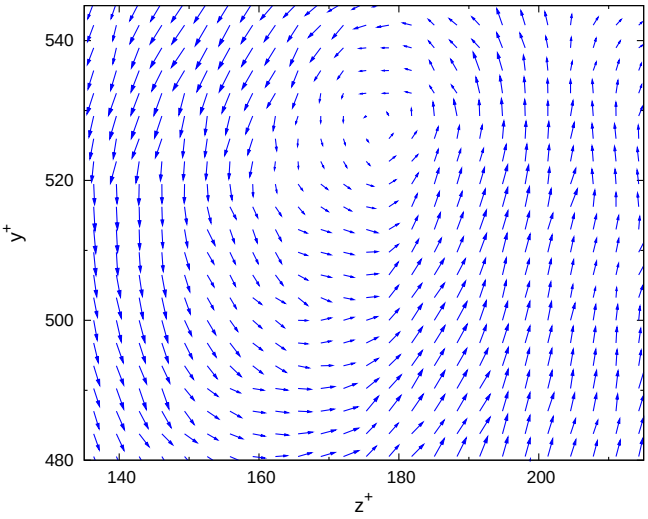

(b) AFTER the merging

Figure 4.6: Fluctuating in-plane velocity field in a portion of the overlap region, in the LML dataset at $Re_\theta = 10140$ in the YZ plane, in wall-units

The quality of the merging procedure can be assessed by analyzing some statistical results on the difference between the two 2D-3C velocity fields in the overlap region for each velocity component:

- the bias between the 2D-3C velocity fields for each velocity component :

$$< u_{i,sys1} - u_{i,sys2} >= U_{i,sys1} - U_{i,sys2} \tag{4.1}$$

- the rms of the random part of the difference between the 2D-3C velocity fields for each velocity component :

$$((u_{i,sys1} - u_{i,sys2}) - (U_{i,sys1} - U_{i,sys2}))_{RMS} \tag{4.2}$$

For all setups, the statistics on the two stereoscopic systems in the overlap region show that the bias is always smaller in magnitude than the random difference (more than 10 times smaller for the XY plane, and from 5 to 10 times for the YZ plane). On the overall, the random error is isotropic with an average value around $0.7\%U_\infty$. Some degree of anisotropy is visible for setup C, where $\sigma(\epsilon_u) \geq \sigma(\epsilon_v) \geq \sigma(\epsilon_w)$. The higher level of uncertainty is obtained for the out-of-plane velocity component, and can be attributed to the fact that this component is reconstructed by the SPIV and is thus more sensitive to the SPIV geometry (although a stereo angle $\theta = 45°$ should lead to analogous in-plane and out-of-plane uncertainty).

The misalignment between the calibration target and the laser sheet was computed for each setup, and corrected following the methodology described in section 3.3.1. In any case, the laser sheet was found to be at a distance less than $500\mu m$ from the central calibration plane, with rotation by less than 0.5°.

PIV setup config.(plane-R_θ)	setup A XY-10140, XY-13420, XY-18950	setup B XY-7630, XY-10140	setup C YZ-7630, YZ-10140	setup D YZ-10140, YZ-13420, YZ-18950
calibration planes misalignment	$-1mm, 0mm, +1mm$	$-1mm, 0mm, +1mm$	$-1mm, 0mm, +1mm$	$-1mm, 0mm, +1mm$
number of analysis	3	3	3	3
initial IW (px)	$(64 * 64)$	$(64 * 64)$	$(64 * 64)$	$(64 * 64)$
final IW	$(32 * 32)$	$(32 * 32)$	$(32 * 32)$	$(32 * 32)$
Mesh step	$(250\mu m * 250\mu m)$	$(500\mu m * 500\mu m)$	$(500\mu m * 500\mu m)$	$(250\mu m * 250\mu m)$
Number of points				
lower syst.	$[N_x, N_y] = [85, 163]$	$[N_x, N_y] = [101, 210]$	$[N_z, N_y] = [101, 202]$	$[N_z, N_y] = [81, 153]$
upper syst.	$[N_x, N_y] = [87, 157]$	$[N_x, N_y] = [101, 189]$	$[N_z, N_y] = [101, 191]$	$[N_z, N_y] = [81, 149]$
total syst.	$[N_x, N_y] = [85, 312]$	$[N_x, N_y] = [101, 389]$	$[N_z, N_y] = [101, 391]$	$[N_z, N_y] = [81, 296]$
overlap region (pt)	7	9	8	5
bias of merge (pivlml)				
u	$-0.03\%U_\infty$	$-0.02\%U_\infty$	$-0.37\%U_\infty$	$-0.07\%U_\infty$
v	$-0.02\%U_\infty$	$-0.01\%U_\infty$	$0.13\%U_\infty$	$0.13\%U_\infty$
w	$-0.04\%U_\infty$	$-0.02\%U_\infty$	$0.03\%U_\infty$	$0.07\%U_\infty$
rms of merge (pivlml)				
u	$0.6\%U_\infty$	$0.8\%U_\infty$	$0.9\%U_\infty$	$0.8\%U_\infty$
v	$0.6\%U_\infty$	$0.6\%U_\infty$	$0.7\%U_\infty$	$0.7\%U_\infty$
w	$0.6\%U_\infty$	$0.6\%U_\infty$	$0.5\%U_\infty$	$0.7\%U_\infty$

Table 4.4: Parameters of the evaluation of the SPIV images acquired in the LML wind-tunnel

4.4 Estimation of the measurement uncertainty

The various ways of assessing the PIV random error have been reviewed in section 2.1.3. The estimation of the error in the LML SPIV measurements was carried out using the same techniques as for the LTRAC SPIV experiments (see section 3.4): first, a method using an existing study of numerically generated PIV records; then, a method based on the real images acquired in the overlap region of the two stereo-systems.

4.4.1 Using synthetic images

In this section, the parameteric study by Foucaut et al (2003) is used as described in section 2.1.3 to evaluate the uncertainty of the SPIV experiments. This study made use of the Europiv Synthetic Image Generator described in Lecordier and Trinite (2003) to generate PIV recording of known content, which were then evaluated with an FFT based cross-correlation algorithm, similar to that employed in the LML evaluation software. The evolution of the PIV error with a range of different PIV recording parameters (diameter, concentration, out-of-plane motions, velocity gradient) was established. Using this parametric study, the random error associated to each parameter of the LML experiment can be retrieved (this is the error on the in-plane projection of the displacement), the greatest of these RMS errors being the global uncertainty of the experiment. Foucaut et al (2003) and Soria (1996) showed that for optimal recording parameters (Raffel et al (1998) : $d_{p,opt} = 2-3px$, $N_{p,opt} = 10$, and ideally no velocity gradient and no out-of-plane motion), the PIV interrogation uncertainty is $0.06px$. According to the PIV parameters summarized in table 4.3, the only recording parameters that can be considered as non-optimum are the presence of velocity gradient (the wall-normal gradient of streamwise velocity $\frac{dU}{dy}$), of out-of-plane motions, and the particle image diameter (for setup B only, where $d_p = 1.2px$ instead of $d_p = 1.8px$ for the other setups). The global PIV uncertainty can then be taken as:

$$\sigma(\epsilon_{int}) = max\left(\sigma_{dU/dy}, \sigma_{out-of-plane}, \sigma_{dp}, 0.06px\right) \tag{4.3}$$

The PIV uncertainty associated with a mean velocity gradient $\frac{dU}{dy}$ is due to non-uniform particle displacement across the interrogation window IW during the separation time Δt. This difference in particle displacement is noted $(dU)_{IW,\Delta t}$. It is computed, in pixels, at three wall-normal positions: inside the buffer region ($y^+ = 16$), at the interface of the buffer region and of the logarithmic region ($y^+ = 40$), and inside the logarithmic region ($y^+ = 60$). The following set of formulae is used:

$$(dU)_{IW,\Delta t} = \Delta t * \frac{u_\tau}{px_{\text{obj}}} \int_{y^+ - \frac{l^+_{IW}}{2}}^{y^+ + \frac{l^+_{IW}}{2}} \frac{dU^+}{dy^+} dy^+$$

$$\frac{dU^+}{dy^+} = \frac{2}{1 + \sqrt{1 + 4(Ky^+(1 - exp(-y^+/A^+))^2}} \quad \text{(van Driest)} \quad \text{for} \quad y^+ = 16, y^+ = 40$$

$$\frac{dU^+}{dy^+} = \frac{1}{Ky^+} \quad \text{(Log law)} \quad \text{for} \quad y^+ = 60$$

It can be seen in the above formulae that $(dU)_{IW,\Delta t}$ depends on the Reynolds number of the measurements (through u_τ, Δt, IW^+, and px_{obj}) but not on the orientation of the measurement plane (the ratio $\Delta t/px_{\text{obj}}$ is the same for the XY plane and for the YZ plane. Accordingly, $(dU)_{IW,\Delta t}$ and the PIV noise induced is presented in table 4.5 for each Reynolds number, and apply for both measurement planes. A scaling of $(dU)_{IW,\Delta t}$ with the particle image diameter is presented, as it is on this non-dimensional parameter that depends the noise level (Keane and Adrian (1990), Foucaut et al (2003)): for a velocity gradient displacement above $0.5d_p$, the velocity gradient strongly increases the RMS error.

Re_θ	7630	10140 ($67\mu m/px$)	10140 ($27\mu m/px$)	13420	18950
$y^+ = 16$					
$(dU)_{IW,\Delta t}$	$4.4px$	$9.1px$	$3.3px$	$5.5px$	$6.7px$
$(dU)_{IW,\Delta t}$	$2.4d_p$	$5.1d_p$	$1.8d_p$	$3.1d_p$	$3.7d_p$
(setup B)	$(3.7d_p)$	$(7.6d_p)$			
$\sigma_{dU/dy}$	$> 0.5px$	$> 0.5px$	$> 0.5px$	$> 0.5px$	$> 0.5px$
$y^+ = 40$					
$(dU)_{IW,\Delta t}$	$1.0px$	$1.93px$	$0.8px$	$1.2px$	$1.5px$
$(dU)_{IW,\Delta t}$	$0.5d_p$	$1.1d_p$	$0.4d_p$	$0.7d_p$	$0.8d_p$
(setup B)	$(0.83d_p)$	$(1.6d_p)$			
$\sigma_{dU/dy}$	$0.09px$	$0.3px$	$0.09px$	$\approx 0.22px$	$\approx 0.26px$
$y^+ = 60$					
$(dU)_{IW,\Delta t}$	$0.25px$	$0.49px$	$0.21px$	$0.31px$	$0.38px$
$(dU)_{IW,\Delta t}$	$0.14d_p$	$0.27d_p$	$0.12d_p$	$0.17d_p$	$0.21d_p$
(setup B)	$(0.21d_p)$	$(0.41d_p)$			
$\sigma_{dU/dy}$	$0.06px$	$0.08px$	$0.06px$	$0.06px$	$0.06px$
(setup B)	$(0.06px)$	$(0.13px)$			

Table 4.5: Error induced by the velocity gradient in the LML database

According to table 4.5, the velocity gradient is a significant source of measurement noise below $y^+ = 60$, such that:

$$\sigma(Re_\theta = 10140_{27\mu m/px}) < \sigma(Re_\theta = 7630) < \sigma(Re_\theta = 13420)$$

$$< \sigma(Re_\theta = 18950) < \sigma(Re_\theta = 10140_{67\mu m/px})$$

This ordering of the uncertainties mainly finds its origin in the ordering of the present interrogation window size in wall units (see table 4.7): in general, the larger the interrogation window size, the more impact the velocity gradient has, and the highest the uncertainty is. At $y^+ = 16$, the sharp velocity gradient induces a displacement difference across the interrogation window larger than $1.5d_p$ for all datasets. This displacement is

outside the range explored by Foucaut et al (2003). For the datasets at $Re_\theta = 10140$ (with a resolution of $67\mu m/px$) and at $Re_\theta = 18950$ in particular, it is equal to $5.1d_p$ and $3.7d_p$ respectively: the measurements in this region are clearly not reliable. At the end of the buffer layer ($y^+ = 40$), the velocity gradient has drastically decreased. The most highly resolved dataset ($Re_\theta = 10140$ with a resolution of $27\mu m/px$) and the dataset at $Re_\theta = 7630$ in the YZ plane now present a displacement difference equal to or lower than $0.5d_p$, and the related uncertainty is on the order of $0.09px$. Finally, at $y^+ = 60$, the velocity gradient is now negligible, and the uncertainties are therefore close to PIV uncertainty for optimal conditions (that is $0.06px$), with the exception of the measurement at $Re_\theta = 10140$ (with a resolution of $67\mu m/px$) in the XY plane where the uncertainty is still on the order of $0.13px$ [1].

The out-of-plane motions are the other source of uncertainty to evaluate. For the measurements in the XY plane, they corresponds to the spanwise velocity fluctuations. Following classical turbulent boundary layer results, these fluctuations have a maximum standard deviation of $w_{\mathrm{RMS}} \approx u_\tau$ in the buffer region and a Gaussian distribution of total width $K = 3w_{\mathrm{RMS}} \approx 3u_\tau$. The larger out-of-plane motion occurring during the separation time Δt is obtained for the measurements in the lower Reynolds number range ($Re_\theta =$ 7630 and 10140, setup B) because the smaller spatial resolution ($67\mu m/px$) induces a larger separation time (to maintain a constant maximum displacement in pixels). It is on the order of $0.06mm$, representing 0.06 laser sheet thicknesses. According to the parametric study by Foucaut et al (2003), this level of out-of-plane motions does not generate any additional uncertainty. Hence, the measurements in the XY plane are free from out-of-plane related uncertainties. As far as the YZ measurements are concerned, the strategy that consisted in shifting the two laser sheets in the out-of-plane direction allowed to reduce drastically the out-of-plane motions: they correspond to the streamwise *fluctuations*, rather than to the *mean* streamwise velocity. Their maximum amplitude is then on the order of $u_{\mathrm{RMS}} \approx 3u_\tau$ with a total width (for a Gaussian distribution) of $K = 3u_{\mathrm{RMS}} \approx 9u_\tau$. In the same fashion as in the XY plane, the larger out-of-plane motions are obtained in the lower Reynolds number range ($Re_\theta = 7630$ and 10140, setup C), and are on the order of $0.3mm$, that is $0.27l_x$. The results of Foucaut et al (2003) indicate that this generates an uncertainty of $0.08px$. For the measurements in the higher Reynolds number range (at $Re_\theta = 10140$, 13420 and 18950 with a resolution of $27\mu m/px$) the out-of-plane motions are lower than $0.13mm = 0.13l_x$, and do not generate any uncertainty. Note that these uncertainties are valid for the buffer region (where the peak of fluctuation occurs). Further up in the boundary layer (typically from the log layer) the out-of-plane motions are weaker and do not cause measurement uncertainty.

Finally, as far as the particle image diameter is concerned, Foucaut et al (2003) and Raffel et al (1998) report on an optimum particle images diameter close to $2px$. This optimum particle image diameter is achieved for all measurements (with $d_p = 1.8px$), at the exception of the measurements at $Re_\theta = 7630$ and $Re_\theta = 10140$ in the XY plane with a spatial resolution of $67\mu m/px$ (with $d_p = 1.2px$). For a particle image concentration close to $10px/IW$, both studies showed that the curve of the RMS error as a function of d_p is relatively flat around $d_p = 2px$, so that diameters between 1 and 3 pixels are acceptable. The difference in the RMS error between diameters of $1.2px$ and $1.8px$ appears negligible.

[1] for this dataset, it becomes negligible above $y^+ = 100$

The global PIV uncertainty can finally be derived as the maximum of the uncertainties associated with the velocity gradient, the out-of-plane motions, and with the particle image diameter (see equation 4.3). Two regions must be distinguished: the region below $y^+ = 60$ and the region above $y^+ = 60$. In the region below $y^+ = 60$, the global PIV uncertainty is dominated by the uncertainty associated with velocity gradients. In this region, the PIV uncertainty increases with decreasing wall normal distance. At $y^+ = 40$ the values of this uncertainties read:

$$\sigma(\epsilon_{int}, Re_\theta = 10140_{27\mu m/px}) \approx \sigma(\epsilon_{int}, Re_\theta = 7630) = 0.09px$$

$$\sigma(\epsilon_{int}, Re_\theta = 13420) = 0.22px$$

$$\sigma(\epsilon_{int}, Re_\theta = 18950) = 0.26px$$

$$\sigma(\epsilon_{int}, Re_\theta = 10140_{67\mu m/px}) = 0.3px$$

Above $y^+ = 60$, the effect of velocity gradients and out-of-plane motions have vanished. The PIV uncertainty is equal to the uncertainty obtained for optimal PIV recordings, that is $\sigma_{PIV} = 0.06px$ for all datasets.

Using the stereoscopic error analysis proposed by Willert (1997) and Prasad (2000), this noise on the PIV evaluation $\sigma(\epsilon_{int})$ can now be related to the random error on the three velocity components reconstructed in the object plane, using equation 2.7 and equation 3.5. Because the stereoscopic angle is $\theta = 45°$ for all setups, the measurements uncertainties are the same for the three velocity components. Recall that the separation time between the two exposures has been adjusted to keep a maximum displacement of $10px$ for all datasets. Accordingly, above $y^+ = 60$, the uncertainties in percentage of the free-stream velocity are the same, on the order of $0.4\%U_\infty$. At $y^+ = 40$, the uncertainties read:

$$\sigma(\epsilon_{int}, Re_\theta = 10140_{27\mu m/px}) \approx \sigma(Re_\theta = 7630) = 0.6\%U_\infty$$

$$\sigma(\epsilon_{int}, Re_\theta = 13420) = 1.5\%U_\infty$$

$$\sigma(\epsilon_{int}, Re_\theta = 18950) = 1.8\%U_\infty$$

$$\sigma(\epsilon_{int}, Re_\theta = 10140_{67\mu m/px}) = 2.0\%U_\infty$$

Note that, as any error analysis based on synthetic particle images, it does not take into account all the sources of measurement noise of the experiment: for instance the influence of the turbulent fluctuations, of the CCD transfer function, and of the optics transfer functions are not taken into account. As a consequence, the uncertainties $\sigma(\epsilon_u)$, $\sigma(\epsilon_v)$, $\sigma(\epsilon_w)$ computed in this section should be understood as a *lower bound of the uncertainty.*

4.4.2 Using real images

Another way to compute the measurement uncertainty is to consider the simultaneous measurement of the flow in the overlap region by the two stereo systems as two independents realizations. The rms of the difference between the two 2D-3C velocity fields can thus be interpreted as the measurement random error $\sigma(\epsilon_{u_i})$ (Kostas et al (2005)) *at the position of the merging region.* For setup A and D, the uncertainty is thus evaluated at $y/\delta = 0.13$, and for setup B and C at $y/\delta = 0.3$. At these wall-normal positions,

config	setup A	setup B	setup C	setup D
$\sigma(\epsilon_u)$	$0.6\%U_\infty$	$0.8\%U_\infty$	$0.9\%U_\infty$	$0.8\%U_\infty$
$\sigma(\epsilon_v)$	$0.6\%U_\infty$	$0.6\%U_\infty$	$0.7\%U_\infty$	$0.7\%U_\infty$
$\sigma(\epsilon_w)$	$0.6\%U_\infty$	$0.6\%U_\infty$	$0.5\%U_\infty$	$0.7\%U_\infty$

Table 4.6: Measurement uncertainty for the LML experiments

the influence of the velocity gradient and of the out-of-plane motion is expected to be negligible, as shown in the previous paragraph. The values are recalled in table 4.6.

For all setup the uncertainties are quite isotropic and at a comparable level, around an average value of $\sigma(\epsilon_{u,i}) = 0.7\%U_\infty$, which represents about $0.08px$ in terms of displacement. This isotropy, observed for a stereoscopic viewing angle of $\theta = 45°$, is in good agreement with the stereoscopic error analysis derived by Willert (1997) and Prasad (2000):

$$\frac{\sigma(\text{out-of-plane})}{\sigma(\text{in-plane})} = tan(\theta)$$

However, some degree of anisotropy is present for setup C (measurement in the YZ plane in the lower Reynolds number range): $\sigma(\epsilon_u) = 0.9\%$, $\sigma(\epsilon_v) = 0.7\%$. and $\sigma(\epsilon_w) = 0.5\%$. Recall that in this flow configuration, the streamwise component corresponds to the out-of-plane motion. This difference in behavior between setup C and the other setup was not accounted for.
These uncertainties computed on the real PIV images are approximately two times larger than the level of uncertainty obtained from the synthetic particle image study ($\sigma(\epsilon_{u,i}) = 0.4\%U_\infty$).

This difference in the level of uncertainty obtained from the real PIV images and the synthetic PIV images can be attributed to the fact that, unlike the study based on synthetic particle images, the uncertainties computed on the real PIV images take into account all the sources of noise of the experiment (and in particular the turbulent fluctuations occurring inside the IW). They can be regarded as the *actual uncertainty* of the SPIV experiment.

4.5 Summary of the database

The characteristics of the entire database acquired in the LML wind-tunnel are finally summarized in table 4.7. Using these informations, the spatial dynamic range of the LML experiments and the range of scales to be resolved in the flow were computed and compiled in table 4.8 (cf section 2.3 and equations 2.10 and 2.11). It can be compared to the spatial dynamic range achieved in previous PIV studies (cf table 2.1 in section 2.3). This comparison is carried out for the XY plane only, as the large scale structures are mainly organized in the streamwise direction. For all Reynolds numbers, the spatial

dynamic range is similar, as expected because the same equipement was used. It is on the order of $SDR_{th} = 12.5$, which is close to the value achieved in the experiments of Hutchins et al (2005). Due to the large Reynolds number of the experiment, the range of scales in the flow is quite large, and the SDR is clearly not sufficient for a full resolution. More specifically, the database is suitable for the study of individual vortices thanks to the small interrogation window size, but it is not appropriate for the study of the large scale organization due to the limited streamwise extent of the field of view.

Plane (1-2)	Re_θ	δ^+ Re_τ	Field of View S_1, S_2	L_{IW}	Mesh step Δ_i	1st mesh point $\frac{L^+_{IW,ini}}{2} \leq y^+$	n° records
XY	7630	2590	0.15δ, 0.6δ	16.8^+	3.9^+	$8.4 \leq y^+$	3840
XY	10140	3620	0.18δ, 0.7δ	27.8^+	6.5^+	$13.9 \leq y^+$	2816
XY	10140	3620	0.08δ, 0.28δ	11.2^+	3.2^+	$5.6 \leq y^+$	4096
XY	13420	5020	0.08δ, 0.28δ	15.4^+	4.5^+	$7.7 \leq y^+$	4096
XY	18950	6860	0.08δ, 0.28δ	20.6^+	6.0^+	$10.3 \leq y^+$	3840
ZY	7630	2590	0.15δ, 0.6δ	16.8^+	3.9^+	$16.8 \leq y^+$	2048
ZY	10140	3620	0.18δ, 0.7δ	27.8^+	6.5^+	$27.8 \leq y^+$	3840
ZY	10140	3620	0.08δ, 0.28δ	11.2^+	3.2^+	$11.2 \leq y^+$	4096
ZY	13420	5020	0.08δ, 0.28δ	15.4^+	4.5^+	$15.4 \leq y^+$	4352
ZY	18950	6860	0.08δ, 0.28δ	20.6^+	6.0^+	$20.6 \leq y^+$	4608

Table 4.7: Characteristics of the LML database

Plane	Re_θ	SDR_{th}	W_{str}
XY	7630	11.5	388
XY	10140	11.7	543
XY	10140	12.9	753
XY	13420	13	753
XY	18950	13	1029

Table 4.8: Spatial dynamic range (SDR_{th}) and range of scales to resolved (W_{str}) for the LML database

Chapter 5

Validation of the database

The LTRAC and the LML database are validated through an analysis of some of the single point statistics such as the mean flow, the Reynolds stresses, the probability density functions of the fluctuations, and the longitudinal and spanwise power spectra. For each flow configuration, these quantities were obtained through an ensemble average over the number of records acquired, and also through an average along the homogeneous directions of the measurement planes (the streamwise direction for the XY planes, and the spanwise direction for the YZ planes). Note that the homogeneity assumption along the streamwise direction can be used because the streamwise extent of the field of view (at most $165mm$ for the LTRAC and $50mm$ for the LML) is small with respect to the total development length of the boundary layer ($3.7m$ for the LTRAC and $18m$ for the LML). In order to facilitate the analysis of these statistical results, the fundamental equations governing turbulent boundary layer flows are first presented.

5.1 Mean flow

5.1.1 Theoretical mean streamwise velocity profile

The turbulent boundary layer equations are derived from the Reynolds-Averaged Navier-Stokes equations, simplified with the thin shear layer assumptions. They read:

$$\begin{cases} \dfrac{\partial U}{\partial x} + \dfrac{\partial V}{\partial y} = 0 \\ U\dfrac{\partial U}{\partial x} + V\dfrac{\partial U}{\partial y} = -\dfrac{1}{\rho}\dfrac{dP}{dx} + \nu\dfrac{\partial^2 U}{\partial y^2} + \dfrac{\partial}{\partial y}(- < u'v' >) \end{cases} \tag{5.1}$$

The continuity equation shows that the mean wall-normal velocity is small with respect to the mean streamwise velocity. A theoretical profile can be derived for the mean streamwise velocity.

At the wall, for a zero pressure gradient, and using the no-slip boundary condition, the turbulent boundary layer equations (5.1) simplify to:

$$\left.\frac{\partial \tau}{\partial y}\right|_0 = 0$$

where $\tau = -\rho\overline{u'v'} + \mu\partial U/\partial y$ is the total shear stress. Moreover, taking the derivative of the boundary layer equations with respect to y leads to:

$$\left.\frac{\partial^2 \tau}{\partial y^2}\right|_0 = 0$$

Thus, in the neighbourhood of the wall, the total shear stress can be approximated by the wall shear stress τ_p with an error of the third order:

$$\tau = \tau_p + O(y^3) \tag{5.2}$$

As a consequence, the mean streamwise velocity profile can be expressed as a function of the characteristics of the fluid ρ and μ and of the wall shear stress τ_p only:

$$U = f(y, \tau_p, \rho, \mu)$$

Taking as primary quantities τ_p, ρ and μ, dimensional analysis leads to the universal 'Law of the wall':

$$U^+ = f(y^+) \tag{5.3}$$

The $^+$ superscript denotes the wall units scaling : $U^+ = U/U_\tau$ and $y^+ = yU_\tau/\nu$ with $U_\tau = \sqrt{\tau_p/\rho}$ the friction velocity.

Very close to the wall ($y^+ \leq 5$) the turbulent shear stress $-\rho < u'v' >$ is negligible with respect to the viscous shear stress $\mu\partial U/\partial y$. Equation (5.2) simplifies to:

$$\mu\frac{\partial U}{\partial y} = \tau_p$$

Integrating this equation with the no-slip condition at the wall gives:

$$U^+ = y^+ \qquad \text{for } 0 \leq y^+ \leq 5 \tag{5.4}$$

Away from the wall, the viscous shear stress $\mu\partial U/\partial y$ is negligible with respect to the turbulent shear stress $\tau = -\rho < u'v' >$. The structure of the flow is thus completely dominated by turbulence. The relevant length scale is given by the boundary layer thickness δ, the time scale by the gradient $\partial U/\partial y$, and the velocity scale by the friction velocity U_τ (as the covariance $< u'v' >$ is of the order of U_τ^2). In this region, the velocity gradient $\partial U/\partial y$ is thus completely determined by y, U_τ and δ:

$$\frac{\partial U}{\partial y} = \frac{\partial U}{\partial y}(y, U_\tau, \delta)$$

Taking as primary quantities y, U_τ and δ, dimensional analysis yields:

$$\frac{\partial U}{\partial y} = \frac{U_\tau}{\delta}\Phi'\left(\frac{y}{\delta}\right)$$

Integrating this relationship between y and infinity gives:

$$\frac{U_\infty - U(y)}{U_\tau} = \Phi\left(\frac{y}{\delta}\right) \quad \text{with} \quad \Phi = \int_y^\infty \Phi'\left(\frac{y}{\delta}\right) d\left(\frac{y}{\delta}\right) \tag{5.5}$$

This law is called the velocity defect law. It is not universal, as it depends on several parameters such as the pressure gradient and the Reynolds number.

Now, if there exists an overlap region between the wall region and the outer region, then both the law of the wall (equation (5.3)) and the velocity defect law (equation (5.5)) must apply in this overlap region. In particular, the limit of the derivatives of these two laws must be equal:

$$\lim_{y/\delta \to 0} -\frac{1}{\delta}\Phi'\left(\frac{y}{\delta}\right) = \lim_{y^+ \to \infty} \frac{U_\tau}{\nu} f'(y^+)$$

Multiplying by y, one gets in the overlap region:

$$-\frac{y}{\delta}\Phi'\left(\frac{y}{\delta}\right) = y^+ f'(y^+)$$

As the variables y^+ and y/δ are independent, the two sides of this equation must be constant. Integrating these two relationships leads to:

- The law of the wall in the overlap region:

$$U^+ = \frac{1}{K} ln(y^+) + C \tag{5.6}$$

- The velocity defect law in the overlap region:

$$\frac{U_\infty - U}{U_\tau} = \frac{1}{K} ln\left(\frac{y}{\delta}\right) + B \tag{5.7}$$

To ensure continuity, the compatibility equation must be satisfied:

$$\frac{U_\infty}{U_\tau} = -\frac{1}{K} ln\left(\frac{\delta U_\tau}{\nu}\right) + B + C$$

The overlap region is therefore an area where the mean streamwise velocity profile is logarithmic. The von Karman constant K and constant C are universal, but constant B depends on the Reynolds number and on the pressure gradient. In the following the universal law of the wall in the overlap region (equation (5.6)) will be referred to as the logarithmic law. It is valid for $40 \leq y^+$ and $0.2 \leq y/\delta$.
The wall region $5 \leq y^+ \leq 40$ is called the buffer region. In this region, the viscous shear stress is on the same order of magnitude as the turbulent shear stress. No analytical expression for the mean streamwise velocity profile exist in this region. Assuming a mixing length model in the form:

$$< u'v' >= l_m^2 \frac{\partial U}{\partial y}$$

$$l_m = Ky(1 - exp(-y/A)) \text{ with } A = \frac{26\nu}{u_\tau}$$

van Driest proposed the following expression for the mean streamwise velocity profile in the buffer region:

$$U^+ = \int_0^{y^+} \frac{2dy'}{1+\sqrt{1+4(Ky'(1-exp(-y'/A^+))^2}} \tag{5.8}$$

In the next paragraph, the mean streamwise velocity profiles computed from the LML and LTRAC databases are compared to the theoretical mean streamwise velocity profile defined by:

$$\begin{cases} U^+ = \displaystyle\int_0^{y^+} \frac{2dy'}{1+\sqrt{1+4(Ky'(1-exp(-y'/A^+))^2}} & \text{for } 0 \leq y^+ \leq 55 \\ U^+ = \dfrac{1}{K} ln(y^+) + C \qquad \text{for } 55 \leq y^+ \text{ and } 0.2 \leq y/\delta \end{cases} \tag{5.9}$$

The values of the universal constants K and C are taken as $K = 0.41$ and $C = 5$.

5.1.2 Mean streamwise velocity of the LTRAC database

The mean streamwise velocity profiles scaled in wall units are shown in figure 5.1 with a zoom in the near wall region in figure 5.2. For comparison, the profiles are plotted against the law of the wall defined by equation (5.9). The wall friction velocity U_τ is obtained from a fit of the SPIV data in the logarithmic region to the log law (equation (5.6)). As can be seen in figure 5.1, the datasets at $Re_\theta = 1300$ and 2200 show an excellent collapse with the law of the wall in the logarithmic region ($55 < y^+ < 150$). In the outer region, the wall-unit representation reveals the effect of the Reynolds number on the mean streamwise velocity profile: the extent of the logarithmic region is slightly larger at $Re_\theta = 2200$ than at $Re_\theta = 1300$. There is also an influence of the free-stream turbulence intensity on the strength of wake (maximum deviation of the mean profile from the log law in the outer region, see Coles (1962)). In the buffer layer ($y^+ \leq 55$), the mean velocity profile show a very good agreement with the Van Driest law down to the first measured points for both datasets ($y^+ \approx 13$). This was expected as both dataset have similar interrogation window size in wall-units ($L_{IW} = 14^+$ at $Re_\theta = 2200$ and $L_{IW} = 15.2^+$ at $Re_\theta = 1300$). In the very near-wall region, no influence of the free-stream turbulence intensity ($Tu = 5.4\%$ at $Re_\theta = 2200$ and $Tu = 2.6\%$ at $Re_\theta = 1300$) is visible on the profiles.

5.1.3 Mean streamwise velocity of the LML database

The mean streamwise velocity profiles scaled in wall units are shown in figure 5.3 for the XY planes (with a zoom in the near wall region in figure 5.4) and in figure 5.5 for the YZ planes (with a zoom in the near wall region in figure 5.6). For comparison, the profiles are plotted against the law of the wall defined in equation (5.9). The values of the wall friction velocity U_τ are obtained from a fit of the PIV data to the log law. These values of U_τ are not reported here, but they are in very good agreement with those deduced from the hot-wire measurements (shown in table 4.1): the maximum difference is on the order of 1.6%.

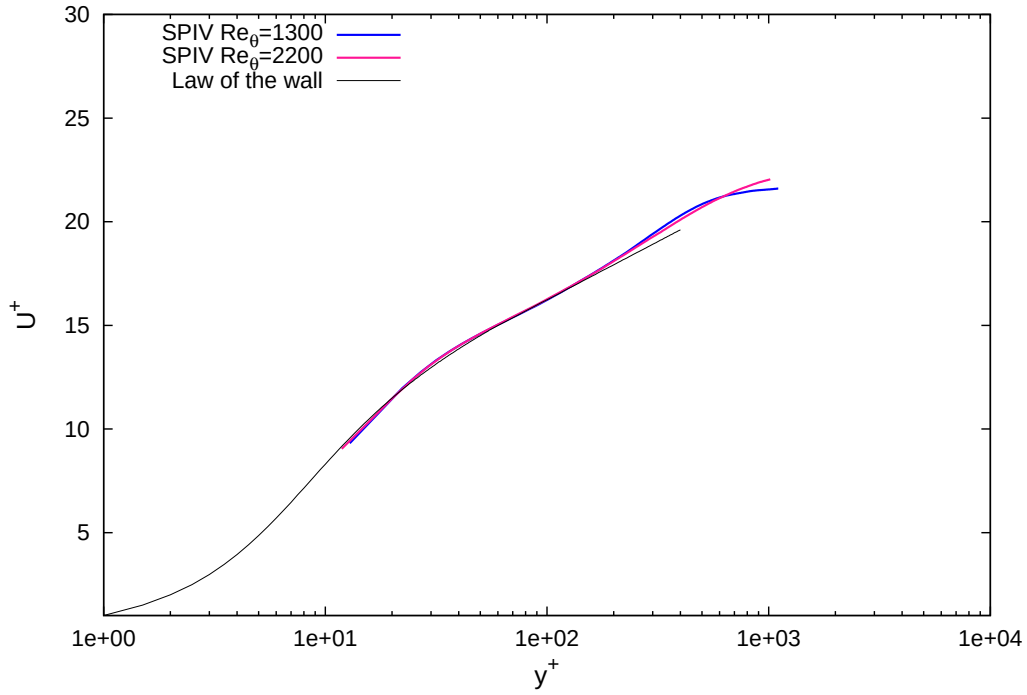

Figure 5.1: Mean streamwise velocity profiles for the LTRAC database

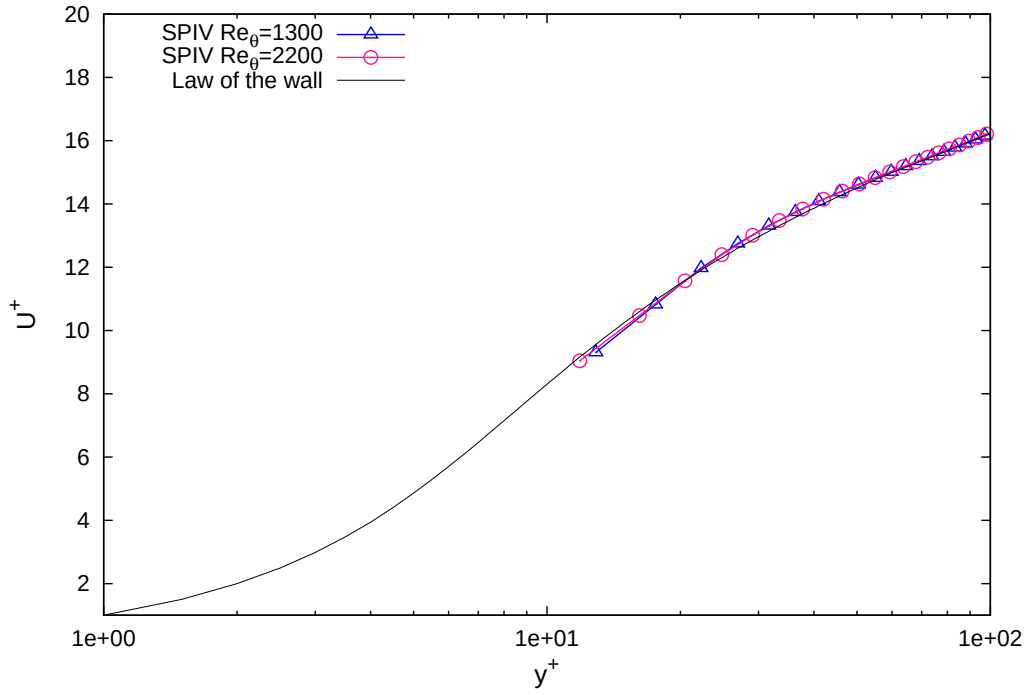

Figure 5.2: Mean streamwise velocity profiles for the LTRAC database: zoom in the near-wall region

As can be seen in figures 5.3 and 5.5, the data display an excellent collapse with the law of the wall in the logarithmic region ($55 < y^+ < 400$) for all Reynolds numbers and for both measurement planes.
Beyond that region, the wall unit representation reveals the effect of the Reynolds num-

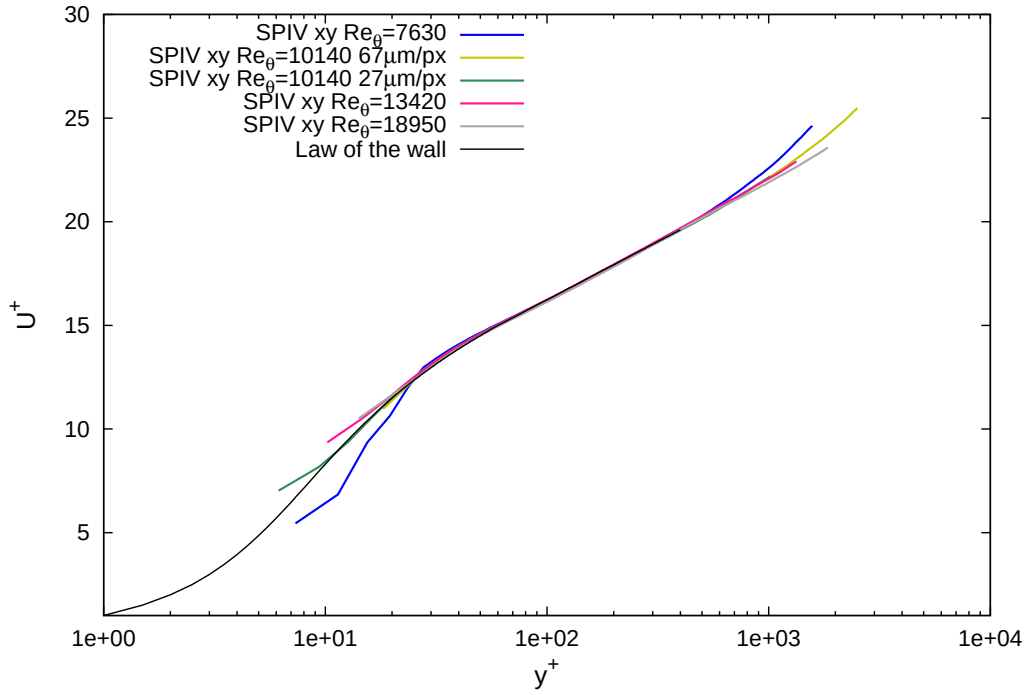

Figure 5.3: Mean streamwise velocity profiles of the LML database in the XY plane

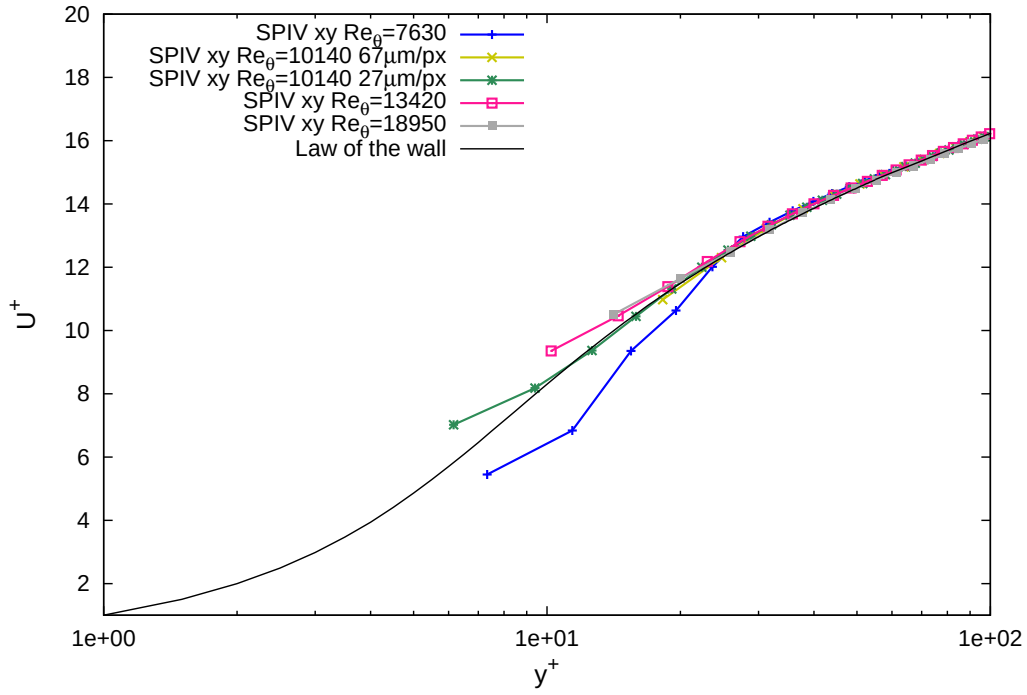

Figure 5.4: Mean streamwise velocity profiles of the LML database in the XY plane: zoom in the near-wall region

ber on the mean streamwise velocity profile: the higher the Reynolds number of the flow, the larger the extent of the logarithmic region. In the lower Reynolds number range ($Re_\theta = 7630$ and $Re_\theta = 10140$) with a resolution of $67\mu m/px$, the boundary layer is measured up to $y/\delta = 0.6$ and $y/\delta = 0.7$ respectively, and some part of the wake region

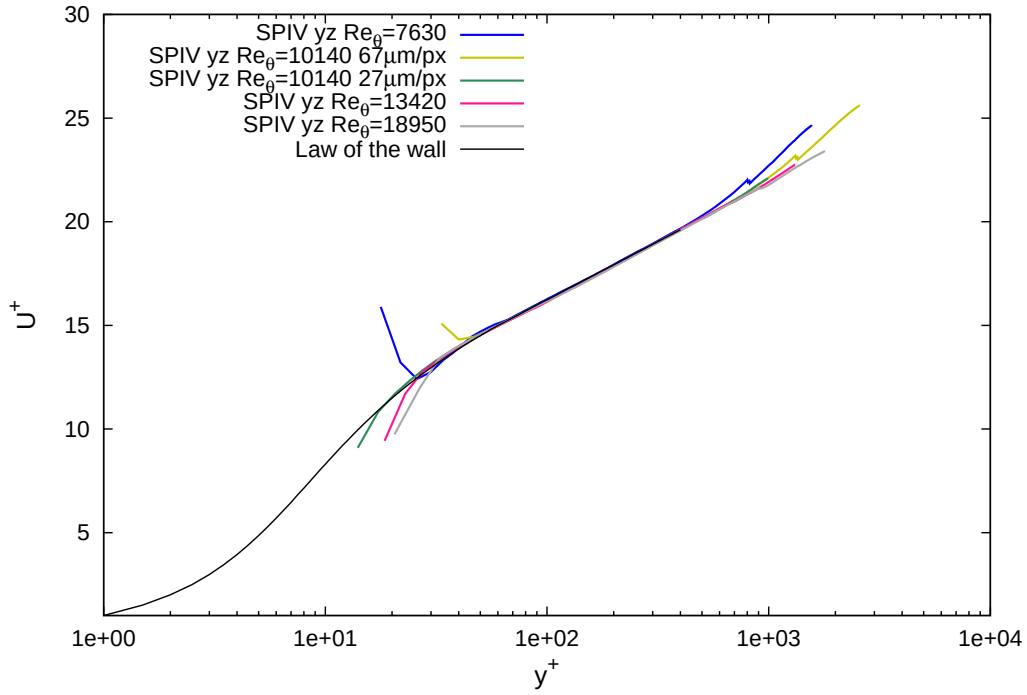

Figure 5.5: Mean streamwise velocity profiles of the LML database in the YZ plane

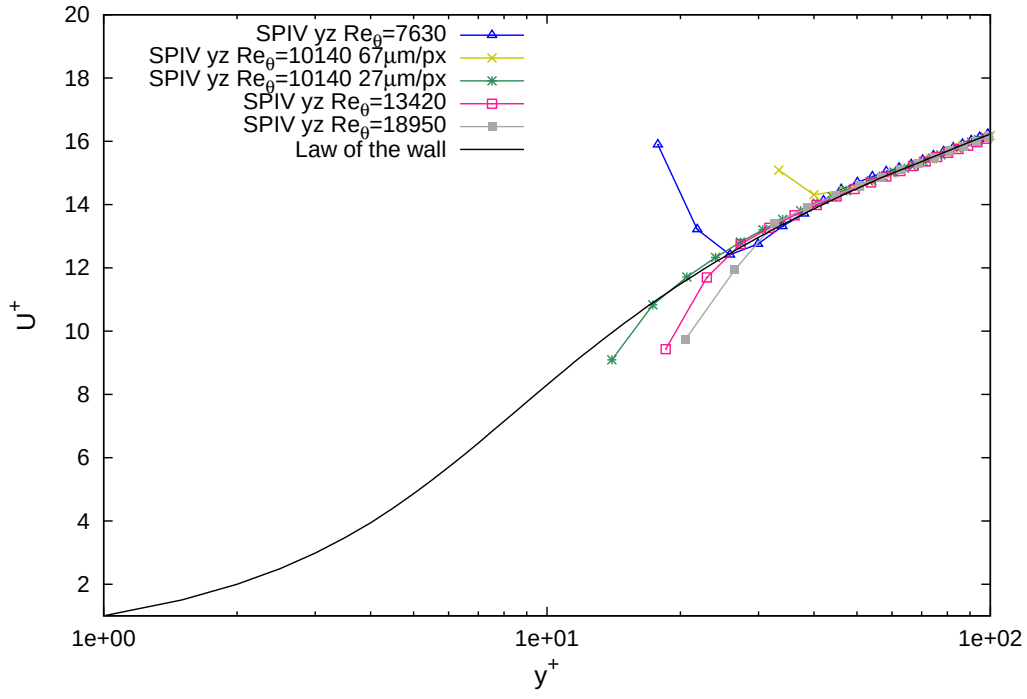

Figure 5.6: Mean streamwise velocity profiles of the LML database in the YZ plane: zoom in the near-wall region

is visible on the velocity profiles.
For the measurements in the YZ planes (figure 5.5), a small discontinuity is visible on

the profiles at $y^+ \approx 800$ and $y^+ \approx 1300$ for the datasets $Re_\theta = 7630$ and $Re_\theta = 10140$ (with $67\mu m/px$) respectively. This corresponds to a slight mismatch during the merging between the velocity fields from the two stereoscopic systems for setup C. All the other profiles are free from this effect. In section 4.3, the RMS of the difference between the two stereoscopic velocity fields in the overlap region was computed for each velocity component and for each setup (the values are compiled in table 4.4). The highest level of mismatch (of the order of $1.5\%U_\infty$) was indeed obtained on the streamwise velocity component for $Re_\theta = 7630$ and $Re_\theta = 10140$ (with $67\mu m/px$).
In the buffer region ($y^+ \leq 55$) of the XY planes (figure 5.4) and of the YZ planes (figure 5.6), the velocity profiles are variously affected by the strength of the mean velocity gradient. The influence of the Reynolds number is clearly visible: for a given spatial resolution, the lower the Reynolds number, the better the agreement with the van Driest law (or more precisely, the agreement with the Van Driest law occurs at lower y^+). This behavior was predicted using a synthetic particle image study in section 4.4.1 (see table 4.5). It find its origin in the fact that for a constant interrogation window size in pixels, the higher the Reynolds number, the larger the interrogation window size in wall units, and therefore the stronger the effect of the velocity gradient. The differences between the XY plane and the YZ plane may now be addressed: at a given Reynolds number the agreement with the van Driest law is noticeably better for the XY plane than for the YZ plane. This difference may originate from the fact that the out-of-plane motion corresponds to a velocity component of larger amplitude for the YZ datasets (the streamwise velocity component). In section 4.4.1, it was explained that the error due to this large out-of-plane motion could be drastically reduced thanks to the shifting of the two laser sheets by a distance corresponding to the mean displacement over the field of view. Now, it should be reminded that this shift cannot be appropriate for the *whole* field of view because of the boundary layer velocity gradient in the wall normal direction. It is therefore possible that the measurements in the buffer region, where the velocity is significantly lower than in the rest of the boundary layer, were more affected by the out-of-plane motions for YZ datasets.
In conclusion, the first wall normal positions where the agreement between the PIV velocity profiles and the van Driest law is observed are compiled in table 5.1. These positions give the first valid datapoint in the wall normal direction for each dataset. In the rest of the thesis, only the region above these wall normal positions will be taken into consideration for the computation of the statistics. It is of interest to note that, for the measurements at $Re_\theta = 10140$ and $Re_\theta = 13420$ (with a spatial resolution of $27\mu m/px$), the position of the first valid mesh point in the wall-normal direction ($y^+ = 13$ and $y^+ = 15$ respectively) is comparable to the ones of the LTRAC datasets ($y^+ = 15$).

plane	Re_θ	1st valid mesh point
XY	7630	$y^+ = 24$
XY	10140	$y^+ = 18$
XY	10140	$y^+ = 13$
XY	13420	$y^+ = 15$
XY	18950	$y^+ = 20$
ZY	7630	$y^+ = 34$
ZY	10140	$y^+ = 53$
ZY	10140	$y^+ = 17$
ZY	13420	$y^+ = 27$
ZY	18950	$y^+ = 33$

Table 5.1: Position of the 1st valid mesh point in y^+ for the LML database

5.2 Reynolds Stresses

5.2.1 Introduction

The Reynolds stresses are the covariances of the velocity fluctuations. In the Reynolds Averaged equations, they appear as additional terms (as compared to the laminar equation) that play the role of apparent turbulent stresses. The sum of the normal Reynolds stresses $k' = 1/2(< u_i' u_i' >)$ is the turbulent kinetic energy of the flow. In the turbulent boundary layer case, the covariances $< u'w' >$ and $< v'w' >$ are zero given that the flow is statistically two-dimensional and invariant under reflection of the spanwise axis. The shear stress $< u'v' >$ is of primary importance (see equations (5.1)). Its product by the mean velocity gradient is responsible for the production of turbulent kinetic energy. In the following, only the normal stresses $< u_i' u_i' >$ and the shear stress $< u'v' >$ will be presented.
The accuracy of the Reynolds stresses measured with PIV can be affected by spatial averaging of the fluctuations over the IW (which tends to attenuate their magnitude) and by PIV measurement uncertainties in the instantaneous velocities. As will be seen in the analysis of the power spectra, the measurement noise ϵ_i is pre-eminent over spatial averaging in the high wavenumber domain. Its effect on the Reynolds stresses $< u_i' u_j' >$ can be expressed as (assuming that the noise is not correlated with the velocity):

$$< (u_i' + \epsilon_i)(u_j' + \epsilon_j) > = < u_i' u_j' > + < u_i' \epsilon_j > + < u_j' \epsilon_i > + < \epsilon_i \epsilon_j > \approx < u_i' u_j' > + < \epsilon_i \epsilon_j >$$

Hence, the measurement uncertainties induce an error of $< \epsilon_i \epsilon_j >$ on the estimation of $< u_i' u_j' >$. For the normal stresses $< u_i'^2 >$, this error corresponds to a positive bias equal to $4 * \sigma^2(\epsilon_i)$ with a 95% confidence interval. Recall the random error $\sigma^2(\epsilon_i)$ was evaluated in section 3.4 for each flow configuration using the real PIV images in the overlap region. Accordingly, error bars extending down to $-4 * \sigma^2(\epsilon_i)$ can be used for the normal stresses profiles. For the shear stresses $< u'v' >$, the error $< \epsilon_u \epsilon_v >$ is undetermined.

5.2.2 Reynolds stresses of the LTRAC database

The profiles of Reynolds stresses $< u'u' >$, $< v'v' >$, $< w'w' >$, and $< u'v' >$ measured with SPIV are validated against the profiles from a DNS simulation of channel flow at $Re_\tau = 950$ (see Hoyas and Jiménez (2006), DelAlamo et al (2006)). The characteristics of this DNS are reported in table 5.2.2, and are to be compared with the characteristics of the LTRAC database, compiled in table 3.5. In particular, the Reynolds number of this DNS is quite close to the Reynolds number of the SPIV dataset at $Re_\theta = 1300$ ($Re_\tau = 820$).

Re_τ	S_x	S_y	S_z	Δx^+	Δz^+
950	$8\Pi h$	$2h$	$3\Pi h$	11	5.7

Table 5.2: Characteristics of the DNS of channel flow by DelAlamo et al (2006).

The velocity covariances at $Re_\theta = 1300$ ($Tu = 2.6\%$) are plotted in figure 5.7 and at $Re_\theta = 2200$ ($Tu = 5.4\%$) in figure 5.8. Only one in every two points is shown to preserve the clarity of the graphs. On each figure, error bars corresponding to $-4 * \sigma^2(\epsilon_i)$ as estimated in section 3.4 are reported for the normal stresses. These uncertainties were computed from the RMS of the differences between the two stereoscopic systems in the overlap region. Given the measurement configuration, these uncertainties are therefore global over the wall-normal extent of the velocity fields. Accordingly, there is no specific wall-normal positioning for the error-bars and their position in the figures is arbitrary. Also, the level of free-stream turbulence intensity is reported on each figure on the right hand side axis.

The boundary layer at $Re_\theta = 1300$ ($Re_\tau = 820$ and $Tu = 2.6\%$) is overall in good agreement with the DNS data. The normal stresses computed from the SPIV data reach a minimum at $y/\delta = 1.3$, with isotropic values of $< u'u' >$, $< v'v' >$ and $< w'w' >$ close to the free-stream turbulence intensity (the small difference is due to the PIV uncertainty). It is of interest to note that this level is comparable with the turbulence intensity of the DNS data on the centerline of the channel ($y = \delta = h$). The streamwise velocity fluctuations profile $< u'u' >$ present a good agreement with the DNS data in the near-wall region, but its level is significantly higher in the outer region ($y/\delta > 0.15$) with an 'outer plateau' around $y/\delta = 0.35$. It is unlikely that this plateau is due to measurement uncertainty, as it would result in an overestimation near the wall rather than away from the wall (see section 3.4). Moreover the amplitude of the difference between the two profiles is larger than the SPIV uncertainty on the u component. This higher level of $< u'u' >$ in the outer region may be linked to the difference between a boundary layer flow and a channel flow, and in particular to the very large scale motions commonly observed in that region (Hutchins and Marusic (2007)). It can be observed in the figures that the minimum value of the Reynolds stresses is reached at $y = h$ for the channel flow, and at $y/\delta = 1.3$ for the boundary layer flow. The normal stress $< v'v' >$ displays an excellent collapse

with the DNS stress over the whole boundary layer thickness. As far as the $< w'w' >$ is concerned, it appears in good agreement in the outer region but increasingly overestimated with decreasing wall-normal distance. The w component corresponds to the out-of-plane component and is the most impacted by the measurement noise. This overestimation of $< w'w' >$ in the near-wall region is clearly due to measurement uncertainty. As far as the shear stress is concerned, it displays an excellent collapse with the data of Hoyas and Jiménez (2006) over the whole boundary layer thickness. It finds its origin in the fact that the measurement noise on u is uncorrelated with the measurement noise on v: $< \epsilon_u \epsilon_v >= 0$.

The Reynolds stresses of the boundary layer at $Re_\theta = 2200$ ($Re_\tau = 1390$ and $Tu = 5.4\%$) are shown in figure 5.8. Only one in every two points is shown. For the $< u'u' >$ and $< w'w' >$ covariances, their amplitude for the SPIV data is twice as high as for the DNS data. This is due to the fact that the free-stream turbulence intensity of the water-tunnel ($Tu^{2+} = 1.5$) is much larger than the centerline turbulence intensity of the channel ($Tu^{2+} = 0.3$). On the other hand, the $< v'v' >$ covariance seems affected by this large free-stream turbulence intensity for $y > 0.3\delta$ only. Closer to the wall, there is good agreement between the SPIV data and the DNS data. The shear stress $< u'v' >$ also displays good agreement with the DNS for $y/\delta \leq 0.3$. The difference observed in the outer region may be due to a boundary layer/channel flow difference.

The very near-wall region $y^+ \leq 100$ is shown in wall units in figure 5.9 for the two boundary layers (every point is shown). The $< v'v' >$ and the $< u'v' >$ of the two SPIV datasets display an excellent agreement with DNS down to the first measured point ($y^+ = 15$). $< u'u' >$ is also in good agreement at $Re_\theta = 1300$ ($Re_\tau = 820$ and $Tu = 2.6\%$), but increasingly overestimated with increasing wall-normal distance at $Re_\theta = 2200$ ($Re_\tau = 1390$ and $Tu = 5.4\%$). For $< w'w' >$, the influence of the measurement uncertainty due to the mean velocity gradient is visible on the $Re_\theta = 1300$ profile. This uncertainty becomes negligible for $y^+ = 50$, which is in good agreement with the synthetic particle image study undertaken in section 3.4.1. The $< w'w' >$ profile of the SPIV data at $Re_\theta = 2200$ has a higher amplitude than the DNS profile due to the high free-stream turbulence intensity.

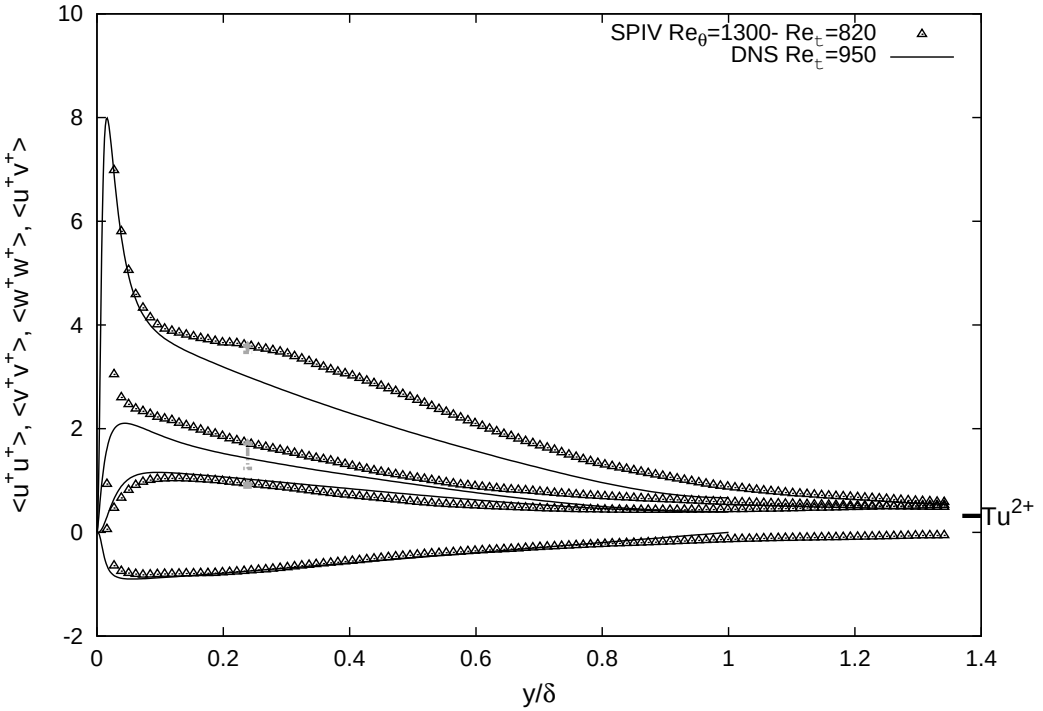

Figure 5.7: Reynolds stresses of the LTRAC database at $Re_\theta = 1300$. The error bar, computed as described in section 3.4, and the level of the free stream turbulence intensity ($Tu = 2.6\%$) is reported on the graph.

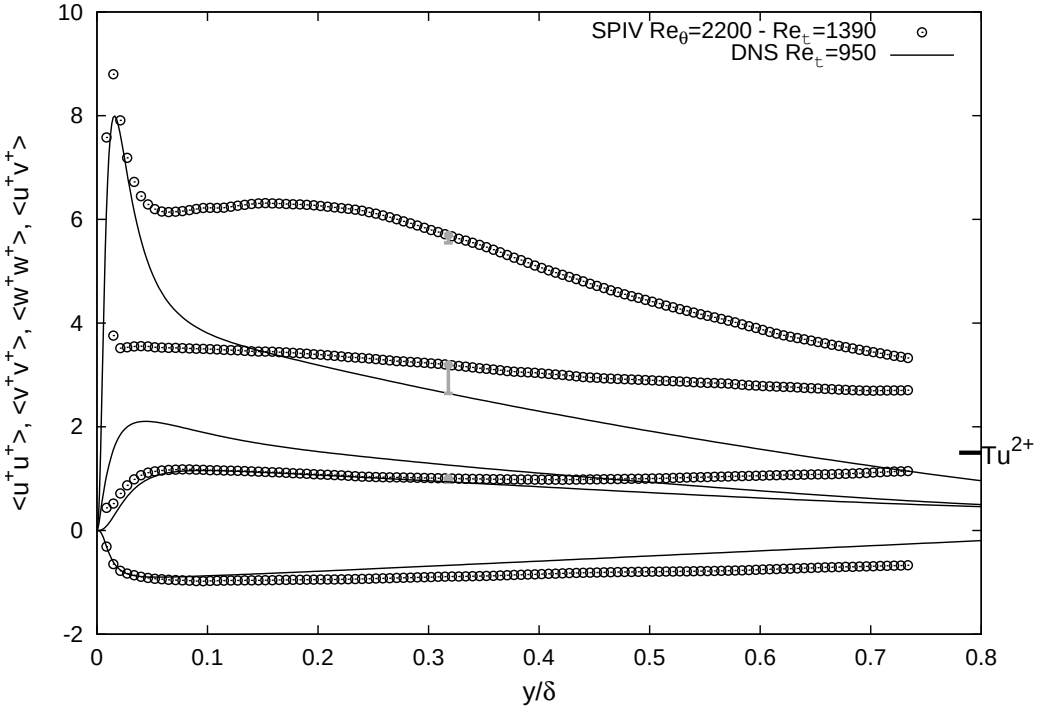

Figure 5.8: Reynolds stresses of the LTRAC database at $Re_\theta = 2200$. The error bar, computed as described in section 3.4, and the level of the free stream turbulence intensity ($Tu = 5.4\%$) is reported on the graph.

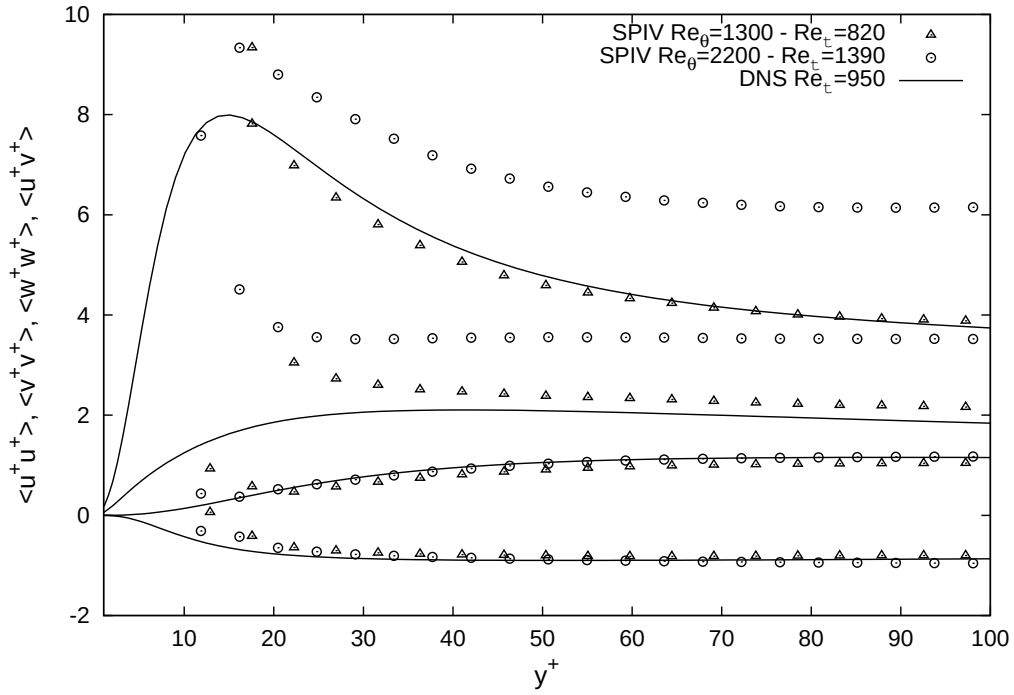

Figure 5.9: Reynolds stresses of the LTRAC database at all Reynolds numbers in the near-wall region

5.2.3 Reynolds stresses of the LML database

The profiles of Reynolds stresses $< u'u' >$, $< v'v' >$, $< w'w' >$, and $< u'v' >$ measured with SPIV are validated against the profiles obtained from hot-wire anemometry at $x = 19.6m$ (see table 4.2) using X-wires probes (from which the covariances of the three velocity components can be computed). The velocity covariances computed from the SPIV measurements at $Re_\theta = 7630$ and $Re_\theta = 10140$ with a spatial resolution of $67\mu m/px$ are plotted in figure 5.10, and the covariances computed from the measurements at $Re_\theta = 10140$, $Re_\theta = 13420$ and $Re_\theta = 18950$ with a spatial resolution of $27\mu m/px$ are plotted in figure 5.11. At each Reynolds number, the XY profiles are represented using hollow symbols, and the YZ profiles using filled symbols. For the sake of clarity, only one in every five points is shown. In this representation, good universality is observed for each Reynolds stress over the whole range of Reynolds number under investigation ($7630 \leq Re_\theta \leq 18950$). Therefore, these profiles are compared to the hot-wire anemometry at $Re_\theta = 10140$ only. As was shown in section 4.2, the ratio of the uncertainty over the friction velocity is constant for a given orientation of the measurement plane and at given spatial resolution. Accordingly, for each Reynolds stress in each figure, only one error bar is shown for all Reynolds numbers (for clarity, only the error bar corresponding to the YZ plane are shown). These error bars are positioned in the overlap region for each case, ie at $y/\delta \approx 0.3$ for figure 5.10, and at $y/\delta \approx 0.13$ for figure 5.11.
Globally, the SPIV Reynolds stresses at the four Reynolds numbers and in both measurement planes are in good agreement with the HWA data, with a noticeably better collapse for the $< v'v' >$ and $< u'v' >$ profiles than for $< u'u' >$ and $< w'w' >$ (some discrepancies are visible in the very near wall region $y/\delta < 0.05$, this region will be studied in greater details with figure 5.12 in the next paragraph). Among the normal stresses, the better

agreement of the $< v'v' >$ component finds its origin in the fact that this quantity is measured in the same fashion for the XY plane as for the YZ plane: in both cases, v is an in-plane velocity component along a direction with optical stretching; hence, the error on this quantity is comparable for all measurements configurations. In contrast, u corresponds to the in-plane non-stretched component for the XY plane and to the out-of-plane component for the YZ plane, and w corresponds to the out-of-plane component for the XY plane and to the in-plane non-stretched component for the YZ plane. Hence, the slight differences between the two planes visible on the $< u'u' >$ and on the $< w'w' >$ profiles are expected. In particular, the discrepancies for the $< u'u' >$ profiles in figure 5.11 are coherent with the associated errorbar. A specific comment may be made for the dataset at $Re_\theta = 7630$ (figure 5.10): the $< u'u' >$ profile of the SPIV appears overestimated with respect to the HW profile in the outer region of the flow. This is due to the fact that the free-stream velocity changed slightly during the acquisition of this SPIV dataset (on the order of 3%), while the RMS values of u were computed using a single profile of mean velocity for the whole dataset. Finally, the excellent collapse of the shear stresses $< u'v' >$ is explained by the fact that the measurement noise on u is uncorrelated with the measurement noise on v: $< \epsilon_u \epsilon_v >= 0$.

The Reynolds stresses in the near-wall region ($y^+ < 100$) are plotted in figure 5.12 for all Reynolds numbers and for all measurements planes. Both the stresses and the wall-normal distance are scaled in wall units. In this plot, every measurement point is shown. Overall, a good universality is observed in this representation. In particular, the extrema of $< u'u' >$, $< v'v' >$, $< w'w' >$ and $< u'v' >$ have the expected intensities: $< u'u' >^+_{max} \approx 9$, $< v'v' >^+_{max} \approx 1$, $< w'w' >^+_{max} \approx 2$ and $< u'v' >^+_{max} \approx -1$. As the lowest measurement point it located at $y^+ = 13$ (for $Re_\theta = 10140$ in the XY plane with a resolution of $27\mu m/px$), only the decreasing side of the peak of $< u'u' >$ is visible. On the $< u'u' >$ and $< v'v' >$ curves at $Re_\theta = 10140$ with the lowest spatial resolution ($67\mu m/px$), a noticeable difference is visible between the XY measurements and the YZ measurements. As explained in the analysis of the mean velocity profiles, this difference may be due to the influence of the out-of-plane velocity component in the YZ plane, associated to the high velocity gradient across the IW for the resolution of $67\mu m/px$. For the other Reynolds numbers, the $< v'v' >$ SPIV profiles coincide well and are in good agreement with the hot-wire profile. The SPIV profiles of shear stress $< u'v' >$ show an excellent collapse down to the first measured points. In the region $y^+ < 30$, some small differences with the HWA profile are visible. It is likely that the SPIV measurements of the shear stress are indeed more reliable than the HWA ones in this region.

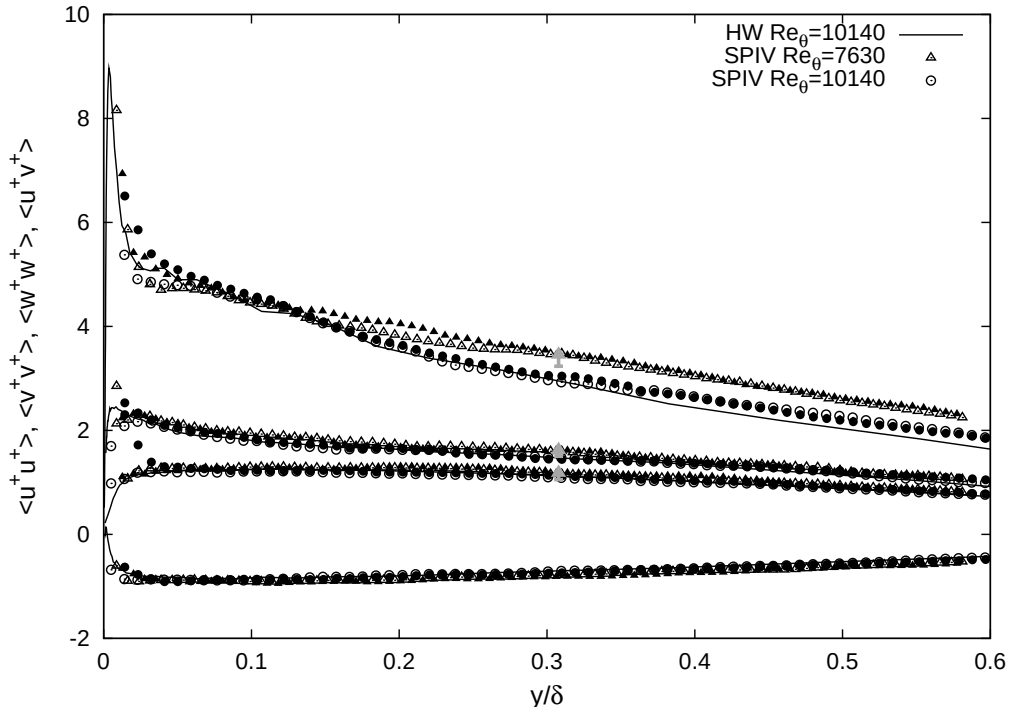

Figure 5.10: Reynolds stresses of the LML database at $Re_\theta = 7630$ and $Re_\theta = 10140$ with a resolution of $67\mu m/px$ (XY plane: hollow symbols; YZ plane: filled symbols)

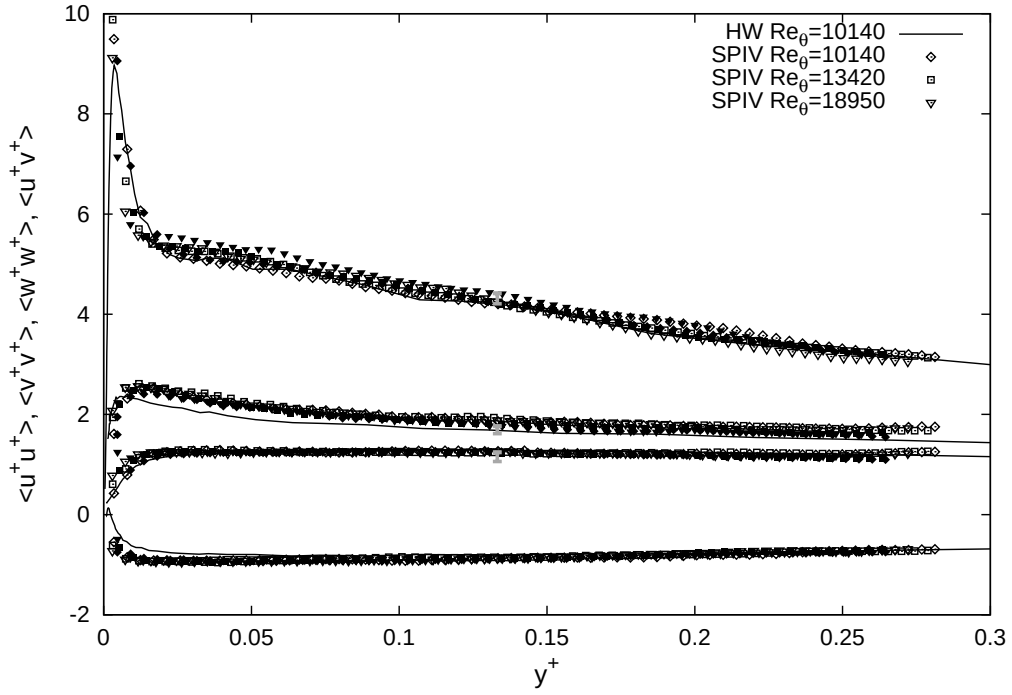

Figure 5.11: Reynolds stresses of the LML database at $Re_\theta = 10140$, $Re_\theta = 13420$ and $Re_\theta = 18950$ with a resolution of $27\mu m/px$ (XY plane: hollow symbols; YZ plane: filled symbols)

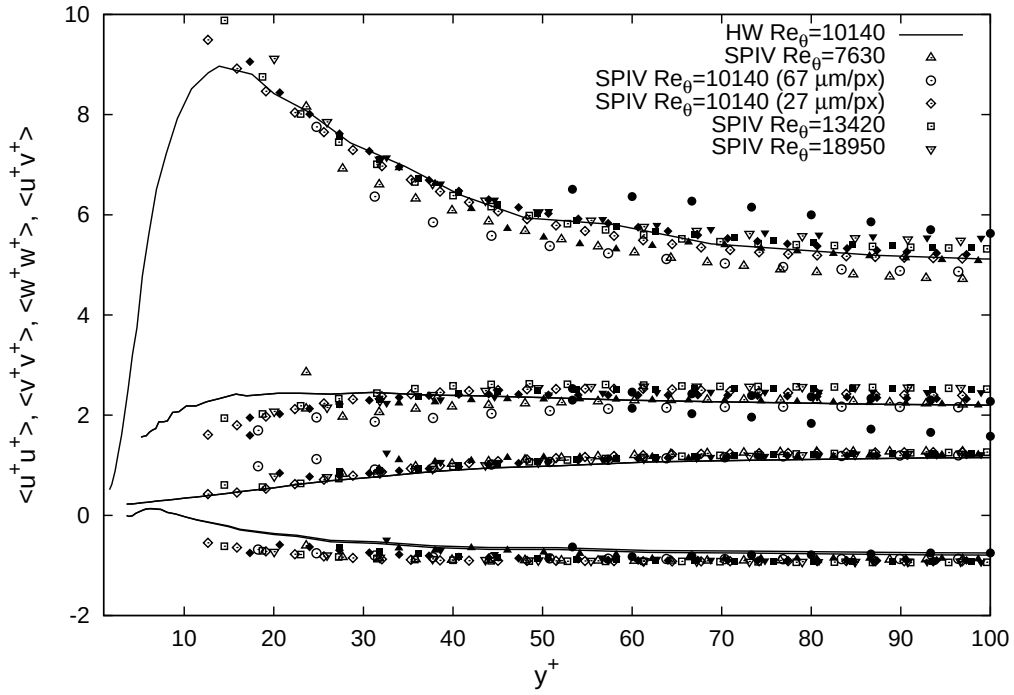

Figure 5.12: Reynolds stresses of the LML databases at all Reynolds numbers in the near-wall region (XY plane: hollow symbols; YZ plane: filled symbols)

5.3 PDF of the fluctuations

5.3.1 Definition

The Probability Density Function $PDF_X(x)$ of a variable X is defined by:

$$PDF(x) = \lim_{\Delta x -> 0} \frac{\text{Prob}[x \leq X \leq x + \Delta x]}{\Delta x}$$

It is the probability that a variable X has a value between x and $x + \Delta x$ normalized by the width of the interval Δx, as Δx tends to zero, .

The knowledge of the PDF of a variable X allows the retrieval of the statistical moments of this variable. For instance, the moment of order n is given by:

$$< x^n >= \int_{-\infty}^{\infty} x^n PDF_X(x) dx \tag{5.10}$$

If the PDF of X is Gaussian:

$$PDF_X\left(\frac{x}{\sigma_X}\right) = G\left(\frac{x}{\sigma_X}\right) = \frac{1}{2\pi} e^{-\frac{1}{2}\left(\frac{x}{\sigma_X}\right)^2} \tag{5.11}$$

then the moments of odd order are zero, and the even ones are constant when non-dimensionalized with the standard deviation.

For the LTRAC and LML database, the PDF of the normalized velocity fluctuations $u_i'/\sigma(u_i)$ is evaluated over the domain $[-4;+4]$. Because the number of realizations available and the resolution of the measurements are finite, the PDF is estimated using an interval $\Delta u_i/\sigma(u_i)$ of finite width. It is chosen such that it is larger than the measurement uncertainty, but small enough to minimize the bias of the estimation:

$$\Delta u_i = \frac{8 * \sigma(u_i)}{128}$$

5.3.2 Methodology to quantify the effect of peak-locking

The evaluation of flow displacements with PIV can be affected by the peak-locking effect (Westerweel (1997)) which tends to bias displacements towards integer values in pixels. This effect is minimized in this study due to good resolution of the particle images (from 2 to 3 pixels per particle image) and the use of a Gaussian peak-fitting algorithm. However, as will be shown in the next paragraph, this effect is still visible in some of the fluctuations. It is of interest to quantify the peak-locking effect as well as its impact on the statistical moments. In the event that the PDF of the velocity is Gaussian (see equation (5.11)), Carlier (2001) proposed that the peak-locking effect on the PDF can be modelled as:

$$PDF_X\left(\frac{x}{\sigma_X}\right) = G\left(\frac{x}{\sigma_X}\right)\left(1 + A\,cos\left(2\pi\left(B\frac{x}{\sigma_X} + C\right)\right)\right) \tag{5.12}$$

where A corresponds to the amplitude of the peak-locking, B to its frequency, and C to its phase. A fit of equation (5.12) via coefficients A, B and C to the PDF gives a full characterization of the peak-locking effect. The effect on the moments of the velocity component can then be derived as:

$$\epsilon(\overline{x^n}) = \int_{-\infty}^{\infty} x^n \left(PDF_X\left(\frac{x}{\sigma_X}\right) - G\left(\frac{x}{\sigma_X}\right)\right) dx \tag{5.13}$$

For $n = 1$ (giving the mean of the variable X) and $n = 2$ (giving the variance of variable X) one finds the following analytical expression for the error:

$$\begin{aligned} \epsilon(\overline{x^1}) &= -Aexp(-2\pi^2 B^2) sin(2\pi C)(2\pi)^{0.5} \\ \epsilon(\overline{x^2}) &= +Aexp(-2\pi^2 B^2) cos(2\pi C)(4\pi^2 B^2 - 1) \end{aligned} \tag{5.14}$$

This error has been evaluated for the LTRAC and LML database, in the cases where the PDF of the velocity fluctuations present some peak-locking.

5.3.3 PDF for the LTRAC database

The PDF of the normalized velocity fluctuations are computed at $y^+ = 100$ from the two PIV datasets ($Re_\theta = 1300$ and $Re_\theta = 2200$). As the same setup was used, (see section 3.2), the PDF of the two datasets should have a similar behavior. In the logarithmic layer, the intermittency with the wall and the free-stream is negligible, and hence the fluctuations should have a Gaussian distribution.

The PDF of the normalized streamwise, wall-normal, and spanwise fluctuations are shown respectively in figures 5.13, 5.14 and 5.15. The PDF of u'/σ_u and w'/σ_w display a Gaussian behavior, free from peak-locking effect (although a very small peak-locking is visible for u'/σ_u). Given the measurement configuration, these two components correspond respectively to the in-plane stretched and to the out-of plane velocity component. Jie (2006) suggested that the peak-locking effect on these two velocity components was smoothed out during the stereoscopic reconstruction. In contrast, the PDF of v'/σ_v are clearly affected by peak-locking.

The methodology detailed in the previous paragraph can be used on v'/σ_v to characterize this peak-locking and its effect on the statistics. This process is illustrated in figure 5.16. The PDF of v'/σ_v is plotted against a 'peak-locked' Gaussian (as defined in equation (5.12)) that has been fitted to the PIV data via coefficients A, B and C. The values of these coefficients are compiled in table 5.3. The associated bias on $\overline{v'}/\sigma_v$ and on σ_v, computed using equations (5.14) are also reported. The amplitude of the peak-locking (coefficient A) appears smaller for $Re_\theta = 1300$ ($A = 0.09$) than for $Re_\theta = 2200$ ($A = 0.16$). The period, given by coefficient B, is of the order of 0.66 for both datasets. It can be related to the period in pixels T_{px} using the following formulae, where px_{obj} is the local spatial resolution in the wall-normal direction at $y^+ = 100$ and Δt is the time separation between the two laser cavities (cf table 3.2 in section 3.2):

$$T_{px} = \frac{1/B\sigma_{ui}\Delta t}{px_{obj}} \tag{5.15}$$

It was checked that the period is close to 1 pixel, as expected for the peak-locking effect. The values of $\epsilon(\overline{u^1})/\sigma$ and $\epsilon(\overline{u^2})/\sigma$ show that bias on the moments of first and second order of v is negligible.

config (plane-resolution)	$Re_\theta = 1300$	$Re_\theta = 2200$
A	0.09	0.16
B	0.68	0.64
C	0.78	0.84
$\epsilon(\overline{u^1})/\sigma$	-2.67E-005	-1.24E-004
$\epsilon(\overline{u^2})/\sigma$	-1.11E-005	-3.25E-004

Table 5.3: Peak-locking effect on the in-plane non-stretched velocity component for the LTRAC database

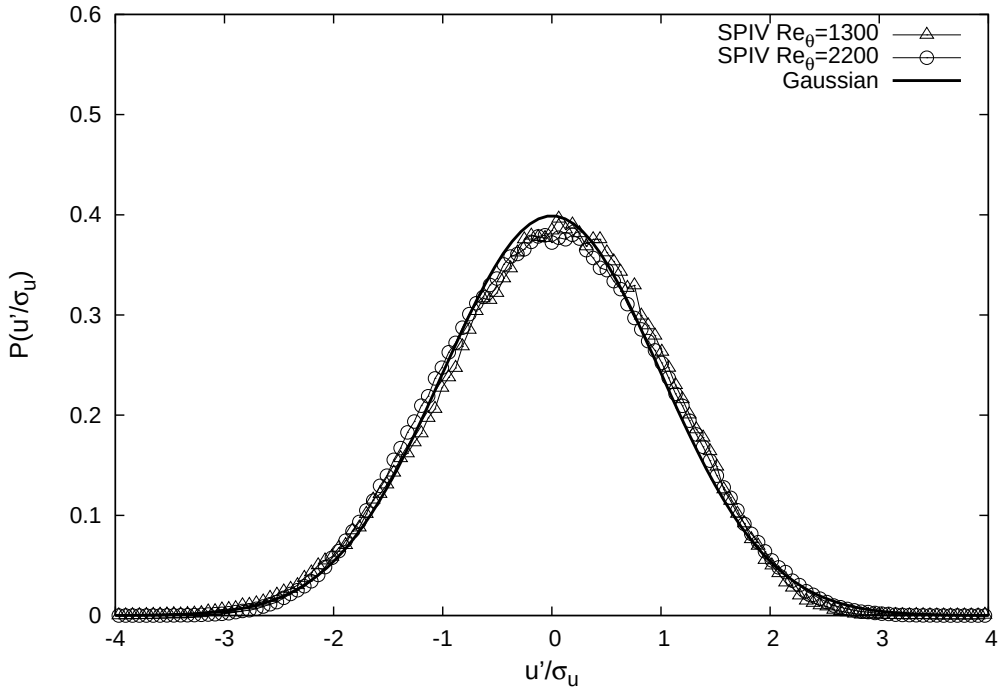

Figure 5.13: PDF of the streamwise fluctuations for the LTRAC database

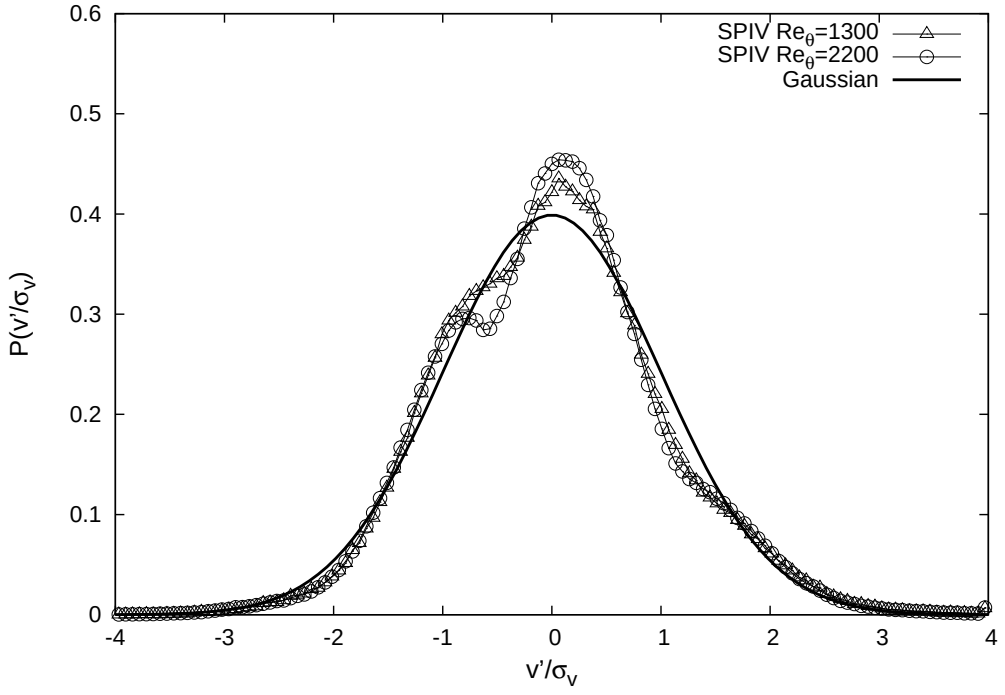

Figure 5.14: PDF of the wall-normal fluctuations for the LTRAC database

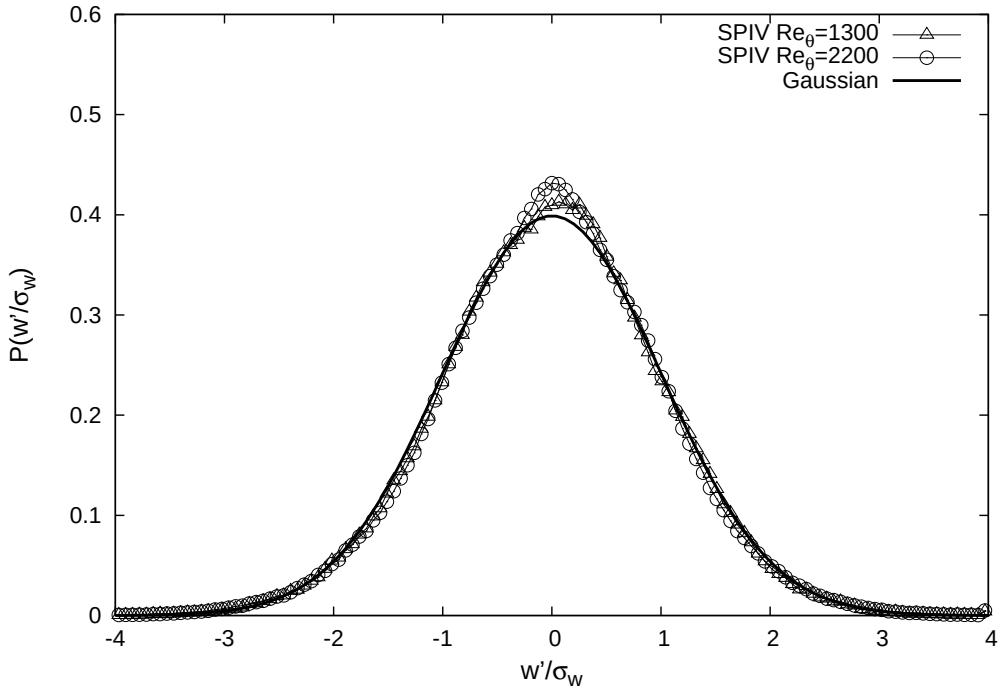

Figure 5.15: PDF of the spanwise fluctuations for the LTRAC database

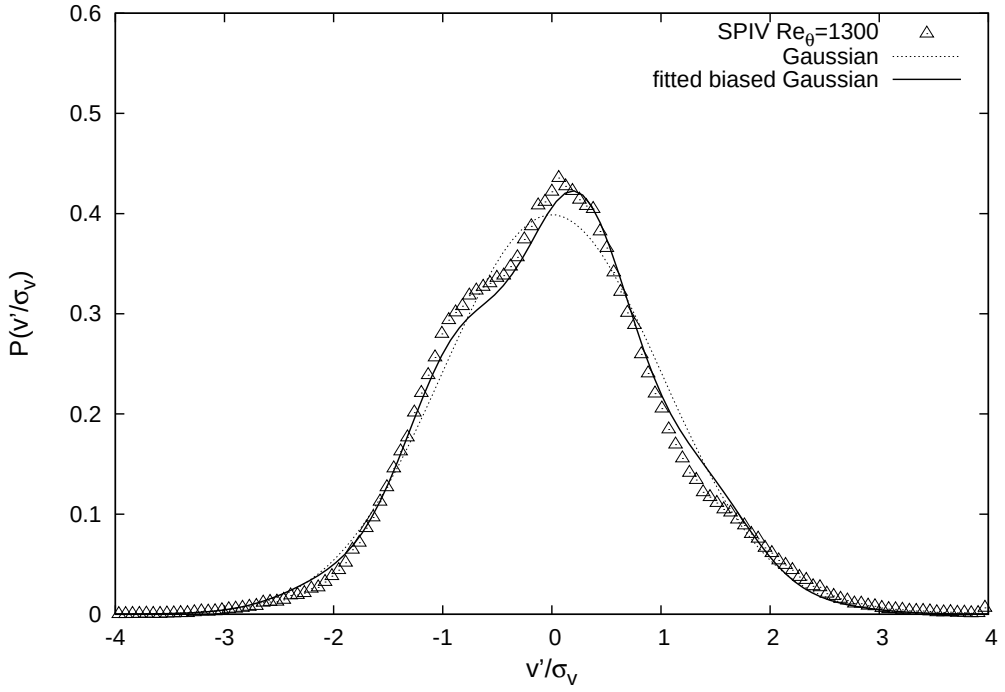

Figure 5.16: Modelling of the peak-locking effect for the LTRAC database

5.3.4 PDF for the LML database

The PDF of the normalized velocity fluctuations are computed at $y^+ = 100$ from the PIV datasets. At a given orientation of the measurement plane and spatial resolution, it was found that the behavior of these PDF was essentially the same for all Reynolds numbers. Hence, only the measurements at $Re_\theta = 10140$ are shown. For each measurement plane orientation (XY or YZ) and spatial resolution ($27\mu m/px$ and $67\mu m/px$), the PDF computed from PIV velocity fields are compared to those obtained from hot-wire anemometry measurements at $x = 19.6m$ (see table 4.2).

The PDF of the normalized streamwise fluctuations are shown in figure 5.18 for the XY plane and in figure 5.19 for the YZ plane. The peak-locking effect appears as small for the YZ plane, and more significant for the XY plane. The influence of the spatial resolution is not clearly visible on the amplitude of the peak-locking in the XY plane.

The PDF of the normalized spanwise fluctuations are shown in figure 5.20 for the XY plane and in figure 5.21 for the YZ plane. For this velocity component, it is the measurements in the YZ plane that are affected by peak-locking, the measurements in the XY plane showing a good agreement with hot-wire anemometry. The peak-locking look slightly stronger for the lower spatial resolution dataset ($67\mu m/px$) than for the higher one ($27\mu m/px$).

The PDF of the normalized wall-normal fluctuations are shown in figure 5.22 for both measurement planes. As can be seen, all PDFs are free from peak-locking effect. The agreement with hot-wire is quite good, except that the central peak, corresponding to the probability of having an instantaneous velocity equal to the mean velocity, is higher for PIV than for HW.

Finally, it can be said that, as already noticed for the LTRAC database, the out-of-plane velocity component (w for the XY plane, and u for the YZ plane) and the in-plane stretched velocity component (v for both planes) are globally unaffected by peak-locking. In contrast, the PDFs of the in-plane non-stretched velocity component (u for the XY plane, and w for the YZ plane) are affected by peak-locking. The methodology detailed in the previous paragraph can be used on this component to characterize this peak-locking and its effect on the statistics. This process is illustrated in figure 5.17. The PDF of u'/σ_u in the XY plane with a resolution of $67\mu m/px$ is plotted against a Gaussian distribution, to underline the effect of peak-locking. The model defined in (5.12), which represent a 'peak-locked' Gaussian, has been fitted to the PIV data. This 'peak-locked' Gaussian displays a good agreement with the PIV data. The equation defining the 'peak-locked' Gaussian has also been successfully fitted to the PDF of u in the XY plane with a resolution of $27\mu m/px$ and to the PDF of w in the YZ plane for both spatial resolutions. For each case, the values of the fitted coefficients A, B and C of the closest peak-locked Gaussian are compiled in table 5.4. The resulting bias on the mean and variance of the velocity component under interest (computed using (5.14)) are also reported.
The period of this 'peak-locked' Gaussian is given by coefficient B. It can be related to the period in pixels T_{px} using equation (5.15). It was checked that the value of B=1, common to all cases, corresponds to a period of 1 pixel, as expected for the peak-locking effect.
The coefficient A, which represents the amplitude of the peak-locking, is of particular

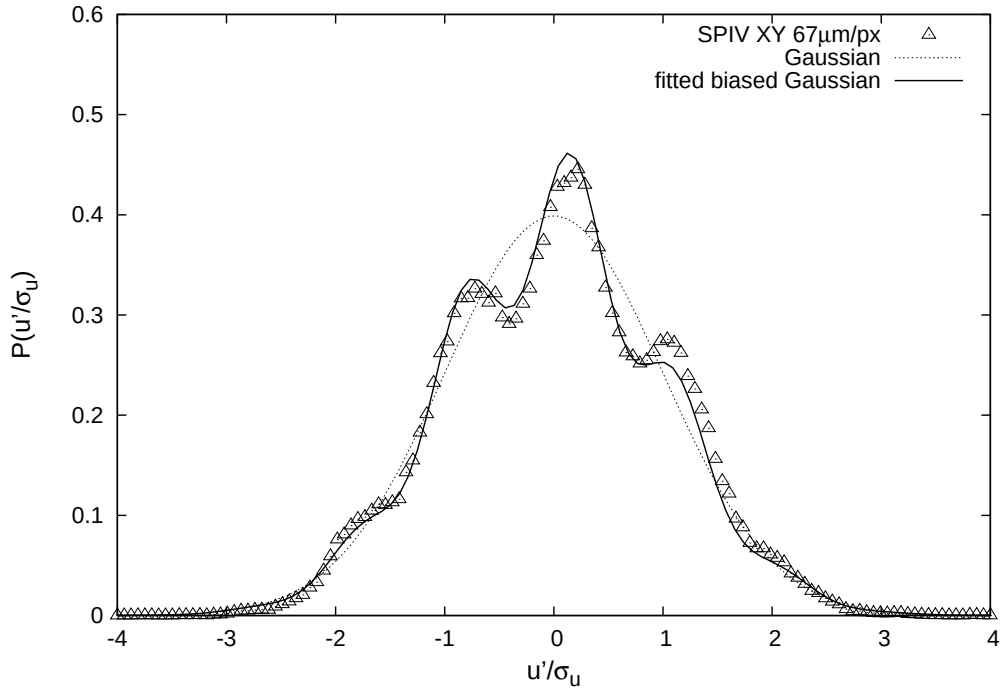

Figure 5.17: Modelling of the peak-locking effect for the streamwise component in the XY plane (LML)

interest. This amplitude is about 0.17 for the XY plane and lower spatial resolution in the YZ plane, and about 0.1 for the higher spatial resolution in the YZ plane. These values are comparable to those obtained for the LTRAC database. The fact that this peak-locking is less important for the highest spatial resolution in the YZ plane only was not accounted for. In all cases, the bias created by this peak-locking on the mean and variance of the in-plane non-stretched velocity component is negligible, even more than for the LTRAC database. The difference can be explained by the fact that, at $y^+ = 100$, the standard deviation of the wall-normal fluctuations (where the peak-locking occurs for the LTRAC database) is lower than the standard deviation of the streamwise fluctuations (where the peak-locking occurs for the LML database). Hence, v' is coded on a smaller number of pixels than u', and its moments are therefore more sensitive to peak-locking, as shown by Christensen (2004).

config (plane-resolution)	XY $27\mu m/px$	XY $67\mu m/px$	YZ $67\mu m/px$	YZ $27\mu m/px$
A	0.18	0.17	0.18	0.10
B	1.11	0.95	0.92	1.01
C	0.68	0.84	0.97	0.99
$\epsilon(\overline{u^1})/\sigma$	-1.26E-011	-4.38E-008	-4.29E-009	-2.25E-011
$\epsilon(\overline{u^2})/\sigma$	1.12E-010	-3.95E-007	-3.29E-007	-8.31E-009

Table 5.4: Peak-locking effect on the in-plane non-stretched velocity component for the LML database

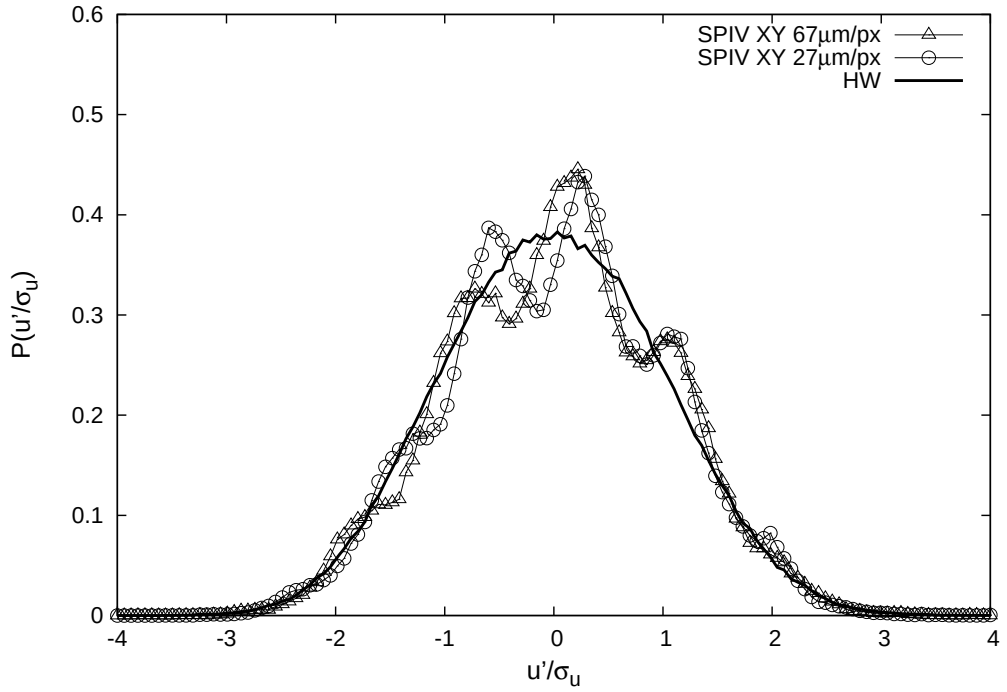

Figure 5.18: PDF of the streamwise fluctuations for the LML database in the XY plane

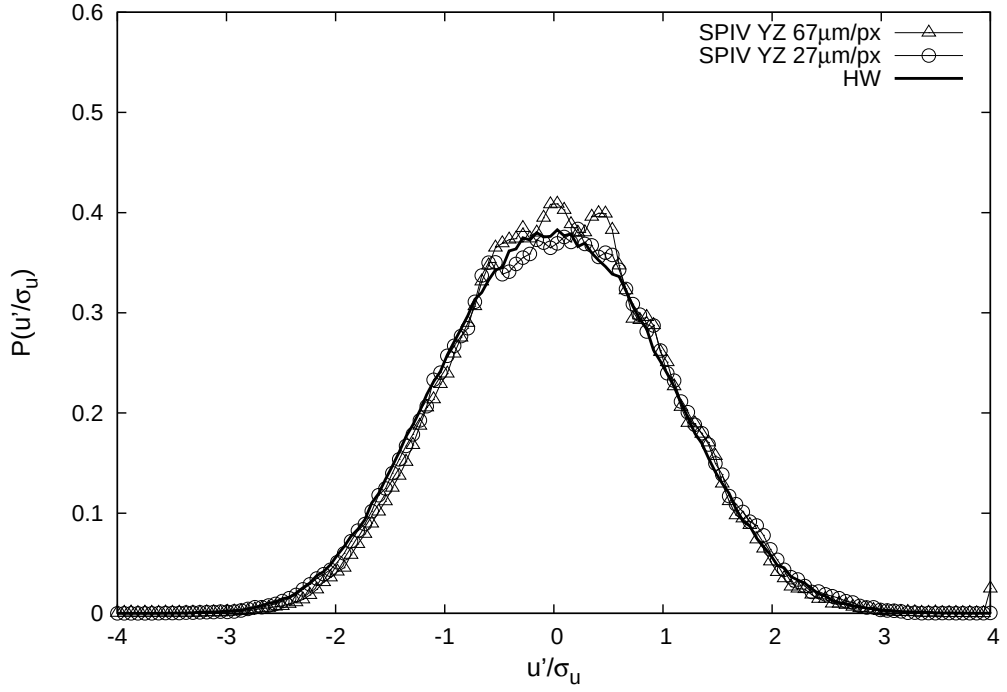

Figure 5.19: PDF of the streamwise fluctuations for the LML database in the YZ plane

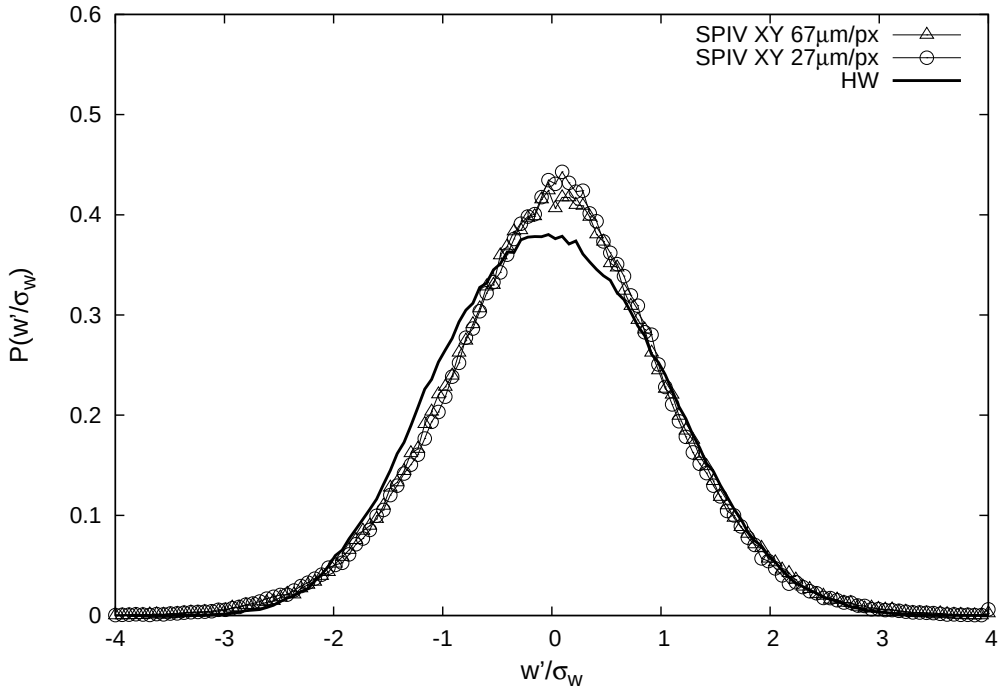

Figure 5.20: PDF of the spanwise fluctuations for the LML database in the XY plane

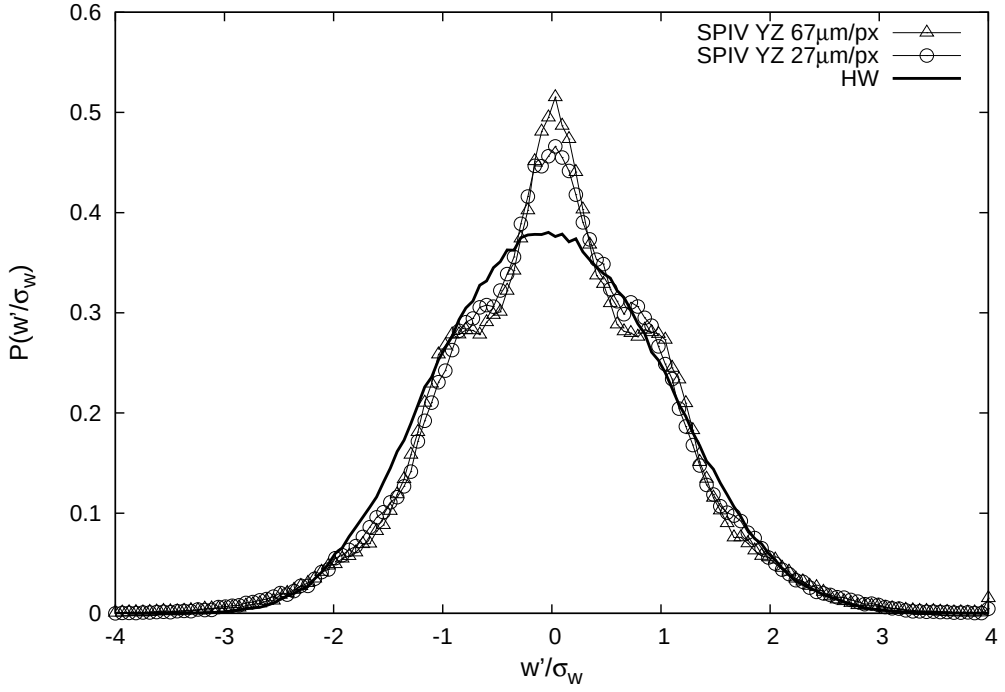

Figure 5.21: PDF of the spanwise fluctuations for the LML database in the YZ plane

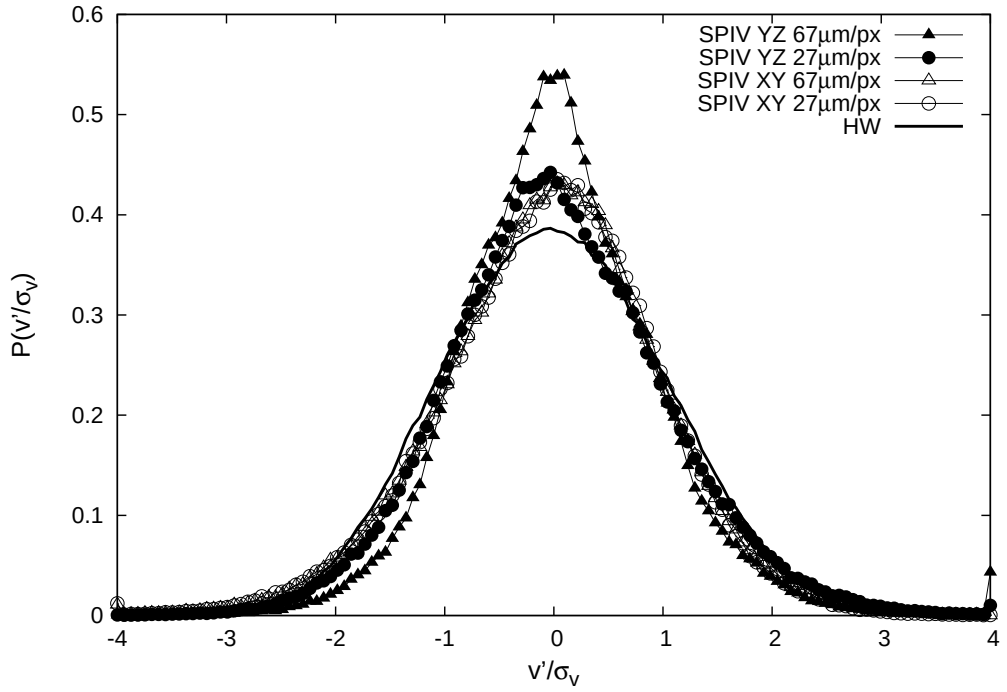

Figure 5.22: PDF of the wall-normal fluctuations for the LML database in the XY and YZ planes

5.4 Power spectra

5.4.1 Definition and estimation of the power spectra

Spectral analysis is a tool of special interest for the analysis of turbulence which is, in essence, a multi-scale phenomenon. The spectral tensor $\Phi_{ij}(k)$ represents the Reynolds stress density in the wave number space. Here we consider only the one-dimensional power spectra $E_{ii}(k_m)$ of the velocity component i along the homogeneous direction m. It is equal to twice the Fourier transform of the two-point correlation of velocity component i along direction m:

$$E_{ii}(k_m) = \frac{1}{\pi} \int_{-\infty}^{\infty} R_{ii}(r_m) e^{-ik_m r_m} dr_m \tag{5.16}$$

Perry et al (1986) derived similarity laws for the longitudinal power spectra ($m = x$), in the framework of the attached-eddy hypothesis. For a probe positioned at a height y, they identified three regions in the wave-number space where E_{11} can be non-dimensionalized with an appropriate scaling:

- the 'outer scaling' in the low wavenumber range:

$$g_1(k_1\delta) = \frac{E_{11}(k_1\delta)}{u_\tau^2} = \frac{E_{11}(k_1)}{u_\tau^2 \delta} \tag{5.17}$$

- the 'inner scaling' in the intermediate wavenumber range:

$$g_2(k_1 y) = \frac{E_{11}(k_1 y)}{u_\tau^2} = \frac{E_{11}(k_1)}{u_\tau^2 y} \tag{5.18}$$

- the 'Kolmogorov scaling' in the high wavenumber range:

$$g_3(k_1 \eta) = \frac{E_{11}(k_1 \eta)}{v^2} = \frac{E_{11}(k_1)}{v^2 \eta} \tag{5.19}$$

These regions, and their respective scaling are shown in figure 5.23.

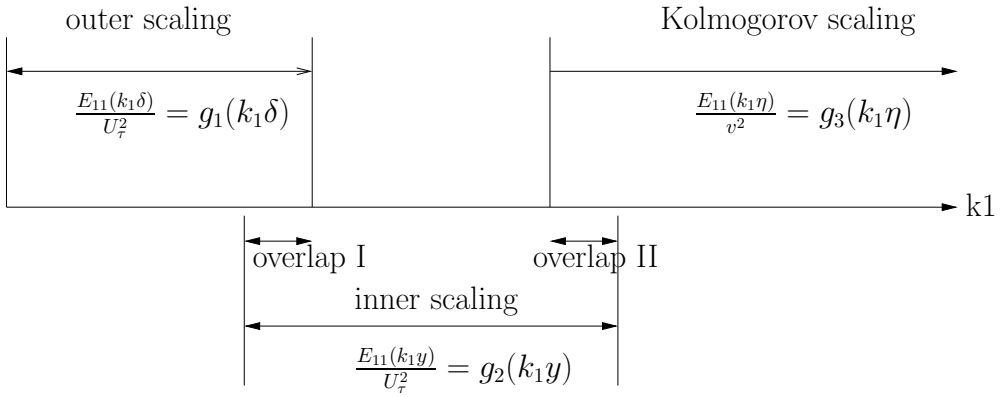

Figure 5.23: Different wavenumber ranges of the E_{11} spectra, and associated scaling

From the assumption that there exist an overlap between the "'outer-flow"'scaling and the "'inner-flow"' scaling (overlap I), and between the "'inner-flow"' scaling and the "'Kolmogorov"' scaling (overlap II), two power laws can be derived for the spectra. In inner scaling it reads:

$$\frac{E_{11}(k_1 y)}{U_\tau^2} = \frac{A_1}{k_1 y}$$
$$\frac{E_{11}(k_1 y)}{U_\tau^2} = \frac{A_2}{(k_1 y)^{5/3}}$$

These regions appear as lines of slope -1 and -5/3 on log-log spectra plot in inner scaling. Region of overlap II is sometimes also called the *inertial subrange*. Perry et al (1986) indicate that the same analysis can be carried on the w motions and yields similar results (existence of 2 regions of overlap). On the other hand, the v motions are not expected to exhibit an outer-flow scaling law, and as a result only one region of overlap (of slope -5/3) should exist in the $E_{22}(k_1)$ spectra.

The power spectra $E_{ii}(k_m)$ are computed from the SPIV datasets as the product of the Fourier transform of velocity component i along direction m with its conjugate, divided by the extent of the field (in direction m):

$$E_{ii}(k_m) = \frac{1}{L_m} F_m(u_i)\overline{F_m(u_i)} \tag{5.20}$$

The Fourier transform are evaluated using a periodization of the velocity field and an FFT algorithm (Foucaut et al (2004)). The spectra are averaged over the number of realizations and over the homogeneous directions of the flow field (at the exception of the direction along which the spectrum was computed).

The effect of the PIV spatial averaging (which tends to attenuate the signal) and of the measurement noise (which tends to add up to the signal) on the power spectra has been described in section 2.3.3. In particular a methodology to retrieve the non-dimensional cut-off wavenumber $\tilde{k}_{SNR=1}$ at a signal-to-noise ratio of 1 has been derived (see also Herpin et al (2008)). This wavenumber can be related to the size of a structure that will be resolved with a signal-to-noise ratio of 1 using equation (2.14).

5.4.2 Power spectra of the LTRAC database

The longitudinal power spectra for the u, v and w velocity components at $y^+ = 100$ are shown in figures 5.24, 5.25 and 5.26 respectively, using an inner scaling (cf equation (5.18)). They are plotted against the power spectra computed from the DNS of channel flow at $Re_\tau = 950$ from DelAlamo et al (2006), already used for the validation of the Reynolds stresses.
As can be seen on the domain of definition of the SPIV and DNS spectra, the smallest wavenumber is retrieved with the DNS data, and the highest wavenumber is retrieved with the SPIV data. This is consistent with the characteristics of the DNS (cf table 5.2.2) and with the characteristics of the SPIV datasets (cf table 3.5): the streamwise extent of the DNS domain (non dimensionalized with the half channel height h) is 10 times longer than the streamwise extent of the SPIV dataset at $Re_\theta = 2200$, and 6 times longer than the streamwise extent of the SPIV dataset at $Re_\theta = 1300$ (non-dimensionalized with the boundary layer thickness δ); on the other hand, the longitudinal spatial resolution is better for the SPIV datasets ($\Delta x^+ = 4.5$) than for the DNS simulation ($\Delta x^+ = 11$).
The '-5/3' power law, derived by Perry et al (1986) in the framework of the attached eddy hypothesis, is also plotted for comparison. In the logarithmic representation, all the SPIV spectra tend to that slope in the inertial subrange, without exhibiting a clear region of constant slope, probably owing to the moderate Reynolds numbers of the flow under investigation: Perry et al (1986) showed that the extent of this region decreases with decreasing Reynolds number.
For each of the three velocity components, the spectra of the two SPIV datasets fall into a close vicinity, and are in excellent agreement with the DNS spectrum at low and moderate wavenumber. However, in the high wavenumber domain, the PIV spectra present a spurious lift-up with respect to the DNS spectra. This effect is due to the PIV measurement noise.
Following the methodology described in section 2.3.3, the cut-off wavenumbers $k_{SNR=1}$, and the radius of the smallest resolvable radius $r^+_{SNR=1}$ (at a signal-to-noise ratio of 1) are retrieved for the three velocity components and for the two SPIV datasets. As the values $\tilde{k}_{SNR=1}$ are comparable for the two datasets, only one of them is reported on each figure. The values of $\tilde{k}_{SNR=1}$ and of $r^+_{SNR=1}$ are compiled in table 5.5. Comparing the cut-off wavenumbers of the three velocity components, we find that:

$$\tilde{k}_{SNR=1}(w) \leq \tilde{k}_{SNR=1}(u) \leq \tilde{k}_{SNR=1}(v)$$

This ordering is consistent with the level of measurement uncertainty that was found on the three velocity components (cf table 3.3):

$$\sigma(\epsilon_v) \leq \sigma(\epsilon_u) \leq \sigma(\epsilon_w)$$

Based on an average between the three velocity components, the smallest resolvable structure (at a SNR of 1) will have a radius of $r^+ = 23.5 \pm 2$ for the two SPIV datasets.

	$Re_\theta = 1300$	$Re_\theta = 2200$
$\tilde{k}_{SNR=1}$		
u	12.8	12.6
v	16.9	15.5
w	12.3	11.7
$r^+_{SNR=1}$		
u	24.5	24.5
v	18.5	20.5
w	25.5	27.0

Table 5.5: Values of $\tilde{k}_{SNR=1}$ and $r^+_{SNR=1}$ for the 3 velocity components for the LTRAC database

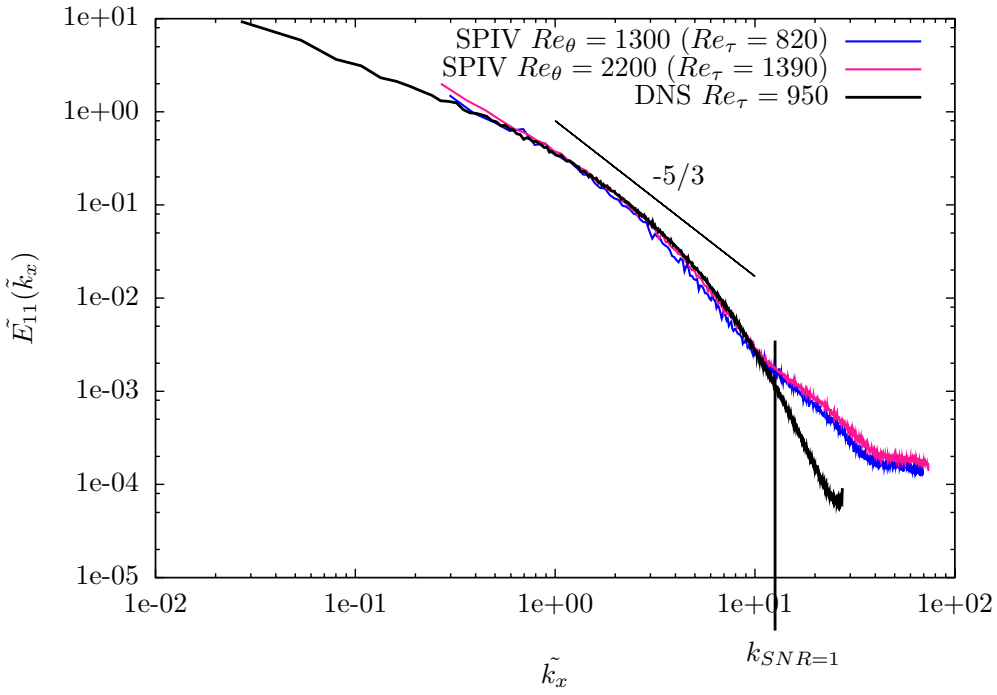

Figure 5.24: LTRAC longitudinal power spectra for the u component at $y^+ = 100$, compared with the DNS spectrum from DelAlamo et al (2006)

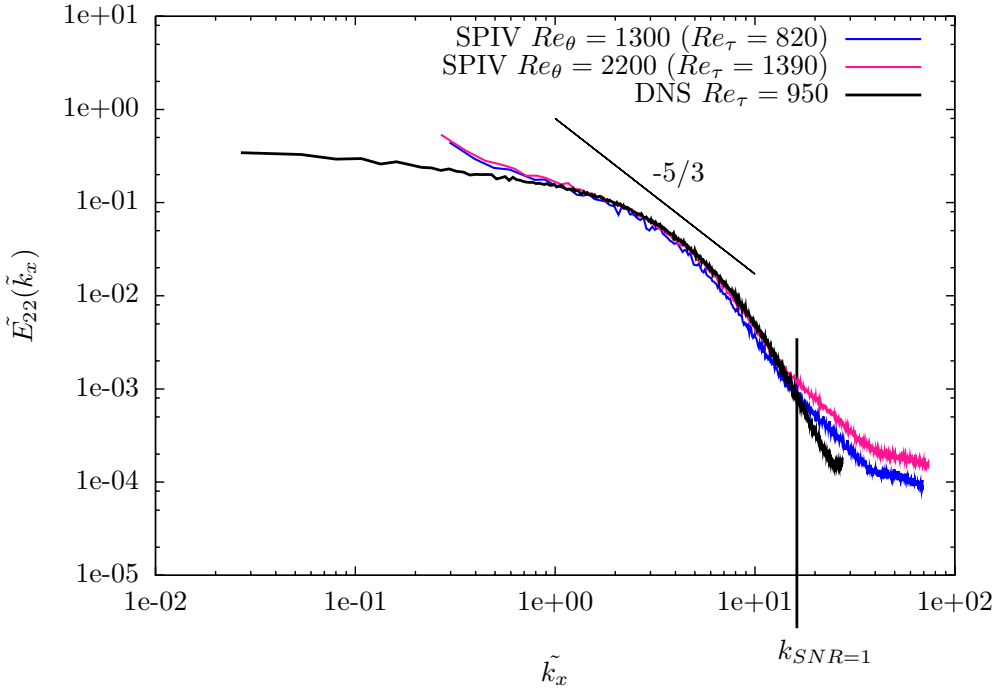

Figure 5.25: LTRAC longitudinal power spectra for the v component at $y^+ = 100$, compared with the DNS spectrum from DelAlamo et al (2006)

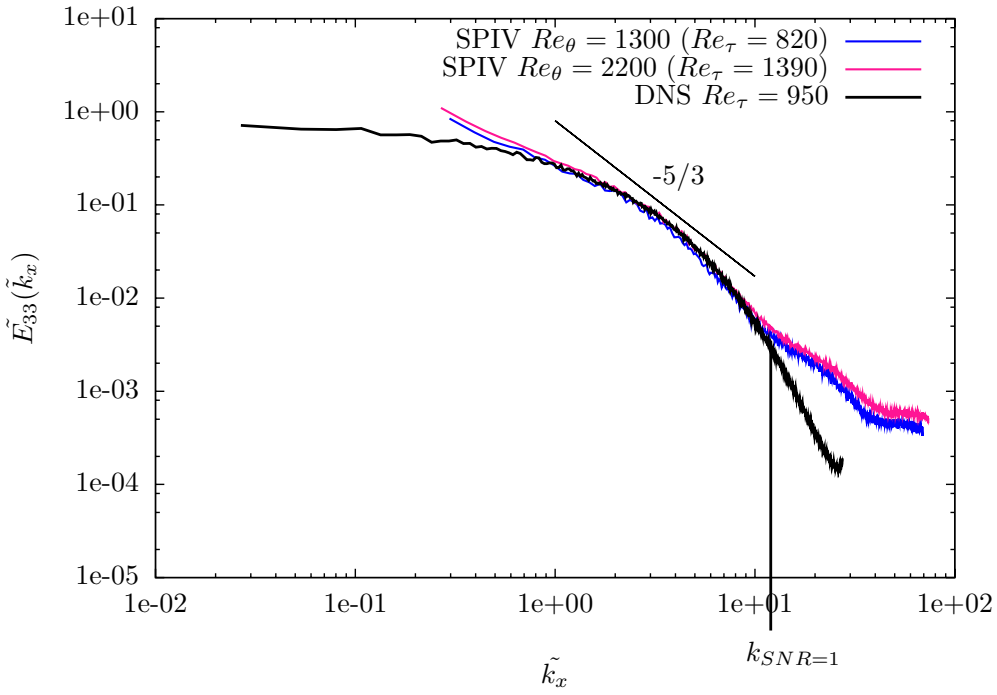

Figure 5.26: LTRAC longitudinal power spectra for the w component at $y^+ = 100$, compared with the DNS spectrum from DelAlamo et al (2006)

5.4.3 Power spectra of the LML database

The longitudinal power spectra of the SPIV measurements in the LML wind-tunnel can be compared either with the power spectra of the hot-wire measurements, or with the power spectra of the DNS by DelAlamo et al (2006). At first, the power spectra from these two possible references are compared with each other, in order to select the most appropriate reference for the power spectrum of the flow. These spectra are plotted in figure 5.27 at $y^+ = 100$ in inner scaling. As can be seen, in spite of the differences in Reynolds number (from $Re_\tau = 950$ for the DNS up to $Re_\tau = 6860$ for the highest Reynolds number of the wind-tunnel), there is a good collapse of the spectra for $\tilde{k} \leq 14$. It is of interest to note that this value of $\tilde{k}$ is inside the range of cut-off values found for the LTRAC dataset ($11.7 \leq \tilde{k}_{SNR=1} \leq 16.9$). For $\tilde{k} \geq 14$, the hot-wire spectra are affected by measurement uncertainty, especially in the lower Reynolds number range ($Re_\tau \in [2590; 3620]$). This is due to the fact that the gain and the offset of the hot-wire measurements were kept constant over the whole measurement campaign, and therefore the uncertainty in volts represents a higher percentage of the velocity in the lower Reynolds number range. Clearly, the hot-wire spectra cannot be used as a reference because of this measurement uncertainty. In the following, we will use the spectra computed from the DNS by DelAlamo et al (2006) as reference to retrieve $k_{SNR=1}$ of the Lille SPIV spectra, both in the longitudinal and spanwise directions.

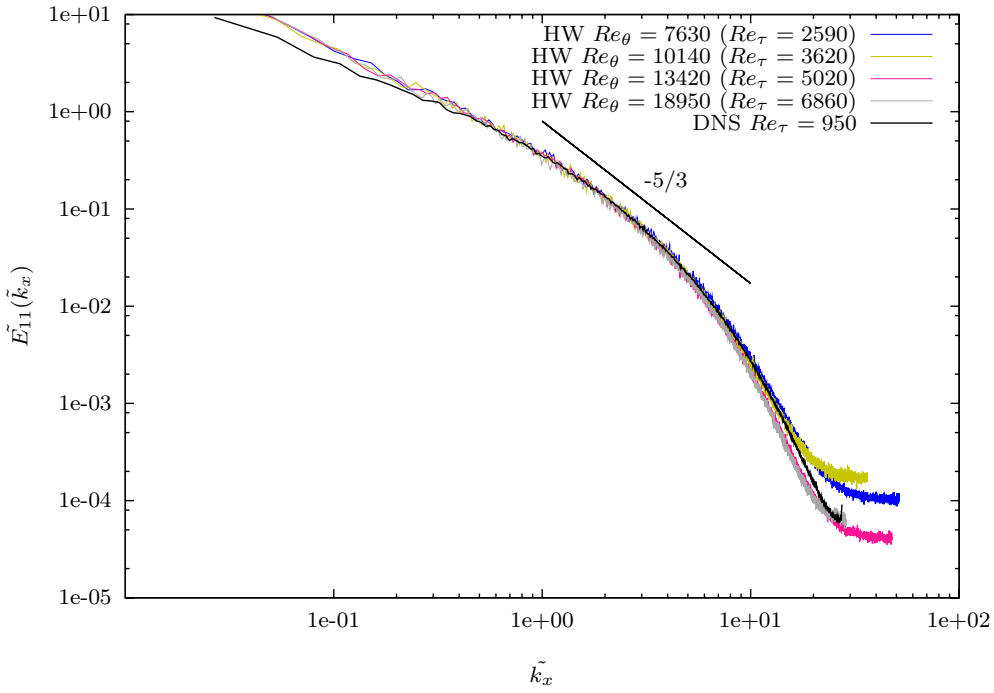

Figure 5.27: Comparison of the HW spectrum with the DNS spectrum from DelAlamo et al (2006) for the u component, at $y^+ = 100$

The longitudinal power spectra for the u, v and w velocity components in the XY plane at $y^+ = 100$ are shown in figures 5.28, 5.29 and 5.30 respectively, and the spanwise power spectra for the u, v and w velocity components in the YZ plane at $y^+ = 100$ are shown in figures 5.31, 5.32 and 5.33 using an inner scaling (cf equation (5.18)). Looking at the domain of definition of the spectra, the smallest wavenumber is retrieved with the DNS data, and the highest wavenumber is retrieved with the SPIV data. This is consistent with the characteristics of the DNS (cf table 5.2.2) and with the characteristics of the SPIV datasets (cf table 4.7).

All the SPIV spectra are in good agreement with the DNS spectra at low and intermediate wavenumbers. In the high wavenumber domain, the effect of measurement noise is clearly visible, with a spurious lift-up of the SPIV spectra. For the measurements in the XY plane (figures 5.28, 5.29 and 5.30), the larger the interrogation window size (cf table 4.7), the larger the effect of spatial averaging in the high wavenumber domain (cf equation (2.12)), and therefore the closest the SPIV spectra appears to be to the DNS spectrum. This should not be interpreted as a better restitution of the spectrum of the flow with larger IWs, because in fact both the signal and the noise are averaged over the interrogation spot. Applying the methodology described in paragraph 2.3.3, the cut-off wavenumbers $\tilde{k}_{SNR=1}$, and the radius of the smallest resolvable vortex $r^+_{SNR=1}$ (at a signal-to-noise ratio of 1) are retrieved for the four Reynolds numbers and in both measurements planes. These values are compiled in table 5.6 for the XY plane, and in table 5.7 for the YZ plane. As one can see, the highest cut-off wavenumbers are indeed obtained for the datasets where the interrogation window was the smallest (that is $Re_\theta = 10140$ with a spatial resolution of $27\mu m/px$).

On the whole, the cut-off wavenumbers in the x direction (retrieved with the XY planes) and in the z direction (retrieved using the YZ planes) are comparable, with an average value around $\tilde{k}_{SNR=1} \approx 14.5$. This average cut-off wavenumber leads to a smallest resolvable vortex (at a SNR=1) with a radius on the order of $r^+ = 21.7$. This size is slightly better than, but on the same order as, the size obtained for the LTRAC datasets ($r^+ = 23.5$). Among the three velocity components, no clear trend for the ordering of $\tilde{k}_{SNR=1}$ exists in the XY plane, however, in the YZ plane, it is the out-of-plane velocity component u that possess the highest cut-off wavenumbers for all Reynolds numbers. It is consistent with the ordering of the measurement uncertainties in table 4.4 (although it was not clear why the u component for the measurement in the YZ plane is less impacted by measurement noise, since the stereo angle of $\theta = 45°$ should lead to isotropic measurement noise).

config.(plane-R_θ)		$XY-7630$	$XY-10140$ $67\mu m/px$	$XY-10140$ $27\mu m/px$	$XY-13420$	$XY-18950$
$\tilde{k}_{SNR=1}$						
	u	14.8	12.0	17.9	15.4	12.9
	v	14.5	11.3	15.4	14.1	12.1
	w	16.1	12.6	16.5	15.0	13.2
$r^+_{SNR=1}$						
	u	21.4	26.2	17.6	20.4	24.4
	v	21.7	27.8	20.4	22.3	26.0
	w	19.5	24.9	19.0	20.9	23.8

Table 5.6: Values of $\tilde{k}_{SNR=1}$ and $r^+_{SNR=1}$ for the 3 velocity components in the XY plane for the LML database

config.(plane-R_θ)		$YZ-7630$	$YZ-10140$ $67\mu m/px$	$YZ-10140$ $27\mu m/px$	$YZ-13420$	$YZ-18950$
$\tilde{k}_{SNR=1}$						
	u	16.0	11.3	20.0	16.2	14.4
	v	15.4	11.0	19.1	15.7	13.7
	w	14.5	10.8	16.4	13.7	12.7
$r^+_{SNR=1}$						
	u	19.7	21.8	15.7	19.4	21.8
	v	20.4	28.6	16.6	20.0	22.9
	w	21.7	29.1	19.2	22.9	24.7

Table 5.7: Values of $\tilde{k}_{SNR=1}$ and $r^+_{SNR=1}$ for the 3 velocity components in the YZ plane for the LML database

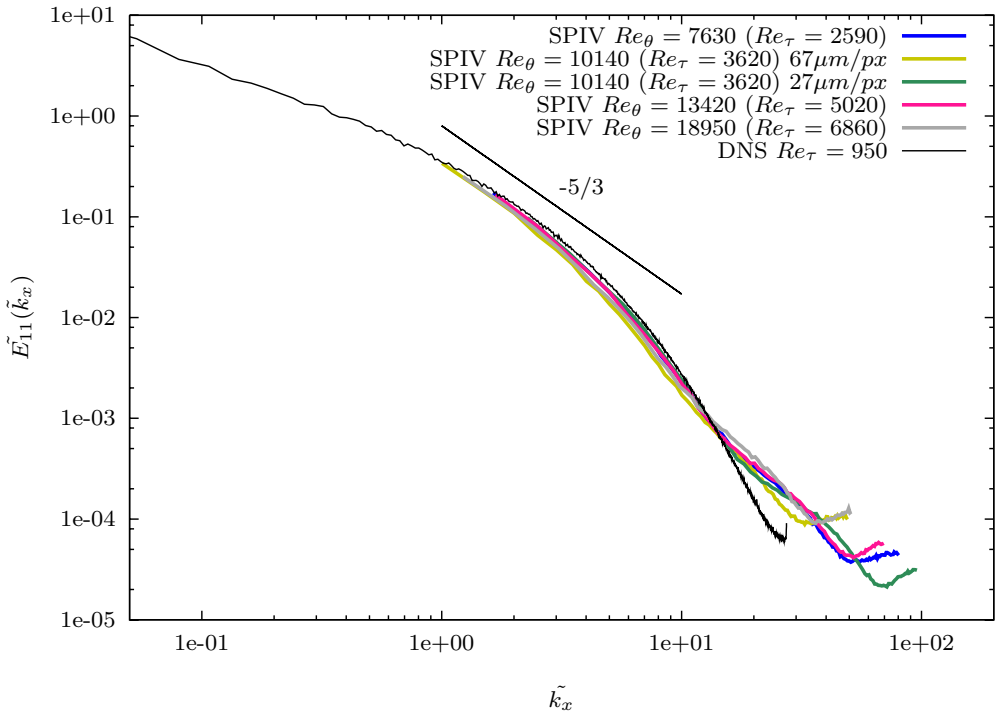

Figure 5.28: LML longitudinal power spectra for the u component in the XY plane at $y^+ = 100$, compared with the DNS spectrum from DelAlamo et al (2006)

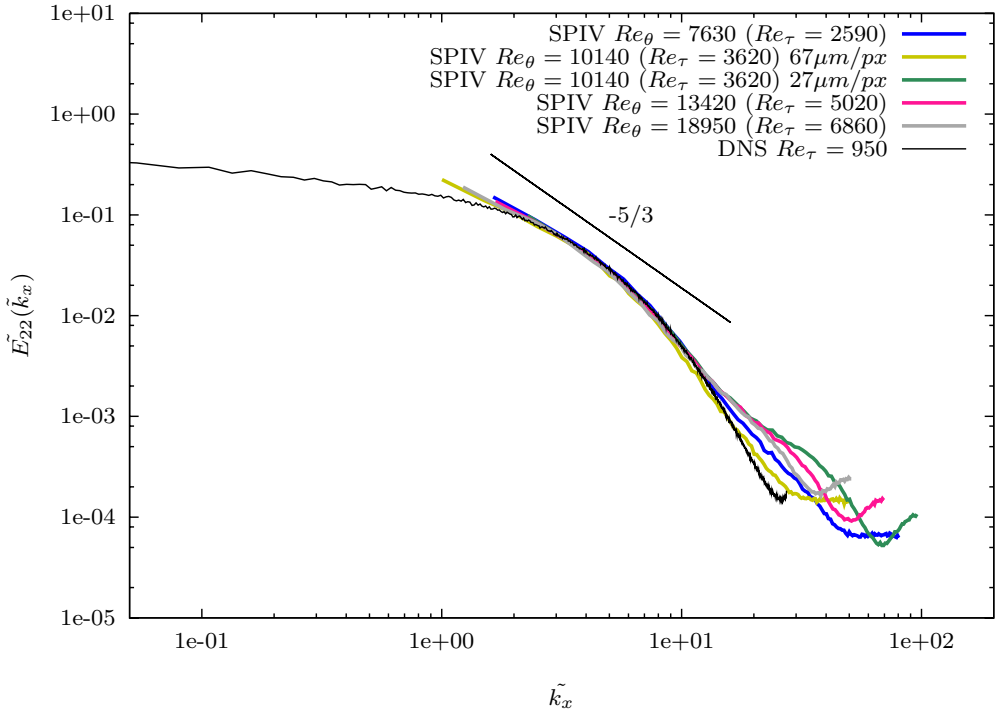

Figure 5.29: LML longitudinal power spectra for the v component in the XY plane at $y^+ = 100$, compared with the DNS spectrum from DelAlamo et al (2006)

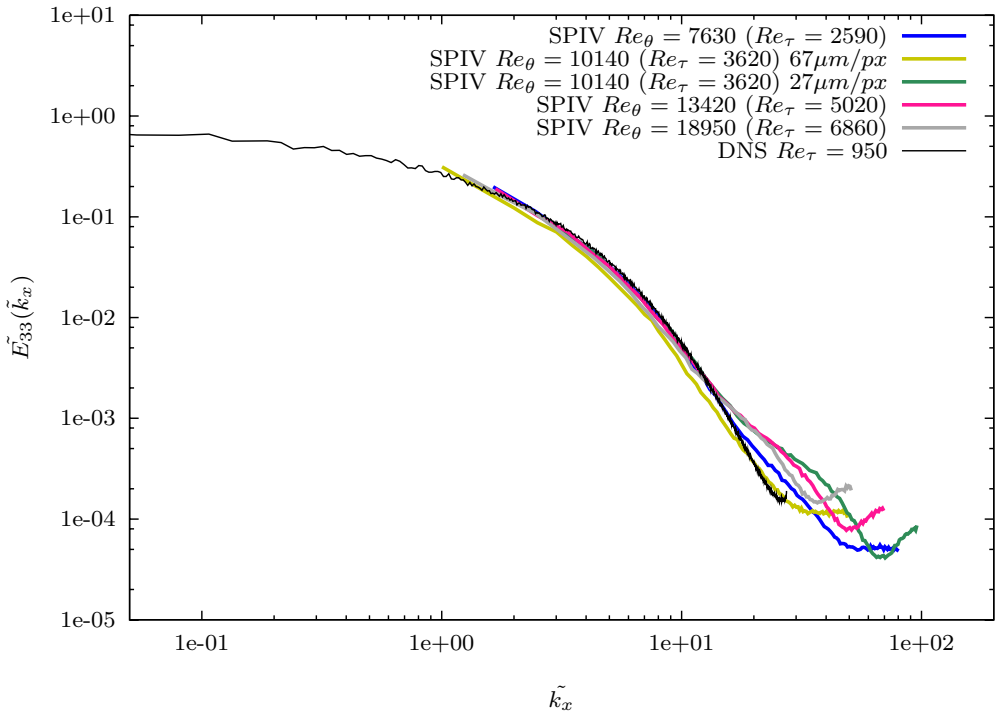

Figure 5.30: LML longitudinal power spectra for the w component in the XY plane at $y^+ = 100$, compared with the DNS spectrum from DelAlamo et al (2006)

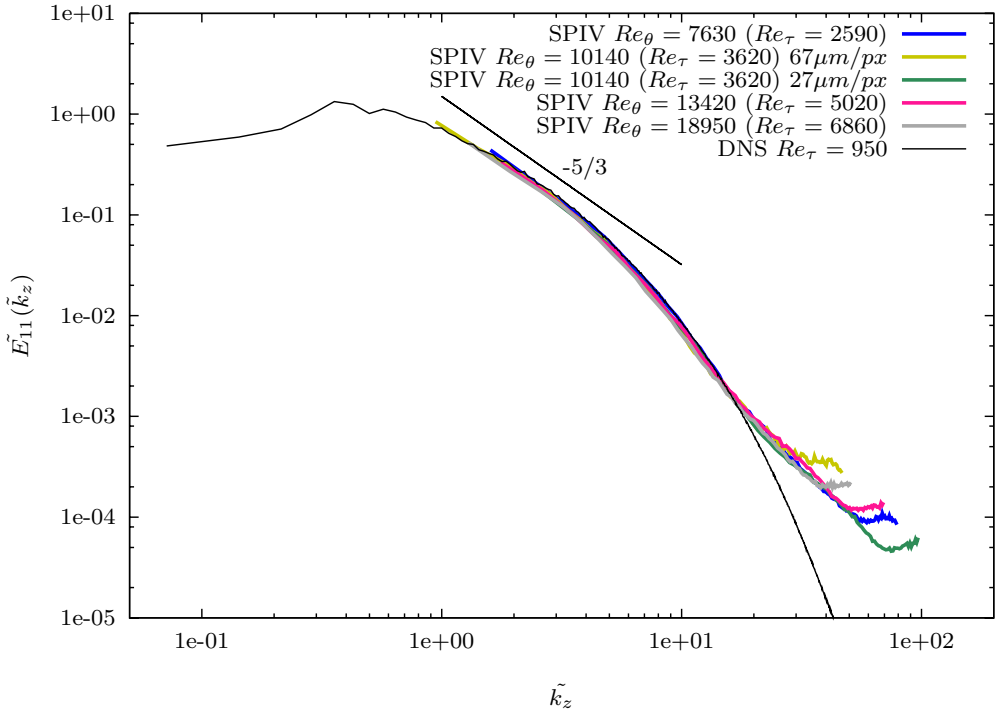

Figure 5.31: LML spanwise power spectra for the u component in the YZ plane at $y^+ = 100$, compared with the DNS spectrum from DelAlamo et al (2006)

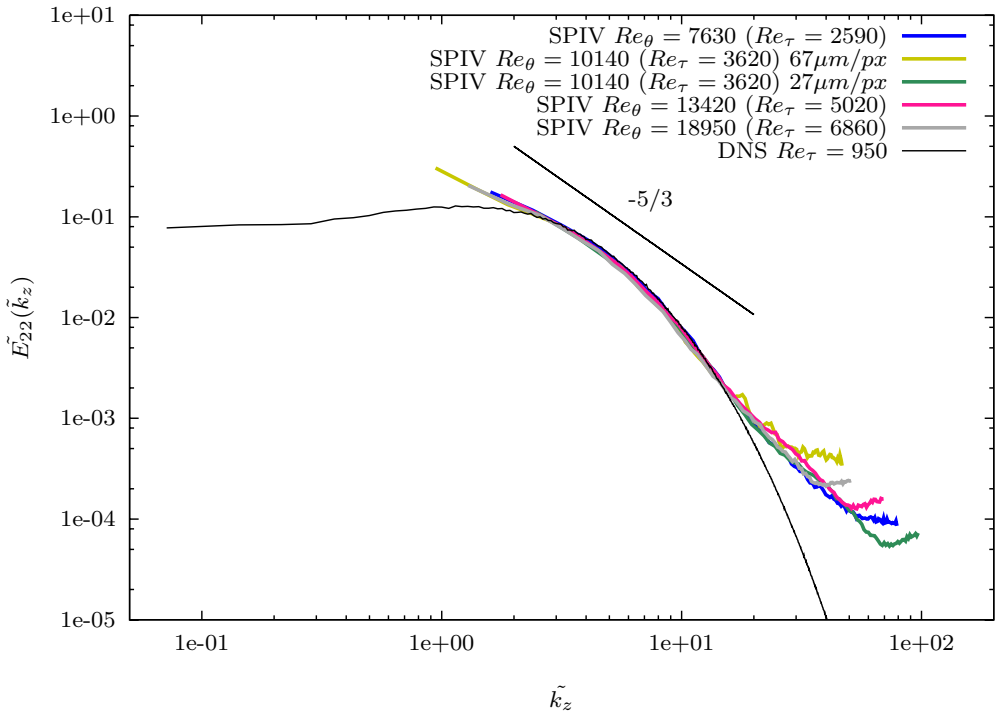

Figure 5.32: LML spanwise power spectra for the v component in the YZ plane at $y^+ = 100$, compared with the DNS spectrum from DelAlamo et al (2006)

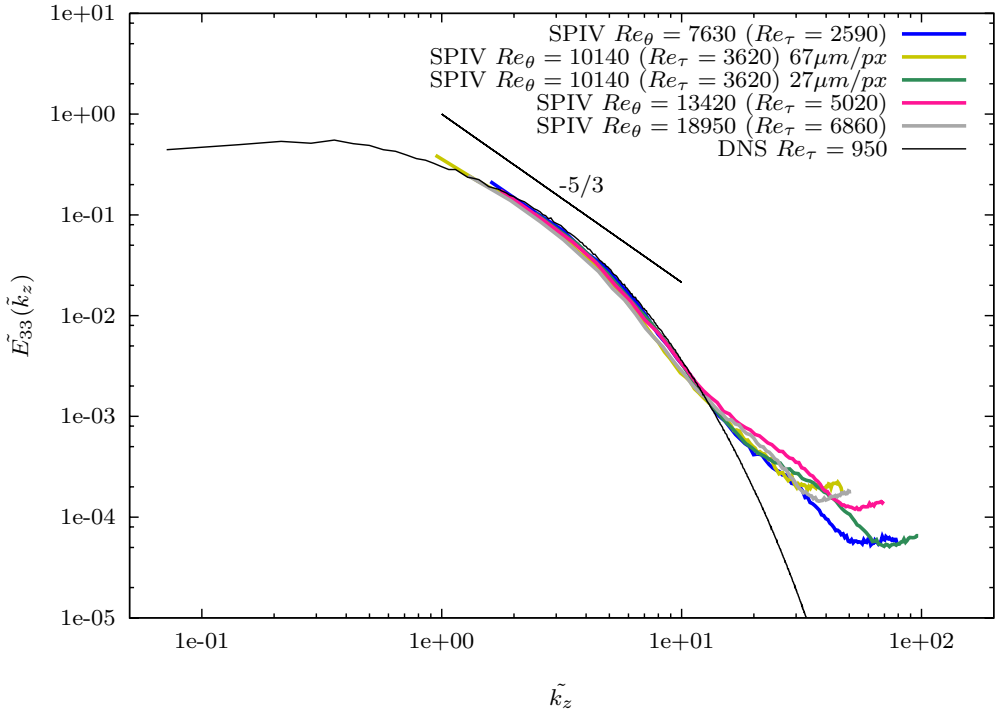

Figure 5.33: LML spanwise power spectra for the w component in the YZ plane at $y^+ = 100$, compared with the DNS spectrum from DelAlamo et al (2006)

5.5 Dissipation and Kolmogorov scales

5.5.1 Definition

In turbulence, motions exist in a wide range of sizes. However, the size of the small scale motions admits a lower bound, which is fixed by the viscosity: when the Reynolds number associated to the small scale structures becomes small enough, then all the kinetic energy of the structure is dissipated into heat under the action of viscosity. The characteristics length scale η, velocity scale v, and time scale τ of these smallest motions are called *Kolmogorov scales*.
The characteristic time scale τ is built from the mean turbulent dissipation rate ϵ and the viscosity ν:

$$\epsilon = \frac{\nu}{\tau^2} \tag{5.21}$$

The characteristics length scale η and velocity scale v are then given by the fact that the Reynolds number of the smallest motions is unity, and by homogeneity considerations:

$$\frac{v\eta}{\nu} = 1 \quad \text{and} \quad \tau = \frac{\eta}{v} \tag{5.22}$$

Equations (5.21) and (5.22) finally give the following expressions for the Kolmogorov scales:

$$\tau = \left(\frac{\nu}{\epsilon}\right)^{1/2} \quad \eta = \left(\frac{\nu^3}{\epsilon}\right)^{1/4} \quad v = (\nu\epsilon)^{1/4} \tag{5.23}$$

5.5.2 Computation of the dissipation

The computation of the Kolmogorov scales requires the knowledge of the dissipation rate ϵ of the turbulent kinetic energy. It will be called hereafter 'dissipation'. The dissipation is given by:

$$\epsilon = 2\nu < s'_{ij} s'_{ij} > \tag{5.24}$$

with s'_{ij} the symmetric part of the fluctuating velocity gradient tensor: $s'_{ij} = \frac{1}{2}\left(\frac{\partial u'_i}{\partial x_j} + \frac{\partial u'_j}{\partial x_i}\right)$.
The dissipation is a very hard quantity to measure, as all nine components of the fluctuating velocity gradient tensor must be known with sufficient accuracy. When the flow is homogeneous and isotropic, equation (5.24) reduces to:

$$\epsilon = 15\nu < \left(\frac{\partial u'_1}{\partial x_1}\right)^2 > \tag{5.25}$$

In fact, this approximation can be extended to locally isotropic flows, as suggested by Schlichting and Gersten (2001). Shear flows can be considered as locally isotropic in most of their domain, at the exception of regions in close proximity to walls.
Sometimes, dissipation is evaluated using another length scale called the Taylor micro scale λ, defined as:

$$\left(\frac{\partial u'_1}{\partial x_1}\right)^2 = 2\frac{u'^2_1}{\lambda_1^2}$$

This length is representative of the *most* dissipative motions. It can be retrieved using the osculating parabola to the two-points correlation coefficient of the streamwise velocity fluctuation:

$$R_{11}(\Delta x_1) = \frac{< u_1'(x_1) u_1'(x_1 + \Delta x_1) >}{< u_1'^2 >}$$

$$R_{11}(\Delta x_1)|_{\Delta x -> 0} = 1 - \frac{\Delta x_1^2}{\lambda_1^2}$$

In the local isotropy approximation, the dissipation ϵ can thus be computed using equation (5.26), with the Taylor micro scale evaluated using the second derivative of the two-points correlation coefficient at its origin (see equation (5.27)).

$$\epsilon = 30\nu \frac{< u_1'^2 >}{\lambda_1^2} \tag{5.26}$$

$$\lambda_1 = \sqrt{\frac{-2}{\frac{\partial R_{11}(\Delta x_1)}{\partial \Delta x_1}|_{\Delta x_1 = 0}}} \tag{5.27}$$

5.5.3 Profiles of ϵ and η for the LTRAC database

The dissipation of the LTRAC boundary layer was computed using the SPIV datasets acquired in the XY plane at $Re_\theta = 1300$ and $Re_\theta = 2200$, using the local isotropy hypothesis (see equation (5.26)). The Taylor microscale was evaluated at 18 wall-normal positions in the boundary layer (with a logarithmic distribution) from the longitudinal two-point correlation of the streamwise velocity fluctuations. A fourth order centred scheme was employed to compute the second derivative of the correlation function about its origin. The scheme takes into account the evenness of the streamwise correlation function; the point at $\Delta x = 0$ is not used in the stencil, as it may be contaminated with measurement noise (the points at $\Delta x \neq 0$ are assumed to be free from this effect, as the measurement noise is supposed to be incoherent in space).
The wall-normal evolution of the dissipation in the LTRAC boundary layer is shown in figure 5.34. It is plotted against the dissipation in a DNS of turbulent channel flow at $Re_\tau = 950$ (DelAlamo et al (2006)), computed using the 'exact' formula of the dissipation (see equation (5.24)). The Reynolds number of this DNS is quite close to that of the LTRAC dataset at $Re_\theta = 1300 \Leftrightarrow Re_\tau = 820$. It is of interest to note that the dissipation in the LTRAC dataset at $Re_\theta = 1300$ is in very good agreement with that of the turbulent channel flow, supporting the validity of the local isotropy approximation. The peak of ϵ at the wall, visible on the DNS dataset, is quite well captured with both datasets.
The Kolmogorov scales are retrieved from the profiles of ϵ using equations (5.23). The wall-normal evolution of the Kolmogorov length scale is plotted in figure 5.35 for the LTRAC and DNS datasets using a wall-unit scaling. Again, it can be seen that the agreement is excellent between the LTRAC dataset at $Re_\theta = 1300$ and the DNS dataset. All the profile collapse well near the wall $y^+ < 300$, but some difference between the dataset at $Re_\theta = 2200$ and the two others are visible further away from the wall. This is probably linked to Reynolds number effects.

5.5.4 Profiles of ϵ and η for the LML database

The dissipation and Kolmogorov length scale were computed on the datasets acquired in the XY planes of the LML database, using the same method as for the LTRAC database. The wall-normal evolution is shown in figure 5.36. It is plotted against the dissipation in a DNS of turbulent channel flow at $Re_\tau = 2000$ (DelAlamo et al (2006)), computed using the 'exact' formula of the dissipation (see equation (5.24)). The Reynolds number of that simulation is very close to that of the LML dataset at $Re_\theta = 7630$. Overall, the profiles of dissipation for the LML datasets is in good agreement with the DNS. The peak of ϵ at the wall, visible on the DNS dataset, is quite well captured by all the datasets, at the exception of the dataset at the highest Reynolds number ($Re_\theta = 18950$) and of the dataset with the lowest spatial resolution ($Re_\theta = 10140$ with $67\mu m/px$). These two datasets underestimate clearly this peak, owing to a lack of spatial resolution. Away from the wall ($y^+ >= 200$), the level of dissipation in the LML boundary layer is slightly higher than in the DNS of channel flow. As far as the dataset at $Re_\theta = 7630$ is concerned, this may by due to the fact that the free-stream velocity changed slightly during the acquisition, which results in artificially higher RMS value of u in the outer region of the flow (see figure 5.10, and related comments), and thus in a artificially higher value of dissipation. As for the other datasets, this difference in dissipation levels in the outer region of the flow may be due to Reynolds number effects. These dissipation profiles can be compared to the ones obtained by Stanislas et al (2008) for the same boundary layer, but using hot-wire anemometry. It appears that the dissipation is better estimated using the present PIV data, especially in the near-wall region.
The Kolmogorov scales are retrieved from the ϵ profiles using equations (5.23). The wall-normal evolution of the Kolmogorov length scale is plotted in figure 5.35 for the LML and DNS datasets using a wall-unit scaling. At the exception of the dataset at $Re_\theta = 10140$ with the lowest spatial resolution ($67\mu m/px$), the agreement between all the SPIV datasets and the DNS dataset is quite good in the inner layer ($y^+ \leq 300$). The differences further away from the wall are due to a combination of Reynolds number effect and spatial resolution effect.

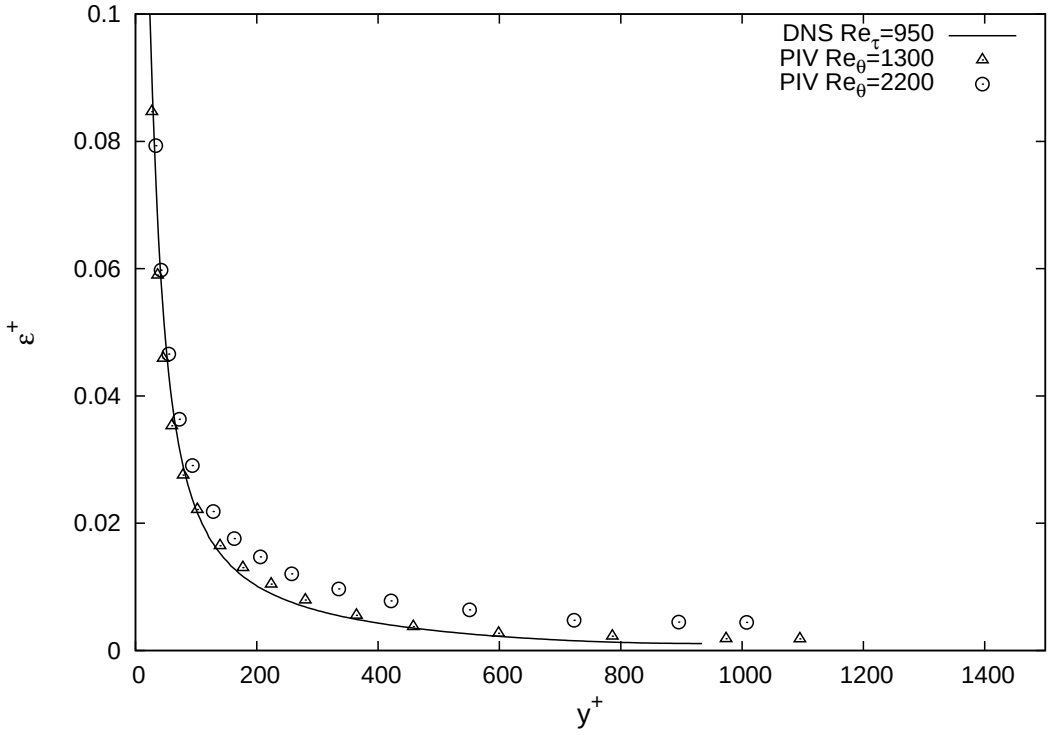

Figure 5.34: Wall-normal evolution of the mean dissipation (LTRAC database), in wall units

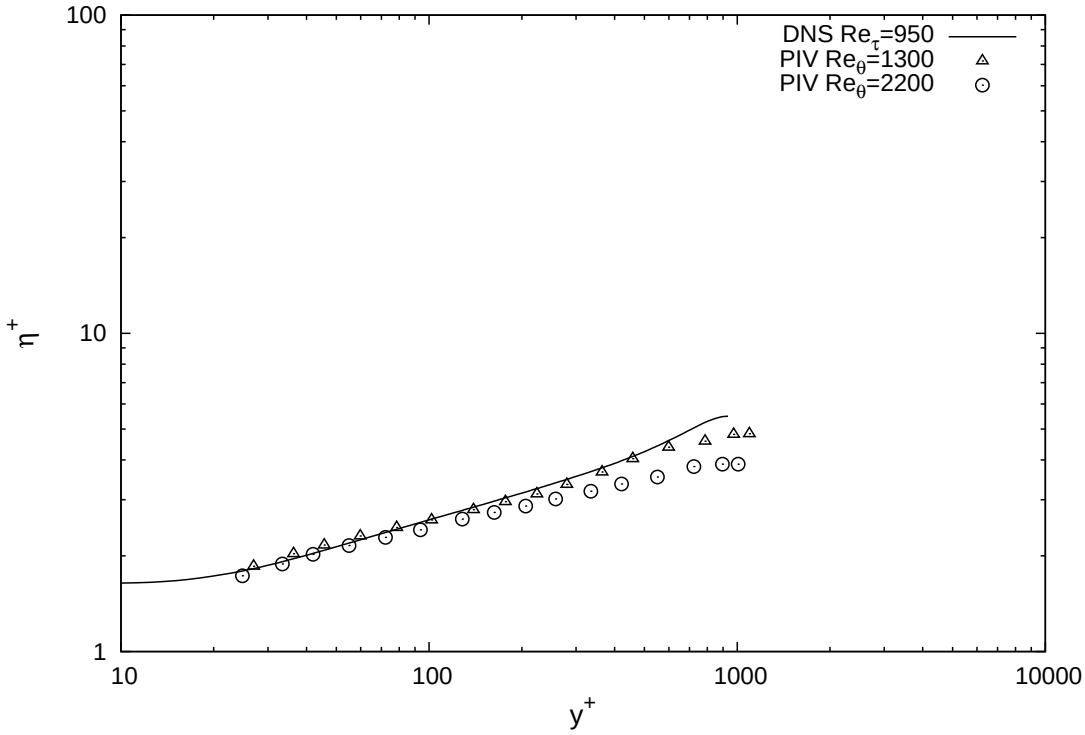

Figure 5.35: Wall-normal evolution of the Kolmogorov length scale (LTRAC database), in wall units

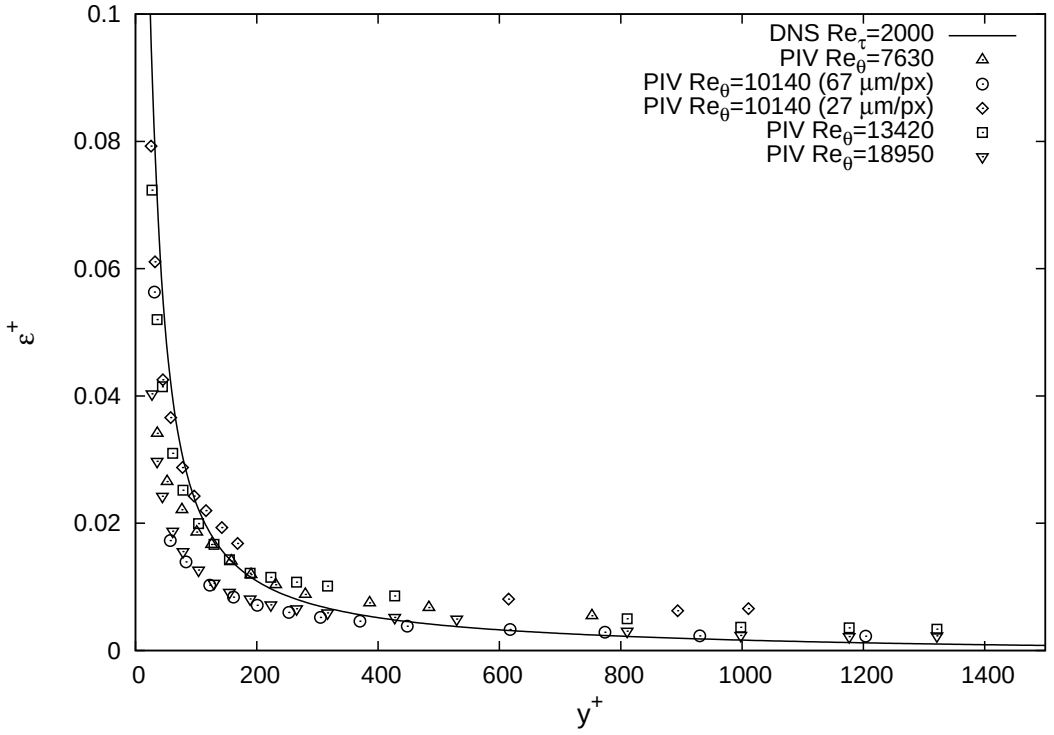

Figure 5.36: Wall-normal evolution of the mean dissipation (LML database), in wall units

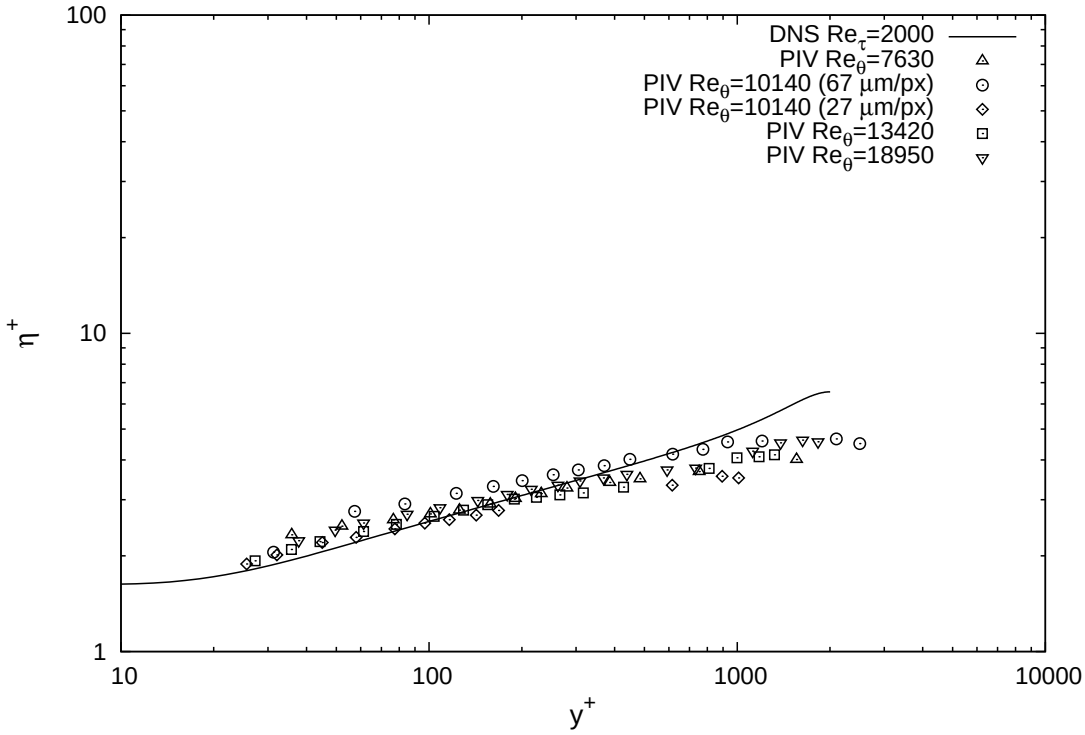

Figure 5.37: Wall-normal evolution of the Kolmogorov length scale (LML database), in wall units

Chapter 6

Coherent structures detection

6.1 Detection technique

6.1.1 Overview of the existing methods

The different methods for identifying vortex cores in velocity vectors fields obtained from PIV or DNS have been reviewed in great details by Jeong and Hussain (1995), Adrian et al (2000a) and Chakraborty et al (2005).
Some common intuitive criteria, such as vorticity isosurfaces and closed or spiraling streamlines and pathlines are in fact inadequate to detect vortices in turbulent boundary layers, as shown by Jeong and Hussain (1995): iso-vorticity surfaces fail to identify vortex cores in shear flows, whereas closed or spiraling streamlines and pathlines, which are not Galilean invariant, are unable to detect vortices convected at different speeds.
Local detection techniques based on the 3D velocity gradient tensor $A_{ij} = \frac{\partial u_i}{\partial x_j}$ (the Δ criterion Chong and Perry (1990), the Q criterion Hunt et al (1988)), or on the Hessian of the pressure (the λ_2 criterion of Jeong and Hussain (1995)) have been successfully used in a variety of flows, including turbulent boundary layers. Chakraborty et al (2005) have shown that all these methods are approximately equivalent.
The Δ criterion finds its origin in critical point analysis of the 3D velocity gradient tensor (Chong and Perry (1990)): this tensor has one real eigenvalue λ_r and a pair of complex conjugate eigenvalues $\lambda_{cr} \pm i\lambda_{ci}$ when the discriminant Δ of its characteristic equation is positive. When this condition is met, the particle trajectory about the eigenvector corresponding to λ_r have a swirling motion (Zhou et al (1999)). The imaginary part of the complex eigenvalues, λ_{ci} quantifies *the strength of this swirling motion*: the period required for a particle to complete one revolution about its axis is given by $2\pi/\lambda_{ci}$. The Δ criterion (positive discriminant of the characteristic equation) and the swirling strength criterion (non-zero λ_{ci}) are equivalent and reliable criteria for vortex identification (Zhou et al (1999)).
When the data is not volumetric, but only planar, 2D forms of the velocity gradient tensor can be used, as suggested by Adrian et al (2000a). Christensen and Adrian (2001), Tomkins and Adrian (2003), Hutchins et al (2005) and Stanislas et al (2008) used the 2D swirling strength to detect vortices in PIV planes of a turbulent boundary layer. Hutchins

et al (2005) studied the limits of the two-dimensional swirling strength, with respect to the full 3D form. The ratio $\lambda_{2D}/\lambda_{3D}$ was computed for different inclination angle α of a vortex (modelled with the Biot-Savart law) with respect to the measurement plane. This confirmed that vortices whose axis are perpendicular to the measurement plane will be successfully detected with the 2D approximation ($\lambda_{2D}/\lambda_{3D} = 1$ for $\alpha = 90°$), whereas the detection will fail when the vortex axis lies in the measurement plane ($\lambda_{2D}/\lambda_{3D} = 0$ for $\alpha = 0°$). The functional dependence of $\lambda_{2D}/\lambda_{3D}$ with α is found to be of cosine type; in particular, one gets $\lambda_{2D}/\lambda_{3D} = 0.5$ for an angle $\alpha = 30°$
Once a vortex has been detected using a detection function (such as the swirling strength, the Q criterion, etc...), it is of interest to retrieve the characteristics of this vortex (radius, circulation...). One method consist in fitting the velocity field surrounding the extrema of the detection function to a model vortex. The characteristics of the vortex are given by the fitted parameters of the model. This method has been employed by Carlier and Stanislas (2005) and Stanislas et al (2008) using as a model an Oseen vortex.

6.1.2 Methodology employed

The technique implemented to identify and to characterize vortices in the LML and LTRAC database consists of:

- the computation of a detection function,
- the localization of the extrema of this detection function and
- a fit of a model vortex to the velocity field surrounding the extrema of the detection function.

Details on each one of these three steps are now given.

Computation of a detection function

The detection function used to educt vortices in the LML and LTRAC database is a *smoothed* and *normalized* 2D swirling strength. This detection function is based on the 2D swirling strength defined in Adrian et al (2000a), but with a number of adaptations designed to prevent its contamination with the PIV measurement noise.
At first, the derivative scheme used to compute the 2D swirling strength was chosen with care. Raffel et al (1998) tested several derivation schemes and recommend a 2nd order scheme that minimizes the propagation of measurement noise. This scheme is referred to as the '2nd order least square' scheme. Foucaut and Stanislas (2002) realized a comparative study of the different derivation schemes (centered differences, compact differences, Richardson extrapolation, and least square) applied to PIV data. They considered the derivations schemes as filters, and recommended that the upper cut-off wavenumber of the filter corresponds to the cut-off wavenumber of the PIV data at a signal to noise ratio of 1. In this manner, the slope of the filter will cancel the noise amplification. The cut-off wavenumbers of the different derivative schemes, non-dimensionalized with the mesh

spacing, are given. The cut-off wavenumber of the PIV power spectra at a signal-to-noise ratio of 1 were computed in section 5.4, and it is therefore possible to determine the best-suited derivative scheme for our database. The average cut-off wavenumber was found to be:

$$\tilde{k} = ky \approx 14.5 \quad \Leftrightarrow \quad k\Delta x \approx 0.7$$

According to the findings of Foucaut and Stanislas (2002), this cut-off wavenumber corresponds to the one of the 2nd order least-square derivative scheme. The 2D swirling strength was therefore computed using this scheme. An example from a map of 2D swirling strength, computed on a velocity field of the LTRAC database at $Re_\theta = 2200$ is shown in figure 6.1. The same velocity field will be used throughout this section to illustrate the methodology used for the detection. Peaks of swirling strength allow the visualization of vortex cores. As one can see, the intensity of these peaks decreases with increasing wall-normal distance, as expected in wall-bounded turbulence (DelAlamo et al (2006)). Therefore structures at the wall and away from the wall cannot be visualized using the same surface levels, as already observed by Blackburn et al (1996)
In order to overcome this difficulty, a normalization is then applied to the detection function. The 2D swirling strength is divided by the wall-normal profile of its RMS value:

$$\bar{\lambda}_{ci}(x_{1/3}, x_2) = \frac{\lambda_{ci}(x_{1/3}, x_2)}{\lambda_{ci,RMS}(x_2)}$$

This type of normalization was first used by DelAlamo et al (2006) and Wu and Christensen (2006). It is illustrated in figure 6.2: the intensity of the detection function is now independent of wall-normal distance. Finally a 3*3 sliding average is applied to remove the remaining noise. The smoothed and normalized 2D swirling strength is visible in figure 6.3.

Localization of the extrema of the detection function

The local maxima of this detection function are then localized using an iterative process. It is important that one and only one extrema per vortex core is retrieved, as each extrema will be used as an initial guess for the center of a vortex. For this purpose, only the maxima whose neighborhood does not intersect with the neighborhood of the previously detected maxima are retained. This neighborhood is set to a square with sides of 7 mesh points. It ensures that the maxima will be separated from each other by no less than 6 mesh points. The maxima are retrieved in decreasing order of magnitude. The iterative process is stopped when the value of the maxima of the detection function becomes lower than a fixed threshold. In practice, a non-zero threshold of the detection function is often used, even with data that are free of measurement noise, because zero threshold leads to confusing results in which all the vortices merge into a few complex objects (Blackburn et al (1996), DelAlamo et al (2006)). Thanks to the normalization of the detection function, a uniform threshold can be used for the entire velocity field. Its value is set to 1.5, which means that only extrema where $\lambda_{ci}(x_{1/3}, x_2) > 1.5\lambda_{ci,RMS}(x_2)$ are considered. For comparison, Wu and Christensen (2006) used the same threshold on their PIV data of turbulent channel flow and turbulent boundary layer.

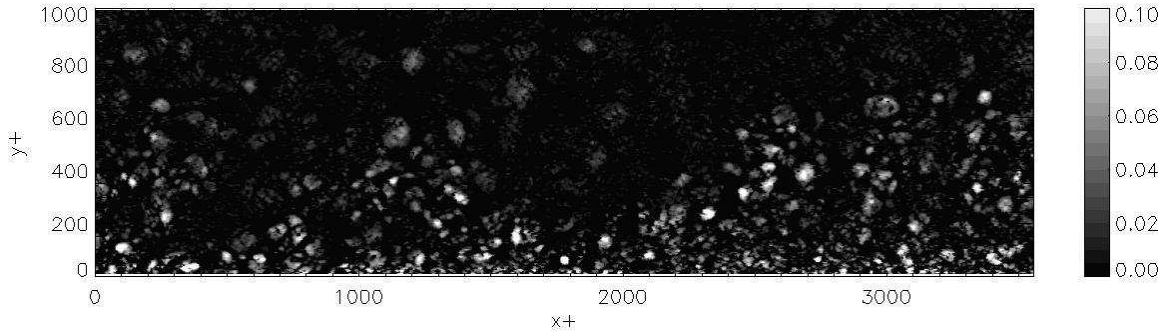

Figure 6.1: Example of map of swirling strength, in wall units

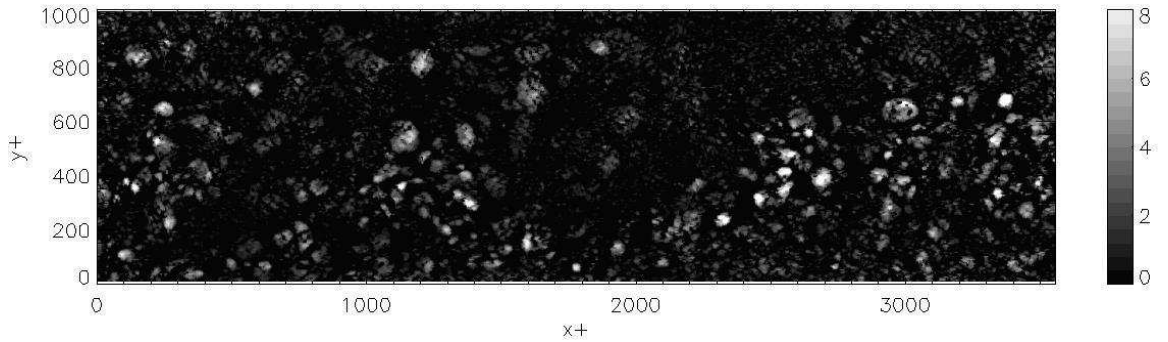

Figure 6.2: Example of map of normalized swirling strength

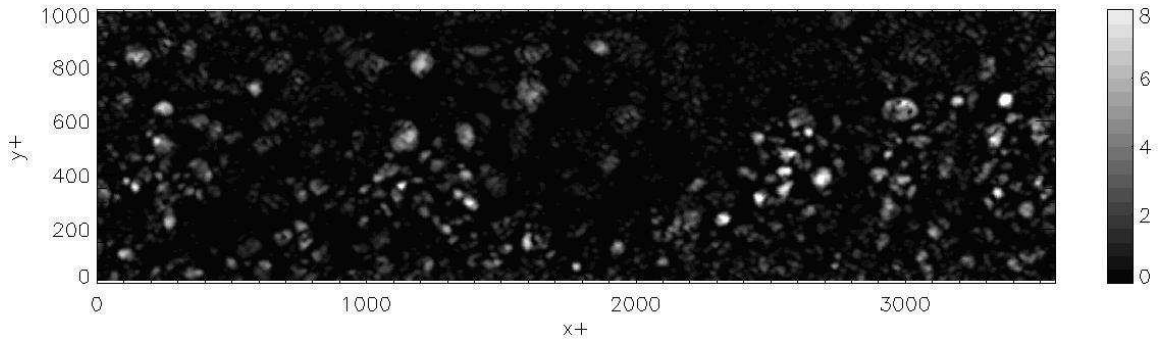

Figure 6.3: Example of map of normalized and smoothed swirling strength

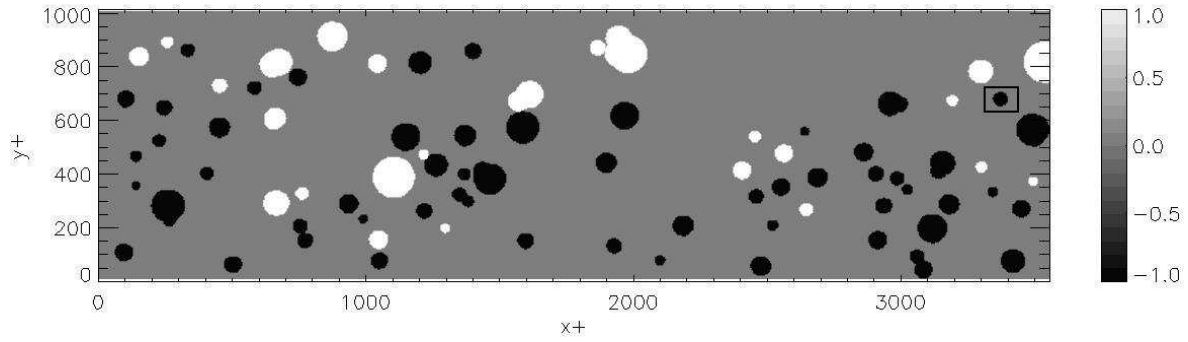

Figure 6.4: Example of map of detected vortices. Prograde vortices ($\omega_0 < 0$) are colored in black, and retrograde vortices ($\omega_0 > 0$) are colored in white. The little rectangular box centered at $(x^+; y^+) \approx (3370; 680)$ indicates which vortex is used to illustrate the fit to an Oseen vortex in the paragraph 'Fit to a model vortex'

Fit to a model vortex

The velocity field surrounding each maxima of the detection function is fitted to a model vortex. This process is undertaken for two reasons:

- it allows to validate if the extrema of the detection function correspond effectively to vortex cores.
- it enables the retrieval of the characteristics of this vortex (radius, circulation ...) through the fitted parameters of the model.

The model chosen is an Oseen vortex, convected with a constant velocity (see equation 6.1), and the parameters fitted are the two components of the convection velocity $\vec{u_c}$, the coordinates of the center, the radius r_0, and the circulation Γ.

$$\vec{u}(r,\theta) = \vec{u_c} + \frac{\Gamma}{2\pi}\frac{1}{r}\left(1 - exp\left(-\left(\frac{r}{r_0}\right)^2\right)\right)\vec{e_\theta} \tag{6.1}$$

The algorithm implemented for the fit is summarized in an organigram in figure(6.5). The velocity field domain used for the fit is square centered on the detection peak, and of constant size: it extends along 7 mesh points on each sides of the detection peak (that is 15 mesh points of total extent). The extent of 7 mesh points corresponds to a wall unit extent comprised between 24^+ and 45^+, depending on the dataset considered. The parameters of the model are initialized using: the local velocity at the peak as the convection velocity; the coordinates of the peak as the coordinate of the center; 4 times the mesh spacing as the radius. The circulation is initialized using the vorticity at the peak. A first fit of the model to the velocity field inside this domain is realized, using a non-linear least-square method: the Levenberg-Marquardt method (see *numerical recipes in C* for more details). It is iterative, and the tolerance and maximum number of iterations are fixed in section 6.1.3. This method was adapted to handle two variables depending on two dimensions. If convergence is reached within the maximum number of iterations, the correlation coefficient between the fitted model and the velocity field is computed (see equation 6.2). The structure is retained if it is larger than 0.75.

$$R(\text{model/PIV}) = \left(\frac{< (\vec{u}_{\text{PIV}} - \vec{u}_c).(\vec{u}_{\text{model}} - \vec{u}_c) >}{\sqrt{< (\vec{u}_{\text{PIV}} - \vec{u}_c)^2 >}\sqrt{< (\vec{u}_{\text{model}} - \vec{u}_c)^2 >}}\right)^{1/2} \tag{6.2}$$

This method has one drawback: the domain used for the fit of all the vortices is of constant size. When a vortex is smaller than this domain, then some part of the outer flow is fitted as well, which may disturb the fitting procedure. On the other hand, when a vortex is larger than this domain, then only a portion of the vortex is fitted, which may induce inaccurate results. In order to overcome this drawback, a second fit is realized. This time, the size of the domain of the fit is adjusted using the radius found from the first fit, and the parameters of the model are initialized with the outputs from the first fit. If the fit converges, the new correlation coefficient is computed, and the structure is finally accepted as a vortex if the coefficient is superior to 0.75.

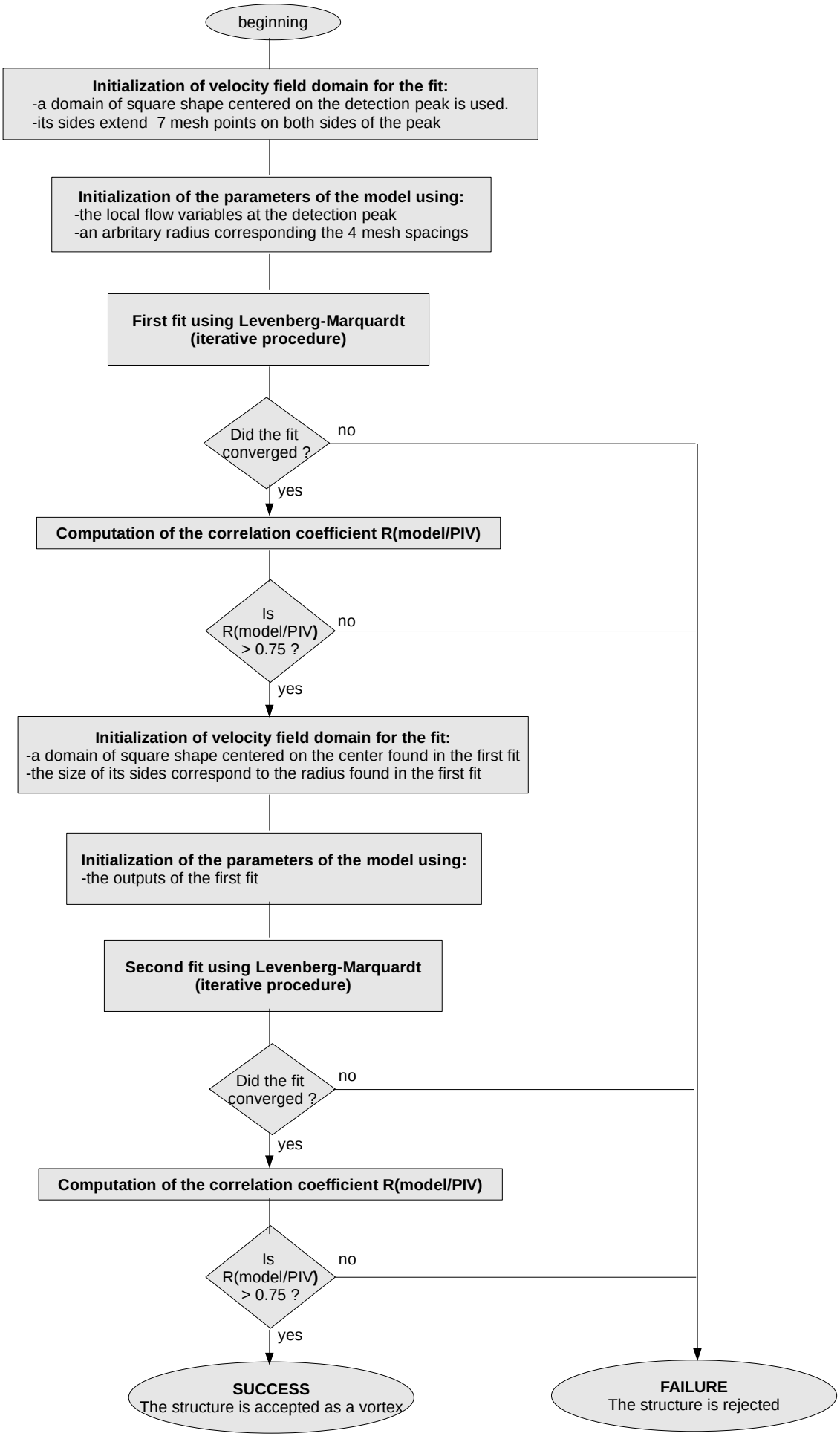

Figure 6.5: Organigram of the fit algorithm

Finally, the informations retrieved for an accepted vortex are: its radius r, its circulation Γ, its convection velocity $\vec{u_c}$, the coordinates of its center and the vorticity at its center (defined as $\omega_0 = \Gamma/(\pi r^2)$). For each velocity field, a map of the indicative function of the detected vortices is constructed. This function is defined as being: 1 within a vortex of positive vorticity; -1 within a vortex of negative vorticity; 0 elsewhere. A map of this indicative function is shown is figure 6.4. Prograde ($\omega_0 < 0$) and retrograde ($\omega_0 > 0$) vortices with a wide range of radii were detected. It can be seen that the position of these vortices coincide with peaks of the detection function (see figure 6.3).

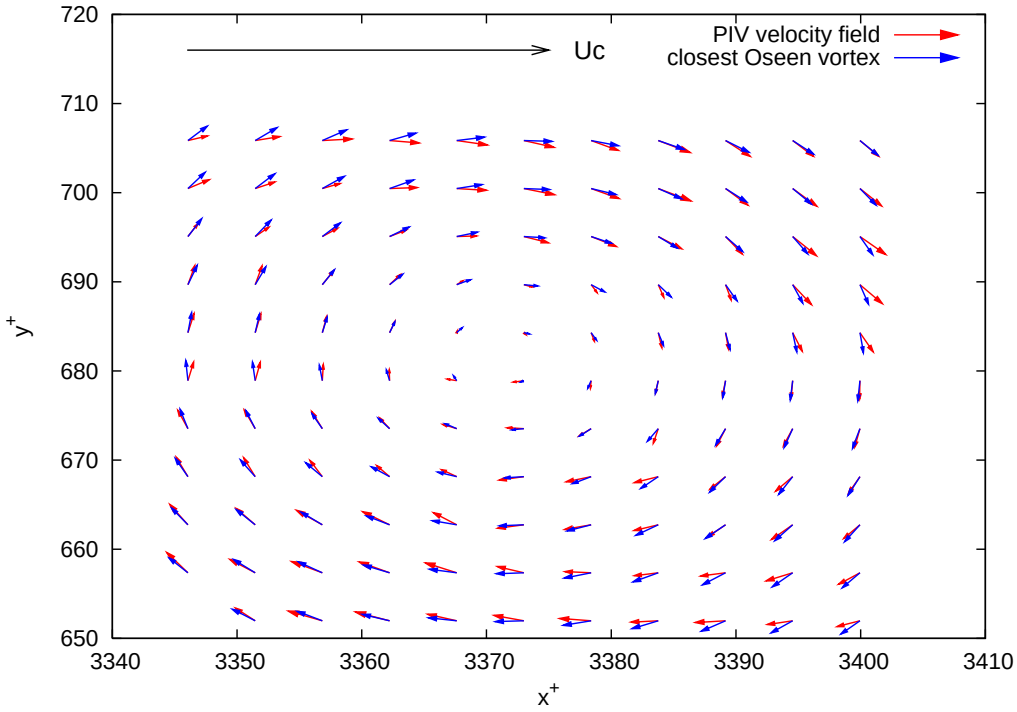

Figure 6.6: Comparison of a vortex and its closest Oseen model . The convection velocity (shown in black at the top of the figure) has been subtracted to the PIV velocity field.

An example of accepted vortex is shown in figure 6.6. It is plotted against the closest Oseen vortex obtained with the fitting procedure (the correlation coefficient is equal to 0.96). It corresponds to the vortex enclosed within a square in figure 6.4. The radius of this vortex is 26 wall units.

6.1.3 Validation using synthetic data

The detection technique was validated using a synthetic Oseen generator. At first, a synthetic Oseen vortex was generated with the following parameters: $r^+ = 25$, $\Gamma^+ = 250$ and no convection velocity. The vortex was discretized on a grid with a spacing of $\Delta x^+ = \Delta y^+ = 4$. The grid spacing was chosen to be close to the mean spacing of

the database. The radius and circulation are close to mean values observed in the literature (Carlier and Stanislas (2005)). The initial size of the fitting domain was set to 15 mesh points (it corresponds to the size used for the detection on the database). It was checked that the detection procedure enables the retrieval of the correct radius and circulation with a correlation coefficient of 1. The influence of the discretization of the vortex on the performance of the detection technique was then studied. For that purpose, the radius of the vortices was varied while keeping the mesh spacing (as well as the circulation) constant: in total, 16 Oseen vortices with radius varying linearly from $r = 1\Delta x$ up to $r = 16\Delta x$ were generated. The larger vortex is twice as big as the size of the fitting domain. All the vortices could be detected with the correct parameters and a correlation coefficient of 1. This indicates that the spatial discretization of the vortices (corresponding to the mesh spacing of the SPIV dataset) is expected to have none or little influence on their detection. Finally, it was checked that adding a convection velocity to the vortex, and having the center of the vortex located in between two grid points have no influence on the performance of the detection procedure. The tolerance and the maximum number of iterations of the Levenberg-Marquadt method were adjusted using these synthetic tests.

6.1.4 Effect of the PIV filtering on the detection

The influence of the PIV spatial averaging on the performance of the detection technique was then assessed. For this purpose, two SPIV datasets at the same Reynolds number, but with different spatial resolutions, were used. The characteristics of the two datasets are summarized in table 6.1. The two datasets consist of XY planes of the LML boundary layer at $Re_\theta = 10140$, one with a resolution of $67\mu m/px$, and the other one with a resolution of $27\mu m/px$. As the PIV interrogation window size was the same in pixels, the two datasets have different size of interrogation window in wall units: for the dataset at $67\mu m/px$, the averaging area is on the order of 27.8^+, while for the dataset at $27\mu m/px$, it is equal to 11.2^+. Note that the mesh spacing in wall units also varies between the two datasets. However, the discretization is expected to have little influence on the detection, as shown with the study using a synthetic Oseen generator (provided the radius is discretized on no less than one mesh spacing).

facility	Plane (1-2)	Re_θ	δ^+ Re_τ	Domain extent S_1, S_2	L_{IW}	Mesh step Δ_i	$\sigma(\epsilon_{u,i})$	radius at $SNR = 1$
LML	XY	10140	3620	0.18δ, 0.7δ	27.8^+	6.5^+	$0.7\%U_\infty$	27^+
LML	XY	10140	3620	0.08δ, 0.28δ	11.2^+	3.2^+	$0.7\%U_\infty$	19.0^+

Table 6.1: Characteristics of the 2 datasets at $Re_\theta = 10140$ with different spatial resolutions

The influence of the spatial resolution on the wall-normal evolution of the mean radius and vorticity of the vortices detected in the two datasets is first studied. These profiles

are shown in figures 6.7 and 6.8, in wall units. Each point of the profiles was obtained by taking into account eddies contained in a layer of 25^+ in height.
As it can be seen, the evolution of the mean radius follows the same trend for the two datasets: a slow increase with increasing wall-normal distance. However, the values of these mean radii are fairly different: the vortices detected in the dataset with the lowest spatial resolution ($67\mu m/px$) possess a radius on average 60% bigger than in the dataset with the highest spatial resolution ($27\mu m/px$). This effect of spatial resolution was already observed by Stanislas et al (2008) between a YZ plane of the LML boundary layer at $Re_\theta = 7800$ and a YZ plane of the LML boundary layer at $Re_\theta = 15000$. It is likely that the small vortices are in fact filtered out in the dataset with the lowest spatial resolution, resulting in a higher value of the mean radius.
In contrast, the wall-normal evolution of the mean vorticity at the center of the vortices seems less affected by the PIV spatial resolution: it is in quite good agreement between the two datasets. This quantity appears slightly underestimated in the dataset with the lowest spatial resolution ($67\mu m/px$): a difference of about 25% is noted with respect to the dataset with the highest spatial resolution. In fact the vorticity is homogeneous to the inverse of a time, and hence is more related to the PIV time separation than to the PIV spatial resolution. While the PIV optical magnification was adjusted 'only' three times during the acquisition of the database (once for the LTRAC, and twice for the LML), the PIV time separation was continuously adjusted to keep a maximum displacement of 10 pixels for all datasets (see sections 3.2 and 4.2). This may explain why the estimation of the vorticity is less affected than that of the radius by the PIV parameters employed.

As the mean radius seems to be the quantity that is the most impacted by the spatial resolution of the datasets, it is of interest to analyze the distribution of the radius of the detected vortices. For this purpose, the joint density function of the vortex radius and center wall normal location $DF(r, y_0)$ was computed for both datasets. The bin value used for the radius is equal to 1/6 of its RMS value, and the bin value used for the wall-normal location is equal to 50^+. This density function is normalized so that it represents the vortex density per wall-unit square and per bin value of the radius. Cuts of $DF(r, y_0)$ at different wall-normal locations were then extracted, and superimposed in figure 6.9. Within each dataset, it can be seen that the density function of radii shows a weak dependence on the wall-normal position of the vortex. Although the shape of the DFs is similar for the two datasets, the smallest radius detected and the most probable radius detected is noticeably smaller for the dataset with the highest spatial resolution. On the other hand, the vortices with a large radius are detected with both spatial resolutions. Therefore, the spatial resolution affects mainly the detection of the small vortices, which are filtered out by the dataset at $67\mu m/px$ due to the spatial averaging.

Another statistical result of interest to study the influence of the PIV filtering on the vortex radius is the wall-normal evolution of the vortex density per wall-unit square $N^+(y^+)$. It is plotted in figure 6.10 for both datasets. The density of detected vortices appears to be strongly dependent on the spatial resolution, especially in the near wall region: close to the wall, the density in the dataset at $27\mu m/px$ is eight times as high as the density in the dataset at $67\mu m/px$; away from the wall, the density in the dataset at $27\mu m/px$ is twice as high as the density in the dataset at $67\mu m/px$. As already shown in figure 6.7, the mean radius of the vortices decreases with decreasing wall-normal distance: this may explain why more vortices are filtered out close to the wall than away from the wall in the dataset with the lowest spatial resolution.

Finally, it is of interest to study the influence of the PIV filtering on the vortex radius using another scaling: the Kolmogorov scaling. The wall-normal evolution of the vortex mean radius in the two datasets, non dimensionalized using the same Kolmogorov lengthscale profile is shown in figure 6.11. The Kolmogorov lengthscale profile was computed from hot-wire measurements of the LML boundary layer at $Re_\theta = 10140$, and can be found in Stanislas et al (2008). In this representation, the radius is found to slowly decrease with increasing wall-normal distance. The mean vortex radius in the dataset with the lowest spatial resolution ($67\mu m/px$) is found to be on average 60% bigger than in the dataset with the highest spatial resolution ($27\mu m/px$). As expected, this is comparable to what was obtained with the wall-unit scaling. Now, another methodology is tested to non-dimensionalize the mean radius. It consist in using, for each PIV dataset, the Kolmogorov lengthscale profile that was computed from the PIV data itself (see figure 5.37 in section 5.5). When comparing the dissipation and Kolmogorov lengthscale profiles obtained from HW and PIV, it can be seen that the dissipation profile obtained from HW is comparable to that of the PIV at $67\mu m/px$ in the near-wall region; both underestimate the dissipation peak at the wall, and consequently overestimate the Kolmogorov lengthscale. In contrast, the PIV dataset with the high spatial resolution ($27\mu m/px$) seem to estimate correctly the dissipation in the near-wall region. The wall-normal evolution of the mean radius non-dimensionalized using the Kolmogorov lengthscale from the PIV data is shown in figure 6.12. As it can be seen, the mean radius is now more independent of the wall normal distance. Besides, the difference in radius between the two datasets is much smaller: the mean radius in the dataset at a resolution of $67\mu m/px$ is now only 30% bigger than in the dataset at a resolution of $27\mu m/px$. Therefore, non-dimensionalizing the mean radius of the PIV using the Kolmogorov length scale profile computed from the same data seems to actually compensate spatial averaging errors.

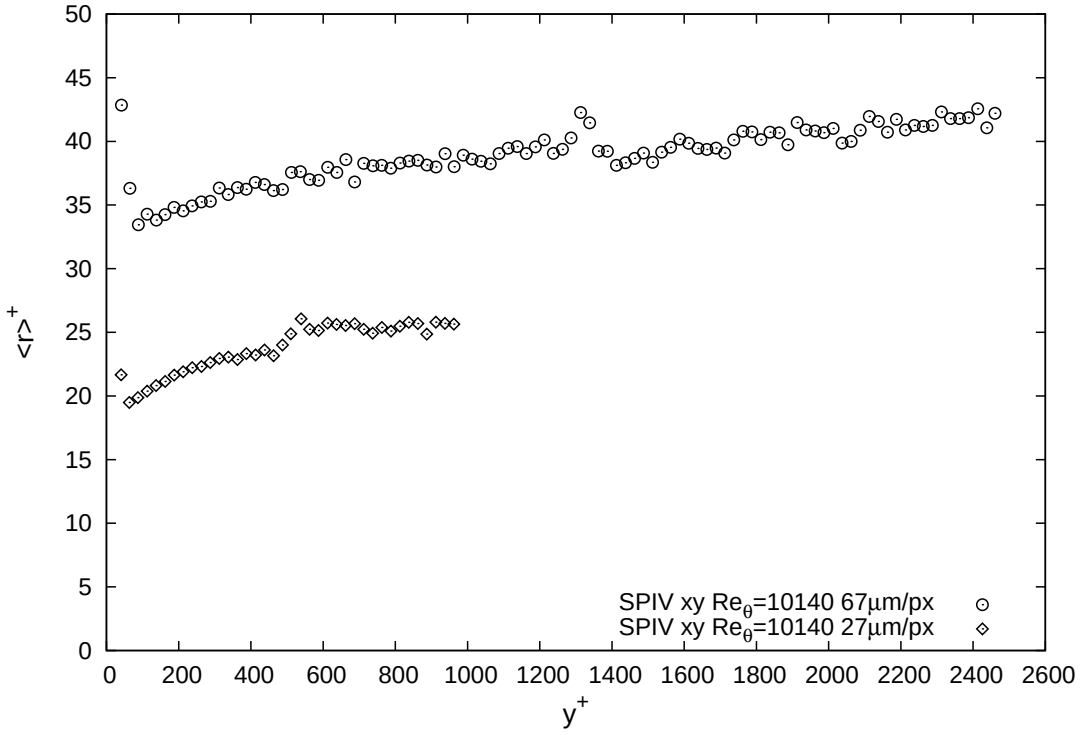

Figure 6.7: Effect of spatial resolution on wall-normal evolution of mean radius

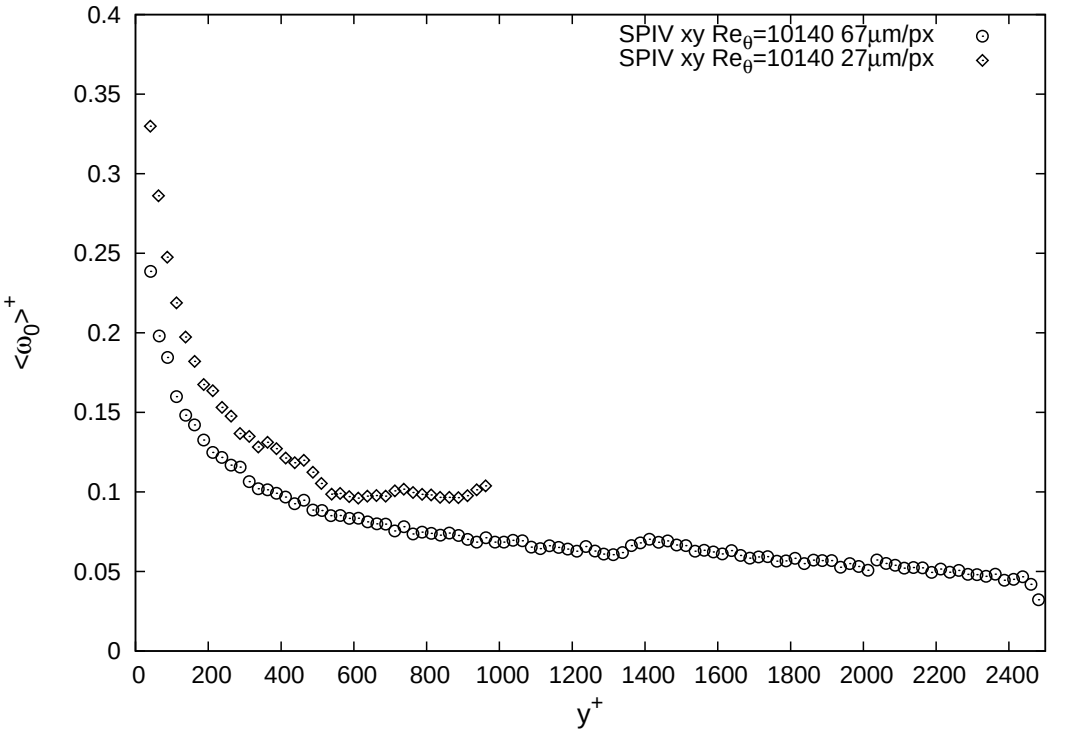

Figure 6.8: Effect of spatial resolution on wall-normal evolution of mean vorticity at the center

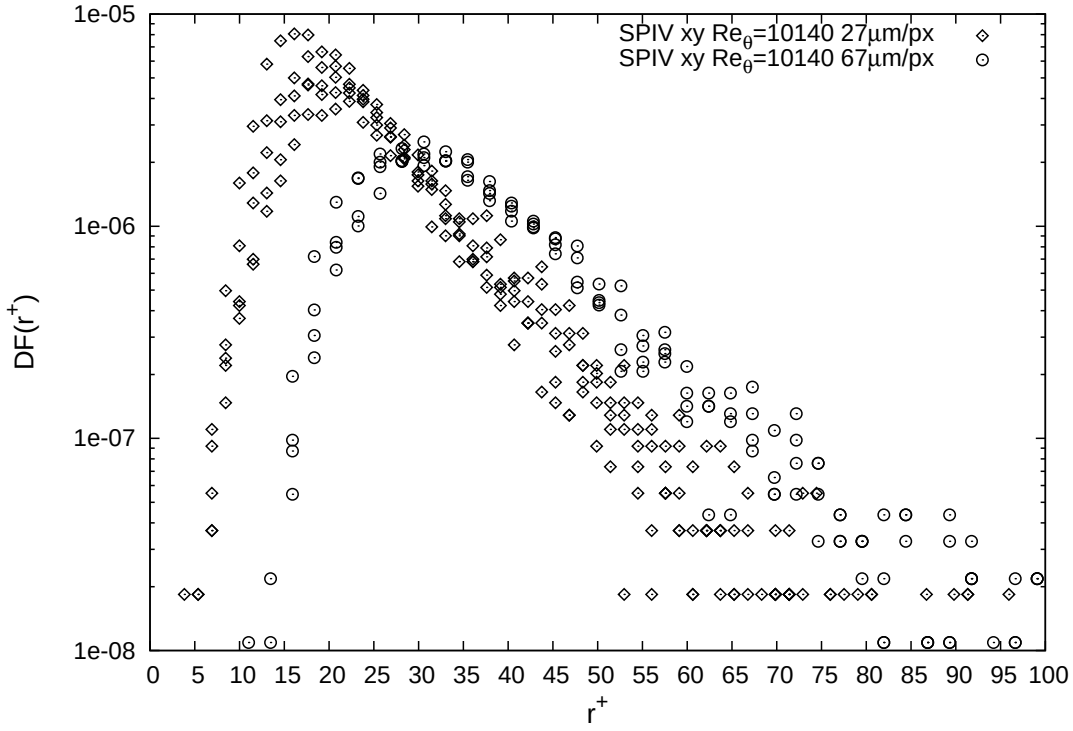

Figure 6.9: Effect of spatial resolution on PDF of radius in wall units scaling, in the logarithmic region

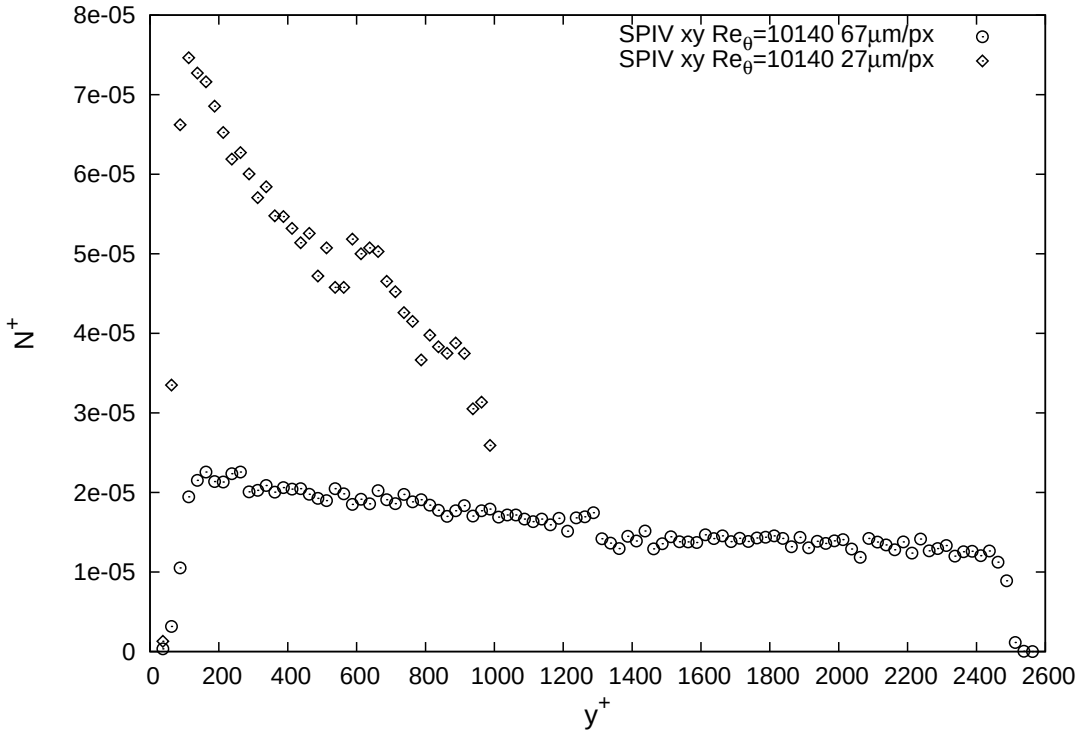

Figure 6.10: Effect of spatial resolution on wall-normal evolution of the density of detected vortices

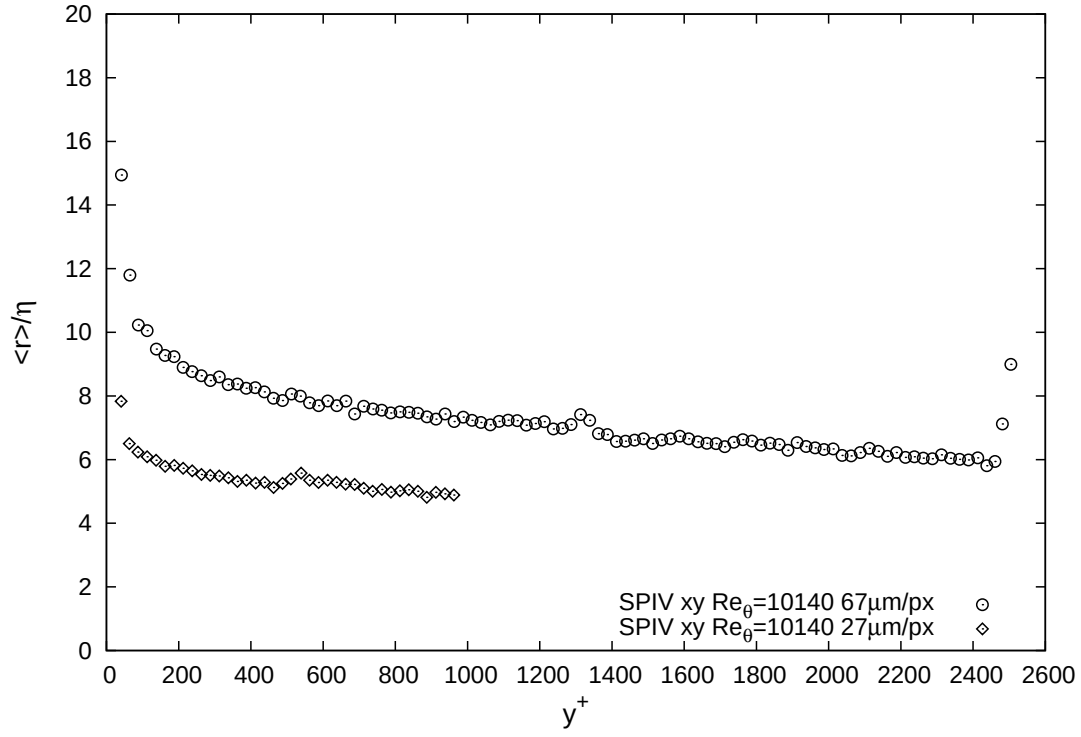

Figure 6.11: Effect of spatial resolution on wall-normal evolution of mean radius, in Kolmogorov scaling (using hot-wire profiles of Kolmogorov length scale)

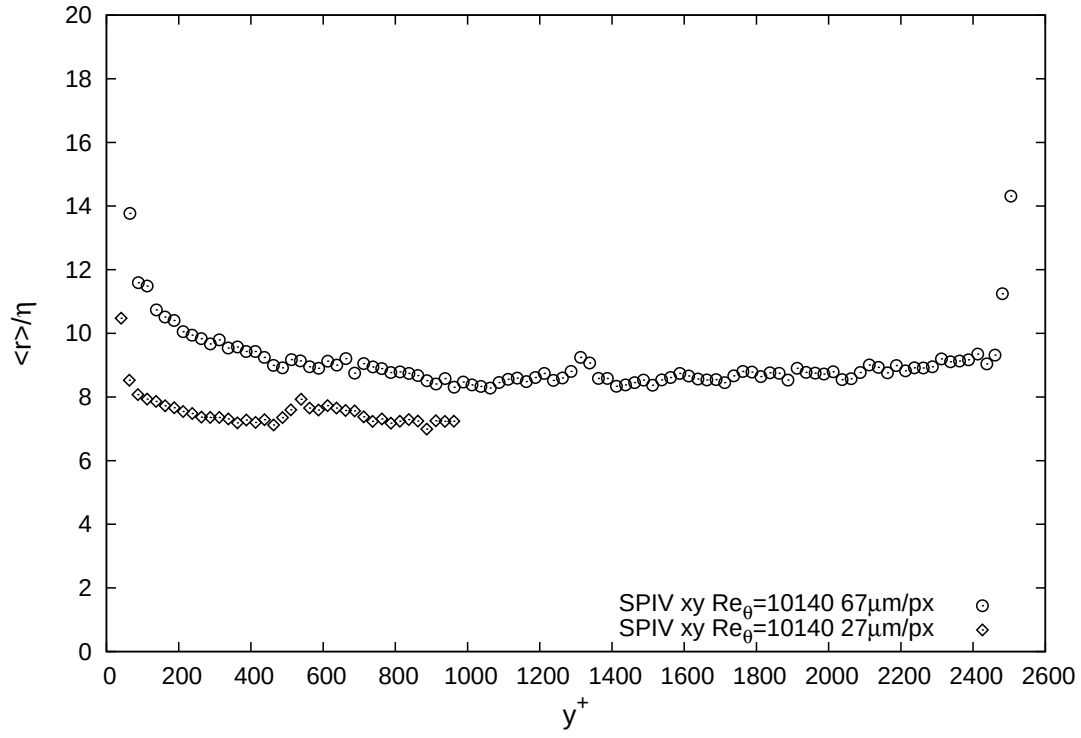

Figure 6.12: Effect of spatial resolution on wall-normal evolution of mean radius, in Kolmogorov scaling (using PIV profiles of Kolmogorov length scale)

6.2 Results on the individual vortices

The coherent structure detection was run on the LML and LTRAC databases. The characteristics of these databases are summarized in table 6.2 for convenience. The database consists of streamwise/wall-normal (XY) and spanwise/wall-normal (YZ) planes of turbulent boundary layers at Reynolds numbers ranging from $Re_\theta = 1300$ up to $Re_\theta = 18950$ (or conversely from $Re_\tau = \delta^+ = 820$ up to $Re_\tau = 6880$). The uncertainty on the velocity (obtained in section 3.4 and 4.4 using the overlap region of the velocity fields) and the radius corresponding to a signal to noise ratio of 1 (obtained in section 5.4 using the power spectra) are also summarized. Uncertainties and cut-off wavenumbers were obtained for the three velocity components, but here only an average value between the two in-planes velocity components is given (as the detection is performed using these two components). The boundary layer at $Re_\theta = 10140$ was measured using two spatial resolutions ($27\mu m/px$ and $67\mu m/px$), but only the dataset with the highest spatial resolution will be used for the analysis of the vortices.

DNS data of turbulent channel flow (DelAlamo et al (2006)) were also used. The characteristics of the full DNS are summarized in table 6.3(a). The detection was run on streamwise/wall-normal and spanwise/wall-normal planes of this DNS, interpolated on a regular mesh. The planes were extracted from nine three-dimensional velocity fields, uncorrelated in time. Successive planes are separated by a distance equal to $h^+/2$ for the XY planes and to h^+ for the YZ planes (where h is the half channel height). The interpolation was undertaken using two-dimensional bi-cubic spline interpolation. The regular mesh have a spacing of 4.5^+ in all directions. This resolution is close to the native resolution of the DNS in the spanwise direction, and to that of the LTRAC dataset. It can be seen that the native mesh spacing of the DNS in the streamwise direction is twice as large as the spacing used for the interpolation. In contrast, the full DNS was more highly resolved in the wall-normal direction. The characteristics of the interpolated XY and YZ planes of the DNS are summarized in table 6.3(b). The total number of points for the DNS planes (over the two spatial directions and over the number of samples) is roughly equal the total number of points for the SPIV dataset at $Re_\theta = 2200$.

In the following subsections, statistical results on the radius $r(y)$, the vorticity $\omega(y)$, the density $N(y)$, and the convection velocity $u_c(y)$ of vortices detected in XY planes and YZ planes of the flow are presented and analyzed.

facility	Plane (1-2)	Re_θ	δ^+ Re_τ	Domain S_1, S_2	L_{IW}	Mesh step Δ_i	1st point	n° records	$\sigma(\epsilon_{u,i})$	radius at $SNR = 1$
LTRAC	XY	1300	820	4δ, 1.4δ	15.2^+	4.7^+	$y^+ = 13$	605	$0.75\%U_\infty$	22^+
LTRAC	XY	2200	1390	2.6δ, 0.75δ	14.2^+	4.3^+	$y^+ = 12$	1815	$0.75\%U_\infty$	22^+
LML	XY	7630	2590	0.15δ, 0.6δ	16.8^+	3.9^+	$y^+ = 24$	3840	$0.7\%U_\infty$	21.5^+
LML	XY	10140	3620	0.08δ, 0.28δ	11.2^+	3.2^+	$y^+ = 13$	4096	$0.7\%U_\infty$	19.0^+
LML	XY	13420	5020	0.08δ, 0.28δ	15.4^+	4.5^+	$y^+ = 15$	4096	$0.7\%U_\infty$	21.3^+
LML	XY	18950	6860	0.08δ, 0.28δ	20.6^+	6.0^+	$y^+ = 20$	3840	$0.7\%U_\infty$	25.1^+
LML	ZY	7630	2590	0.15δ, 0.6δ	16.8^+	3.9^+	$y^+ = 34$	2048	$0.7\%U_\infty$	20.6^+
LML	ZY	10140	3620	0.08δ, 0.28δ	11.2^+	3.2^+	$y^+ = 17$	4096	$0.7\%U_\infty$	19.6^+
LML	ZY	13420	5020	0.08δ, 0.28δ	15.4^+	4.5^+	$y^+ = 27$	4352	$0.7\%U_\infty$	21.5^+
LML	ZY	18950	6860	0.08δ, 0.28δ	20.6^+	6.0^+	$y^+ = 33$	4608	$0.7\%U_\infty$	24.9^+

Table 6.2: Characteristics of the LML and LTRAC databases

(a) Full DNS from DelAlamo et al (2006)

Re_τ	S_x	S_y	S_z	Δx^+	Δy^+	Δz^+
950	$8\Pi h$	$2h$	$3\Pi h$	11	variable	5.7

(b) interpolated planes

Plane (1-2)	h^+ Re_τ	Domain $S_{x/z}, S_y$	Mesh step Δ_i	n° records
XY	950	$8\Pi h$, h	4.5^+	342
ZY	950	$3\Pi h$, h	4.5^+	468

Table 6.3: Characteristics of the the DNS dataset

6.2.1 Properties of the radius

The general trend for the vortex radius distribution in the flow is first examined using the probability density function of the radius at various height in the XY plane (figure 6.13) and in the YZ plane (figure 6.14), with a wall unit scaling. As the same overall behavior was observed for all Reynolds numbers, only a few Reynolds numbers are represented: $Re_\tau = 950$, $Re_\theta = 2200$ and $Re_\theta = 13420$ for the XY plane, and $Re_\tau = 950$ and $Re_\theta = 13420$ for the YZ plane. These PDF were obtained by taking into account eddies contained in layers of 50^+ in height, and using bin values of the radius equal to 1/6 of the RMS value of the radius. The normalization is such that, for each dataset:

$$\int_r \int_{yc} PDF(y_c, r) = 1$$

For all Reynolds numbers and in both planes, the value of the most probable vortex as well as the width of the distribution appear to increase with increasing wall-normal distance. This increase is steeper near the wall, and then diminishes. For all cases, the radius of the detected vortices is comprised between 10^+ and 70^+, with a most probable value of 20^+ at $y^+ \approx 75$. Small differences between the XY plane and the YZ plane can be observed for $Re_\tau = 950$ and for $Re_\theta = 13420$ in the near wall region: the distribution of radius is both wider and lower for the XY plane than for the YZ plane.

The wall-normal evolution of the mean radius for all Reynolds numbers is plotted in wall units in figure 6.15 for the XY plane (where spanwise vortices are detected), and in figure 6.16 for the YZ plane (where streamwise vortices are detected). These profiles were obtained by taking into account eddies contained in layers of 25^+ in height.
Within each plane, the overall evolution of the mean radius with wall-normal distance is identical for all Reynolds numbers. It is of interest to note that, within each measurement plane, the mean radii in wall units of the datasets at $Re_\tau = 950$, $Re_\theta = 1300$, $Re_\theta = 2200$, $Re_\theta = 7630$, $Re_\theta = 13420$ are in good agreement in the near-wall region. This tends to indicate the universality of the mean radius in wall units scaling in the near-wall region. These datasets feature similar interrogation window size and mesh spacing. In contrast, the effect of spatial resolution is clearly visible on the datasets at $Re_\theta = 10140$ and at $Re_\theta = 18950$. The former has the highest spatial resolution, and a smaller radius is retreived, while the latter feature the lowest spatial resolution and a larger radius is retrieved. More details on the influence of the spatial resolution on the detection procedure can be found in section 6.1.4. It is of interest to note that the shift in radius (on the order of 4 wall units) is equal to the corresponding difference in interrogation window size.

The radius of the spanwise vortices (detected in the XY plane) appears to be slowly increasing with wall normal distance over the whole field for all Reynolds numbers, except for the dataset at $Re_\theta = 1300$ where a steep increase of mean radius is observed for $y^+ > 400 \Leftrightarrow y/\delta > 0.5$. This may be due to intermittency with the free stream; as will be shown in section 6.2.3, the density of vortices for that dataset in the region $y/\delta > 0.5$ is quite low, and therefore this part of the profile may not be really meaningful. The behavior of the mean radius in the interpolated DNS dataset of turbulent channel flow appears to be similar to that of the PIV datasets in turbulent boundary layer, and in particular to that of the LTRAC dataset at $Re_\theta = 2200$. Close to the wall ($y^+ \approx 50$), the mean radius is about 20^+ on the dataset with the highest spatial resolution ($Re_\theta = 10140$) which is comparable to the findings of Carlier and Stanislas (2005) at $Re_\theta = 7500$.

The behavior of the streamwise vortices (detected in the YZ plane) is quite different. Two regions must be distinguished: the region $y^+ < 100$, where the radius increases strongly with wall-normal distance, and the region $y^+ > 100$, where the radius increases slowly with wall-normal distance. This composite behavior in the YZ plane was also observed in Stanislas et al (2008) at $Re_\theta = 7800$ and $Re_\theta = 13420$. Close to the wall ($y^+ \approx 50$), the radius is as small as 15^+ on the dataset with the highest spatial resolution ($Re_\theta = 10140$), which is is excellent agreement with the estimation of Sheng et al (2008) for the radius of the streamwise vortices in the upper buffer layer.

Therefore the streamwise vortices (detected in the YZ plane) are found to be smaller than the spanwise vortices (detected in the XY plane) in the near wall region. This may indicate that, being inclined to the wall, the streamwise vortices are stretched by the mean velocity gradient. In the region $y^+ > 100$, the mean radius of the streamwise and spanwise vortices are comparable, slowly increase with increasing wall-normal distance toward a value of 25^+.

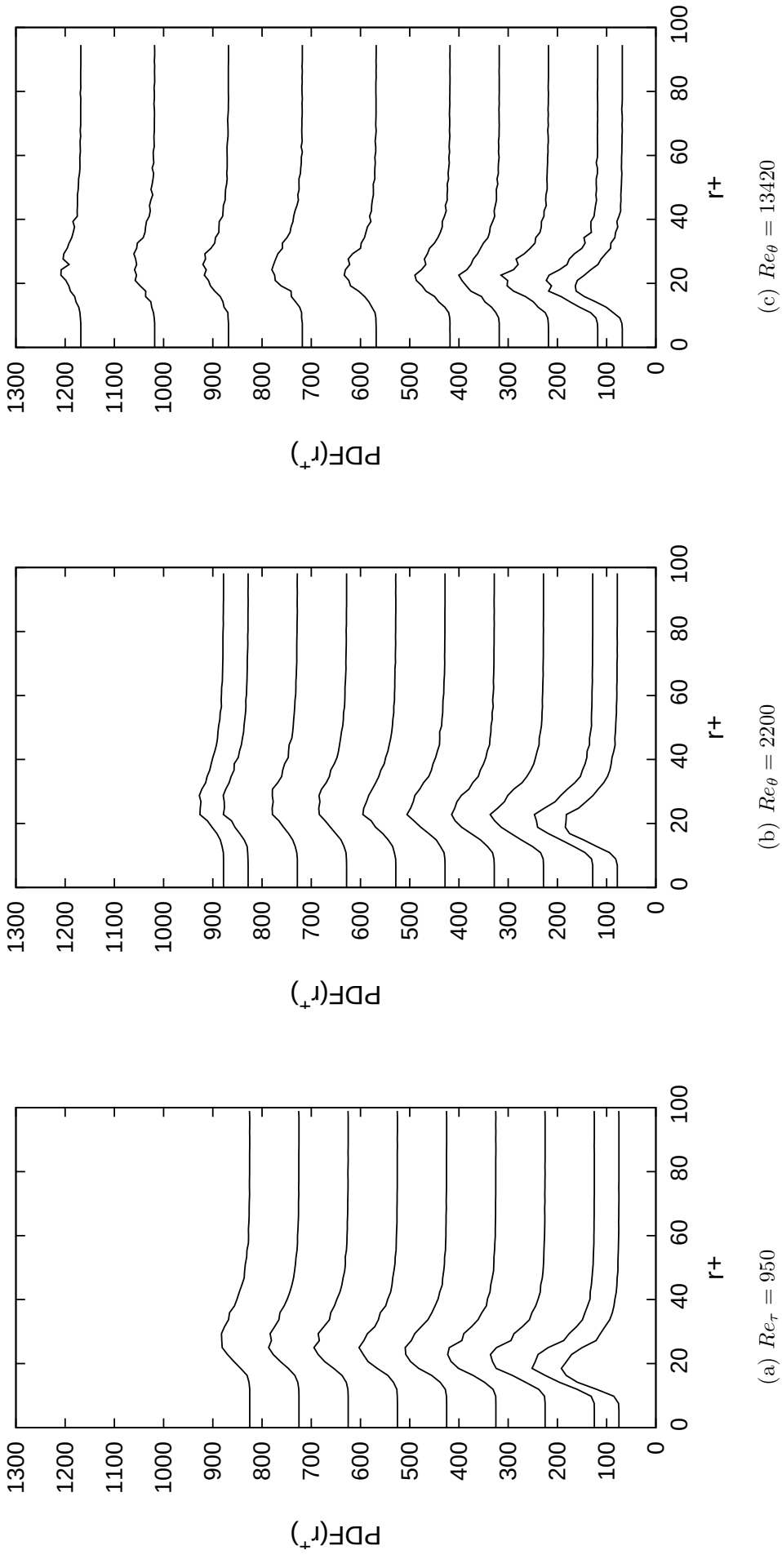

(a) $Re_\tau = 950$ (b) $Re_\theta = 2200$ (c) $Re_\theta = 13420$

Figure 6.13: PDF of radius, obtained at various heights in the XY plane, in wall units

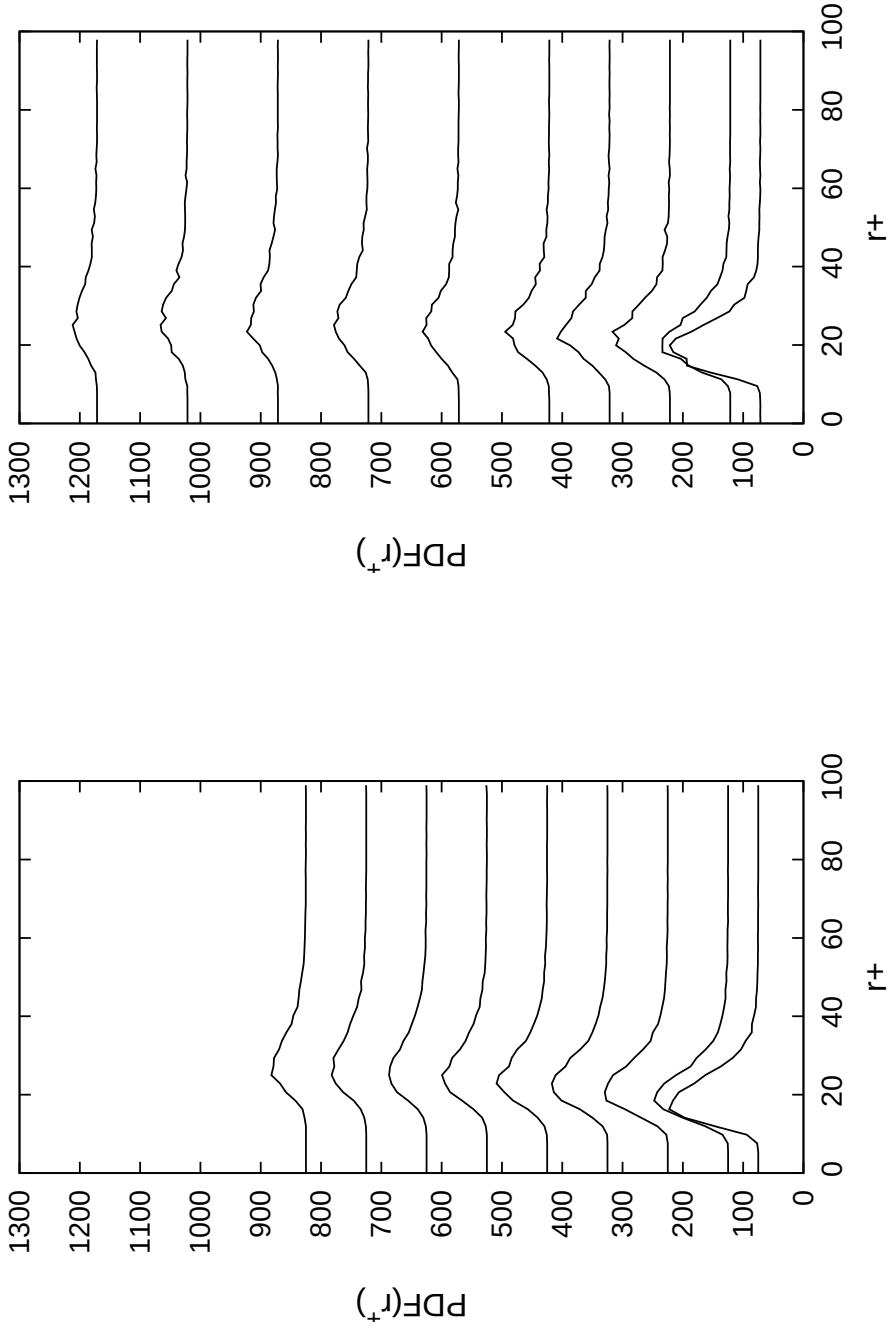

(a) $Re_\tau = 950$

(b) $Re_\theta = 13420$

Figure 6.14: PDF of radius, obtained at various heights in the YZ plane, in wall units

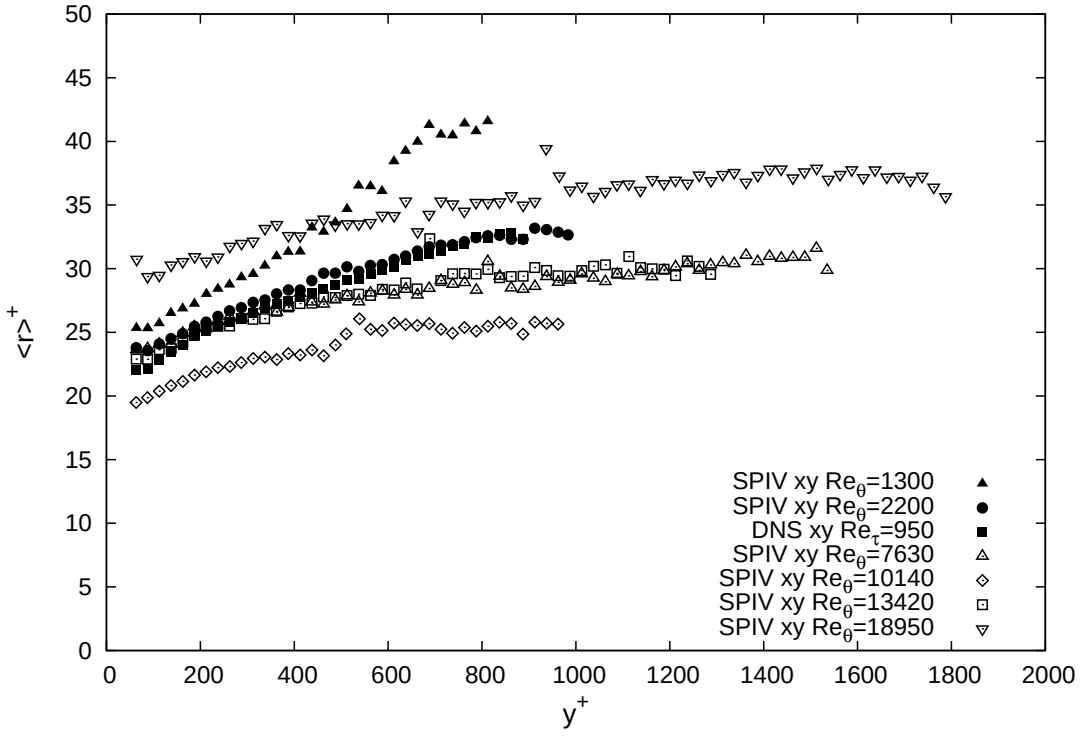

Figure 6.15: Mean radius of the spanwise vortices (detected in the XY plane), in wall units

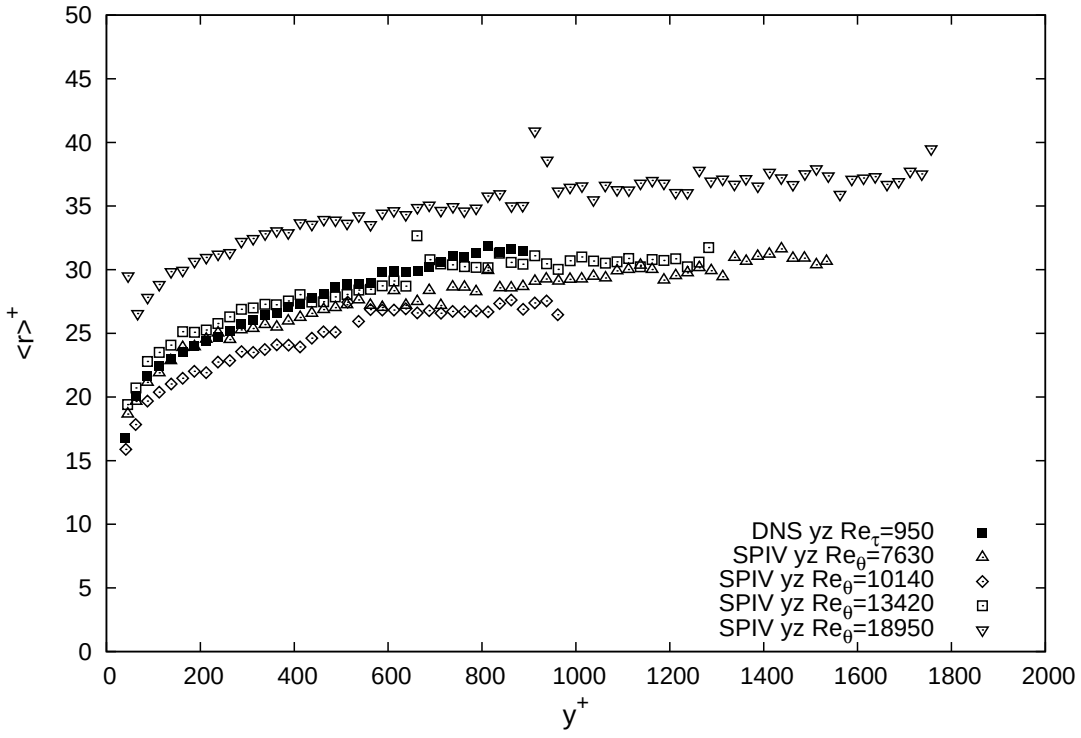

Figure 6.16: Mean radius of the streamwise vortices (detected in the YZ plane), in wall units

In the XY plane, two types of vortices may be distinguished: the prograde ($\omega_0 < 0$) and retrograde ($\omega_0 > 0$) vortices. The profiles of the radius for these two types of vortices are plotted in figure 6.17 for the highest Reynolds range and in figure 6.18 for the lowest Reynolds number range, with a wall units scaling. Note that, in order to present the clarity of the graph for the highest Reynolds number range, not all datasets are shown on this graph. The radius of the prograde vortices is found to be slightly larger than that of the retrograde vortices. The difference between prograde and retrograde vortices increases with decreasing wall-normal distance. It is of interest to note that the behavior of the retrograde vortices in the region $y^+ < 150$ is actually close to that of the vortices in the YZ plane. It was checked that the wall-normal evolution of the mean radius in the YZ plane is identical for the vortices with positive and negative vorticity.

Another possibility to scale the detected vortices is to use Kolmogorov scales. The Kolmogorov length scale $\eta(y)$ represents the characteristic size of the smallest turbulent motions, fixed by viscosity and dissipation. This scaling has been used by Tanahashi et al (2004) for a DNS of turbulent channel flow, and by Stanislas et al (2008) for YZ planes of the LML turbulent boundary layer. In this paragraph, all the radii detected within a layer of given height are scaled with the local Kolmogorov length scale $\eta(y)$, where y is the wall normal location at the centerline of the layer. The profiles of η used for the scaling are plotted in figures 5.35 and 5.37.

The wall-normal evolution of the mean radius scaled with the Kolmogorov length scale is plotted in figure 6.19 for the XY plane and in figure 6.20 for the YZ plane. The influence of the spatial resolution is less noticeable in this representation, as already noted and explained in section 6.1.4.
In the YZ plane of the boundary layer flow (PIV), the mean radius is roughly constant in Kolmogorov units over the full wall-normal extent of the velocity field, and equal to 8η. Stanislas et al (2008) also found a constant value, but slightly smaller, of the order of 6η. It was checked that this difference is indeed due to a difference in the Kolmogorov profile used for the scaling. Stanislas et al (2008) used a profile of dissipation computed from hot-wire measurements (using a Taylor hypothesis), whereas the present data was scaled using a dissipation profile computed from the PIV measurements themselves (see section 5.5 for the PIV dissipation profiles).
In the XY plane of the boundary layer flow (PIV), it is only in the region $y^+ > 150$ that the radius detected in the PIV datasets have an approximately constant value in Kolmogorov scaling, comparable to that of the YZ plane. Below that region, the radius in the XY plane is found to increase with decreasing wall-normal distance. This behavior was also found by DelAlamo et al (2006), although it was not as obvious as in the present data. Here again, it is of interest to distinguish the prograde and the retrograde vortices in the XY plane. The wall normal evolution of mean radius in Kolmogorov scaling are shown in figure 6.21 for the retrograde vortices, and in figure 6.22 for the prograde vortices. The dataset at $Re_\theta = 13420$ is not shown on these figures, because its behavior is very similar to that of the dataset at $Re_\theta = 7630$. It is found that the radius of the retrograde vortices in the XY plane is comparable to that of the vortices in the YZ plane. On the contrary, the radius of the prograde vortices in the region $y^+ < 150$ is not constant in Kolmogorov units, and increases with decreasing wall-normal distance.
A special comment may be made on the radius of the vortices detected in the DNS dataset. In both planes, the mean radius is found to decrease slowly with increasing wall-normal distance, and no constant value of r/η is reached.

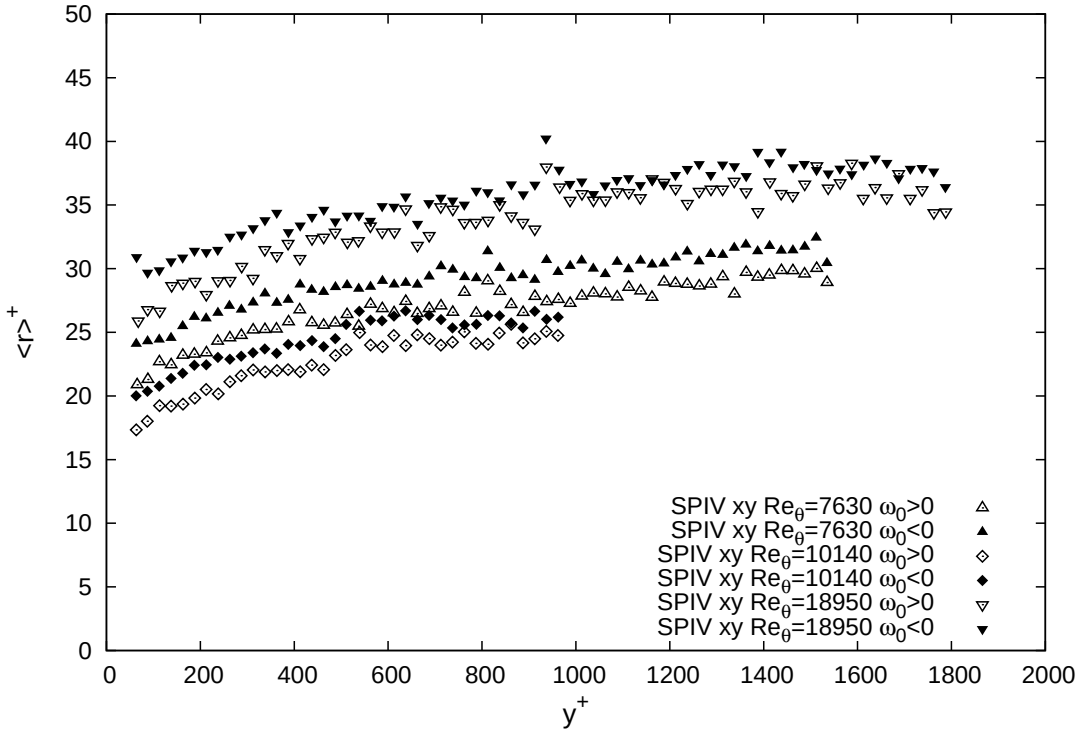

Figure 6.17: Effect of the vorticity sign on the radius of the spanwise vortices (detected in the XY plane), in the highest Reynolds number range

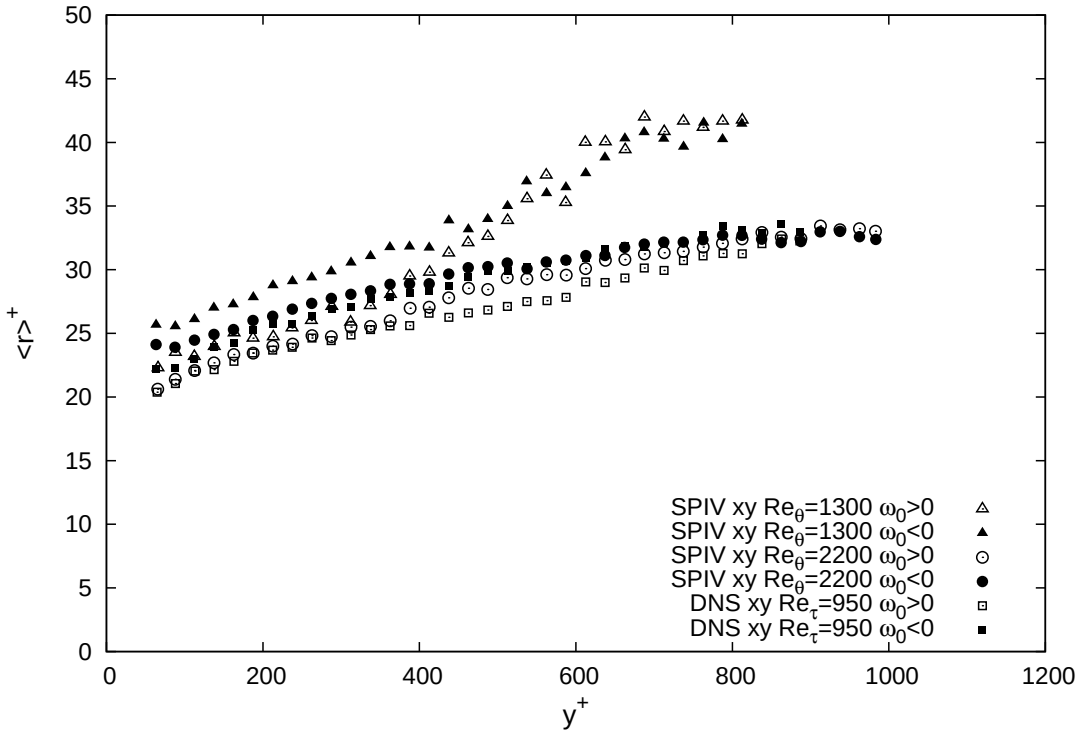

Figure 6.18: Effect of the vorticity sign on the radius of the spanwise vortices (detected in the XY plane), in the lowest Reynolds number range

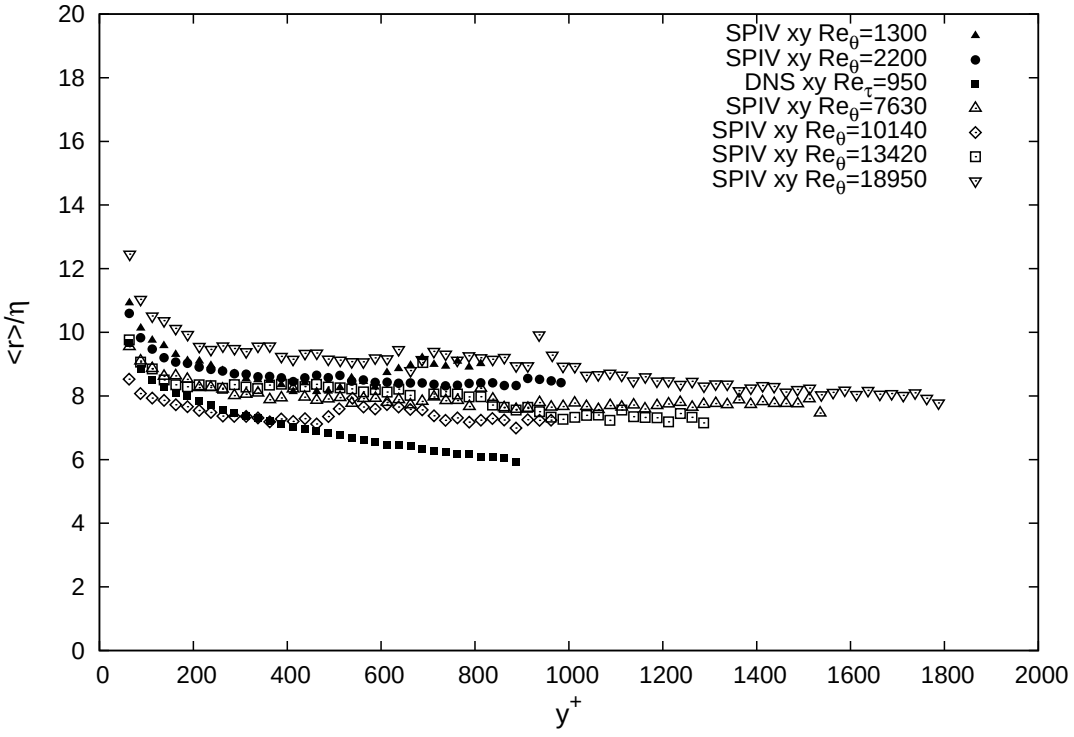

Figure 6.19: Mean radius of the spanwise vortices (detected in the XY plane), in Kolmogorov units

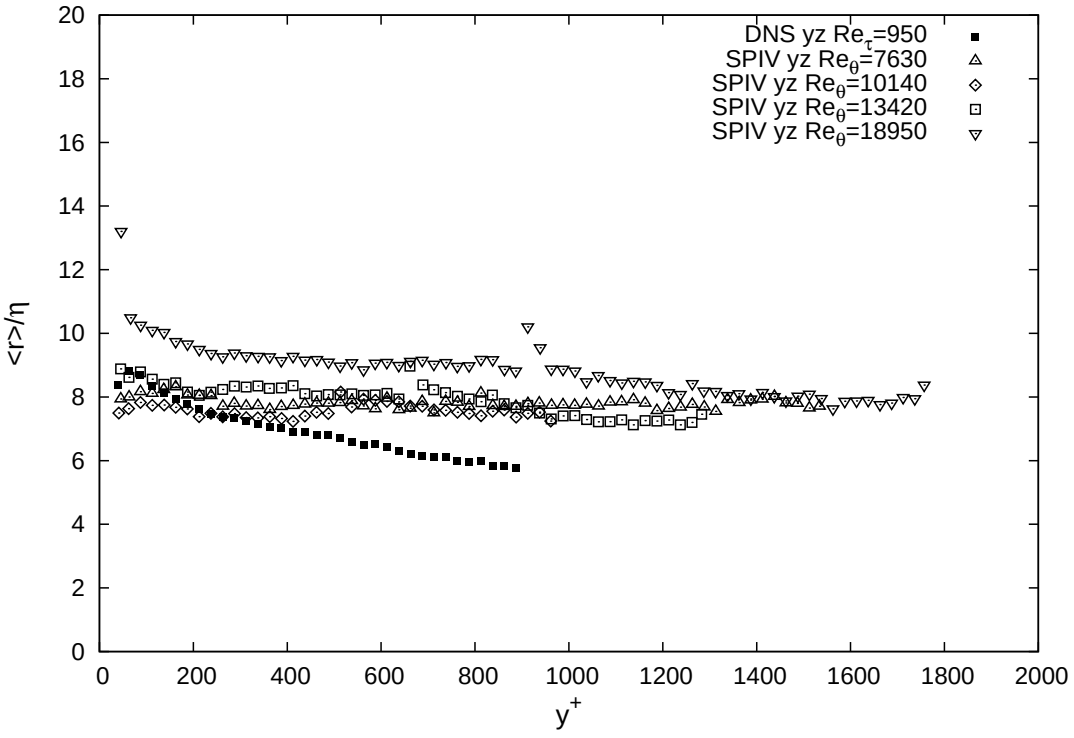

Figure 6.20: Mean radius of the streamwise vortices (detected in the YZ plane), in Kolmogorov units

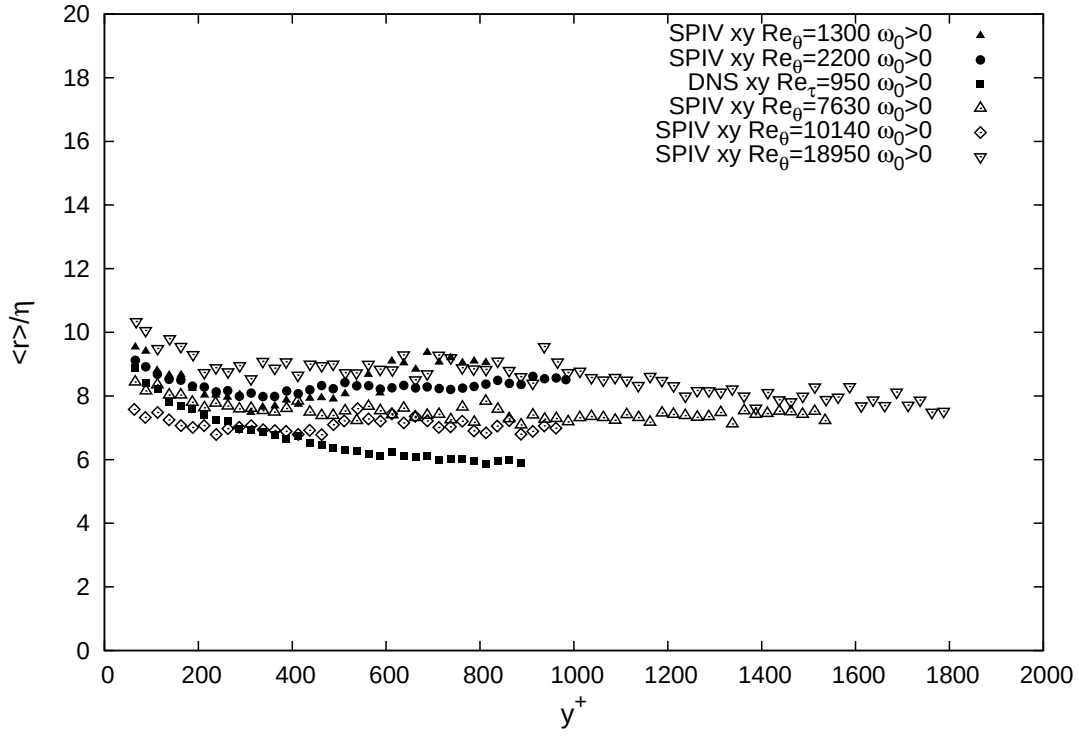

Figure 6.21: Mean radius of the retrograde vortices ($\omega_0 > 0$) in the XY plane, in Kolmogorov units

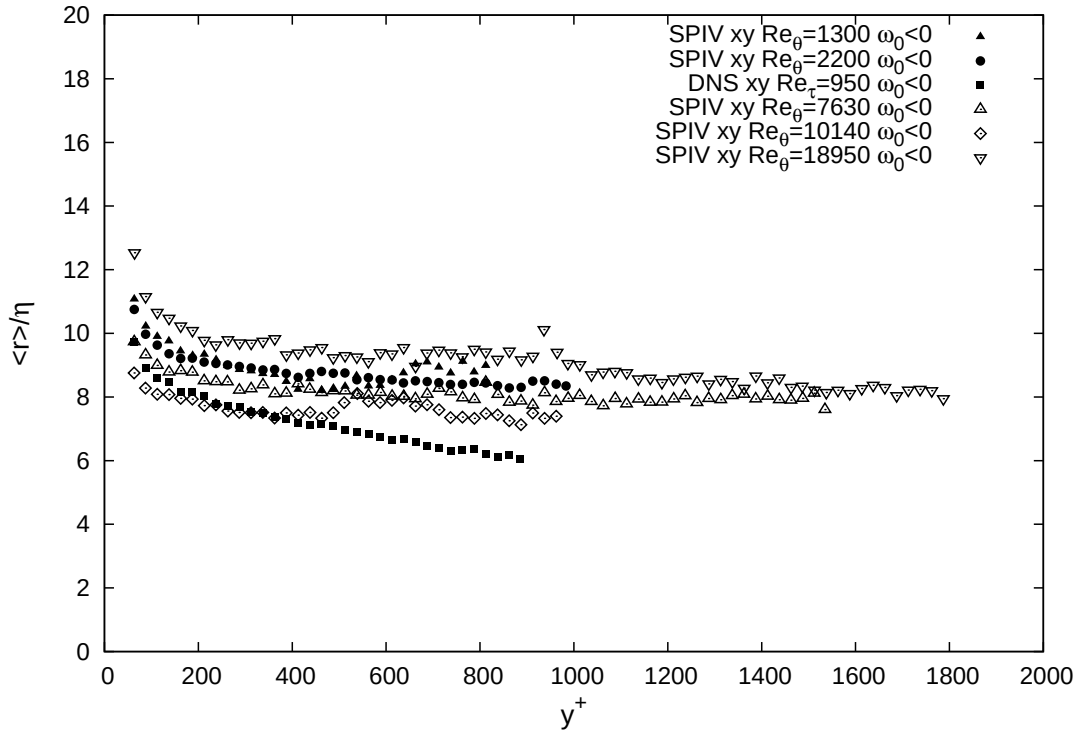

Figure 6.22: Mean radius of the prograde vortices ($\omega_0 < 0$) in the XY plane, in Kolmogorov units

The Kolmogorov scaling is then applied to the probability density functions $PDF(y_c, r)$. This time, the PDF are normalized so that for each layer in y:

$$\int_{r/\eta} PDF_y\left(\frac{r}{\eta}\right) = 1$$

For each plane, the PDF at the different wall-normal location are then superimposed. Three regions in the flow are distinguished:

- the logarithmic layer ($100 < y^+$ and $y/\delta < 0.25$) that is available in all datasets. The PDF at the different wall normal location in this domain are plotted in figure 6.23 for the XY plane and in figure 6.24 for the YZ plane.
- the outer region with $y/\delta \in [0.25; 0.6]$. This region of the flow is measured with the PIV dataset at $Re_\theta = 1300$, 2000 (in the XY plane only) and in both planes at $Re_\theta = 7630$ and with the DNS dataset at $Re_\tau = 950$. The PDF in this domain are plotted in figure 6.25 for the XY plane and in figure 6.26 for the YZ plane.
- the outer region with $y/\delta \in [0.6; 1]$. This region of the flow is only measured with the PIV dataset at Re_θ = 1300,2000 (in the XY plane only) and with the DNS dataset at $Re_\tau = 950$. The PDF in this domain are plotted in figure 6.27 for the XY plane and in figure 6.28 for the YZ plane.

The regions $y/\delta \in [0.25; 0.6]$ and $y/\delta \in [0.6; 1]$ are distinguished because the latter is expected to be influenced by the intermittency with the free stream, which is not the case for the former.

The overall agreement of the PDFs over the full range of Reynolds number and throughout the logarithmic region is quite good for both the XY planes and the YZ planes (see figures 6.23 and 6.24). Vortices with radius in the range $[2\eta; 30\eta]$ are found. A very good collapse of the PDF for the spanwise (detected in the XY plane) and streamwise (detected in the YZ plane) vortices is observed in the lowest range of radius for all Reynolds numbers, and in both PIV and DNS data. In particular, the most probable radius is found to be universal for all Reynolds numbers and for both type of vortices, at a value of 7η. Some scatter is visible for larger radius. A good collapse of the radius PDF was also observed by Stanislas et al (2008) in YZ planes of turbulent boundary layers at $Re_\theta = 7800$ and $Re_\theta = 15000$ in Kolmogorov scaling (in the logarithmic region).

In the region $y/\delta \in [0.25; 0.6]$ (figures 6.25 and 6.26), the agreement is still reasonable between the LTRAC datasets, the DNS dataset, and the LML dataset at $Re_\theta = 7630$, in both plane and the values of the most probable radius are conserved. The PDF of the radius in the DNS dataset has slightly shifted towards smaller radius.

In the region $y/\delta \in [0.6; 1]$ (figures 6.27 and 6.28), only the LTRAC datasets and the DNS dataset can be compared, as this region of the flow was not measured for the LML datasets. The most probable value for the radius in the LTRAC dataset is still

about 7η, but a distorsion of the PDF for the dataset at $Re_\theta = 1300$ in the large radius range is clearly visible. This explains the increase of the mean radius in the outer region that was observed in figure 6.15. The PDF of the radius in Kolmogorov scaling of the DNS dataset in both planes has continued to shift towards smaller radius (with a most probable value at 5η), and is now quite different to that of the LTRAC dataset. As was noted in figures 5.35 and 5.34, the dissipation and Kolmogorov profiles of the LTRAC dataset at $Re_\theta = 1300$ is in excellent agreement with that of the DNS. Consequently the PDF difference in this region cannot be attributed the normalization employed. Instead, it may be linked to a difference in vortical structure in the outer region of boundary layer and channel flows.

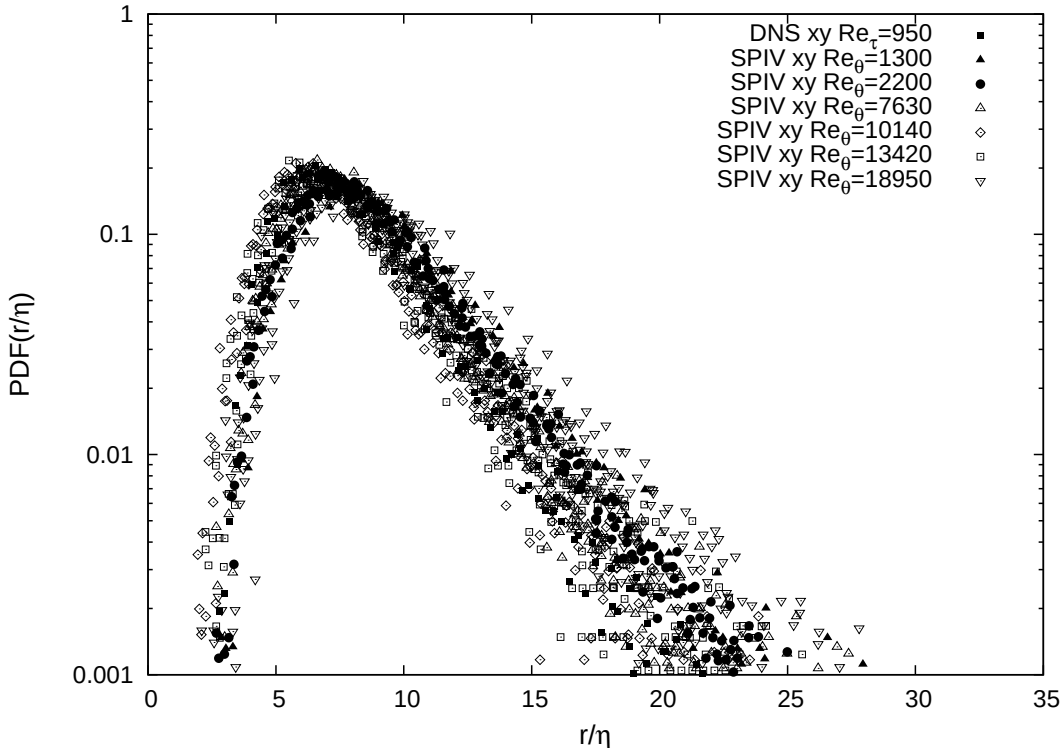

Figure 6.23: PDF of radius of the spanwise vortices (detected in the XY plane) in the logarithmic layer ($100 < y^+$ and $y/\delta < 0.25$)

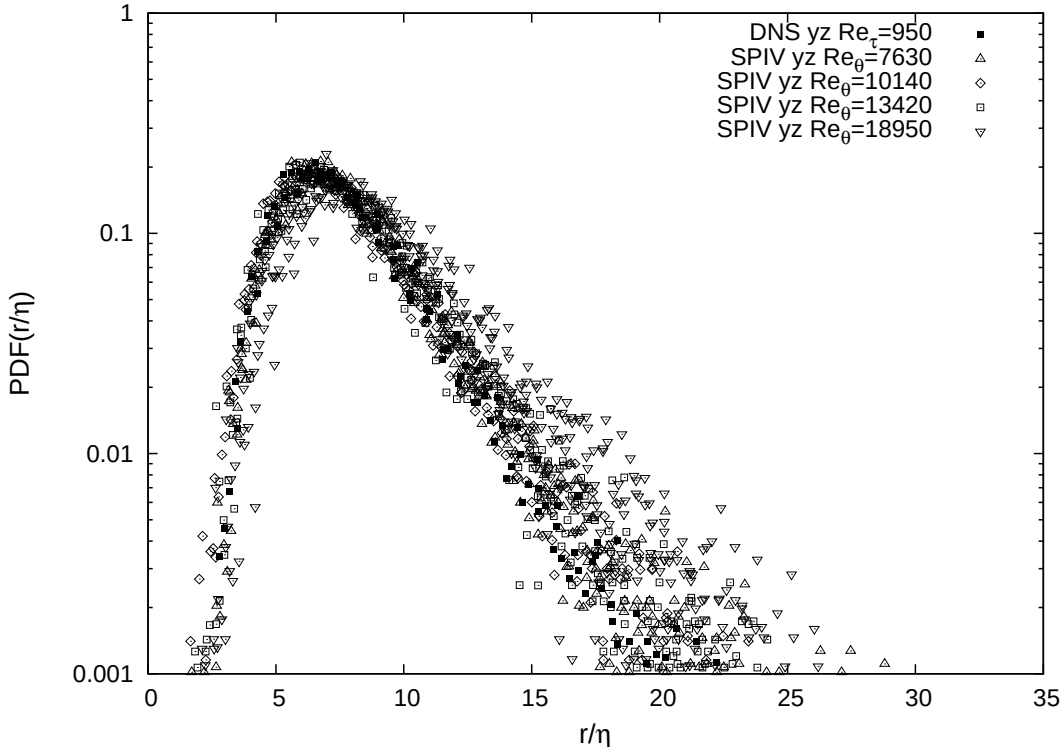

Figure 6.24: PDF of radius of the streamwise vortices (detected in the YZ plane) in the logarithmic layer ($100 < y^+$ and $y/\delta < 0.25$)

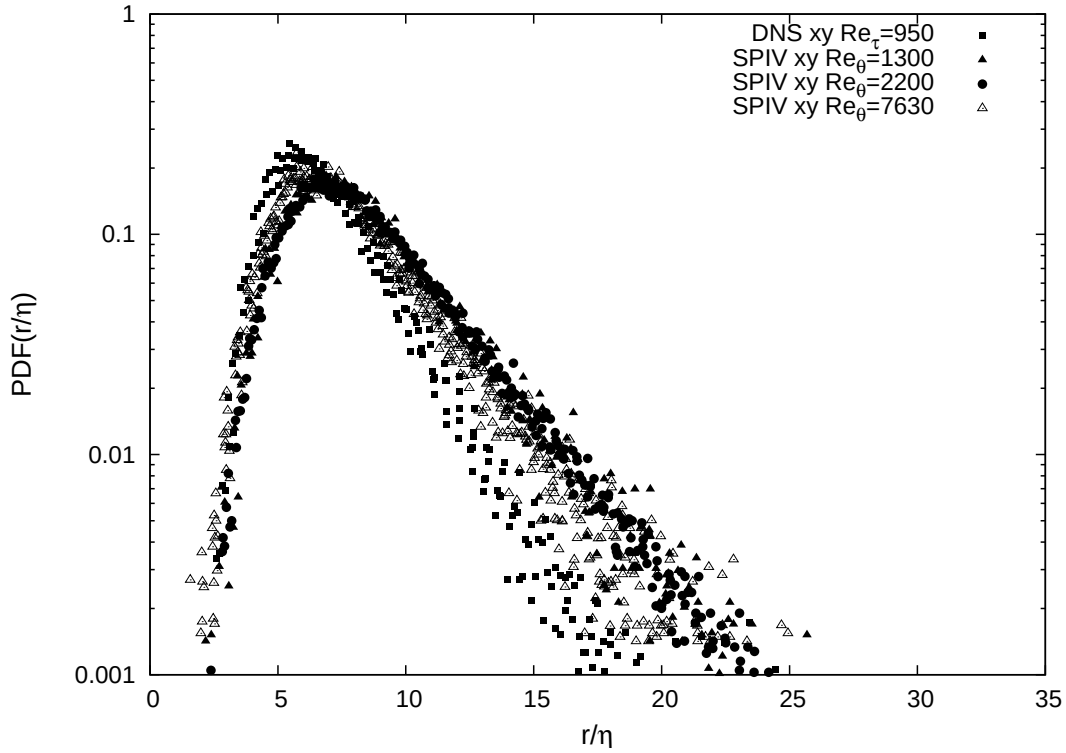

Figure 6.25: PDF of radius of the spanwise vortices (detected in the XY plane) for $y/\delta \in [0.25; 0.6]$

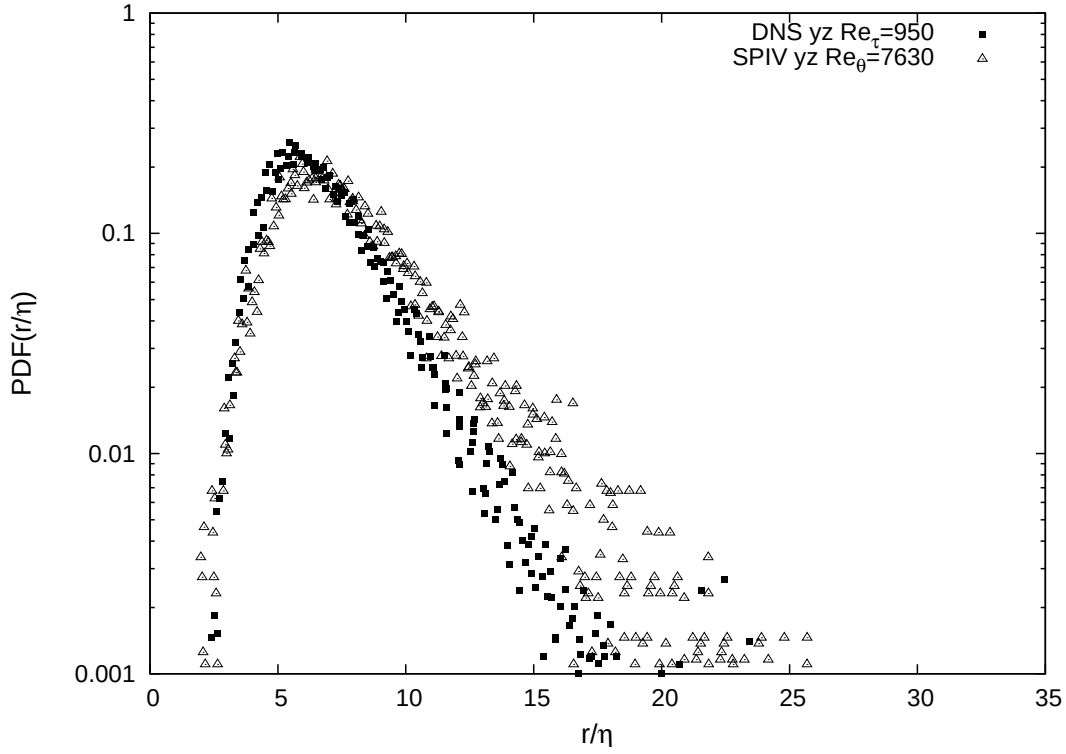

Figure 6.26: PDF of radius of the streamwise vortices (detected in the YZ plane) for $y/\delta \in [0.25; 0.6]$

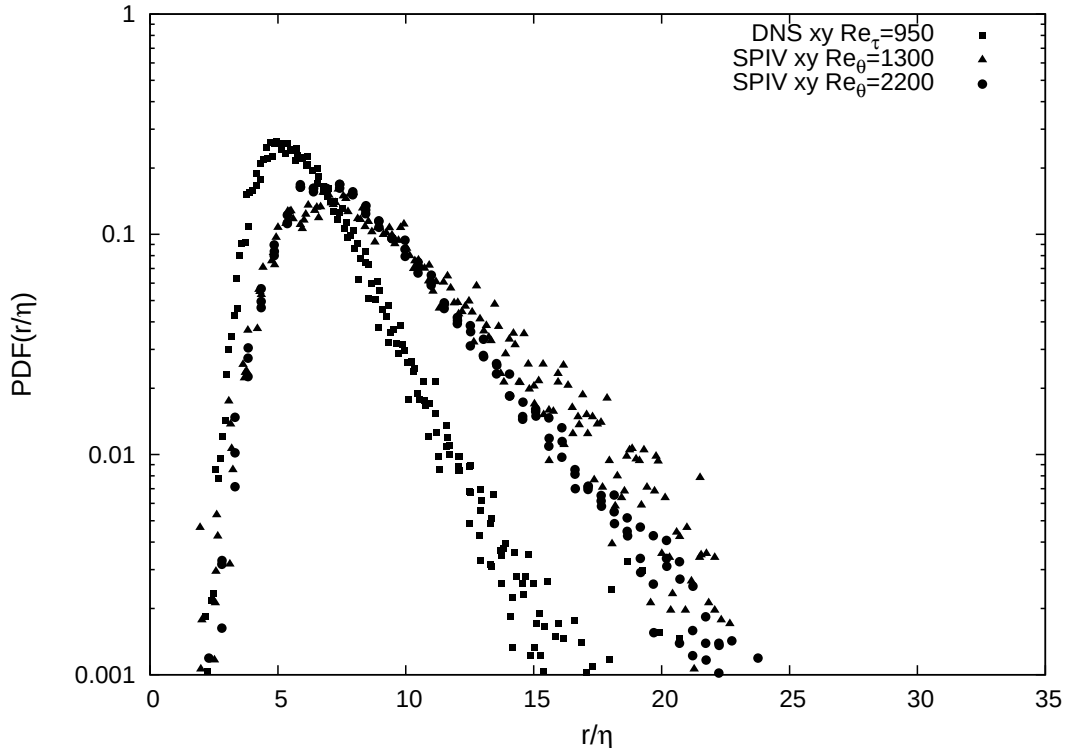

Figure 6.27: PDF of radius of the spanwise vortices (detected in the XY plane) for $y/\delta \in [0.6; 1]$

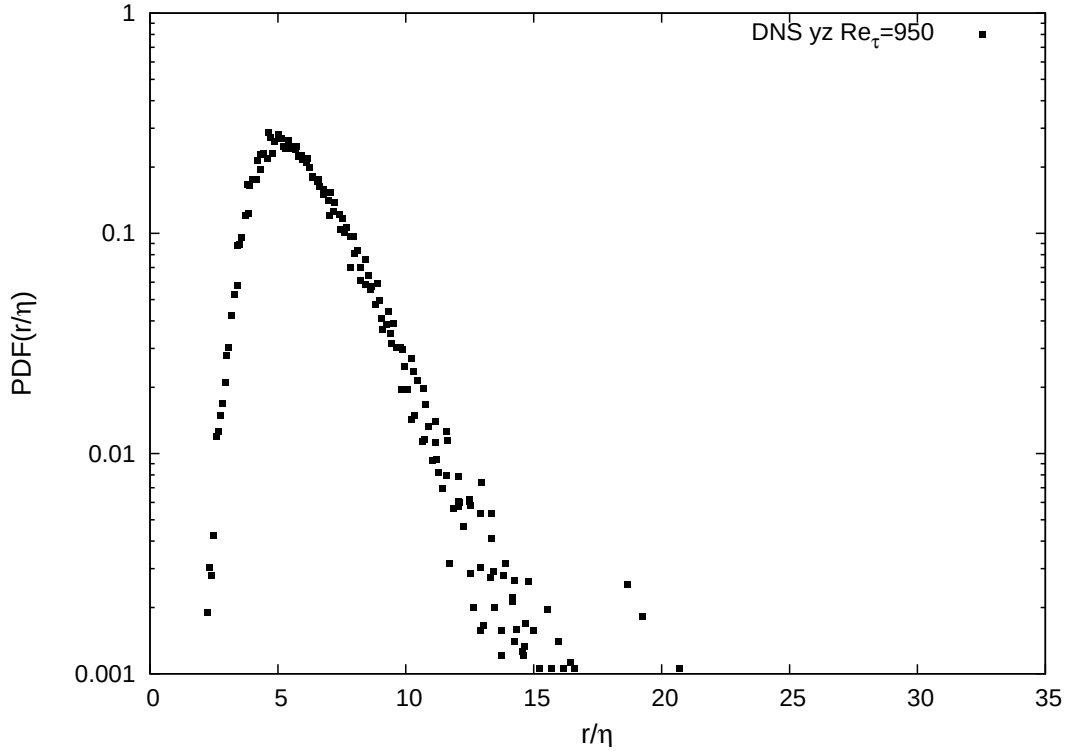

Figure 6.28: PDF of radius of the streamwise vortices (detected in the YZ plane) for $y/\delta \in [0.6; 1]$

6.2.2 Properties of the vorticity

The same kind of statistical analysis is now applied to the absolute value of the vorticity at the center of the vortices. This vorticity is not retrieved directly from the fit to an Oseen vortex, but is computed from the relationship between the circulation, the radius and the vorticity at the center of the vortex: $\Gamma = \omega_0 \pi r^2$. All the PDF are computed using the same normalization, bin values for the wall-normal location (layers of 50^+ in height) and for the vorticity (1/6 of the RMS value) as in the previous subsection; the wall-normal evolution of the mean vorticity is computed by taking into account eddies contained in layers of 25^+ in height.

The general trend for the distribution of the vorticity is first examined using the probability density function of the vorticity at various height in the XY plane (figure 6.29) and in the YZ plane (figure 6.30), with a wall unit scaling. Here again, only a few Reynolds number are represented: $Re_\tau = 950$, $Re_\theta = 2200$ and $Re_\theta = 13420$ for the XY plane, and $Re_\tau = 950$ and $Re_\theta = 13420$ for the YZ plane.
For the XY plane and the YZ plane, the vorticity distribution is such that $\omega_0^+ \in [0 : 0.7]$. The most probable vorticity value as well as the width of the distribution is found to decrease with increasing wall-normal distance; this behavior is inversely proportional to that of the radius. The most probable vorticity value is found to be $\omega_0^+ > \approx 0.2$ close to the wall ($y^+ \approx 75$) and $< \omega_0^+ > \approx 0.05$ away from the wall. The PDF in the region $y^+ \in [400; 900]$ appears to be narrower and centered at a lower value in the lowest Reynolds number range than in the highest Reynolds number range. This is probably because this region is still within the logarithmic layer for the dataset at $Re_\theta = 13420$, while it is in the outer region for the dataset at $Re_\tau = 950$ and $Re_\theta = 1300$. No clear difference appears on these plots between the XY plane and the YZ plane.
Since the vorticity displays a behavior with wall-normal distance that is the inverse of the radius, it is worth having a look at the mean circulation of the vortices. Its wall-normal evolution is plotted in figure 6.31 for the XY plane and in figure 6.32 for the YZ plane. It is found that the circulation of the streamwise vortices (detected in the YZ plane) is roughly constant everywhere, while for the spanwise vortices (detected in the XY plane), the circulation is constant in the region $y^+ > 250$ only.

The wall normal evolution of the absolute mean value of vorticity at the center of the vortices is represented in figure 6.33 for the spanwise vortices (detected in the XY plane) and in figure 6.34 for the streamwise vortices (detected in the YZ plane), in wall units. As it can be seen, in both planes, the vorticity decreases exponentially with the wall normal distance. In the near wall region ($y^+ < 250$) a good collapse of the vorticity in all datasets and in both planes is observed. At the wall, the profile of vorticity is tangent to the velocity gradient dU^+/dy^+ given by the van Driest law. The peak of vorticity at the wall is slightly higher for the streamwise vortices than for the spanwise vortices. This may indicate that the streamwise vortices are more intensified by the mean velocity gradient than the spanwise vortices. In the outer region (visible on the datasets at $Re_\theta = 1300$, $Re_\tau = 950$, $Re_\theta = 2000$ and $Re_\theta = 7630$), a clear Reynolds effect is visible: the lower the Reynolds number, the lower the vorticity at the center of the vortices.

In the XY plane, the wall-normal evolution of the prograde ($w_0 < 0$) and retrograde ($w_0 > 0$) spanwise vortices are compared in figure 6.35 for the highest Reynolds number

range and in figure 6.36 for the lowest Reynolds number range. Note that, in order to preserve the clarity of the graph for the highest Reynolds number range, the mean vorticity of the dataset at $Re_\theta = 13420$ was not represented, because it is very similar to that of the dataset at $Re_\theta = 7630$. For all Reynolds numbers, it can be seen that the prograde vortices have stronger vorticity at their center than the retrograde vortices; this difference increases with decreasing wall-normal distance. The peak of vorticity at the wall is noticeably higher for the prograde vortices than for the retrograde vortices. It was checked that the behavior of the streamwise vortices is the same for both signs of the vorticity.

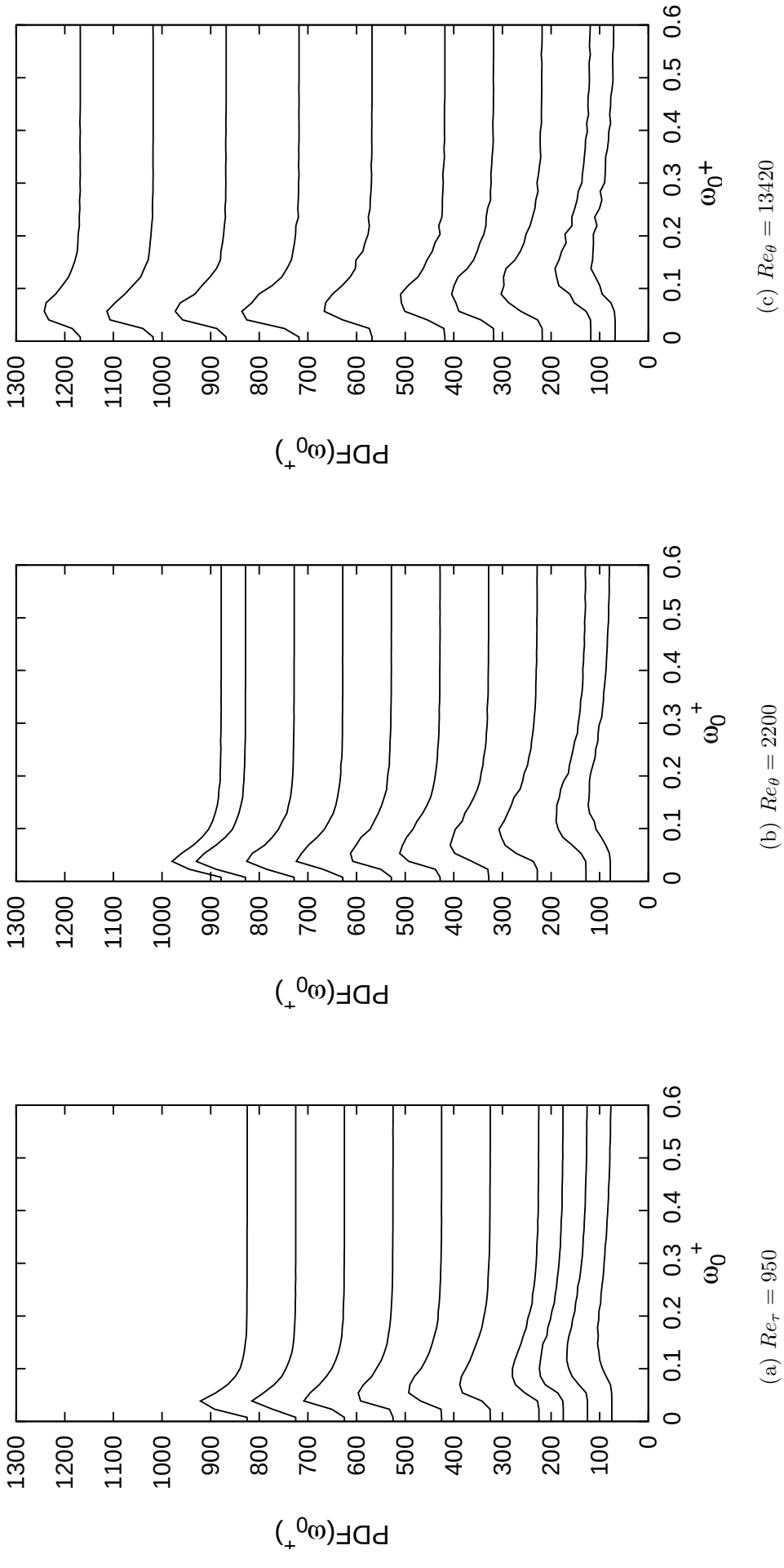

(a) $Re_\tau = 950$ (b) $Re_\theta = 2200$ (c) $Re_\theta = 13420$

Figure 6.29: PDF of vorticity, obtained at various heights in the XY plane, in wall units

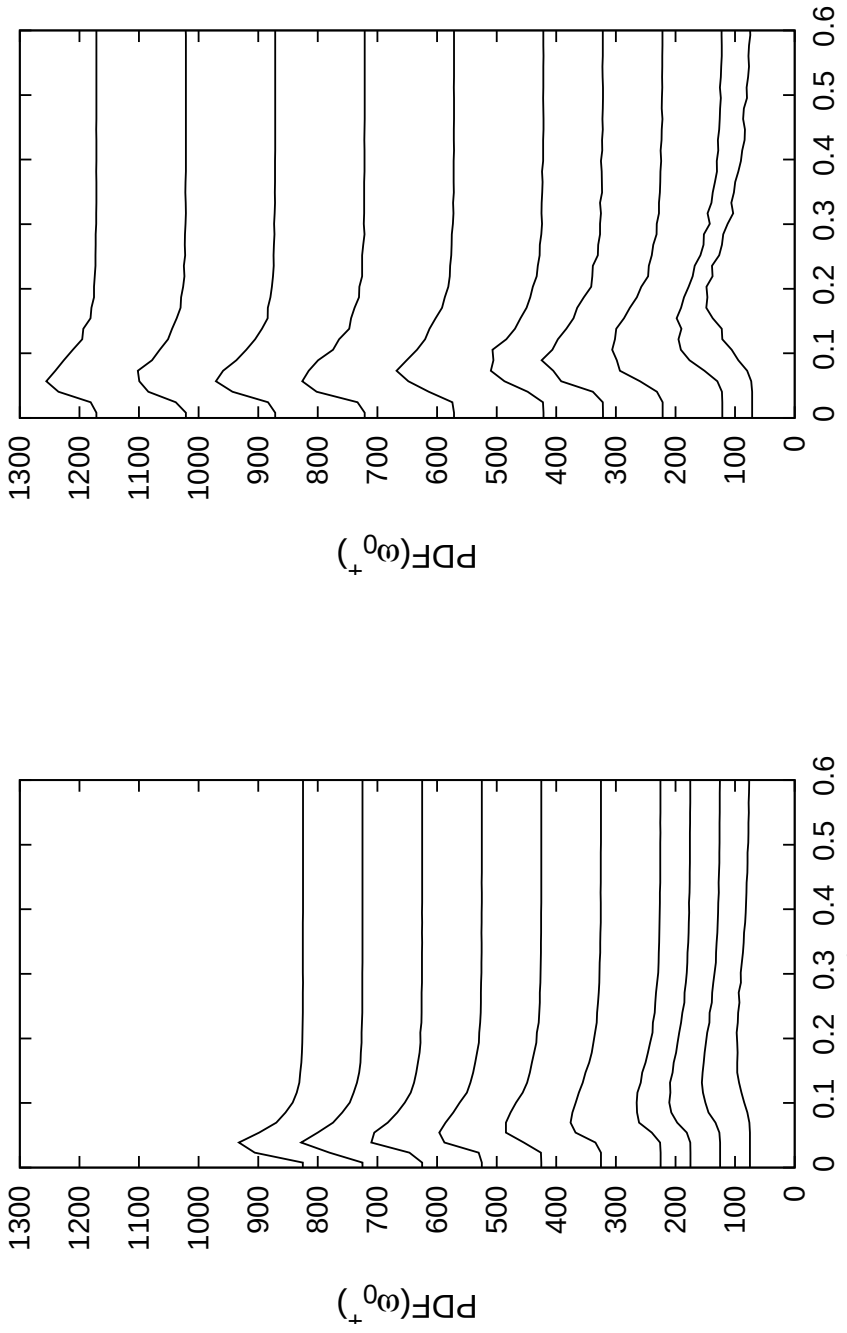

(a) $Re_\tau = 950$

(b) $Re_\theta = 13420$

Figure 6.30: PDF of vorticity, obtained at various heights in the YZ plane, in wall units

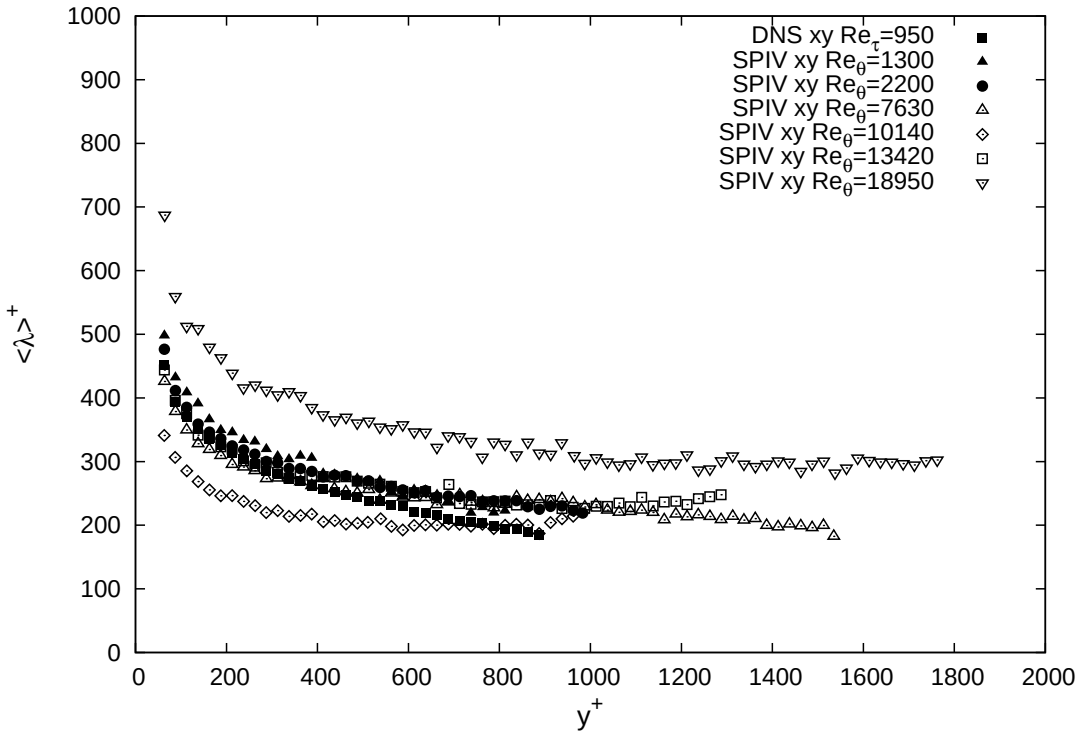

Figure 6.31: Wall-normal evolution of the mean circulation of spanwise vortices (XY plane), in wall-units

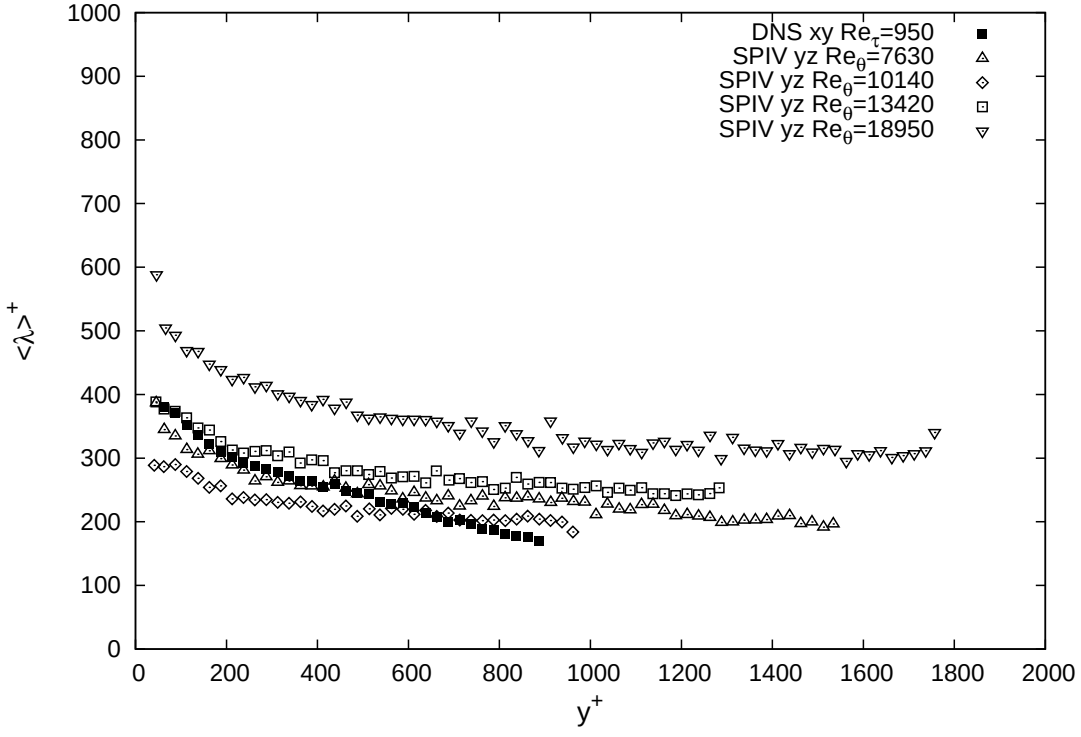

Figure 6.32: Wall-normal evolution of the mean circulation of streamwise vortices (YZ plane), in wall-units

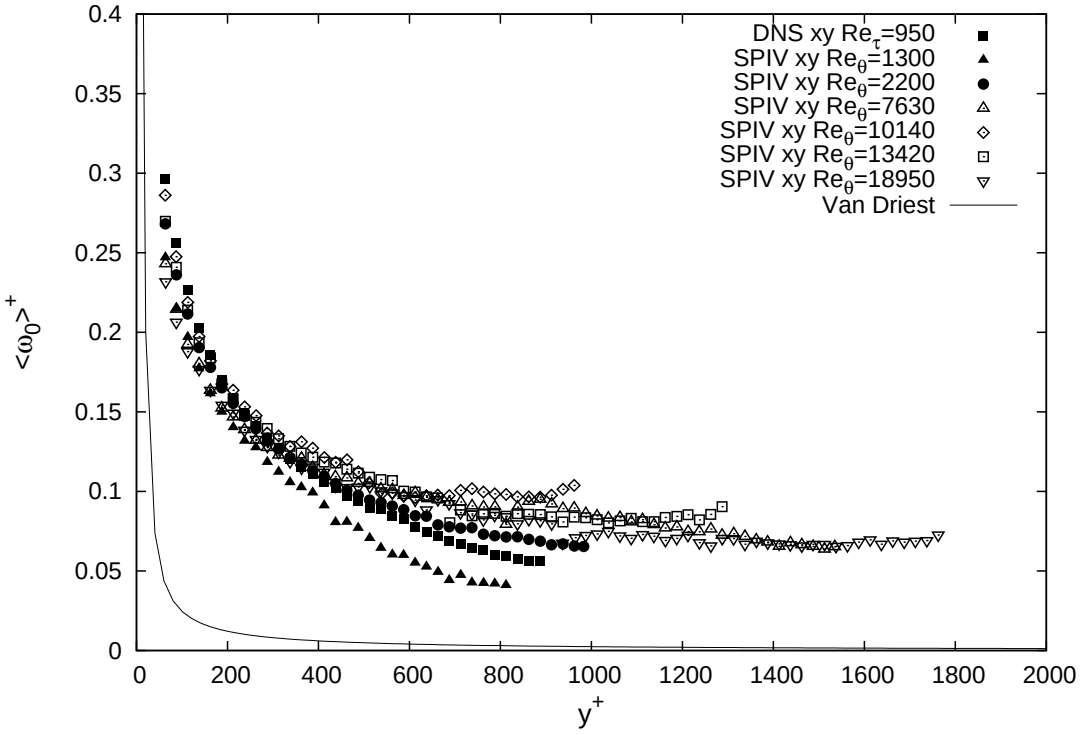

Figure 6.33: Wall-normal evolution of the vorticity of spanwise vortices (XY plane), in wall-units

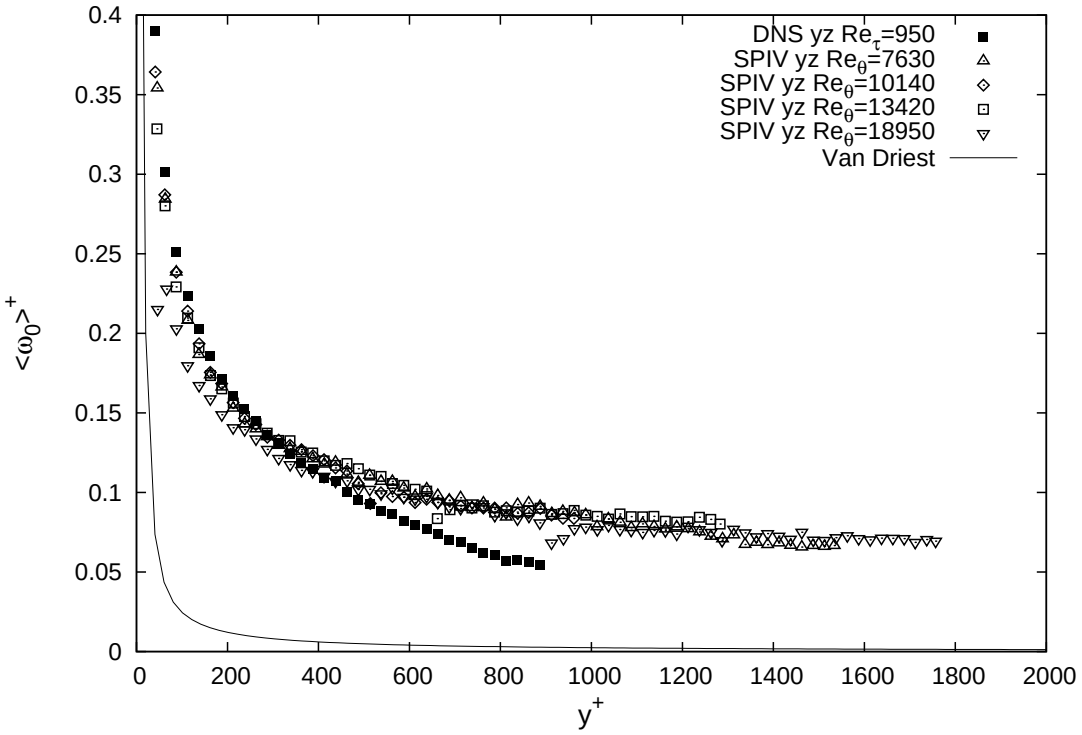

Figure 6.34: Wall-normal evolution of the vorticity of streamwise vortices (YZ plane), in wall-units

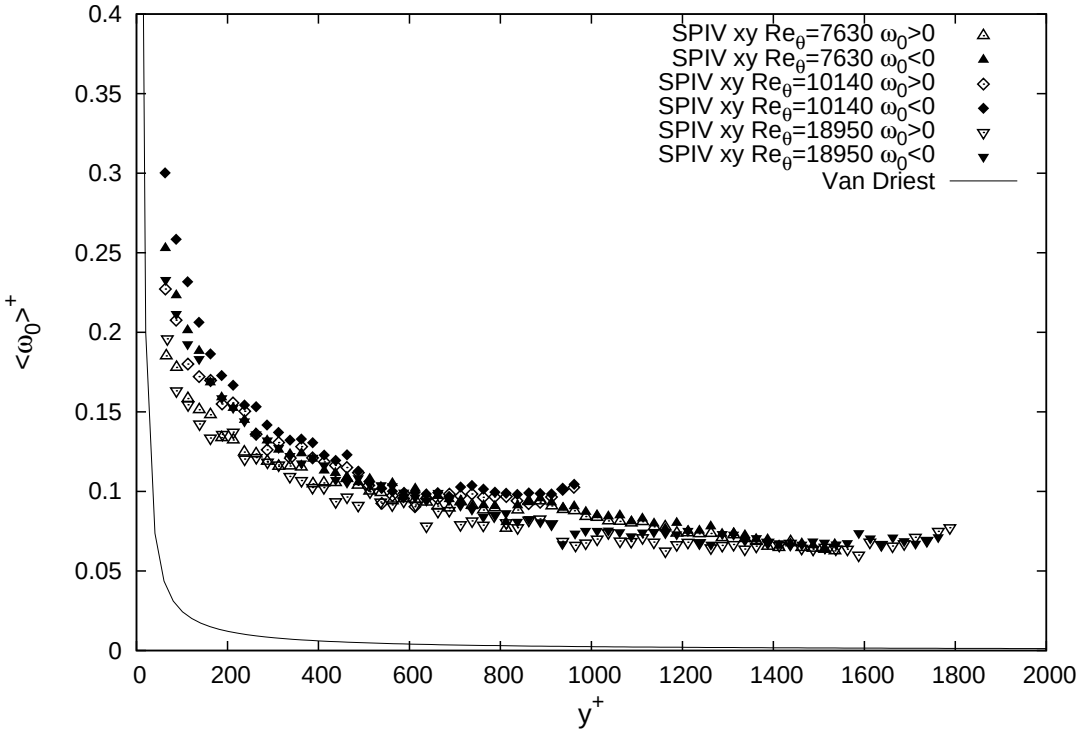

Figure 6.35: Wall-normal evolution of the vorticity of spanwise vortices (XY plane) in the highest Reynolds number range, depending on sign of the vorticity

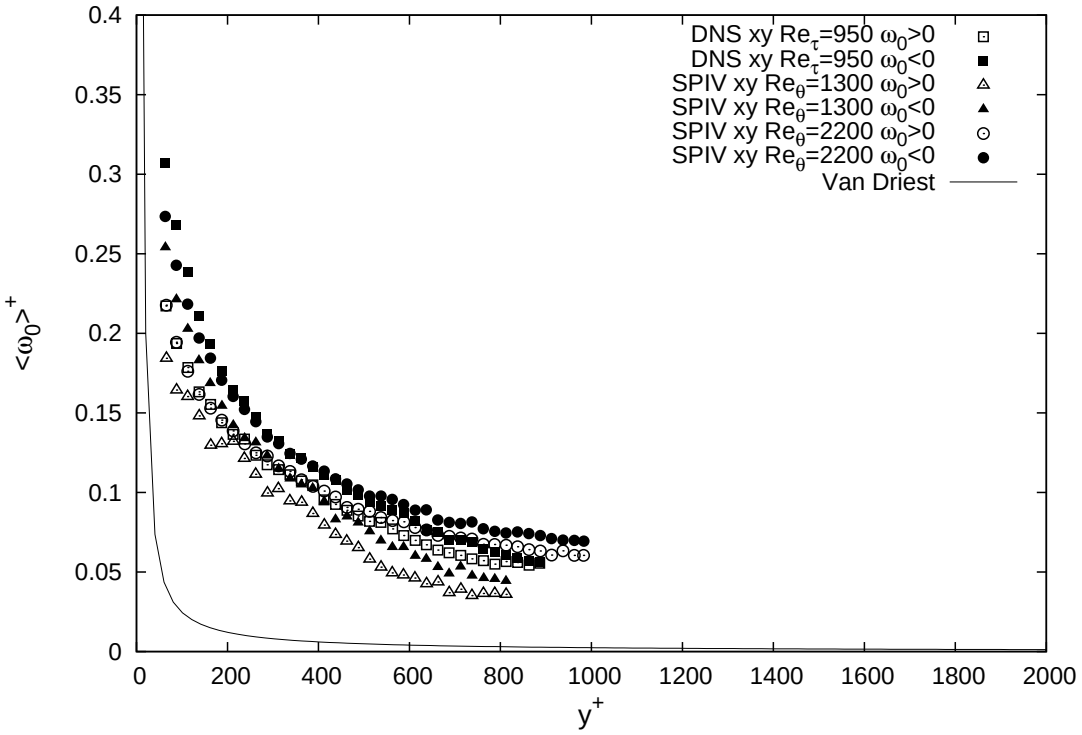

Figure 6.36: Wall-normal evolution of the vorticity of spanwise vortices (XY plane) in the lower Reynolds number range, depending on sign of the vorticity

The wall-normal evolution of the mean vorticity scaled with the inverse of the Kolmogorov time scale is plotted in figure 6.37 for the XY plane and in figure 6.38 for the YZ plane. The behavior is similar in the two planes. The quantity $< w_0 > \tau$ appears to be quite constant in the upper buffer layer and in the logarithmic region of the SPIV datasets ($< w_0 > \tau \approx 1.4 \pm 0.1$), and both in the logarithmic region and outer region of the DNS dataset ($< w_0 > \tau \approx 1.6 \pm 0.05$). In the outer region of the SPIV dataset at $Re_\theta = 1300, 2200, 7630$, it can be observed that the mean vorticity decreases slowly with increasing wall-normal distance (the outer region is not measured at higher Reynolds numbers).

The Kolmogorov scaling is then applied to the probability density functions $PDF(y_c, w_0)$. This time, the PDF are normalized so that for each layer in y:

$$\int_{w_0\tau} PDF_y(w_0\tau) = 1$$

For each plane, the PDF at the different wall-normal locations are then superimposed. Three regions in the flow are distinguished, as for the radius:

- the logarithmic layer ($100 < y^+$ and $y/\delta < 0.25$) that is available in all datasets. The PDF at the different wall normal location in this domain are plotted in figure 6.39 for the XY plane and in figure 6.40 for the YZ plane.
- the outer region with $y/\delta \in [0.25; 0.6]$. This region of the flow is measured with the PIV dataset at $Re_\theta = 1300$, 2000 (in the XY plane only) and in both planes at $Re_\theta = 7630$ and with the DNS dataset at $Re_\tau = 950$. The PDF in this domain are plotted in figure 6.41 for the XY plane and in figure 6.42 for the YZ plane.
- the outer region with $y/\delta \in [0.6; 1]$. This region of the flow is only measured with the PIV dataset at $Re_\theta = 1300$, 2000 (in the XY plane only) and with the DNS dataset at $Re_\tau = 950$. The PDF in this domain are plotted in figure 6.43 for the XY plane and in figure 6.44 for the YZ plane.

The overall agreement of the PDF over the full range of Reynolds number and throughout the logarithmic region is good for both the XY planes and the YZ planes (see figures 6.39 and 6.40). The vorticity at the center of the vortices is found to be in the range $[0.25\tau^{-1}; 8\tau^{-1}]$. In both planes, excellent agreement between the various datasets is found in the small and intermediate vorticity range ($w_0\tau \in [0.25; 3]$). In particular, the most probable value of the vorticity at the center of the vortices is $w_0\tau = 0.9$. In fact, the universality of the PDF for the vorticity seems even better than for the radius; this can be explained by the fact that the vorticity is more sensitive to the PIV time separation than to the PIV spatial resolution (see section 6.1.4). In the large vorticity range, some differences are noted; more vortices with large vorticity are detected in the DNS dataset, which is consistent with the higher value of mean vorticity that was found (see figures 6.37 and 6.38).

In both planes, the PDF of the DNS dataset remains the same in the regions $y/\delta \in [0.25; 0.6]$ and $y/\delta \in [0.6; 1]$. In contrast, a small shift towards smaller vorticity is visible on the PDF of the SPIV datasets at $Re_\theta \in [1300; 7630]$. The most probable vorticity of

these datasets is $w\tau = 0.8$ in the region $y/\delta \in [0.25; 0.6]$ and $w\tau = 0.65$ in the region $y/\delta \in [0.6; 1]$.

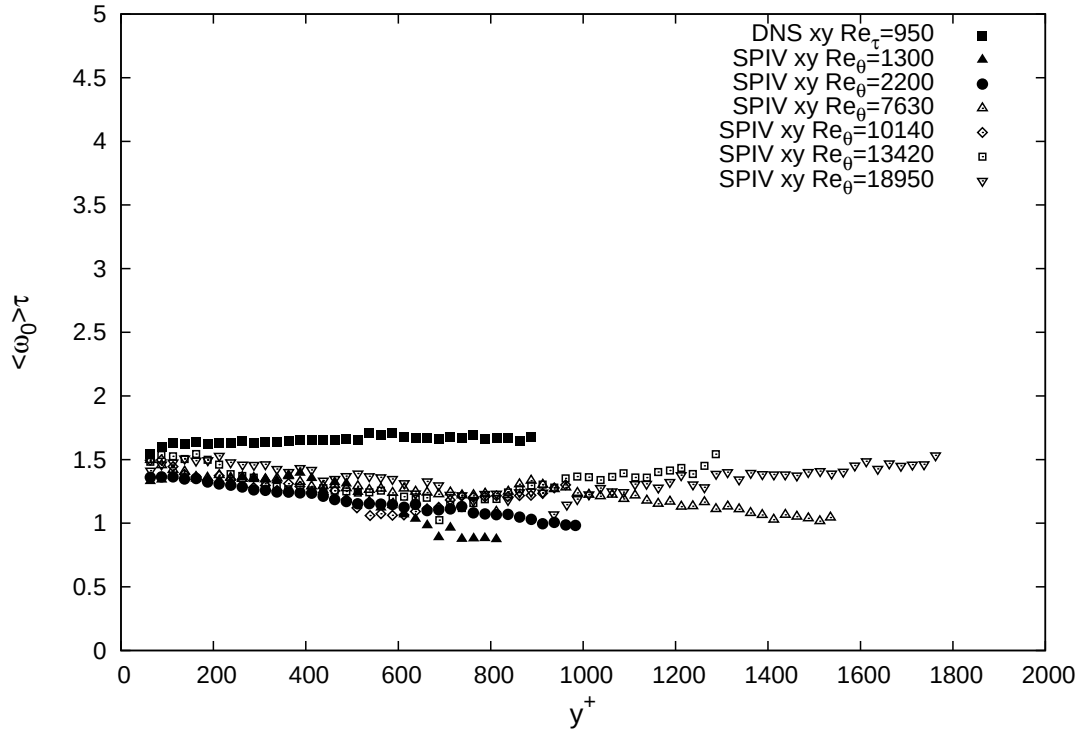

Figure 6.37: Wall-normal evolution of the mean vorticity of spanwise vortices (XY plane), in Kolmogorov units

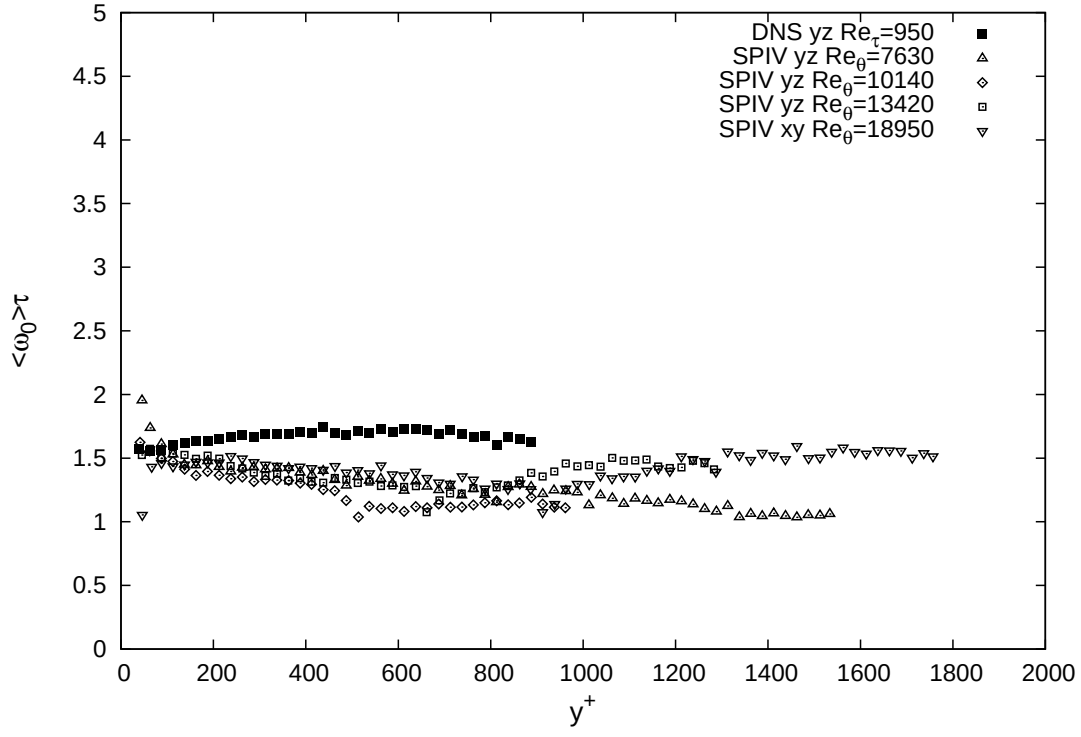

Figure 6.38: Wall-normal evolution of the mean vorticity of streamwise vortices (YZ plane), in Kolmogorov units

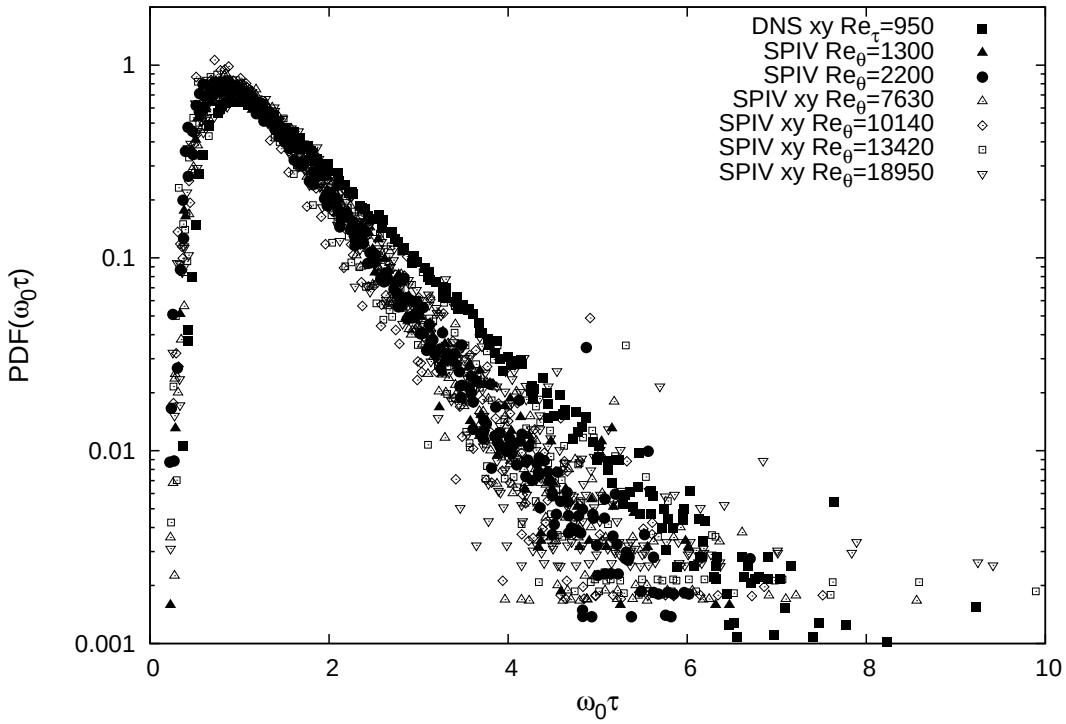

Figure 6.39: PDF of vorticity of the spanwise vortices (XY plane) in the logarithmic layer ($100 \leq y^+$ and $y/\delta < 0.25$)

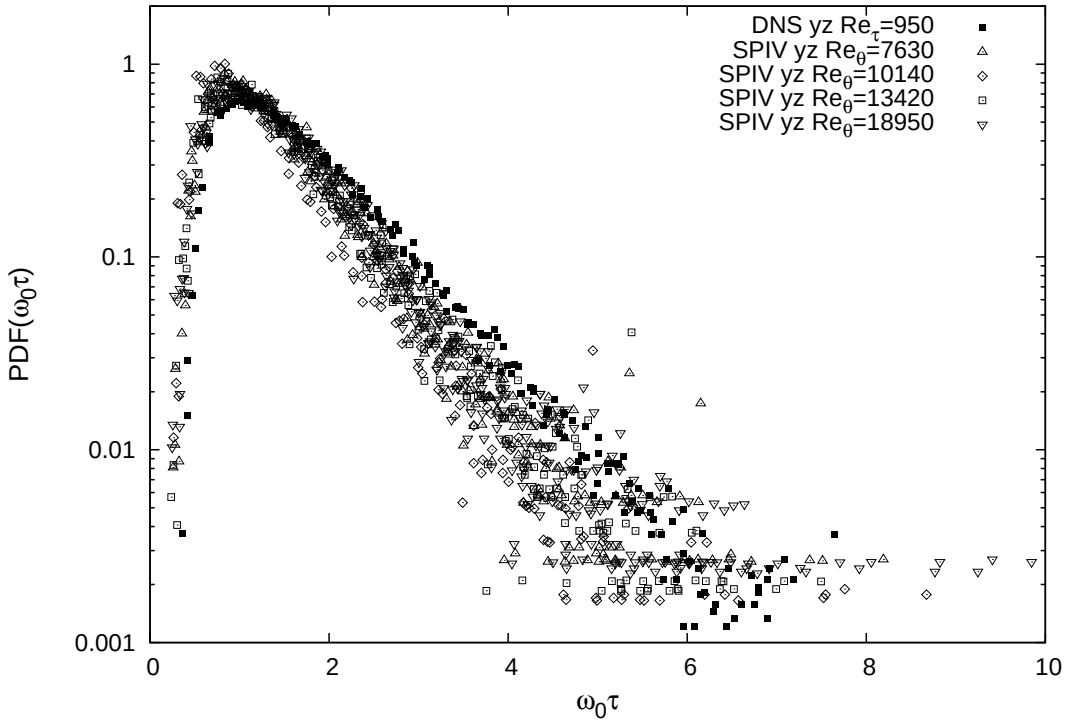

Figure 6.40: PDF of vorticity of the streamwise vortices (YZ plane) in the logarithmic layer ($100 \leq y^+$ and $y/\delta < 0.25$)

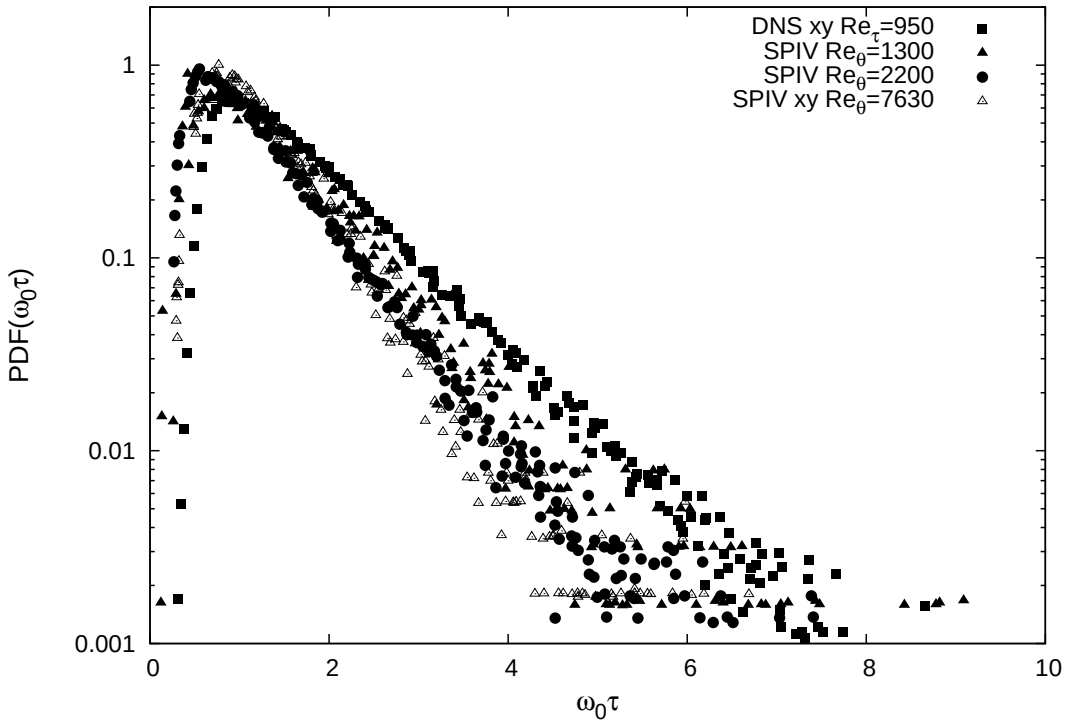

Figure 6.41: PDF of vorticity of the spanwise vortices (XY plane) for $y/\delta \in [0.25; 0.6]$

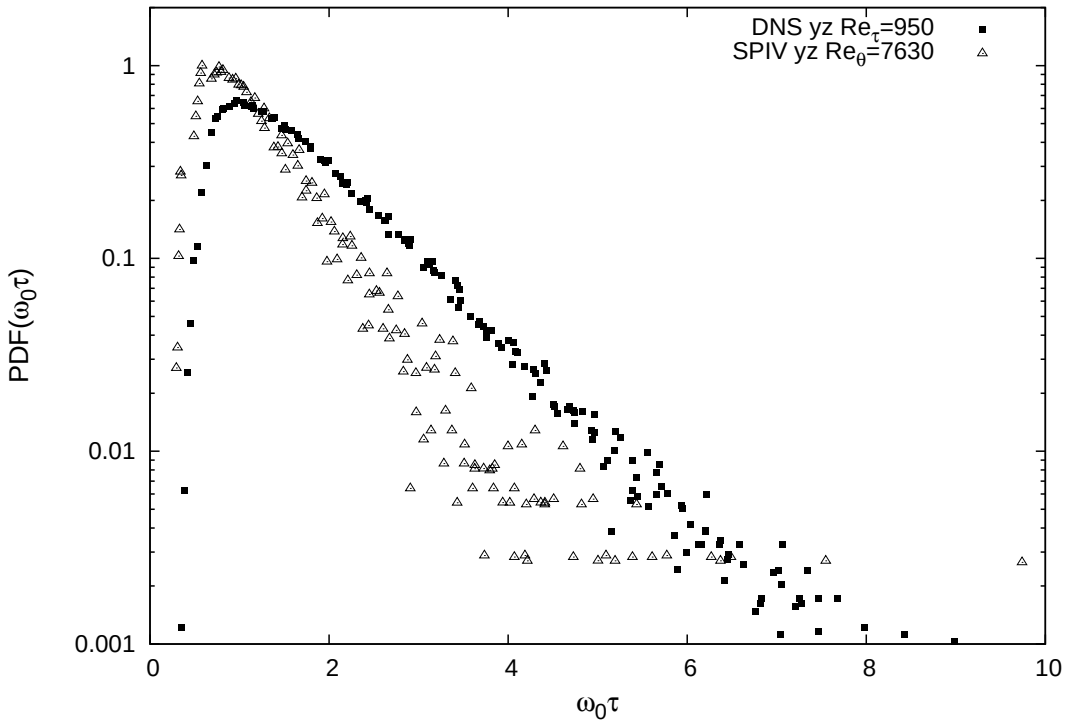

Figure 6.42: PDF of vorticity of the streamwise vortices (YZ plane) for $y/\delta \in [0.25; 0.6]$

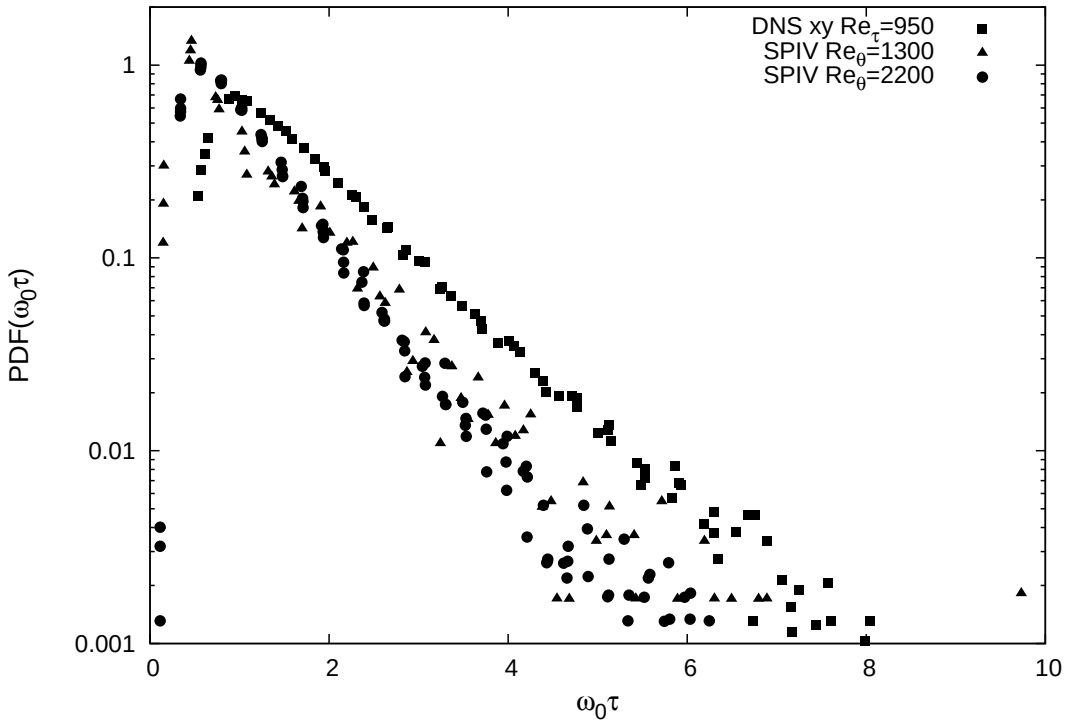

Figure 6.43: PDF of vorticity of the spanwise vortices (XY plane) for $y/\delta \in [0.6; 1]$

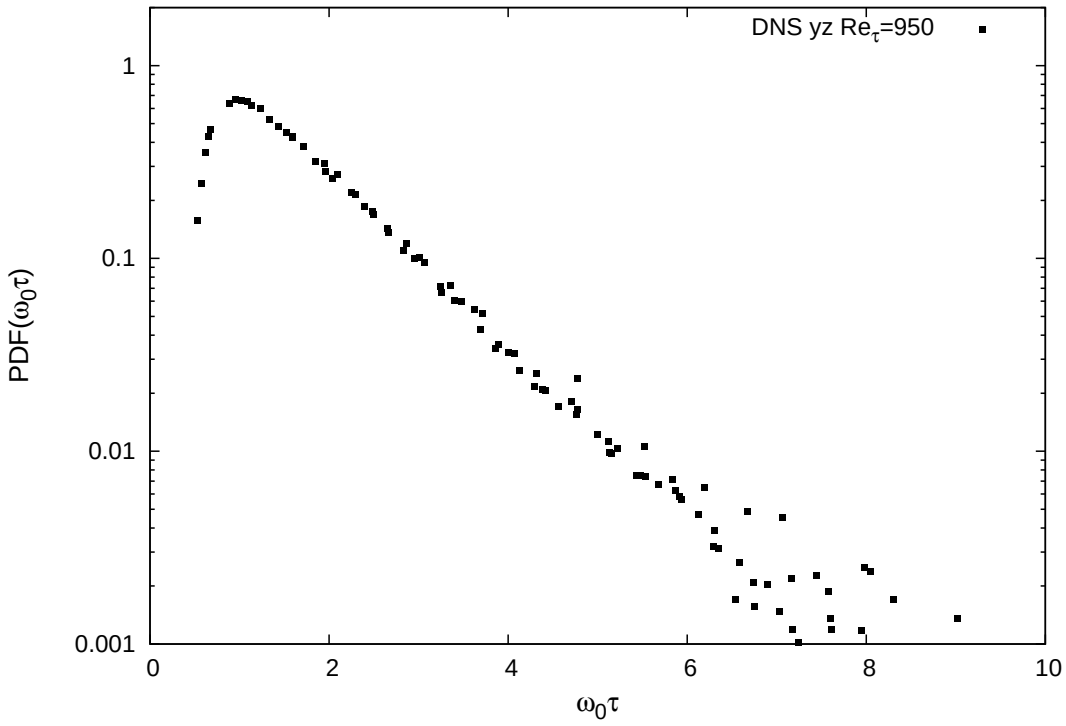

Figure 6.44: PDF of vorticity of the streamwise vortices (YZ plane) for $y/\delta \in [0.6; 1]$

6.2.3 Density of vortices

The general trends for the wall-normal evolution of the vortex densities in the XY plane and in the YZ plane are first analyzed. The densities were computed for all datasets by taking into account eddies contained in layers of 25^+ in height, and normalized so that it represents the density of vortices per wall-unit square. It was shown in section 6.1.4 that the spatial resolution influences the absolute level of the vortex density, especially near the wall. For the Lille turbulent boundary layers, the dataset at $Re_\theta = 10140$ is represented (figure 6.45) because it has the highest spatial resolution, and hence the most accurate density profile; the dataset at $Re_\theta = 7630$ (figure 6.46) is also plotted, because some part of the wake region ($0.25\delta < y < 0.6\delta$) is visible there. It was checked that the vortex densities at $Re_\theta = 13420$ are in very good agreement with those of the dataset at $Re_\theta = 7630$, and that the dataset at $Re_\theta = 18950$ shows no different effects other than spatial-resolution related. For the LTRAC turbulent boundary layer, all datasets are shown ($Re_\theta = 1300$ in figure 6.48 and $Re_\theta = 2200$ in figure 6.49), because it is of interest to check the effect of the free stream turbulence intensity. Finally, the density in the DNS of channel flow at $Re_\tau = 950$ is also represented (figure 6.47). In each figure, the total density of vortices in the XY plane, the density of prograde vortices ($w_0 < 0$) in the XY plane, the density of retrograde vortices ($w_0 > 0$) in the XY plane, and the total density of vortices in the YZ plane are represented. Note that for the LTRAC boundary layers, only the vortices detected in the XY plane are shown, because no YZ measurements were carried out in that facility.

In the region $y^+ < 150$, the streamwise oriented vortices (detected in the YZ plane) are more numerous than the spanwise oriented vortices (detected in the XY plane). The fact that quasi-streamwise vortices are the major constituent of the near-wall region was also observed using a λ_2 criterion by Jeong et al (1997) in a DNS of channel flow at $Re_\tau = 180$ and by Sheng et al (2008) in holographic 3D velocity field of a turbulent boundary layer at $Re_\tau = 1400$. For all datasets, the wall-normal location where the density of the streamwise vortices reaches a maximum is obtained at $y^+ \approx 60$, except for the dataset at $Re_\theta = 18950$ where the peak appears further away from the wall ($y^+ = 90$) owing to a lack of spatial resolution. After this maximum is reached, the density of streamwise vortices decreases rapidly with increasing wall-normal distance. This behavior of the streamwise vortices density in the near-wall region is in good agreement with the findings of Stanislas et al (2008) in SPIV measurements of a turbulent boundary layer at $Re_\theta = 7800$. The density of the spanwise vortices, in contrast, continuously increases from the wall up yo $y^+ \approx 150$ where a maximum is reached. Among the spanwise vortices, the predominance of the prograde vortices is overwhelming. Both prograde and retrograde forms increase with increasing wall-normal distance, but at very different rates: the increase is very fast for the prograde vortices, and rather slow for the retrograde ones. This suggest that different mechanism are responsible for their formation.

In the outer region ($y^+ > 150$), the vortex densities behave differently. Firstly, it is of interest to note that the vortices population is now almost equally constituted of streamwise and spanwise vortices. The density of both vortices decreases at a medium rate with increasing wall-normal distance (more slowly than the rate of decrease of the streamwise vortices in the region $60 < y^+ < 150$). Again, the prograde and the retrograde

vortices follow different evolutions: the density of the prograde vortices continuously decreases with increasing wall-normal distance, while the density of the retrograde vortices stabilizes until $y/\delta = 0.5$, and then starts to increase again, at a very low rate (this portion of the flow is visible in the LTRAC datasets at $Re_\theta = 1300$ and 2200 and in the DNS dataset at $Re_\tau = 950$). It is worth noting that, in these three datasets, the density of prograde and retrograde vortices tends to an equal level at the edge of the boundary layer or on the channel centerline. The prograde and retrograde population densities in boundary layer flow and turbulent channel flow were studied in great details by Wu and Christensen (2006) in this region. They found the same wall normal evolution for the prograde vortices, however some differences are visible in the region $y > 0.5\delta$ for the retrograde vortices. Wu and Christensen (2006) found that, in that region, the density of the retrograde vortices was increasing for the turbulent channel flow only, but not for the turbulent boundary layer flows. They suggested that this difference between both flow was due to the fact that the increase of retrograde vortices at the outer edge of the channel flow may originate from the interaction with the flow along the opposite wall of the channel: retrograde vortices in the reference frame of the bottom wall of the channel are prograde vortices in the reference frame of the upper wall of the channel. The present results indicate that a large free-stream turbulence intensity can also have the same effects on turbulent boundary layers. Finally, comparing the two LTRAC datasets, it seems that the higher free-stream turbulence intensity in the dataset at $Re_\theta = 2200$ results in a larger spanwise vortex density in the outer region.

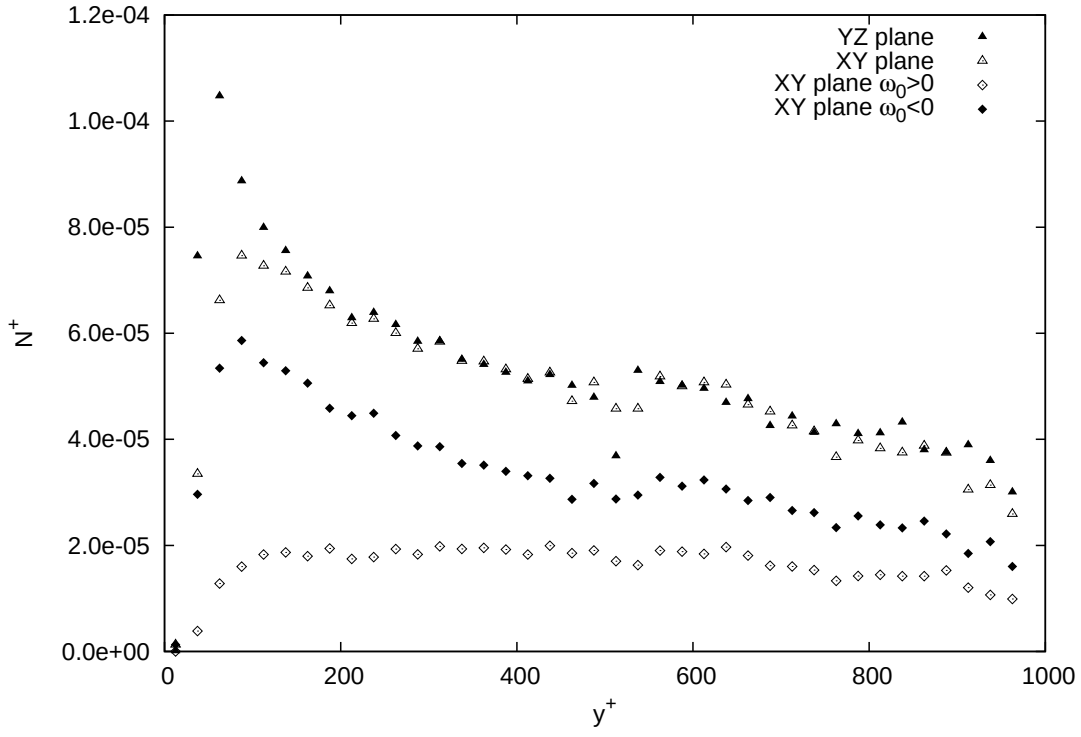

Figure 6.45: Density of vortices in the SPIV dataset at $Re_\theta = 10140$

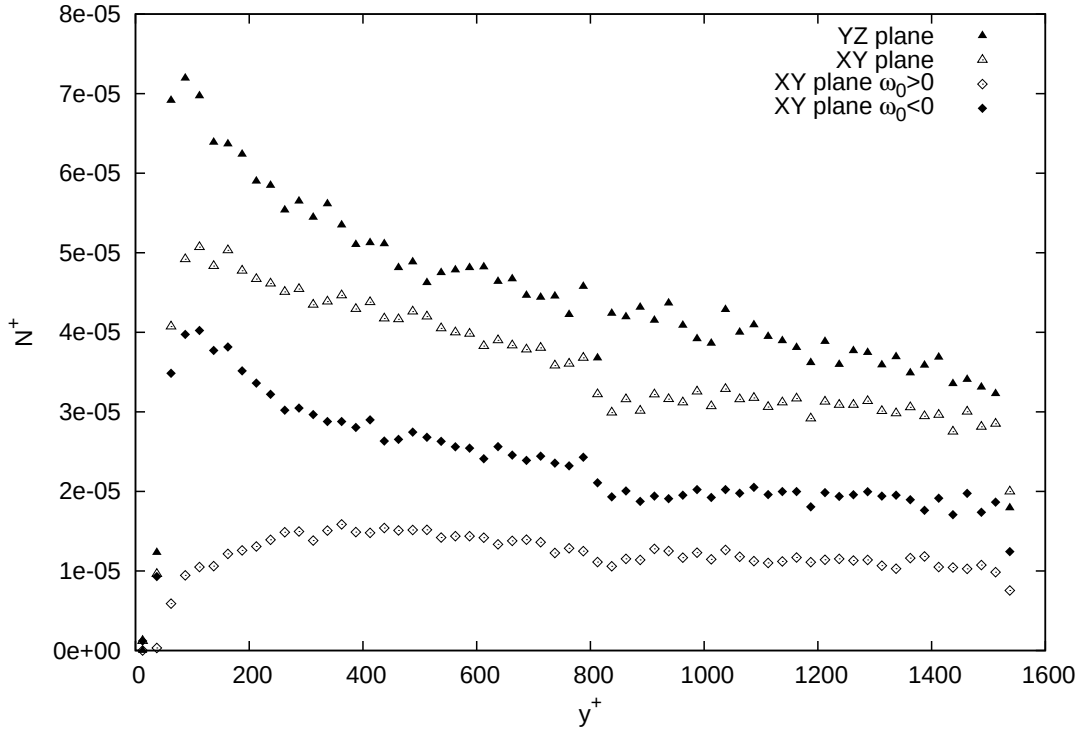

Figure 6.46: Density of vortices in the SPIV dataset at $Re_\theta = 7630$

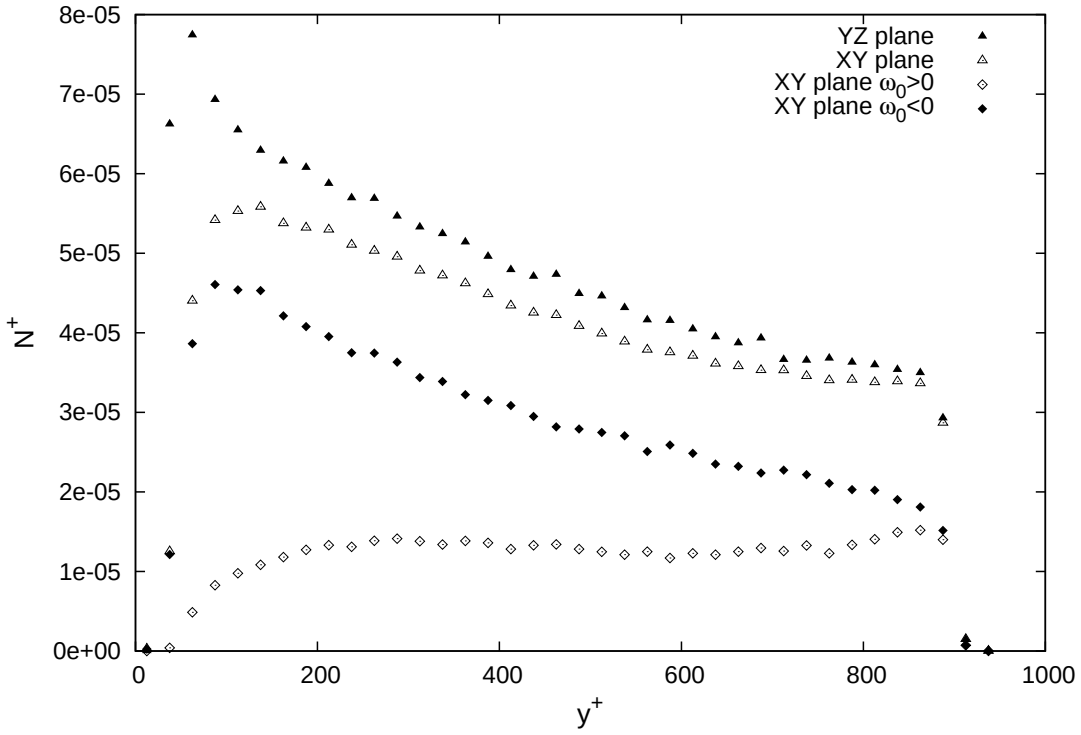

Figure 6.47: Density of vortices in the DNS dataset at $Re_\tau = 950$

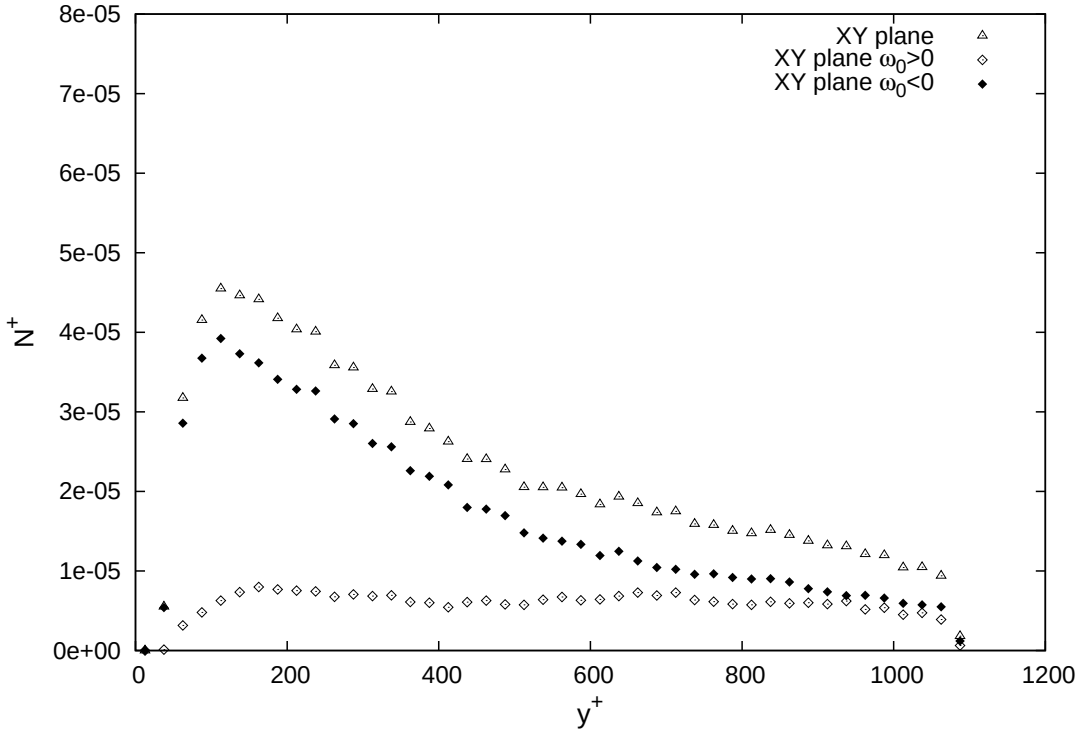

Figure 6.48: Density of vortices in the SPIV dataset at $Re_\theta = 1300$

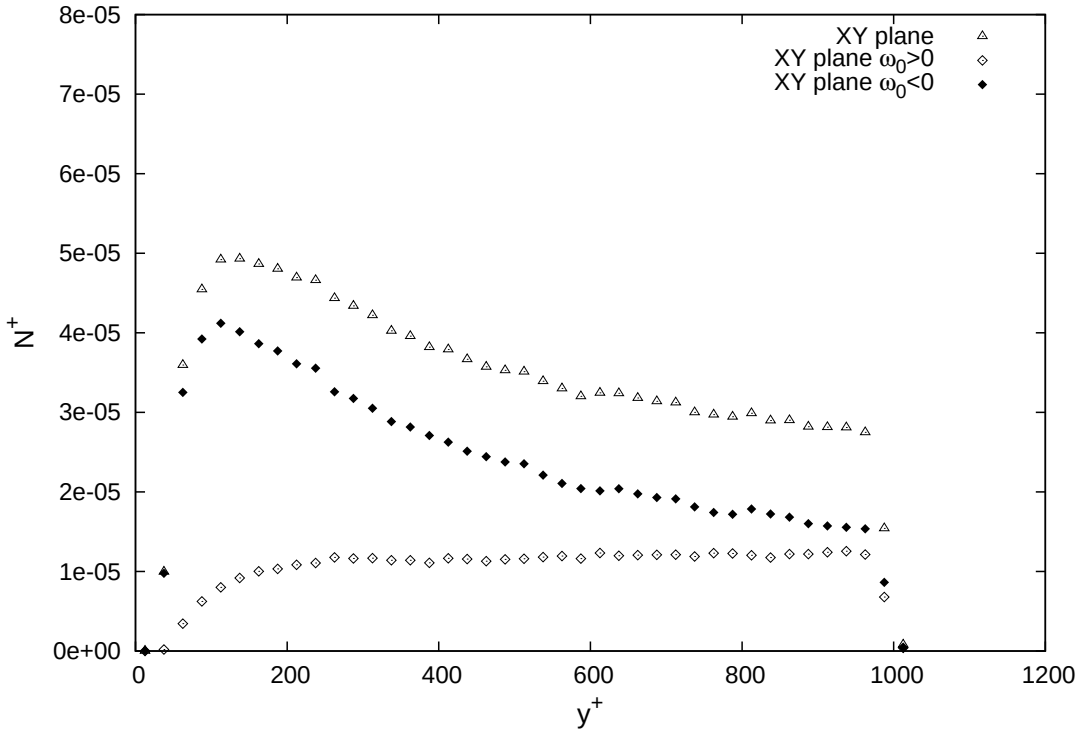

Figure 6.49: Density of vortices in the SPIV dataset at $Re_\theta = 2200$

Finally, the prograde and retrograde relative density is analyzed into more details through the wall normal evolution of the fraction of prograde and retrograde vortices, defined in equation 6.3. They are plotted for all Reynolds numbers, in figures 6.50 for the highest Reynolds number range, and in figure 6.51 for the lowest Reynolds number range. Filled symbols refer to prograde vortices, and hollow symbols refer to retrograde vortices.

$$\Phi_p(y) = \frac{N^+_{w<0}(XY)}{N^+_{w<0}(XY) + N^+_{w>0}(XY)} \qquad \Phi_r(y) = \frac{N^+_{w>0}(XY)}{N^+_{w<0}(XY) + N^+_{w>0}(XY)} \tag{6.3}$$

Note that $\Phi_p(y) = 1 - \Phi_r(y)$, so that one fraction can be deduced immediately from the other, but both of them are represented here for convenience. A value of 0.5 means that as many prograde as retrograde vortices are detected in the XY plane.
For the LML boundary layers (figure 6.50), the fractions $\Phi_p(y)$ collapse quite well for the different datasets, and so do the fractions $\Phi_r(y)$: no clear trend with the Reynolds number or with the spatial resolution can be retrieved. The fraction $\Phi_r(y)$ is zero at the wall, and increases strongly with increasing wall-normal distance in the near-wall region before stabilizing at $y^+ = 600$ at a value of 0.4. Good consistency is also observed between the LTRAC boundary layers and the DNS of channel flow (figure 6.51), but the behavior is different from that of the LML boundary layers: here the retrograde vortices fraction also increases strongly in the near-wall region, but never stabilizes and continues to increase slowly over the whole boundary layer thickness/half channel height. For $y/\delta \approx 1$, the prograde and retrograde vortex density tends to be equal, with $\Phi_p \approx \Phi_r \approx 0.5$. Since no Reynolds number effect is visible in the LML boundary layers, this different behavior may be attributed to the higher turbulence intensity in the channel centerline for the DNS and in the free stream of the LTRAC boundary layers.

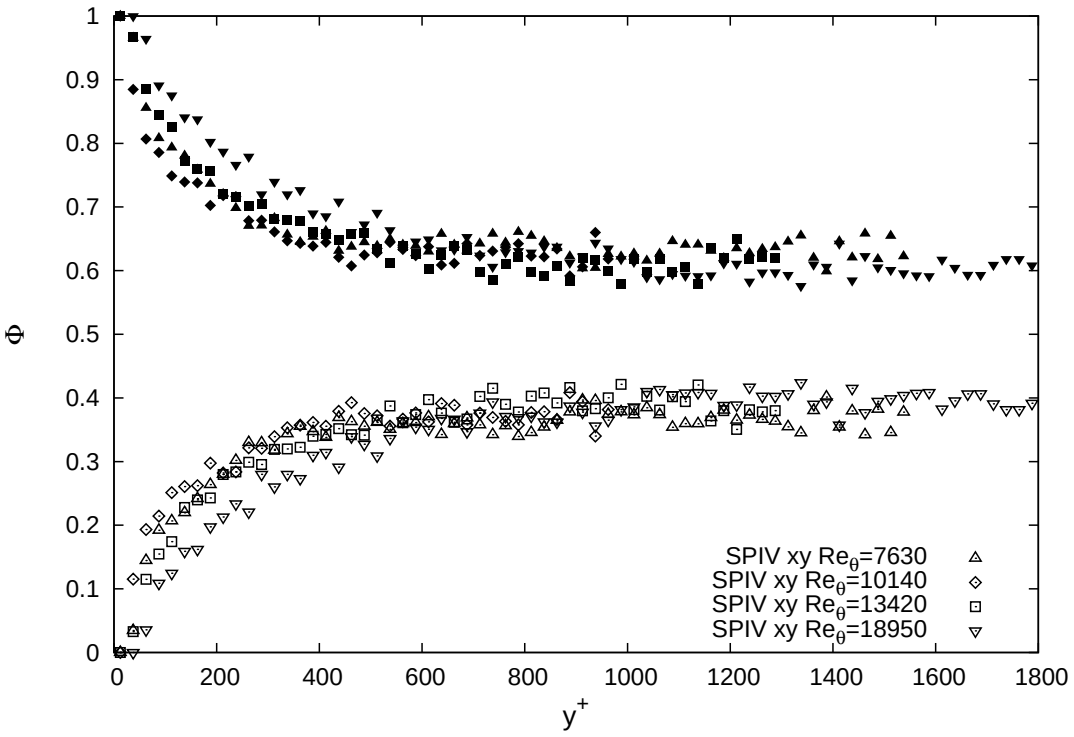

Figure 6.50: Fraction of prograde (black symbol) and retrograde (hollow symbol) vortices in the highest Reynolds number range

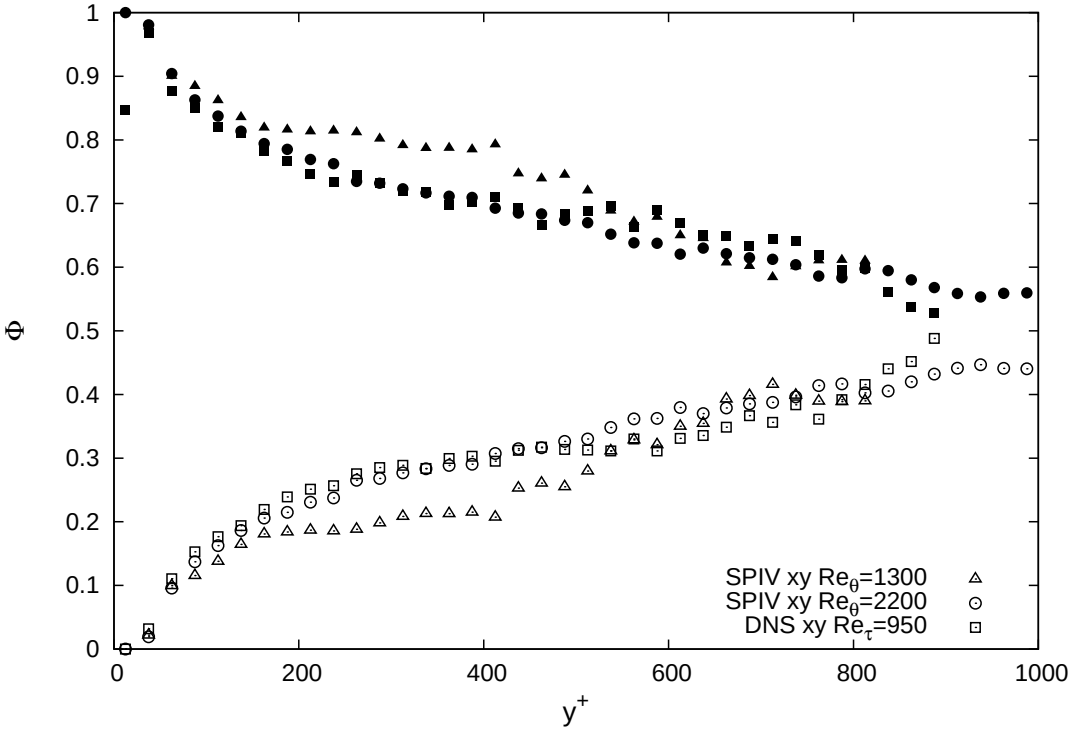

Figure 6.51: Fraction of prograde (black symbol) and retrograde (hollow symbol) vortices in the lowest Reynolds number range

6.2.4 Convection velocity of the vortices

The convection velocity of the vortices detected in the XY plane and in the YZ plane is analyzed for all the datasets of the database. For each plane orientation, the in-plane components of the convection velocity are retrieved through a fit of a convected Oseen vortex to the local in-plane velocity field (see equation 6.1). The out-of-plane component of the convection velocity could not be retrieved with the methodology employed. However, the out-of plane component of the velocity at the position of the fitted center of the vortex is analyzed.

The wall-normal evolution of the mean streamwise convection velocity of the vortices was computed by taking into account eddies contained in layers of 25^+ in height. For each dataset, it is plotted against the corresponding mean streamwise velocity profile.

The evolution for the spanwise vortices (detected in the XY plane) is plotted in figure 6.52 for the highest Reynolds number range and in figure 6.53 for the lowest Reynolds number range. The case of the prograde vortices ($\omega_0 < 0$) and of the retrograde vortices ($\omega_0 > 0$) are distinguished. Over the whole range of Reynolds numbers, it is found that the prograde vortices are convected with the mean streamwise velocity over the whole velocity field. As far as the retrograde vortices are concerned, their mean advection velocity is slightly larger than the mean streamwise velocity in the region $y^+ \in [40; 100]$, and then is in good agreement with the mean streamwise velocity over the rest of the field. These results are in good agreement with those of Wu and Christensen (2006), except that they didn't observe the different behavior of the retrograde vortices in the region $y^+ \in [40; 100]$. Adrian et al (2000a) and Carlier and Stanislas (2005) computed the mean streamwise convection velocity of the vortices, but without differentiating between the prograde and retrograde structures; they also found that the structures were advected with the mean streamwise velocity, although the results of Adrian et al (2000a) in the region $y/\delta > 0.3$ showed a different trend, probably owing to a lack of convergence of their results. According to Adrian et al (2000b), the convection velocity of the prograde hairpin 'heads' can be approximated to the first order by the velocity of the surrounding fluid minus the component due to self-induction, proportional to the circulation of the vortex core divided by its diameter. Consequently, it seems that in the present data, the prograde vortices have none or negligible backward-upward self induction. The inverse reasoning can be applied to the retrograde hairpin 'heads': their convection velocity is expected to be equal to the velocity of the surrounding fluid plus the component due to self-induction. Therefore, it seems that the retrograde vortices in the present data have significant forward-downward self induction in the near-wall region.

The wall-normal evolution of the mean streamwise velocity at the center of the streamwise vortices (detected in the YZ plane) is represented in figure 6.54 for the highest Reynolds number range. It matches quite well with the mean velocity profile for all Reynolds numbers, but is slightly lower in the region $y^+ < 200$. This phenomenon can also be observed in the results of Carlier and Stanislas (2005) in the YZ plane at $Re_\theta = 7500$.

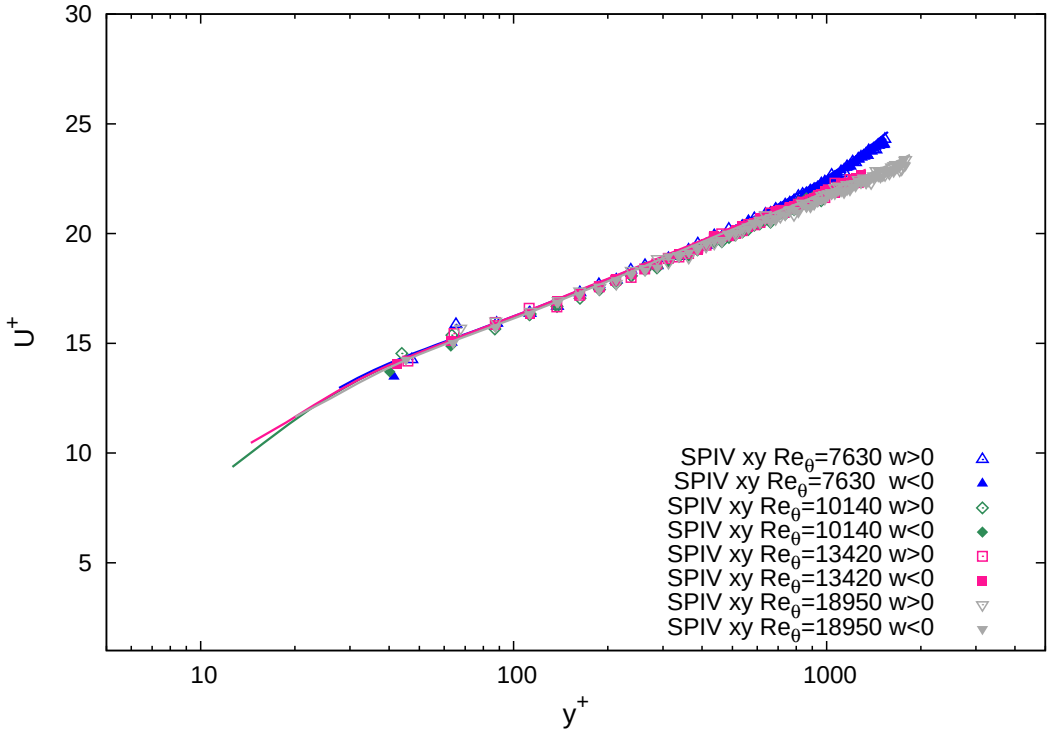

Figure 6.52: Wall-normal evolution of the mean streamwise convection velocity of the spanwise vortices detected in XY plane (points), compared to the mean streamwise velocity profile (solid line) in the highest Reynolds number range

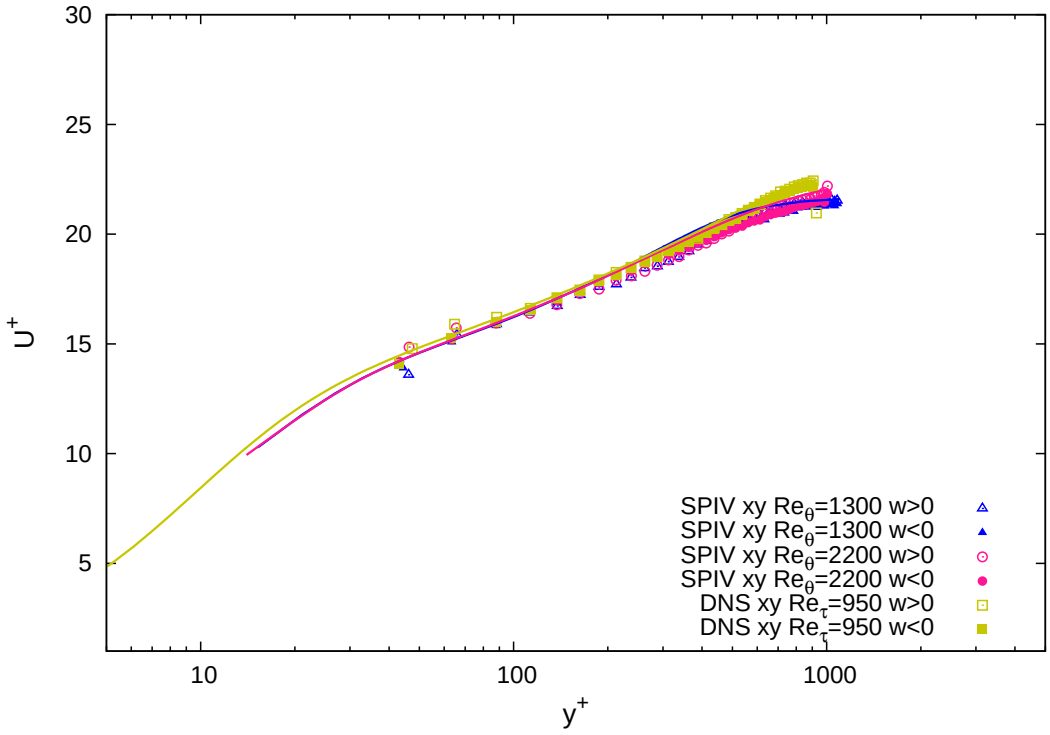

Figure 6.53: Wall-normal evolution of the mean streamwise convection velocity of the spanwise vortices detected in XY plane (points), compared to the mean streamwise velocity profile (solid line) in the lowest Reynolds number range

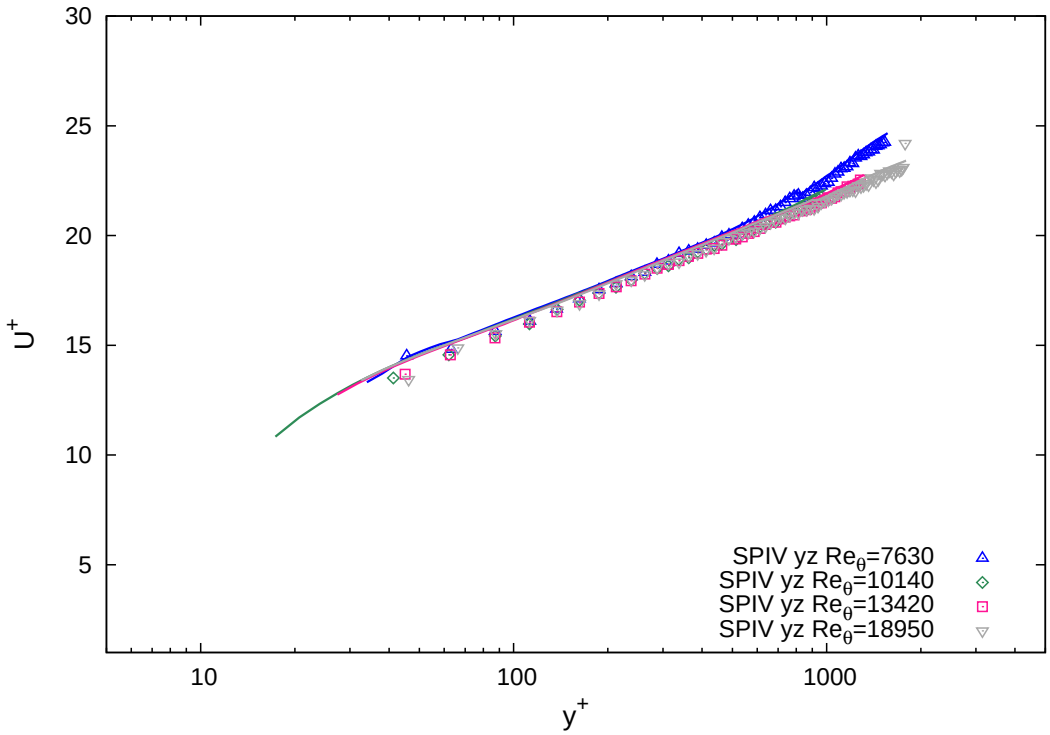

Figure 6.54: Wall-normal evolution of the mean streamwise convection velocity of the streamwise vortices detected in YZ plane (points) of the datasets at $Re_\theta \in [7630; 18950]$, compared to the mean streamwise velocity profile in each of these datasets

The wall-normal evolution of the standard deviation of the three components of the vortices convection velocity was then analyzed. To our knowledge, this is the first time such results are presented. These second-order statistics were computed by taking into account eddies contained in layers of 50^+ in height. As was shown in section 5.2, the standard deviation of the velocities for the LML database, for the LTRAC dataset at $Re_\theta = 2200$ and for the LTRAC dataset at $Re_\theta = 1300$ present some differences, because of the variation of free-stream turbulence intensity. Therefore, the standard deviation of the vortices convection velocity for these three groups are presented on separate figures.

For the LML database, the wall-normal evolution of the standard deviation of the two in-plane components of the convection velocity and of the out-of plane component of the velocity at the center is shown in figure 6.55 for the vortices detected in the XY plane (spanwise vortices) and in figure 6.56 for the vortices detected in the YZ plane (streamwise vortices). For both planes, it was shown in section 5.2 that the Reynolds stresses of this database have a good universality in a mix wall-unit/external scaling, and therefore only the RMS of the velocity $u_i'^+$ at $Re_\theta = 7630$ is used for comparison. Overall, it can be seen that the vortex data follow the velocity data for all Reynolds numbers and in both measurements planes. Wu and Christensen (2006) plotted the histogram of the streamwise convection velocity fluctuations of vortices detected in the XY plane of a channel flow at $Re_\tau = 1760$ and of a boundary layer at $Re_\tau = 2350$, and found that the width of these histograms was proportional to the local RMS streamwise velocity. Besides this overall good agreement between $u_{c,i}'^+$ and $u_i'^+$, some small differences appear in the present data:

- in both planes, the standard deviation of the in-plane convection velocity (the u and v component for the XY plane and the v and w components for the YZ plane) is found to be lower than the local turbulence level, especially in the near wall region ($y/\delta \in [0; 0.05]$). This may indicate that the vortices are more stable in place than the surrounding flow;

- in the XY plane, the standard deviation of the spanwise velocity at the center of the vortices is slightly higher than the local turbulence level, especially in the very near-wall region ($y/\delta \in [0; 0.05]$) where a peak is observed. This component is parallel to the axis of the vortices, and hence the peak in RMS velocity may be indicative of some stretching/compression phenomenon;

- in the YZ plane, the standard deviation of the streamwise velocity is in good agreement with the local turbulence level, except that the near-wall peak is not retrieved;

The trends for the vortices detected in the XY plane are confirmed with the datasets in the lowest Reynolds number range ($Re_\theta = 1300$, $Re_\tau = 950$ and $Re_\theta = 2200$), as can be seen on figures 6.57 and 6.58. In the XY plane, it was checked that the standard deviation of the convection velocity of the prograde and retrograde vortices is the same.

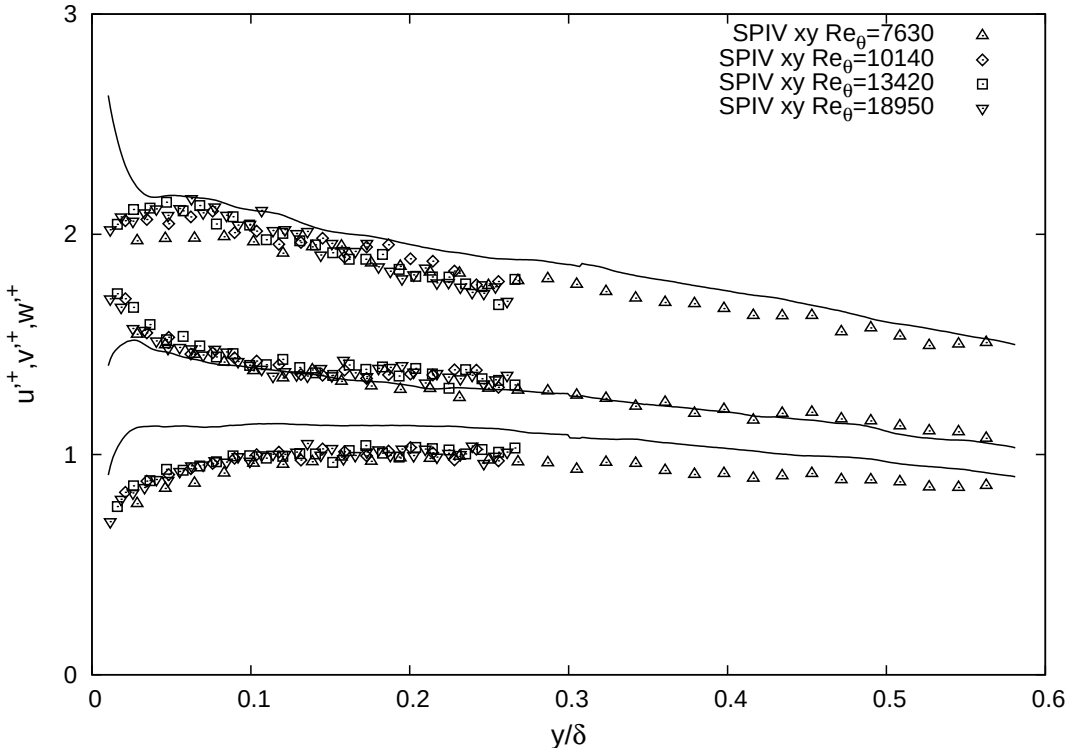

Figure 6.55: Wall-normal evolution of the standard deviation of the three components of the convection velocity of the spanwise vortices detected in XY plane (points) of the datasets at $Re_\theta \in [7630; 18950]$, compared to the standard deviation of the velocity in the dataset at $Re_\theta = 7360$ (solid line)

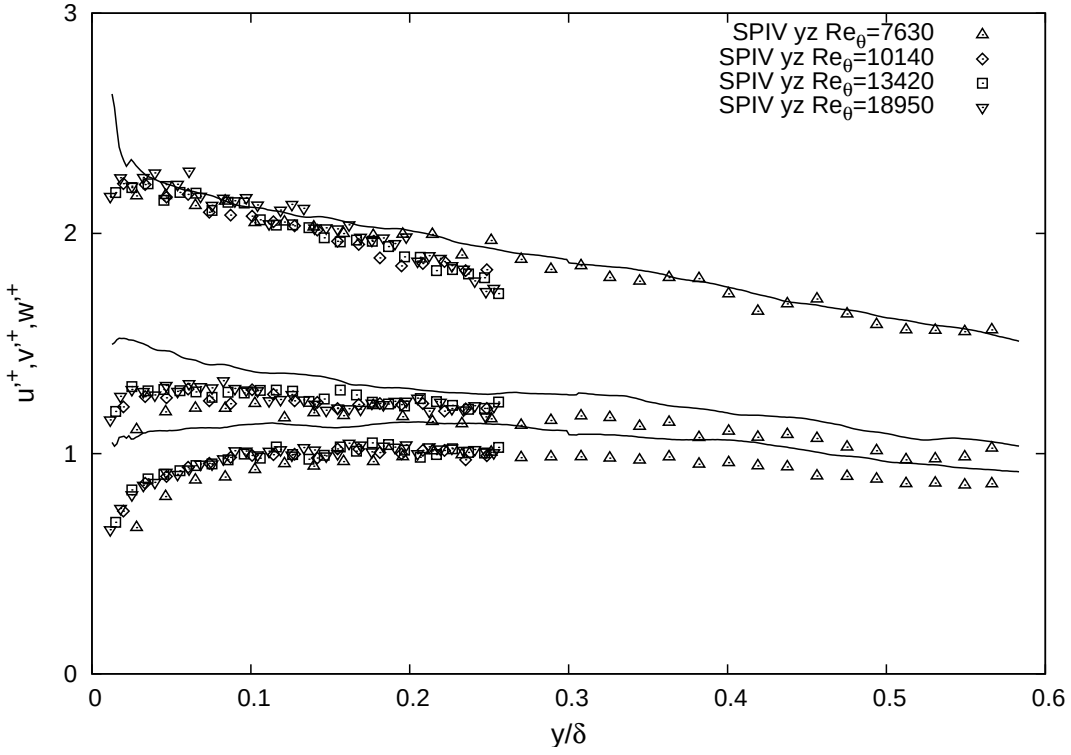

Figure 6.56: Wall-normal evolution of the standard deviation of the three components of the convection velocity of the streamwise vortices detected in YZ plane (points), compared to the standard deviation of the velocity in the dataset at $Re_\theta = 7360$ (solid line)

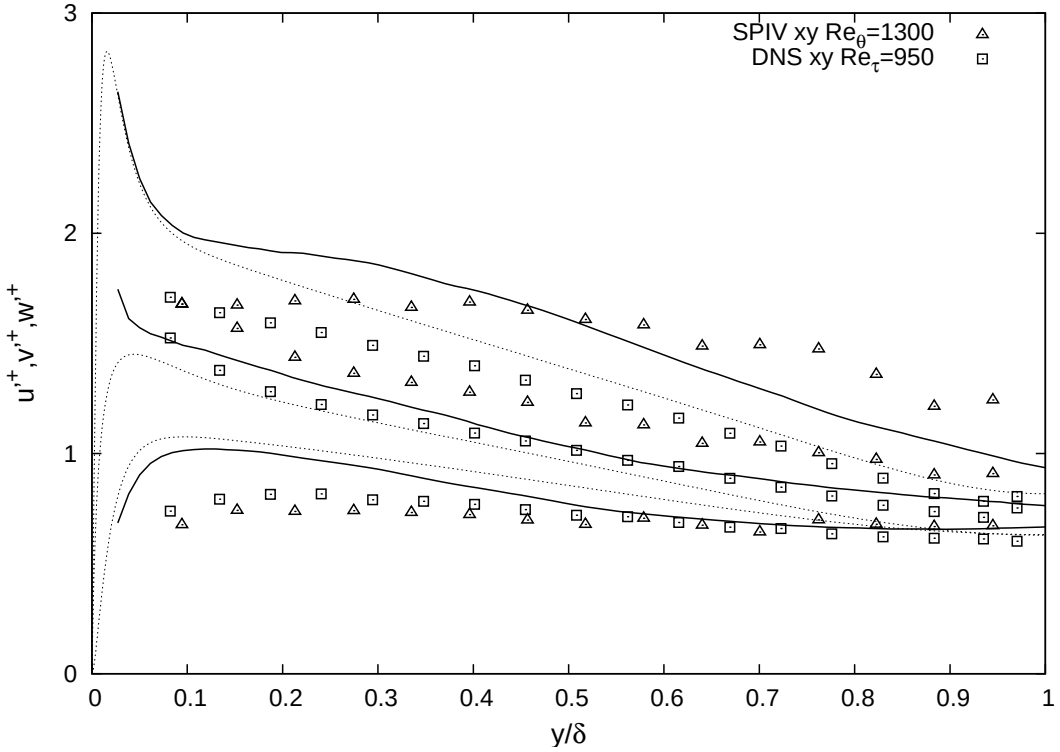

Figure 6.57: Wall-normal evolution of the standard deviation of the three components of the convection velocity of the spanwise vortices detected in XY plane (points) of the datasets at $Re_\theta = 1300$ and $Re_\tau = 950$, compared to the standard deviation of the velocity in these datasets (solid line and dashed line respectively)

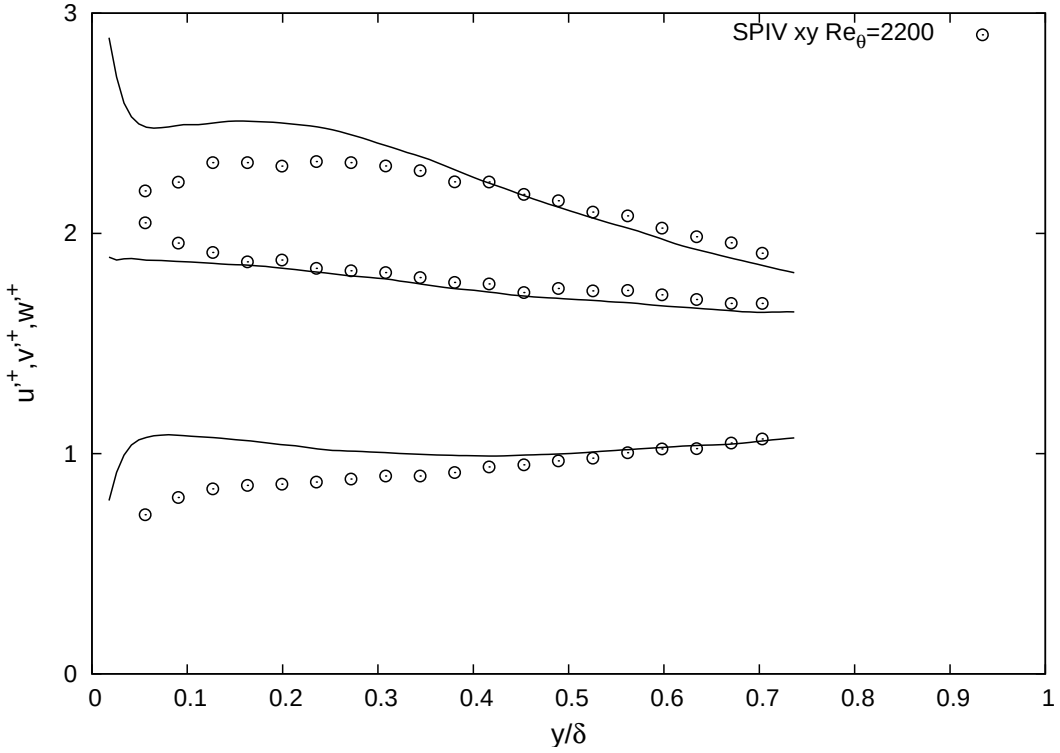

Figure 6.58: Wall-normal evolution of the standard deviation of the three components of the convection velocity of the spanwise vortices detected in XY plane (points) of the dataset at $Re_\theta = 2200$, compared to the standard deviation of the velocity in this dataset (solid line)

Chapter 7

Discussion

As stated by Robinson (1991), the study of streamwise and spanwise vortices *'lies at the heart of turbulent boundary layer research [...] because [these vortices] have the potential to function as a pump that transports mass and momentum across the mean velocity gradient'*. In the present contribution, these two types of vortices were analyzed using stereo-PIV datasets acquired in a streamwise/wall-normal (XY) and in spanwise/wall-normal (YZ) sections of turbulent boundary layers in a range of Reynolds number varying from $Re_\theta = 1300$ up to $Re_\theta = 18950$. Given the characteristics of the data, the logarithmic region ($40 < y^+$ and $y < 0.2\delta$) and the upper buffer layer ($20 < y^+ < 40$) is the main focus of the present study, but the wake region was also partially investigated. In the previous chapter, each characteristic of the vortices (radius, intensity, circulation, density and convection velocity) was separately discussed; in the present chapter, we try to relate these various findings in order to construct a global synthesis on the structure of near-wall turbulence in the context of the current knowledge in the scientific community.

A short preliminary point may be made on the nature of the data investigated in this thesis, and on their appropriateness for the study of streamwise and spanwise vortices. The strength of the present data resides in: the range of Reynolds number covered (6 Reynolds number distributed in the range $[1300; 18950]$); the good spatial resolution and low uncertainty of the measurements (that were carefully assessed); the fact that at a given Reynolds number, any comparison between the streamwise vortices and the spanwise vortices is expected to be entirely free from measurement effects, since the PIV parameters in the XY planes and the YZ planes are identical. One difficulty arises from the fact that the spatial resolution is not constant over the range of Reynolds number explored: the averaging areas of the datasets at $Re_\theta = 1300$, 2200, 7630, 13420 are pretty similar, while the dataset at $Re_\theta = 10140$ is significantly better resolved and the dataset at $Re_\theta = 18950$ is significantly lower resolved. This difficulty was minimized thanks to a careful assessment of the impact of the spatial averaging on the characteristics of the vortices detected, which makes it possible to distinguish between spatial resolution effects and Reynolds number effects.

The first main result of this thesis consist of a detailed characterization of the coherent structures in the near-wall region, the logarithmic region and the outer region of wall-bounded turbulent flows.

The near-wall region ($20 \leq y^+ \leq 100$), comprised of the upper buffer-layer and innermost part of the logarithmic layer, is predominantly populated with quasi streamwise vortices, in agreement with the findings of Robinson (1991), Jeong et al (1997), Carlier and Stanislas (2005) and Sheng et al (2008). The population of streamwise vortices increases very rapidly with wall-normal distance between $y^+ = 0$ and $y^+ = 60$, where a maximum density is reached (in agreement with Stanislas et al (2008)), and then starts to decrease, also very rapidly. The spanwise vortices are less numerous in that region; their density also increases with wall-normal distance, but at a slower rate, and the maximum density is reached at $y^+ \approx 100$ approximately. The wall-normal evolution of the radius and vorticity in wall-units shows that the streamwise vortices are on average smaller and more intense than the spanwise vortices in this region. The differences in radius magnitude between the different Reynolds number are consistent with the effect of the PIV IW size (see 6.1.3), which tends to indicate that the wall-normal evolution of the radius is in fact universal in wall-units. In particular, the datasets at $Re_\theta = 7630$ and $Re_\theta = 13420$, which have the same spatial resolution in wall-units, are in excellent agreement in this representation. On the dataset with the highest spatial resolution, it is found that at $y^+ \approx 50$, the radius of the streamwise vortices is about 15^+, in agreement with the estimation of Sheng et al (2008), while that of the spanwise vortices is about 20^+, in agreement with Carlier and Stanislas (2005). As far as the vorticity is concerned, a good universality in wall-units is observed for the streamwise and spanwise vortices, and the profiles are tangent to the van Driest profile as the wall-normal distance tends to zero. The vorticity decreases strongly with increasing wall-normal distance. In the near-wall region, the circulation of the vortices decreases strongly with wall-normal distance (especially the spanwise vortices). When non-dimensionalized with the local Kolmogorov scales, the vorticity of all vortices is found to be remarkably constant in both Reynolds number and wall-normal distance, while the radius is universal for the streamwise vortices only. Among the spanwise vortices, the retrograde vortices are much less numerous than the prograde vortices. Their radius is slightly smaller and less intense, with a radius comparable to that of the streamwise 'legs'. The density of the prograde vortices increases much faster with wall-normal distance than that of the retrogrades.

The logarithmic region ($100 \leq y^+$ and $y \leq 0.25\delta$) is found to be equally constituted of streamwise and spanwise vortices, in good consistency with them being part of the same 'cane-shaped' coherent structure (Robinson (1991)). Their density decays at a similar rate with wall-normal distance, and almost linearly. The characteristics of the streamwise and spanwise vortices are essentially similar in the logarithmic region. In particular, the radii of the streamwise and spanwise vortices are similar in wall-units. Again, the differences in radius within the range of Reynolds number investigated appear to be more a spatial-resolution effect rather than a Reynolds number effect. The mean radius increases slowly with wall-normal distance, and at the end of the logarithmic region, it tends to a value of 25^+ in the dataset with the highest spatial resolution. The vorticity of all vortices decreases with increasing wall-normal distance, but at a diminishing rate. The vorticity of the streamwise vortices shows excellent universality over the whole logarithmic region; in contrast that of the spanwise vortices show a good collapse for $100 < y^+ < 400$ only. The circulation of the streamwise vortices is found to be constant in wall units

roughly everywhere, while that of the spanwise vortices is approximately constant in the region $y^+ > 250$ only. The mean radius, non-dimensionalized with the local Kolmogorov lengthscale, does not depend on wall-normal distance anymore, and a relatively good universality is observed in Reynolds number around a value of 8η. For the mean vorticity, the universality in Reynolds number and in wall-normal distance is of even better quality, around a value of $\omega_0 = 1.5\tau^{-1}$. The PDF of the radius of the streamwise vortices shows better universality than for the spanwise vortices, with the most probable value for the radius being 7η. Finally, the PDF of vorticity of the streamwise and spanwise vortices show an excellent collapse in Kolmogorov scaling in the logarithmic region, with a most probable value of $0.9\tau^{-1}$.

The outer region ($0.25\delta < y < \delta$) could be analyzed in the PIV datasets at $Re_\theta = 1300$ and partially in the datasets at $Re_\theta = 2200$ and $Re_\theta = 7630$. The density of streamwise and spanwise vortices are still comparable, and continue to decrease with increasing wall-normal distance. It is found that while the density of the retrograde vortices stabilizes, that of the prograde vortices continues to decrease. It is noticeable that on the dataset with $Re_\theta = 2200$, the density of vortices is almost twice that of the dataset at $Re_\theta = 1300$ and that a slow increase of the number of retrograde vortices is visible at the edge of the boundary layer. This is probably an effect of the higher free-stream intensity for the dataset at $Re_\theta = 2200$. In each dataset, the prograde and retrograde vortex densities tend to be equal towards the edge of the boundary layer (or towards the channel centerline). In wall unit scaling, the mean radius of streamwise vortices in the dataset at $Re_\theta = 1300$ is found to increase strongly with wall-normal distance, while the behavior for the dataset at $Re_\theta = 2200$ and $Re_\theta = 7630$ is similar to that in the logarithmic region. It probably reveals a low Reynolds effect on the dataset at $Re_\theta = 1300$. However, in Kolmogorov scaling, the mean radius of the streamwise vortices are found to be constant with wall-normal distance for all dataset, similar to that in the logarithmic region. Some Reynolds number effects are clearly visible on the wall-normal evolution of the vorticity in wall-units in the outer region, but disappear when the vorticity is scaled in Kolmogorov units. Finally the PDF of vorticity and radius in Kolmogorov scaling are universal both in wall-normal distance and Reynolds number, comparable to that of the logarithmic region.

Now, it is of interest to discuss the similarities and differences with the structures detected in the DNS of channel flow at $Re_\tau = 950$. First of all, the streamwise and spanwise vortex densities show the same overall evolution with wall-normal distance across the three layers considered (near-wall, log, and outer region). In particular, the magnitude of vortex density is comparable to that of the BL dataset at $Re_\theta = 2200$ in the outer region, and the same increase of the retrograde density is visible towards the channel centerline, confirming that it is an intermittency effect with the external flow (with the free-stream turbulence intensity for the BL, and with the BL on the opposite wall for the channel flow). Wu and Christensen (2006) obtained a similar behavior in their measurements of the vortex densities in a channel flow. The evolution of the mean radius and vorticity in the channel flow are comparable to that of the boundary layer flow in wall-units (and especially to the dataset at $Re_\theta = 2200$), but show some differences in Kolmogorov scaling. The quantity $\omega\tau$ is found to be independent of wall-normal distance, but at a slightly higher level than in the boundary layer flow (about 10%), while the radius non dimensionalized with the Kolmogorov lengthscale is not independent of wall-normal distance and decreases with increasing wall-normal distance. Since the wall-normal evolution of the dissipation and Kolmogorov lengthscale in the LTRAC datasets at $Re_\theta = 1300$ was found to be in

excellent agreement with that of the DNS, this cannot be attributed to a difference in the Kolmogorov profiles. This behavior probably reveals a channel flow effect. As far as the PDF are concerned, they show a good collapse for the vorticity, but for the radius a shift towards smaller radii with increasing wall-normal distance is visible.

The second main result is the understanding of the generation mechanisms that can be inferred from the above vortex characterization. The maximum density of the streamwise and prograde spanwise vortices was observed in the near-wall region which indicates that they mostly find their origin at the wall. In this region, the density of streamwise vortices is larger than that of the spanwise vortices, and the density difference increases with decreasing wall-normal distance. This result clearly contradicts the generation mechanism of Hinze (1975), where hairpin structures are generated from an initial spanwise vortex being deformed into a hairpin loop through the joint action of wall-normal perturbation and mean shear. In fact it is more consistent with the mechanism proposed by Schoppa and Hussain (1997), where streamwise vortices are generated first through a streak instability, and spanwise vortices are generated in a second step through the roll up of an internal shear layer. In the logarithmic region, it appears that one spanwise vortex (of either sign) is statistically associated with one streamwise vortex. The population of progrades and streamwise vortices decreases with increasing wall-normal distance, probably because of vortex pairing or viscous destruction. In the region $60 < y^+ < 150$, the population of streamwise vortices decreases faster with wall-normal distance than in the region $y^+ > 150$. Stanislas et al (2008) showed that most of the vortex interaction occurs below $y^+ \approx 150$, and therefore the aforementioned difference in density rate can be attributed to a more intense streamwise vortex pairing occurring in the region $60 < y^+ < 150$.
The generation mechanism of retrograde vortices has never been clearly addressed in the past. In the present results, it was shown that the scaling of their radius and vorticity is overall comparable to that of prograde vortices. This tends to suggest that they have a common origin. However, it is unlikely that the retrograde vortices are created at the wall, because the mean velocity gradient is in strong opposition with their swirling motion in this region. One possibility is that the retrograde vortices originate from a half turnaround of some of the prograde vortices, occurring in the logarithmic and outer region. Then, moving towards the wall, the retrograde vortices have to face an increasingly strong velocity gradient and are progressively destroyed. On the wall-normal evolution of their mean density, it can be seen that the destruction of retrograde vortices starts at $y^+ = 150$, where the mean velocity gradient is about 1% of its maximum value at the wall.

The third set of results of this thesis are related to the scaling laws of the streamwise and spanwise vortex radius and vorticity throughout the range of Reynolds number explored ($Re_\theta \in [1300; 18950]$) and the three regions investigated (near-wall, log, outer regions). Two different scaling were tested: a wall-units scaling, and a Kolmogorov scaling. As far as the wall-unit scaling is concerned, it seems appropriate to reach Reynolds number universality in the near-wall and logarithmic region throughout the range of Reynolds number investigated (although the PIV spatial resolution did affect the values of radius retrieved). This result is in good agreement with the findings of Carlier and Stanislas (2005) in the highest range of Reynolds number. In the outer region, some low-Reynolds number effect were visible for the radius of the streamwise vortices at $Re_\theta = 1300$ (a steep increase of radius with wall-normal distance) and for the vorticity of the streamwise vortices in the dataset $Re_\theta = 1300$, $Re_\tau = 950$, and $Re_\theta = 2200$ (with was found to decrease with wall-normal distance while that of the dataset at $Re_\theta = 7630$ was sta-

bilized). The use of a Kolmogorov scaling could improve the universality of the radius and vorticity in two ways: first, it allows the reaching of wall-normal independence in addition to Reynolds number independence; and second, it is found to apply also in the outer region. The universality in Kolmogorov scaling was already tested (successfully) by Stanislas et al (2008), but only for the streamwise vortices over a more restricted range of Reynolds number ($Re_\theta = 7800$ and $Re_\theta = 15000$). Finally, the following values were found for the vortex radius and vorticity in Kolmogorov units: $r = 8\eta$ and $\omega_0 = 1.5\tau^{-1}$ in terms on mean values, and $r = 7\eta$ and $\omega_0 = 0.9\tau^{-1}$ in terms of most probable values. The Reynolds number of the vortices based on their mean radius and vorticity is about $(r^2\omega_0)/\nu = 8^2 * 1.5 * \eta^2/\tau \approx 100$.

Finally, the last set of results are related to the in-plane convection velocity of the vortices and to the axial flow velocity at their center. It was found, that on the whole, the vortices are convected with the mean flow, showing no significant self-induction consistently with the previous results of Carlier and Stanislas (2005) and Wu and Christensen (2006). The RMS of the in-plane convection velocity was also examined, and their wall-normal evolution was found to follow that of the surrounding flow, but at a lower level, indicating that the vortices are on average more stable than their environment. The RMS of the axial velocity of the vortices at their center was found to be comparable to that of surrounding flow, except for the spanwise vortices in the near-wall region where a peak of RMS spanwise velocity was observed.

Conclusions and perspectives

Conclusions

The goal of this work was to investigate coherent structures of near-wall turbulence, and more specifically to obtain statistical results over a large range of Reynolds numbers on the characteristics of the streamwise and spanwise vortices in order to better assess their scaling laws and generation mechanisms.

For that purpose, stereo-PIV measurements in streamwise/wall-normal and spanwise/ wall-normal planes of turbulent boundary layer flow were conducted in the LTRAC water-tunnel and LML wind-tunnel at six Reynolds numbers comprised between $Re_\theta = 1300$ and $Re_\theta = 18950$. The measurements feature good spatial resolution and low measurement uncertainty, as required for the study of the fine scale structure of turbulence.

The database was validated through the analysis of single point statistics and power spectra, that were compared with reference profiles derived from theory, hot-wire data, and DNS data. Some peak-locking effect on the PDF of the fluctuations was evidenced, but its effect on the moments of the velocity were shown to be negligible. In particular, the mean velocity profile and Reynolds stresses were in excellent agreement with the reference profiles. The SPIV power spectra showed excellent agreement with some DNS spectra in the low and intermediate wavenumber range, while the impact of measurement noise on the high wavenumber range was quantified. More specifically, the size of a structure that would be resolved with a signal-to-noise ratio of 1 was derived.

A coherent structure detection was then undertaken on the SPIV database, as well as on a DNS dataset at $Re_\tau = 950$. The detection is based on a fit of an Oseen vortex to the velocity field surrounding extrema of 2D swirling strength. For each vortex detected, this procedure allows the retrieval of circulation, radius, position of the center, convection velocity and vorticity at the center (defined as $\omega_0 = \Gamma/(\pi r^2)$). The effect of the PIV filtering over the interrogation window on the estimation of these characteristics was assessed. Therefore, it was possible to distinguish between spatial resolution effects and Reynolds number effects when analyzing the results.

The wall-normal evolution of some statistical quantities (mean, RMS, PDF) of the vortex characteristics were analyzed to obtain a better characterization of coherent structures in wall-bounded turbulence. It was found that the structures were convected with the mean velocity and a standard deviation following that of the surrounding flow, but

at a lower level indicating that the vortices were on average more stable than their environment. At all Reynolds numbers, the near-wall region is the most densely populated region, predominantly with streamwise vortices that are on average smaller and more intense than spanwise vortices. In contrast, the logarithmic region was equally constituted of streamwise and spanwise vortices having equivalent characteristics, and whose density was regularly decreasing with wall-normal distance. In the outer region, some differences between the datasets were observed depending on the scaling employed.

Two different scalings for the vortex radius and vorticity were tested: the wall-units scaling and the Kolmogorov scaling. In wall-unit scaling, a good universality in Reynolds numbers was observed in the near-wall and logarithmic region: the vorticity was found to be maximum at the wall, decreasing first rapidly and then slowly with increasing wall-normal distance; the radius was found to increase slowly with wall-normal distance in both regions, except for the streamwise vortices for which a sharp increase in radius was observed in the near-wall region. The wall-units scaling was found to be deficient in the outer region, where Reynolds number effects were observed. In contrast, the Kolmogorov scaling was found to be universal both in Reynolds number and wall-normal distance across the three regions investigated. Finally, the following values were found for the vortex radius and vorticity in Kolmogorov units: $r = 8\eta$ and $\omega_0 = 1.5\tau^{-1}$ in terms on mean values, and $r = 7\eta$ and $\omega_0 = 0.9\tau^{-1}$ in terms of most probable values.

Finally, the results obtained were interpreted in terms of vortices generation mechanisms. It was found that all vortices (streamwise, spanwise prograde, and spanwise retrograde) had their origin at the wall. The streamwise and spanwise prograde were found to be directly created there, possibly from a streak instability in good consistency with the model of Schoppa and Hussain (1997). A new generation mechanism is proposed for the spanwise retrograde vortices: it is suggested that they are created from a half turnaround of some prograde vortices, occurring preferentially in the log and outer region where the mean velocity gradient has decreased significantly and is therefore less unfavorable to them.

Perspectives

The post-processing undertaken in this thesis enabled a characterization of individual vortical structures. Now, there exist different post-processing tools, such as two-points correlation analysis (Stanislas et al (1999)), that are appropriate to investigate the spatial relationships existing between these structures. Thanks to the use of PCO 4000 camera with a large CCD array, the measurements in the LTRAC water-tunnel could be realized with a large spatial dynamic range, and hence are suitable for the study of both fine-scale and large scale structure (Herpin et al (2008)). Hence, a two point correlation analysis performed on these datasets could bring some interesting insight into the spatial relationship and large scale organization of individual structures.

Another interesting possibility to extend the results obtained in this thesis would be to investigate coherent structures at higher Reynolds number. In the present study, the range of Reynolds number is already spanning more than one decade ($Re_\theta \in [1300; 18950]$).

The only other flow facility suitable for high-spatial resolution measurements at higher Reynolds numbers is the wind-tunnel of Melbourne University in Australia, with a maximum Reynolds number on the order of $Re_\theta = 50000$. On the numerical side, the progress in Reynolds number is mainly limited by the available computational ressources (Jiménez (2003)). The DNS dataset at the highest Reynolds number currently available was performed recently by Jiménez group and is at $Re_\tau = 2000$. It would be of interest to perform a coherent structure detection on this dataset, and to compare the results with those obtained in the DNS dataset at $Re_\tau = 950$ and with the SPIV dataset at similar conditions that is the lowest Reynolds number in the LML wind-tunnel at $Re_\theta = 7630$.

The repetition rate of PIV systems was drastically improved over the recent years due to the technological advent of CMOS digital camera and Nd:YLF lasers. The associated technique is called high-repetition PIV or time-resolved PIV (Baur and Koengeter (2000)). Recently Foucaut and Coudert (2008) realized a time-resolved SPIV experiments in a plane orthogonal to the mean flow in the LML wind-tunnel. The post-processing of this dataset using the present detection technique could bring some new insight into the dynamics of coherent structures, and in particular into their generation mechanisms. Note that, for technological reasons, the application of true time-resolved PIV is in fact limited in Reynolds numbers (the time-resolved measurement in the LML wind-tunnel were realized at $Re_\theta = 7800$ only), and therefore a complete study involving measurement over a large range of Reynolds number is not possible today with this technique.

The extension towards volumetric data is highly interesting because it can give access to the full flow topology via the three dimensional velocity gradient tensor (Chong and Perry (1990)), and hence to an unambiguous characterization of the coherent structures in turbulent flows. Nowadays, such data is readily available from DNS. A new refinement of the PIV technique, Tomographic PIV, can also give access to instantaneous 3D information (Elsinga et al (2006)) but this technique is still in development: more specifically, the spatial resolution and measurement uncertainty of this technique require further assessment (especially in the spectral domain). Besides, the post-processing of 3D data requires a detection technique generalized to three-dimensions: the algorithm used in the present thesis works only on planar data and would necessitate some adaptation to be extended to three dimensions.

Finally, this study was focused on the small-scale structures created at the wall, and propagating outward from the wall. A number of studies have evidenced the existence of very large scale structure populating the outer region and having an influence on the near-wall region (Hutchins and Marusic (2007)). These structure are clearly beyond the scope of the present study. A recent collaborative experiment (Foucaut et al (2007), Tutkun et al (2009)), performed in the framework of the WALLTURB European project, combined simultaneous SPIV and hot-wire measurements in a YZ plane of the turbulent boundary layer developing in the LML wind-tunnel. It provides a dataset suitable for the investigation of these very large scale structures.

Bibliography

Acarlar MS, Smith CR (1987a) A study of hairpin vortices in a laminar boundary layer. part 1: hairpin vortices generated by hemisphere protuberance. J Fluid Mech 175:1–41

Acarlar MS, Smith CR (1987b) A study of hairpin vortices in a laminar boundary layer. part 2: hairpin vortices generated by a fluid injection. J Fluid Mech 175:43–83

Adrian RJ (1991) Particle imaging techniques for experimental fluid mechanics. Annu Rev Fluid Mech 23:261–304

Adrian RJ (2007) Hairpin vortex organization in wall turbulence. Physics of fluid 19

Adrian RJ, Christensen KT, Liu ZC (2000a) Analysis and interpretation of instantaneous turbulent velocity fields. Exp Fluids 29:275–290

Adrian RJ, Meinhart C, Tomkins C (2000b) Vortex organization in the outer region of the turbulent boundary layer. J Fluid Mech 422:1–54

Agui JC, Jiménez J (1987) On the performance of particle tracking. J Fluid Mech 185:447–468

Baur T, Koengeter J (2000) High-speed piv and the post-processing of time-series results. Euromech 411

Blackburn HM, Mansour NN, Cantwell BJ (1996) Topology of fine-scale motions in turbulent channel flow. J Fluid Mech 310:269–292

Blackwelder RF (1997) An experimental model for near-wall structure. Computational Mechanics Publications

Blackwelder RF, Eckelmann H (1979) Streamwise vortices associated with the bursting phenomenon. J Fluid Mech 94:577–594

Brown GL, Thomas ASW (1977) Large structure in a turbulent boundary layer. Physics of Fluids 20(10):S243–S251

Calluaud D, David L (2004) Stereoscopic particle image velocimetry measurements of the flow around a surface-mounted block. Exp Fluids 36:53–61

Cantwell B (1981) Organized motion in turbulent flow. Annu Rev Fluid Mech 13:437–515

Carlier J (2001) Etude des structures coherentes de la turbulence de paroi a grand nombre de reynolds par velocimetrie par images de particules. PhD thesis, Universite des Sciences et des Technologies de Lille

Carlier J, Stanislas M (2005) Experimental study of eddy structures in a turbulent boundary layer using particle image velocimetry. J Fluid Mech 535:143–188

Chakraborty P, Balachandar S, Adrian R (2005) On the relationships between local vortex identification schemes. J Fluid Mech 535:189–224

Chong MS, Perry AE (1990) A general classification of three-dimensional flow fields. Phys Fluids 5:765–777

Christensen KT (2004) The influence of peak-locking errors on turbulence statistics computed from PIV ensemble. Exp Fluids 36:484–497

Christensen KT, Adrian RJ (2001) Statistical evidence of hairpin vortex packets in wall turbulence. J Fluid Mech 431:433–443

Coles D (1956) The law of the wake in the turbulent boundary layer. J Fluid Mech 1:191–226

Coles DE (1962) The turbulent boundary layer in a compressible fluid. Tech. Rep. R-403-PR, United states airforce project RAND, appendix A: A manual for experimental boundary layer practice for low-speed flow

Corino ER, Brodkey RS (1969) A visual investigation of the wall region in turbulent flow. J Fluid Mech 37:1–30

Coudert S, Schon JP (2001) Back-projection algorithm with misalignement corrections for 2D3C stereoscopic PIV. Measurement science and technology 12:1371–1381

Cousteix J (1989) Turbulence et couche limite. Cepadues-Editions

Das SK, Tanahashi M, Shoji K, Miyauchi T (2006) Statistical properties of coherent fine eddies in wall-bounded turbulent flows by direct numerical simulation. Theor Comput Fluid Dyn 20:55–71

Degraaff DB, Eaton JK (2000) Reynolds-number scaling of the flat plate turbulent boundary layer. J Fluid Mech 422:319–346

DelAlamo JC, Jiménez J, Zandonade P, Moser RD (2004) Scaling of energy spectra of turbulent channels. J Fluid Mech 500:135–144

DelAlamo JC, Jiménez J, Zandonade P, Moser RD (2006) Self-similar vortex clusters in the turbulent logarithmic region. J Fluid Mech 561:329–358

van Doorne CWH, Westerweel J, Nieuwstadt FTM (2003) Measurement uncertainty of stereoscopic-PIV for flow with large out-of-plane motion. EUROPIV2 workshop , Zaragoza, Spain

Elsinga GE, Scarano F, Winieke B, van Oudheusden BW (2006) Tomographic particle image velocimetry. Exp Fluids 41:933–947

Erm L (1988) Low reynolds number turbulent boundary layers. PhD thesis, Melbourne Uni.

Erm L, Joubert P (1991) Low reynolds number turbulent boundary layer. J Fluid Mech 230:1–44

Falco RE (1977) Coherent motions in the outer region of turbulent boundary layers. Physics of Fluids 20(10):S124–S132

Fernholz HH, Finley PJ (1996) The incompressible zero pressure gradient turbulent boundary layer: an assessment of the data. Prog Aerospace Sci 32:245–311

Foucaut JM, Coudert S (2008) Etude de la zone proche paroi de la couche limite turbulente Ã l'aide de la piv stereoscopique rapide. In: CongrÃ¨s Francophone de Techniques Laser, CFTL 2008, Futuroscope, 16 - 19 septembre 2008

Foucaut JM, Stanislas M (2002) Some considerations on the accuracy and frequency response of some derivative filters applied to particle image velocimetry vector fields. Meas Sci Technol 13:1058–1071

Foucaut JM, Milliat B, Perenne N, Stanislas M (2003) Characterisation of different PIV algorithm using the europiv synthetic image generator and real images from a turbulent boundary layer. EUROPIV2 workshop , Zaragoza, Spain

Foucaut JM, Carlier J, Stanislas M (2004) PIV optimization for the study of turbulent flow using spectral analysis. Meas Sci Technol 15:1046–1058

Foucaut JM, Coudert S, Kostas J, Stanislas M, Braud P, Fourment C, Delville J, Tutkun M, Mehdi F, Johansson P, George WK (2007) Study of the unsteady aspects of turbulence in the near wall region of a boundary layer using high speed spiv. In: 7th International Symposium on Particle Image Velocimetry

Ganapathisubramani B, Longmire E, Marusic I (2003) Characteristics of vortex packets in turbulent boundary layers. J Fluid Mech 478:35–46

Ganapathisubramani B, Longmire E, Marusic I (2006) Experimental investigation of vortex properties in a turbulent boundary layer. Physics of Fluids 18:05510,501–05510,514

George WK (2006) Recent advancements toward the understanding of turbulent boundary layers. AIAA journal 44(11)

George WK (2007) Is there a universal log law for turbulent wall-bounded flows ? Philosophical Transactions of the Royal Society of London, series A 365:789–806

Grant I (1997) Particle image velocimetry: A review. Proceedings of the Institution of Mechanical Engineers. Part C. Mechanical engineering science, vol 211

Guala M, Hommema S, Adrian R (2006) Large scale and very large scale motions in turbulent pipe flow. J Fluid Mech 554:521–542

Guezennec YG (1989) On the shape and dynamics of wall structures in turbulent channel flow. Phys Fluids A 1(4)

Guezennec YG, Brodkey RS, Trigui N, Kent JC (1994) Algorithms for fully automated three-dimensional particle tracking velocimetry. Exp Fluids 17:209–219

Guichard L, Lecordier B, Reveillon J (1998) Evaluation des algorithmes utilises en piv grace a la simulation numerique directe. 6eme Congres Francophone de Velocimetrie Laser

Hambleton WT, Hutchins N, Marusic I (2006) Simultaneous orthogonal-plane particle image velocimetry measurements in a turbulent boundary layer. J Fluid Mech 560:53–64

Head MR, Bandyopadhyay P (1981) New aspects of turbulent boundary layer structure. J Fluid Mech 107:297–338

Herpin S, Wong CY, Stanislas M, Soria J (2008) Stereoscopic PIV measurements of a turbulent boundary layer with a large spatial dynamic range. Exp Fluids 45:745–763

Hinze JO (1975) Turbulence. McGraw Hill, New York

Hoyas S, Jiménez J (2006) Scaling of the velocity fluctuations in turbulent channels in turbulent channels up to $re_tau = 2003$. Physics of fluid 18

Hunt JCR, Wray AA, Moin P (1988) Eddies, sreams, and convergence zones in turbulent flows. Summer Program of the Center for Turbulence research, pp 193–207

Hutchins N, Marusic I (2007) Evidence of very long meandering features in the logarithmic region of turbulent boundary layers. J Fluid Mech 579:1–28

Hutchins N, Hambleton WT, Marusic I (2005) Inclined cross-stream stereo particle image velocimetry measurements in turbulent boundary layers. J Fluid Mech 541:21–54

Jeong J, Hussain F (1995) On the identification of a vortex. J Fluid Mech 285:69–94

Jeong J, Hussain F, Schoppa W, Kim J (1997) Coherent structures near the wall in a turbulent channel flow. J Fluid Mech 332:185–214

Jie L (2006) Etude detaillée des structures coherentes de la zone tampon de la turbulence de paroi a l'aide de données de PIV stereoscopique. PhD thesis, Ecole Centrale de Lille et Université de Lille

Jiménez J (2003) Computing high-reynolds-number turbulence: will simulations ever replace experiments ? J of Turbulence 4

Kahler CJ, Kompenhans J (2000) Fundamentals of multiple plane stereo particle image velocimetery. Exp Fluids Suppl:S70–S77

Kang SJ, Tanahashi M, Miyauchi T (2007) Dynamics of fine scale eddy clusters in turbulent channel flows. J of Turbulence 8(52)

Keane RD, Adrian RJ (1990) Optimization of particle image velocimeters. part 1 : Double pulsed systems. Meas Sci Technol 1:1202–1215

Keane RD, Adrian RJ, Zhang Y (1995) Super-resolution particle image velocimetry. Meas Sci Technol 6:754–768

Kim J, Moin P (1986) The structure of the vorticity field in turbulent channel flow. part 2. study of ensemble-averaged fields. appendix: Results from direct numerical simulation. J Fluid Mech 162:339–363

Kim J, Moin P, Moser R (1987) Turbulence statistics in fully developed channel flow at low reynolds number. J Fluid Mech 177:133–166

Kim KC, Adrian RJ (1999) Very large-scale motion in the outer layer. Phys Fluids 11(2):417–422

Klebanoff PS (1955) Characteristics of turbulence in a boundary layer with zero pressure gradient. Tech. rep., NACA

Kline SJ, Reynolds WC, Schraub WC, Runstadler PW (1967) The structure of turbulent boundary layers. J Fluid Mech 30:741–773

Kostas J (2002) An experimental investigation of the structure of a turbulent backward facing step flow. PhD thesis, Monash Uni.

Kostas J, Foucaut J, Stanislas M (2005) Application of double spiv on the near wall turbulence structure of an adverse pressure gradient turbulent boundary layer. 6th Intl. Symp. on PIV, Pasadena, California

Lecordier B, Trinite M (2003) Advanced PIV algorithms with image distorsion for velocity measurements in turbulent flows. EUROPIV2 workshop , Zaragoza, Spain

Lecordier B, Westerweel J (2003) The EUROPIV synthetic image generator (S.I.G.). EUROPIV2 workshop , Zaragoza, Spain

Lin J, Foucaut JM, Laval JP, Perenne N, Stanislas M (2008a) Assessment of different SPIV processing methods for an application to near-wall turbulence, vol 112. Springer Berlin / Heidelberg

Lin J, Laval JP, Foucaut JM, Stanislas M (2008b) Quantitative characterization of coherent structures in the buffer layer of near-wall turbulence. part 1: streaks. Exp Fluids 45:999–1013

Marusic I, Hutchins N (2008) Study of the log-layer structure in wall turbulence over a very large range of reynolds number. Flow Turbulence combust 81:115–130

Meynart R (1983) Mesure de champs de vitesse d'ecoulements fluides par analyse de suites d'images obtenues par diffusion d'un feuillet lumineux. PhD thesis, PhD thesis, Universite libre de Bruxelles

Meynart R (1984) Speckle velocimetry study of vortex pairing in low-re unexcited jet. Phys Fluids 26

Millikan CD (1939) A critical discussion of turbulent flows in channels and circular tubes. proc. 5th Congress of Appl. Mech. Cambridge, Mass., Wiley, pp 386–392

Moin P, Kim J (1985) The structure of the vorticity field in turbulent channel flow. part 1. analysis of instantaneous fields and statistical correlations. J Fluid Mech 155:441–464

Nychas SG, Hershey HC, Brodkey RS (1973) A visual study of turbulent dhear flow. J Fluid Mech 61:513–540

Panton RL (ed) (1997) Self-sustaining mechanisms of wall turbulence. Computational Mechanics Publications

Parker K, von Ellenrieder K, Soria J (2005) Using stereo multigrid (SMDPIV) measurements to investigate the vortical skeleton behind a finite-span flapping wing. Exp Fluids 39:281–298

Perry AE, Chong MS (1982) On the mechanism of wall turbulence. J Fluid Mech 119:173–217

Perry AE, Henbest S, Chong MS (1986) A theoretical and experimental study of wall turbulence. J Fluid Mech 165:163–199

Prandtl L (1904) Uber flussigkeitsbewegung bei sehr kleiner reibung. proc. Third Intern. Math. Congress, Heidelberg, pp 484–491

Prandtl L (1932) Zur turbulenten stromung in rohren und langs. Ergeb Aerodyn Versuchsanst Gottingen 4:18–29

Prasad A, Jensen K (1995) Scheimpflug stereocamera for particle image velocimetry in liquid flow. Applied optics 34(30):7092–7099

Prasad AK (2000) Stereoscopic particle image velocimetry. Exp Fluids 29:103–116

Praturi RK, Brodkey RS (1978) A stereoscopic visual study of coherent structures in turbulent shear flow. J Fluid Mech 89:251–272

Pu Y, Meng H (2000) An advanced off-axis holographic particle image velocimetry (HPIV) system. Exp Fluids 29:184–197

Raffel M, Willert C, Wereley ST, Kompenhans J (1998) Particle image velocimetry – a practical guide, 1st edition. Springer, Germany

Raffel M, Willert C, Wereley ST, Kompenhans J (2007) Particle image velocimetry – a practical guide, 2nd edition. Springer, Germany

Reynolds O (1895) On the dynamical theory of incompressible viscous fluids and the determination of the criterion. Philosophical Transactions of the Royal Society of London, series A 186

Robinson SK (1991) Coherent motions in the turbulent boundary layer. Annu Rev Fluid Mech 23:601–639

Scarano F (2002) Iterative image deformation methods in PIV. Measurement science and technology 13:R1–R19

Scarano F, LDavid, Bsibsi M, Calluaud D (2005) S-PIV comparative assessment: image dewarping+misalignment correction and pinhole+geometric back-projection. Exp Fluids 39:257–266

Schlichting H, Gersten K (2001) Boundary layer theory, 8th revised and enlarged edition

Schoppa W, Hussain F (1997) Genesis and dynamics of coherent structures in near-wall turbulence: a new look. Computational Mechanics Publications

Schoppa W, Hussain F (2002) Coherent structure generation in near-wall turbulence. J Fluid Mech 453:57–108

Sheng J, Malkiel E, Katz J (2008) Using digital holographic microscopy for simultaneous measurements of 3d near wall velocity and wall shear stress in a turbulent boundary layer. Exp Fluids 45:1023–1035

Smith CR (1984) A synthetized model of near-wall behavior in turbulent boundary layers. Proc. of the 8th symposium on turbulence, university of Missouri-Rolla

Smith CR, Walker JDA (1997) Sustaining mechanisms of turbulent boundary layers: the role of vortex development and interactions. Computational Mechanics Publications

Soloff S, Adrian R, Liu ZC (1997) Distortion compensation for generalized stereoscopic particle image velocimetry. Measurement science and technology 8:1441–1454

Soria J (1996) An investigation of the near wake of a circular cylinder using a video-based digital cross-correlation particle image velocimetry technique. Experimental Thermal and Fluid Science 12:221–233

Soria J (2006) chapter 7 of the Lectures notes on Turbulence and Coherent Structures in Fluid, Plasma and non-linear media. World Scientific

Soria J, Atkinson C (2008) Towards 3c-3d : Volume fluid velocity field measurement - tomographic digital holographic PIV (tomo-HPIV). Measurement science and technology 19:doi: 10.1088/0957–0233/19/7/074,002, online at http://stacks.iop.org/MST/19/074,002

Soria J, Cater J, Kostas J (1999) High resolution multigrid cross-correlation digital piv measurements of a turbulent starting jet using half frame image shift shift recording. Optics and laser technology 31:3–12

Spalart PR (1988) Direct simulation of a turbulent boundary layer up to $R_\theta = 1410$. J Fluid Mech 187:61–88

Stanislas M (2005) Main results of the second international piv challenge. Exp Fluids 39:170–191

Stanislas M, Carlier J, Foucaut JM, Dupont P (1999) Double spatial correlations, a new experimental insight into wall turbulence. C R Acad Sci Paris 327:55–61

Stanislas M, Perret L, Foucaut JM (2008) Vortical structures in the turbulent boundary layer: a possible route to a universal representation. J Fluid Mech 602:327–342

Swearingen JD, Blackwelder RF (1987) The growth and breakdown of streamwise vortices in the presence of a wall. J Fluid Mech 182:255–290

Tanahashi M, Kang SJ, Miyamoto T, Shiokawa S, Miyauchi T (2004) Scaling law of fine scale eddies in turbulent channel flow up to $Re_\tau = 800$. Int J Heat and Fluid Flow 25:331–340

Tennekes H, Lumley JL (1972) A first course in turbulence. the MIT press

Theodorsen T (1952) Mechanism of turbulence. Proc. 2nd. Midwestern Conf.on Fluid Mechanics, Ohio State Univ. Columbus

Tomkins CD, Adrian RJ (2003) Spanwise structure and scale growth in turbulent boundary layers. J Fluid Mech 490:37–74

Townsend AA (1976) The structure of turbulent shear flow. Cambridge university press

Tutkun M, George WK, Delville J, Stanislas M, Foucaut JM, Coudert S (2009) Two-point correlations in high reynolds number flat plate turbulent boundary layer. submitted to J of Turbulence

Waleffe F, Kim J (1997) How streamwise rolls and streaks self-sustain in a shear flow. Computational Mechanics Publications

Wallace JM, Eckelmann H, Brodkey RS (1972) The wall region in turbulent shear flow. J Fluid Mech 54:39–48

Westerweel J (1993) Digital particle image velocimetry - theory and application. PhD thesis, Delft university

Westerweel J (1996) Measurement of fully developed turbulent pipe flow with digital particle image velocimetry. Exp Fluids 20:165–177

Westerweel J (1997) Fundamentals of digital particle image velocimetry. Measurement science and technology 8:1379–1392

Westerweel J, van Oord J (2000) Stereoscopic PIV measurements in a turbulent boundary layer. Kluwer academic publishers

Westerweel J, Adrian RJ, Eggels JGM, Nieuwstadt FTM (1993) Measurements with particle image velocimetry of fully developed turbulent pipe flow at low reynolds number. Int. Symp. Appl. Laser Tech. Fluid Mech.

Westerweel J, Dabiri D, Gharib M (1997) The effect of a discrete window offset on the accuracy of cross-correlation analysis of piv. Exp Fluids 23:20–28

White FM (1974) Viscous fluid flow. McGraw-Hill

Wieneke B (2005) Stereo-piv using self-calibration on particle images. Exp Fluids 39:267–280

Willert C (1997) Stereoscopic digital particle image velocimetry for application in wind-tunnel flows. Measurement Science and Technology 8:1465–1479

Willert CE, Gharib M (1991) Digital particle image velocimetry. Exp Fluids 10:181–193

Wu Y, Christensen KT (2006) Population trends of spanwise vortices in wall turbulence. J Fluid Mech 568:55–76

Zang W, Prasad AK (1997) Performance evaluation of a scheimpflug stereocamera for particle image velocimetry. App Opt 36:8738–8744

Zhou J, Meinhart CD, Balachandar S, Adrian RJ (1997) Formation of coherent hairpin packets in wall turbulence. Computational Mechanics Publications

Zhou J, Adrian RJ, Balachander S, Kendall TM (1999) Mechanisms for generating coherent packets of hairpin vortices in channel flow. J Fluid Mech 387:353–396

Résumé

Ce travail est une étude expérimentale de l'influence du nombre de Reynolds sur les structures tourbillonnaires longitudinales et transverses de la turbulence de paroi. Une campagne de mesure par Vélocimétrie par Images de Particules (PIV) stéréoscopique est réalisée dans des plans longitudinaux/normaux à la paroi (XY), et dans des plans normaux/transversaux (YZ) des couche limites de la soufflerie du LML et du tunnel à eau du LTRAC, à six nombre de Reynolds compris entre $Re_\theta = 1300$ et $Re_\theta = 18950$. Les mesures ont une bonne résolution spatiale et une faible incertitude. La base de données est validée au travers de l'analyse de grandeurs statistiques de l'écoulement (moyenne et RMS de la vitesse, histogramme des fluctuations, spectres de puissance), comparées à des profils de référence issus de la théorie, de mesures fils-chauds ou de données issues de la Simulation Numrique Directe (DNS) d'un écoulement turbulent de canal. Une détection de tourbillon, basée sur l'ajustement d'un modèle de tourbillon autour des maxima d'intensité tourbillonaire, est ensuite entreprise sur les données de stéréo-PIV ansi que sur des données DNS à $Re_\tau = 950$. L'évolution des caractéristiques des tourbillons (rayon, vorticité, circulation, vitesse de convection) avec la distance à la paroi 'y' est ensuite analysée dans deux représentations adimensionnées: l'une en unités de paroi, et l'autre en unités de Kolmogorov. Une bonne universalité en nombre de Reynolds est obtenue en unités de paroi dans la zone tampon et la zone logarithmique, mais pas dans la zone externe de l'écoulement. Les unités de Kolmogorov permettent d'obtenir une bonne universalité dans les trois zones étudiées, à la fois en Reynolds et en 'y'. Finalement, les mécanismes responsables de la génération des tourbillons sont discutés.

Abstract

This work is an experimental study of the influence of the Reynolds number on the characteristics of the streamwise and spanwise vortical structures in near-wall turbulence. Stereo-PIV measurements in streamwise/wall-normal (XY) and spanwise/wall-normal (ZY) planes of turbulent boundary layer flow are conducted in the LTRAC water-tunnel and LML wind-tunnel at six Reynolds numbers comprised between $Re_\theta = 1300$ and $Re_\theta = 18950$. The measurements feature good spatial resolution and low measurement uncertainty. The database is validated through an analysis of some single-points statistics (mean and RMS velocity, PDF of the fluctuations) and of the power spectra, compared with reference profiles from theory, hot-wire measurements and DNS data.
A coherent structure detection is then undertaken on the SPIV database, as well as on a DNS dataset at $Re_\tau = 950$. The detection is based on a fit of an Oseen vortex to the velocity field surrounding extrema of 2D swirling strength. The wall-normal evolution of some statistical quantities (mean, RMS, PDF) of the vortex characteristics (radius, vorticity, circulation, convection velocity...) is analyzed, using two different scalings: the wall-unit scaling and the Kolmogorov scaling. In wall-unit scaling, a good universality in Reynolds numbers is observed in the near-wall and logarithmic region, but some Reynolds number effects are visible in the outer region of the flow. In contrast, the Kolmogorov scaling was found to be universal both in Reynolds number and wall-normal distance across the three regions investigated. Finally, the results obtained are interpreted in terms of vortices generation mechanisms.